



MAX-PLANCK-INSTITUT  
FÜR POLYMERFORSCHUNG

# Organic Electrochemical Transistor for Biological Applications

DISSERTATION

zur Erlangung des Grades „Doktor der Naturwissenschaften“

am Fachbereich Chemie, Pharmazie, Geographie und Geowissenschaften

der Johannes Gutenberg-Universität

in Mainz

Leona Viola Lingstedt

geboren in Bad Nauheim

Mainz, den 5. März 2019



The thesis was carried out from March 2015 until February 2019 in the group [REDACTED]

[REDACTED] at the Max Planck Institute for Polymer Research in Mainz.

Dekan: [REDACTED]

Prodekan: [REDACTED]

1. Berichterstatter: [REDACTED]

2. Berichterstatter: [REDACTED]

Tag der mündlichen Prüfung: 29.05.2019



*Was immer Du tun kannst oder wovon Du träumst – fange es an.  
In der Kühnheit liegt Genie, Macht und Magie.*

*(Johann Wolfgang von Goethe)*



# Table of Contents

GLOSSARY .....	I
ABBREVIATIONS.....	III
MOTIVATION & OUTLINE.....	1
INTRODUCTION .....	5
1.1.    BIOELECTRONICS .....	6
1.2.    PEDOT:PSS.....	9
1.3.    ORGANIC ELECTROCHEMICAL TRANSISTOR .....	12
1.3    EPITHELIAL CELLS AND CELL JUNCTIONS .....	17
EXPERIMENTAL .....	21
2.1. DEVICE FABRICATION .....	22
2.1.1. <i>Fabrication of OECTs</i> .....	22
2.1.2. <i>Microfabrication of Electrodes</i> .....	24
2.2. CELL PREPARATION .....	25
2.2.1. <i>Culturing of Caco-2 Cells</i> .....	25
2.2.2. <i>Culturing of MDA Cells</i> .....	26
2.2.3. <i>Filter Preparation</i> .....	26
2.2.4. <i>Preparation of Tight Junction Modulators</i> .....	27
2.2.5. <i>Immunofluorescence Staining</i> .....	27
2.3. CHARACTERIZATION METHODS.....	28
2.3.1. <i>Electrical Characterization</i> .....	28
2.3.2. <i>Spectroscopical Characterization</i> .....	31
2.3.3. <i>Microscopy Characterization</i> .....	32
EFFECT OF DMSO SOLVENT TREATMENTS ON THE PERFORMANCE OF PEDOT:PSS-BASED ORGANIC ELECTROCHEMICAL TRANSISTORS .....	33
3.1. INTRODUCTION.....	34
3.2. RESULTS AND DISCUSSION .....	35
3.3. SUMMARY OF CHAPTER 3.....	42
3.4. SUPPORTING INFORMATION OF CHAPTER 3 .....	43
HIGH-SENSITIVITY ION DETECTION AT LOW VOLTAGES WITH CURRENT-DRIVEN ORGANIC ELECTROCHEMICAL TRANSISTORS .....	51
4.1. INTRODUCTION.....	52

4.2. RESULTS.....	53
4.2.1. Device Structure and Measurements.....	53
4.2.2. Current-Driven OECT Configuration.....	55
4.2.3. Impact of the Ion Concentration.....	57
4.2.4. Investigation of the Ion Sensitivity.....	58
4.2.5. Low-Voltage Operation.....	60
4.2.6. Ion-Selective Operation.....	62
4.2.7. Discussion.....	64
4.3. SUMMARY OF CHAPTER 4.....	66
4.4. SUPPORTING INFORMATION OF CHAPTER 4.....	67
PROBING THE IMPEDANCE OF A BIOLOGICAL TISSUE WITH PEDOT:PSS-COATED METAL ELECTRODES: EFFECT OF ELECTRODE SIZE ON SENSING EFFICIENCY.....	71
5.1. INTRODUCTION.....	72
5.2. RESULTS AND DISCUSSION.....	74
5.3. SUMMARY OF CHAPTER 5.....	81
5.4. SUPPORTING INFORMATION OF CHAPTER 5.....	82
MONITORING OF CELL LAYER INTEGRITY WITH A CURRENT-DRIVEN ORGANIC ELECTROCHEMICAL TRANSISTOR.....	87
6.1. INTRODUCTION.....	88
6.2. RESULTS AND DISCUSSION.....	89
6.3. SUMMARY OF CHAPTER 6.....	95
6.4. SUPPORTING INFORMATION OF CHAPTER 6.....	96
REVERSIBLE OPENING OF MEMBRANOUS BARRIERS BY TIGHT JUNCTION MODULATORS.....	99
7.1. INTRODUCTION.....	100
7.2. RESULTS AND DISCUSSION.....	104
7.3. SUMMARY AND OUTLOOK OF CHAPTER 7.....	108
7.4 SUPPORTING INFORMATION OF CHAPTER 7.....	110
ELECTRICAL MONITORING OF LIGHT-INDUCED CELL-CELL INTERACTIONS.....	111
8.1. INTRODUCTION.....	112
8.2. RESULTS AND DISCUSSION.....	114
8.3. SUMMARY AND OUTLOOK OF CHAPTER 8.....	119
8.4 SUPPORTING INFORMATION OF CHAPTER 8.....	120
CONCLUSION.....	121
ZUSAMMENFASSUNG.....	125
REFERENCES.....	129
APPENDIX.....	139



DECLARATION .....	139
LIST OF PUBLICATIONS.....	140
CONFERENCE CONTRIBUTIONS.....	141

# List of Figures

<b>FIGURE 1.1.</b> PUBLICATION TREND .....	6
<b>FIGURE 1.2.</b> BIOELECTRONICS .....	7
<b>FIGURE 1.3.</b> ELECTRONIC ELEMENTS IN BIOELETRONICS .....	8
<b>FIGURE 1.4.</b> CHEMICAL STRUCTURE OF PEDOT:PSS .....	9
<b>FIGURE 1.5.</b> TRANSISTOR TECHNOLOGIES .....	12
<b>FIGURE 1.6.</b> PEDOT:PSS-BASED OECT .....	13
<b>FIGURE 1.7.</b> OECT CHARACTERISTICS .....	15
<b>FIGURE 1.8.</b> BIOELECTRONIC APPLICATIONS OF OECTS .....	16
<b>FIGURE 1.9.</b> TWO TYPES OF CELLS .....	17
<b>FIGURE 1.10.</b> RELATIVE SCALE OF BIOMATERIAL .....	17
<b>FIGURE 1.11.</b> TWO CATEGORES OF TISSUES .....	18
<b>FIGURE 1.12.</b> CELL JUNCTIONS IN EPITHELIAL CELLS .....	19
<b>FIGURE 2.1.</b> ION-SELECTIVE MEMBRANE .....	23
<b>FIGURE 2.2.</b> FILTER PREPARATION. ....	27
<b>FIGURE 2.3.</b> DEVICE STRUCTURE AND MEASURING SETUP .....	28
<b>FIGURE 2.4.</b> OECT FOR DIFFERENT APPLICATIONS .....	30
<b>FIGURE 2.5.</b> TEER VOLT-OHM METER .....	31
<b>FIGURE 3.1.</b> ORGANIC SOLVENT TREATMENTS .....	35
<b>FIGURE 3.2.</b> OECT ARCHITECTURE AND ITS ELECTRICAL CHARACTERISTICS .....	38
<b>FIGURE 3.3.</b> EXPERIMENTAL TRANSFER CHARACTERISTICS .....	40
<b>FIGURE 3.4.</b> CYCLABILITY .....	42
<b>FIGURE 4.1.</b> TRANSISTOR ARCHITECTURE AND ELECTRICAL CHARACTERISTICS .....	54
<b>FIGURE 4.2.</b> CURRENT-DRIVEN OECT ARCHITECTURE AND ELECTRICAL CHARACTERISTICS .....	56
<b>FIGURE 4.3.</b> CURRENT-DRIVEN OECT USED AS ION SENSOR. ....	58
<b>FIGURE 4.4.</b> OECT CHARACTERISTICS AND PARAMETERS AS A FUNCTION OF THE ION CONCENTRATION .....	60
<b>FIGURE 4.5.</b> ULTRA-LOW VOLTAGE CURRENT-DRIVEN OECT .....	62
<b>FIGURE 4.6.</b> ION-SELECTIVE CURRENT-DRIVEN OECT .....	63
<b>FIGURE 5.1.</b> EXPERIMENTAL SET UP AND ELECTRODE IMPEDANCE SPECTRUM .....	75
<b>FIGURE 5.2.</b> BODE MAGNITUDE AND PHASE SPECTRA OF ELECTRODES OF VARIOUS SIZES WITH AND WITHOUT CELLS .....	77
<b>FIGURE 5.3.</b> EXPERIMENTAL MEASUREMENTS AND SIMULATION OF THE IMPEDANCE MAGNITUDE .....	80
<b>FIGURE 6.1.</b> CARTOON OF A PACKED LAYER OF EPITHELIAL CELLS .....	89
<b>FIGURE 6.2.</b> OECT AS A SENSOR FOR CELL BARRIER INTEGRITY .....	90
<b>FIGURE 6.3.</b> TRANSFER CHARACTERISTICS OF THE CURRENT-DRIVEN CONFIGURATED OECT .....	91
<b>FIGURE 6.4.</b> OECT AS A CELL BARRIER INTEGRITY SENSOR FOR H <sub>2</sub> O <sub>2</sub> .....	92
<b>FIGURE 6.5.</b> THE CORRESPONDING NORMALIZED RESPONSE OF THE OECT IN THE STANDARD AND CURRENT-DRIVEN CONFIGURATION AFTER THE ADDITION OF H <sub>2</sub> O <sub>2</sub> .....	94

<b>FIGURE 7.1.</b> TIGHT JUNCTION MODULATORS AND THEIR TARGETS .....	101
<b>FIGURE 7.2.</b> CARTOON OF THE EFFECT OF TIGHT JUNCTION MODULATORS .....	104
<b>FIGURE 7.3.</b> CELL LAYER INTEGRITY .....	105
<b>FIGURE 7.4.</b> CLSM IMAGES OF CACO-2 CELL LAYERS.....	106
<b>FIGURE 7.5.</b> EFFECT OF CHITOSAN ON TIGHT JUNCTIONS .....	107
<b>FIGURE 7.6.</b> EFFECT OF POLY-L-LYSINE ON TIGHT JUNCTIONS.....	108
<b>FIGURE 8.1.</b> METHODS TO CONTROL CELL-CELL INTERACTIONS .....	113
<b>FIGURE 8.2.</b> INTERACTION IN PHOTOSWITCHABLE PROTEINS .....	114
<b>FIGURE 8.3.</b> VOLT-OHM METER CHAMBER .....	115
<b>FIGURE 8.4.</b> ILID/NANO FOR LIGHT-INDUCED CELL CLUSTERING .....	116
<b>FIGURE 8.5.</b> MICROSCOPIC IMAGES OF MDA CELLS EXPRESSING CPH-1.....	117
<b>FIGURE 8.6.</b> CPH-1 FOR LIGHT-INDUCED CELL-CELL INTERACTIONS .....	118
<b>FIGURE 8.7.</b> LIGHT-INDUCED CELL CLUSTERING USING CPH-1 .....	119

### Supporting Section:

<b>FIGURE S3.1.</b> CONDUCTIVITY BEHAVIOR OF PEDOT:PSS FILMS FOR DIFFERENT ORGANIC SOLVENT TREATMENTS .....	44
<b>FIGURE S3.2.</b> SETUP FOR THE PSVA METHOD.....	45
<b>FIGURE S3.3.</b> THICKNESS AND WASH-OFF BEHAVIOR OF PSPT-TREATED PEDOT:PSS FILMS .....	45
<b>FIGURE S3.4.</b> SPECTROSCOPICAL STUDY OF PEDOT:PSS FILMS TREATED WITH DIFFERENT ORGANIC SOLVENT TREATMENTS .....	47
<b>FIGURE S3.5.</b> XPS DEPTH PROFILE OF A POST-TREATED PEDOT:PSS FILM .....	48
<b>FIGURE S3.6.</b> DEGRADATION OF PEDOT:PSS .....	48
<b>FIGURE S3.7.</b> $I$ - $V$ MEASUREMENT OF AN PEDOT:PSS BASED OECT .....	49
<b>FIGURE S3.8.</b> ELECTROCHEMICAL IMPEDANCE SPECTROSCOPY MEASUREMENTS OF PEDOT:PSS-BASED OECTS.....	49
<b>FIGURE S4.1.</b> MEASURED TRANSFER CHARACTERISTICS ( $V_{OUT}$ - $V_{IN}$ ) OF THE CURRENT-DRIVEN OECT .....	67
<b>FIGURE S4.2.</b> CHARACTERISTICS AND PARAMETERS OF OECS OPERATED AT ULTRA-LOW VOLTAGE.....	68
<b>FIGURE S4.3.</b> OECS IMPEDANCE SPECTRA AS A FUNCTION OF ION CONCENTRATION .....	69
<b>FIGURE S4.4.</b> MOBILITY AS A FUNCTION OF THE ION CONCENTRATION .....	70
<b>FIGURE S5.1.</b> MAGNITUDE OF THE ABSOLUTE DIFFERENCE BETWEEN THE IMPEDANCE OF THE CELL LAYER MINUS THE IMPEDANCE OF ELECTRODES OF VARIOUS SIZES .....	85
<b>FIGURE S6.1.</b> CONTROL EXPERIMENTS WITH $H_2O_2$ .....	96
<b>FIGURE S6.2.</b> RESPONSE TIME OF THE OECS .....	97
<b>FIGURE S6.3.</b> NORMALIZED RESPONSE OF THE TJ DISRUPTION BY $H_2O_2$ .....	98
<b>FIGURE S6.4.</b> EFFECT OF A NON-INCREASED EFFECTIVE CELL LAYER RESISTANCE .....	98
<b>FIGURE S7.1.</b> CONTROL EXPERIMENTS OF CATIONIC POLYMERS.....	110
<b>FIGURE S7.2.</b> EFFECT OF TIGHT JUNCTION MODULATORS.....	110
<b>FIGURE S8.1.</b> MICROSCOPIC IMAGES OF MDA CELLS ON TRANSWELL FILTERS .....	120

# List of Tables

<b>TABLE 3.1.</b> OVERVIEW OF THE ELECTRICAL AND MORPHOLOGICAL CHANGES IN PEDOT:PSS.....	36
<b>TABLE 3.2.</b> OVERVIEW OF THE EXTRACTED VALUES.....	41
<b>TABLE 4.1.</b> SENSITIVITY COMPARISON.....	65
<b>TABLE 7.1.</b> TARGETS AND MODE OF ACTION OF MODULATORS IN EPITHELIAL BARRIERS .....	102
<b>TABLE 8.1.</b> OVERVIEW OF COMMONLY APPLIED OPTOGENETIC PROTEINS .....	113

# Glossary

AE	Absorption enhancers
AFM	Atomic force microscopy
AJ	Adherens junction
EDL	Electric double-layer
FBS	Fetal bovine serum
C10	Sodium caprate
cLSM	Confocal laser scanning microscopy
CPH-1	Cyanobacterial phytochrome 1
CS	Chitosan
DBSA	4-dodecylbenzenesulfonic acid
DMEM	Dulbecco's Modified Eagle Medium
DMSO	Dimethyl sulfoxide
EDTA	Ethylenediamine-N,N,N',N'-tetraacetic acid
EG	Ethylene glycol
EIS	Electrochemical impedance spectroscopy
EGOFET	Electrolyte-gated field-effect transistor
EGTA	Ethylene glycol-bis(beta-aminoethyl ether)-N,N,N',N'-tetra-acetic acid
EMEM	Eagle's Minimum Essential Medium
FMN	Favin mononucleotide
GIWAXS	Grazing incidence wide-angle X-ray scattering
GOPS	3-glycidoxypropyltrimethoxysilane
iLID	Improved light-inducible dimer
IS	Impedance spectroscopy
ISFET	Ion-sensitive field-effect transistor
IS-OECT	Ion-selective organic electrochemical transistor
LOV2	Light-oxygen-voltage-sensing domain

MOSFET	Metal-oxide-semiconductor field-effect transistor
NaTC	Sodium taurocholic acid
OC	Output characteristics
OECT	Organic electrochemical transistor
OEIP	Organic electronic ion pumps
OFET	Organic field-effect transistor
OSC	Organic semiconductor
OTFT	Organic thin-film transistor
PBS	Dulbecco's Phosphate Buffered Saline
PCB	Phycocyanobilin
PDMS	Polydimethylsiloxane
PEDOT	Poly(3,4-ethylenedioxythiophene)
Pen/Strep	Penicillin/Streptomycin
PFA	Paraformaldehyde
PMMA	Poly(methyl methacrylate)
PSS	Poly(styrene sulfonic acid)
PSPT	<i>Polar Solvent Post-Treatment</i>
PSVA	<i>Polar Solvent Vapor Annealing</i>
PLL	Poly-L-lysine
PPE	Paracellular permeability enhancers
RIE	Reactive ion etching
SA	<i>Solvent Additive</i> method
SDS	Sodium dodecyl sulfate
TC	Transfer characteristics
TEER	Transepithelial electrical resistance
THF	Tetrahydrofuran
TJ	Tight junction
XPS	X-ray photoelectron spectroscopy

# Abbreviations

$c$	Concentration
$C_d$	Capacitance at the channel interface
$C_g$	Capacitance at the gate interface
$C_{EL}$	Capacitance at the electrode interface
$C_{MEM}$	Capacitance at the cell membrane interface
$C_V$	Volumetric capacitance
$d$	Thickness
$G$	Conductance
$g_m$	Transconductance
$I_B$	Current bias (current-driven OECT)
$I_D$	Drain current
$L$	Length
$\lambda$	Wavelength
$\lambda$	Impedance ratio of a tissue cell layer to the measuring electrode
$\mu$	Charge carrier mobility
$q$	Elementary charge
$R_d$	Resistance of the channel
$R_L$	Load resistance
$R_{MED}$	Resistance of the medium
$R_{MEM}$	Resistance of the cell membrane
$r_o$	Output resistance
$R_S$	Resistance, depending on the electrode's size
$\rho_0$	Charge carrier density
$\sigma_{dry}$	Conductivity at dry conditions
$\sigma_{wet}$	Conductivity at wet conditions
$t$	Time

$T$	Temperature
$V_G$	Gate voltage
$V_D$	Drain voltage
$V_{DD}$	Supply voltage (current-driven OECT)
$V_{in}$	Input voltage (current-driven OECT)
$V_{out}$	Output voltage (current-driven OECT)
$V_P$	Pinch-off voltage
$V_S$	Source voltage
$V_{SW}$	Switching voltage
$W$	Width
$Z_{EL}$	Impedance of electrode
$Z_{MEM}$	Impedance of cell layer



# Motivation & Outline

The pioneer work of Luigi Galvani in the 1780s has set the trail for the field of bioelectronics, to use bioelectronic forces to study living organisms. But it was with the discovery of conductive polymers at the end of the 1970s, above all by the work of Heeger *et al.*, for which they were awarded the Noble Prize in Chemistry in 2000, that organic bioelectronics has experienced a tremendous growth and attention. Since then, an enormous number of electronic devices have been explored in bioelectronic applications, in which electronic signals are converted into biosignals and vice versa, to understand various biological phenomena as well as to exploit this potential to create improved healthcare products and biomedical diagnostics. One popular theme has been to use the organic electrochemical transistor (OECT), belonging to the class of electrolyte-gated transistors.<sup>[1,2]</sup>

The key advantage of the OECT is the local high amplification at low-voltage operation, offering excellent biocompatibility and ease of fabrication.<sup>[3,4]</sup> As a result, the OECT has yielded a vast array of promising applications ranging from electrophysiology, by recordings of neural activity of organs, to biosensing, by the detection of analytes and metabolites.<sup>[5]</sup> A further interesting aspect is the monitoring of cell coverage and cellular health of non-electrogenetic cells, among other for application in drug screening and targeting.<sup>[5-7]</sup> The OECT has been shown as a complementary sensor for cell barrier integrity in comparison to traditional techniques such as immunofluorescence, permeability assay and transepithelial electrical resistance measurements (TEER).<sup>[6,8]</sup> Nevertheless, the reversible control of cell layer opening in a high sensitive and

temporal resolution, essential for the use in drug delivery systems, still suffers from deficits.<sup>[9]</sup>

In order to take advantage of the attractive properties of the OECT for biomedical applications as in improved assessment of cell layer integrity, the OECT needs to be further pushed towards greater sensitivity and efficiency to meet the requirements of high-performance biosensing. Therefore, the goal of this work is on the one hand to design OECTs of high performance, and on the other hand to establish efficient methods for improving barrier tissue characterization, by exploiting electrical as well as biological possibilities.

This work is organized as followed: The theoretical background regarding the three main issues of bioelectronics, PEDOT:PSS and OECTs, associated with essentials of cell biology, is given in **Chapter 1**, establishing relevant definitions for a sufficient background knowledge for the work presented in this thesis. **Chapter 2** wraps up the experimental details on device fabrication, cell culturing and a series of characterization methods, including electrical, spectroscopical and microscopy techniques.

The next two chapters focus on material improvements and device physics to create the foundation of OECTs for interfacing biology. **Chapter 3** addresses material improvements of PEDOT:PSS as the conductive channel in the OECT, to drive towards high-performance biosensing: Organic solvent treatments, in particular the Post-Treatment method, have been exploited to significantly increase the conductivity of PEDOT:PSS, leading to improved OECT performances on the grounds of a phase segregation in PEDOT:PSS-rich and PSS-rich domains and enhanced structural order. The second part concentrates on alternative device configurations during measurements to increase sensitivity (**Chapter 4**). Next to the large transconductance towards high-performance biosensing, the sensitivity of ion detection can be increased by connecting the OECT in series with a current generator. The current-driven OECT has been demonstrated to yield the highest value for ion sensitivity, normalized to the supply voltage, ever reported for ion-sensitive transistors.

Taking this into account, the following two chapters describe the final interfacing with biological membranes. For efficient biosensing, **Chapter 5** pursues at first a classic approach by using an array of electrodes. Impedance spectroscopy studies on PEDOT:PSS-coated electrodes of various sizes, incorporating a cell layer, have demonstrated sensing and non-sensing regimes, depending on the area of the electrode. The determinant is given by the ratio of the impedance of the cell layer, to the impedance of the electrode, which has to be greater than one for biosensing capability. Next to electrodes, the OECT, as an active element, offers the possibility of creating small circuits. In the following drug screening experiments, the combination of the current-driven configuration of the OECT with integration of a cell layer, has led to a greater sensitive and temporal assessment of cell barrier integrity under the influence of toxins. Hydrogen peroxide has been used to induce permanent changes in its integrity (**Chapter 6**).

The last two chapters are dedicated to explore ways to control the ability of the cells forming tissue barriers by external stimuli. To regain more control in a manner of reversible cell opening instead of permanent damages in the last chapter, tight junction modulators, as a form of chemical stimuli, have been investigated for its temporary impact on cell connections of adherent cells (**Chapter 7**). This issue has been even more intensified by the use of optogenetics tools to control cell-cell interactions with the precise use of light as an optical modulation (**Chapter 8**). Expressing photoswitchable proteins on the surface of a cell, cell-cell interaction in form of cell opening and closing has been investigated by its activation and inactivation upon light irradiation.



# Chapter 1

## Introduction

This chapter is dedicated to the introduction into bioelectronics and its achievements. This involves the general concept and the state-of-the art technologies of this field, including a short flashback to the 18<sup>th</sup> century that blazed the trail of today's bioelectronics. Important materials and devices that shaped bioelectronics on this trail will be outlined. This particularly implies the benchmark material PEDOT:PSS and the organic electrochemical transistor. As these two will be the main focus of this work they will be discussed in more detail, respectively. The chapter concludes with a short introduction in essential cell biology, emphasizing on epithelial cells and cellular junctions, as they will cross our way along the thesis.

## 1.1. Bioelectronics

The realm of bioelectronics is a strong emerging field, bridging the interface of organic electronics with the world of biology.<sup>[10]</sup> It's a relatively novel field and started to approach at the start of this century.<sup>[1]</sup> Based on Figure 1.1, in the last twenty years bioelectronic devices and their use have attracted enormous attention and experienced tremendous growth.<sup>[11]</sup> But the idea of bioelectronics has started long before that and as a matter of a fact can be dated back to the 18th century.<sup>[2,11]</sup> The idea of using electrical signals to interact with biological systems was born by the famous work of Luigi Galvani, when he made a detached leg of a frog twitch upon applying a voltage.<sup>[2,11]</sup> The idea of gaining insight into essential signal pathways in living organisms, as well as understanding of fundamental biological phenomena has been explored ever since.<sup>[12]</sup>

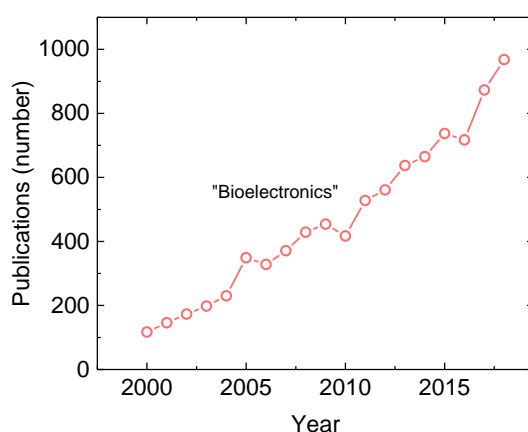


**FIGURE 1.1.** PUBLICATION TREND: The number of publications per year on “bioelectronics” over the last twenty years, using data from the online database Scopus of Elsevier.

It is with the rapid development of highly efficient organic electronic devices that the field of bioelectronics is truly experiencing renaissance.<sup>[11]</sup> Today there is a variety of organic electronic materials and devices entering the field of bioelectronics, offering improved healthcare products, biomedical diagnostics, environmental monitoring and water and food testing and controlling, and even playing a role in agriculture industry and security.<sup>[1,2,10,11]</sup>

The general concept of bioelectronics is demonstrated by the coupling of organic electronic elements with biology, operating as a two-way translator between those systems (Figure 1.2).<sup>[10-12]</sup> In one direction, organic bioelectronics can be integrated with biological systems to sense, monitor and record signals of biological and physical processes.<sup>[12]</sup> For example, the integration of a cell layer changes the impedance of the device.<sup>[5]</sup> Hence, in the other translational direction, organic bioelectronic systems can be used to trigger and regulate physiological and biological processes in cells, tissues and organs, e.g. as in stimulated recordings of action potentials of neural cells.<sup>[5,12]</sup>

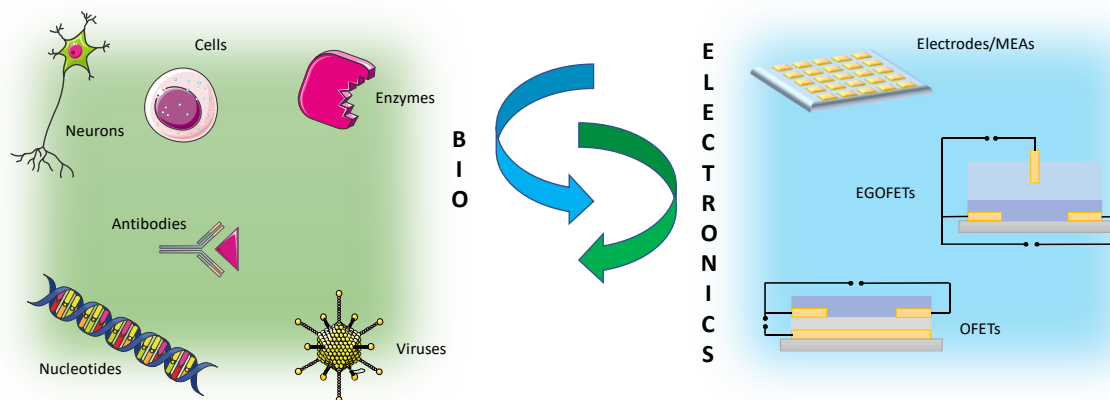


**FIGURE 1.2.** BIOELECTRONICS: Cartoon showing the scope of bioelectronics, by coupling biological components with organic electronic systems, and vice versa. Cartoon has been created by images of SMART.<sup>[13]</sup>

Bioelectronics is strongly limited by the materials, translating signals between two, at first seeming controversial fields.<sup>[11]</sup> Devices based on conventional materials, such as metals, suffer from incompatibility and mechanical mismatch with biological systems and inefficient conversion of biological signals into electrical signals, or vice versa.<sup>[11]</sup> The tremendous development of organic electronics, currently entering the markets in plenty, has offered new or improved electroactive features compared to inorganic materials, and has provided an unique platform to effectively interface with biology.<sup>[2]</sup> The similarity in structural and functional properties, such as the soft nature of conducting polymers ideally mimics those of biological systems.<sup>[11]</sup> Electronics mainly rely on electrons as the dominant charge carriers, as in biology this is rarely the case, instead ions and small molecules are being used.<sup>[12]</sup> Due to the mixed electronic and ionic conductivity of conducting polymers, these materials provide highly efficient signal transduction and amplification between those fields.<sup>[14]</sup> Biocompatibility allows direct interfacing with biological materials.<sup>[1]</sup> De facto, various kinds of standard cell viability tests have been explored to evaluate the biocompatibility of conjugated polymers for biological applications.<sup>[2]</sup> Materials like poly(3,4-ethylenedioxythiophene) (PEDOT), doped with poly(styrene sulfonic acid) (PSS), were found to perform very well in biological milieus.<sup>[2,15]</sup> Finally, including low-cost fabrication and the ease of tuning, these properties have overall made organic bioelectronics truly a unique communication bridge across the biology–electronics gap.<sup>[12]</sup> Especially the oxide-free interface of organics with aqueous electrolytes and the efficient ion transport between biological milieu and the entire volume of the organic film, not just interaction at the surface, has endowed this field with applications, ranging from powerful biosensors to pacemakers, neural implants and biomedical instruments.<sup>[11]</sup>

Today, electrodes, organic field-effect transistors (OFETs) and electrochemical devices like electrolyte-gated field-effect transistors (EGOFETs), organic electronic ion pumps (OEIPs), ionic diodes and circuits have yielded excellent tools for applications (Figure 1.3(a–d)), including

neural interfacing, stimulating and sensing of living organisms, biosensing and drug delivery systems, established for living science and clinic applications.<sup>[12,16]</sup>

One of the most promising devices emerging from this field is the organic electrochemical transistor (OECT) based on the conducting polymer PEDOT:PSS.<sup>[5]</sup> Both systems will be extensively described in the next two sections.

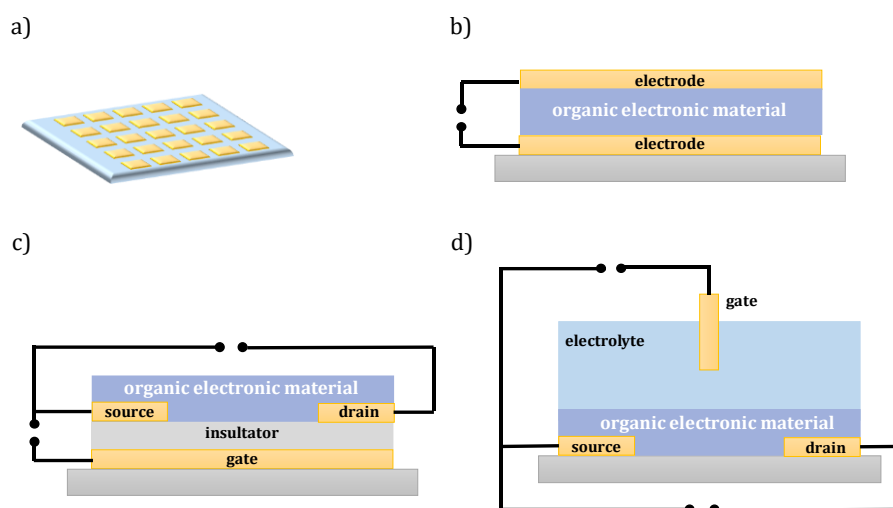


**FIGURE 1.3.** ELECTRONIC ELEMENTS IN BIOELETRONICS: Device structures of **a)** a microelectrode array (MEA), **b)** a diode, **c)** an organic field-effect transistor (OFET) and **d)** an electrolyte-gated field-effect transistor (EGOFET).



## 1.2. PEDOT:PSS

By far the most popular and successfully used conducting polymer in organic electronics is poly(3,4-ethylenedioxythiophene) (PEDOT).<sup>[15,17]</sup> Besides its insolubility, PEDOT outstands with high electro-optical and electrical properties, featuring hole conductivities of  $1\text{--}100\text{ S cm}^{-1}$ .<sup>[15,18]</sup> Its conductivity strongly depends on the morphology and the dopant.<sup>[5]</sup> Traditionally it is doped with the water-dispersible polyelectrolyte poly(styrene sulfonic acid) (PSS), solving the solubility problem.<sup>[15]</sup> The polyanion acts as the counter ion and facilitates a stable suspension and increases solubility for a better processability.<sup>[15]</sup> The chemical structure of PEDOT:PSS is shown in Figure 1.4: PEDOT consists of a thiophene backbone that represents the  $\pi$ -conjugated polymer in this system.

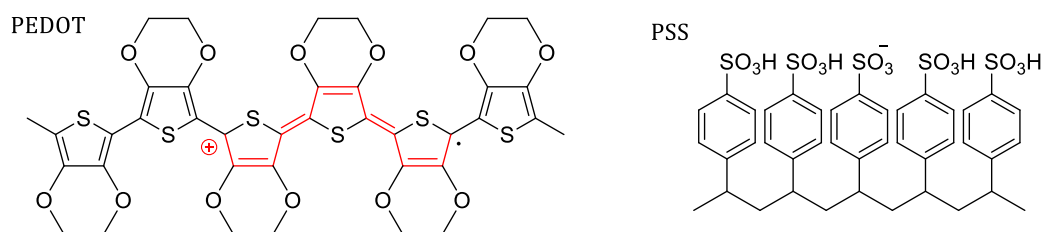


**FIGURE 1.4.** CHEMICAL STRUCTURE OF PEDOT:PSS: The image shows the *p*-type doping in PEDOT, induced by the dopant PSS.

PEDOT:PSS can be prepared by standard oxidative chemical or electrochemical polymerization methods.<sup>[18–20]</sup> The electrochemical polymerization is conducted in an electrochemical cell with a three-electrode configuration using a solution of the monomer 3,4-ethylenedioxythiophene (EDOT) and PSS sodium salt.<sup>[20]</sup> The metal electrode oxidizes EDOT monomers to cations.<sup>[20]</sup> These cations will combine to oligomers and chains, and eventually precipitate on the electrode.<sup>[20]</sup> This technique is a fast and simple method to selectively deposit PEDOT:PSS on surfaces in specific areas.<sup>[20]</sup> The chemical approach involves the oxidation reaction of the monomer EDOT as well, in the form of the initial formation of a radical cation EDOT with the aid of oxidative agents such as iron (III) chloride or nitride and peroxodisulfates.<sup>[18,19]</sup> The presence of PSS is crucial for the process in terms of stability. The polarity of the sulfonate groups enables PSS to solvate PEDOT in form of rich PEDOT-PSS domains, leading to stable dispersions.<sup>[18,19]</sup> Indeed, PSS is always present in excess to form PSS-shells around the highly-conductive PEDOT:PSS gel-like particles to prevent any aggregation.<sup>[14]</sup> The long shelf-life facilitates a variety of commercially available PEDOT:PSS formulations (e.g. Hereaus Clevios™, Sigma-Aldrich), which are ready-for-use without any further instructions.<sup>[21]</sup>

The solid content of polymer in the aqueous solutions generally ranges from 1.3–1.7%.<sup>[22]</sup> The weight ratio between PEDOT and PSS affects the physical but in particular the electrical properties

as it governs the charge carrier density in PEDOT, resulting in a conductivity change.<sup>[21–23]</sup> Commercial available formulations offer a variety of different conductive PEDOT:PSS dispersions, altering the weight ratio between the thiophene groups and sulfonic acid groups.<sup>[22,24]</sup> For instance, the high conductive formulation of Hereaus Clevios™ (PH1000) features a weight ratio of 1:2.5 and is used as the conductive material in electronic devices.<sup>[23]</sup> While an increased ratio of 1:6 leads to the least conductive dispersion (P VP AI 4083), usually used as the hole injection layer of electronic devices.<sup>[23]</sup> The great advantage of the chemical synthesis is the exceptional broad possibility of film deposition.<sup>[18]</sup> The commercially available PEDOT:PSS dispersion can be deposited using the whole spectrum of the conventional coating techniques.<sup>[25]</sup> This embraces drop-casting, spin-coating, spray-coating, inject-printing, doctor-blading, solution-shearing and electro-spinning.<sup>[15,21,23,25]</sup> Depending on the purpose of the PEDOT:PSS coating, each technique possesses its own advantages and might require additional additives to optimize the coating process for a uniform film. Spin-coating is the most commonly used technique for film deposition of PEDOT:PSS.<sup>[25]</sup> It's a simple method to receive homogenous, multiple layers of PEDOT:PSS with high reproducibility, processable even for large areas.<sup>[25]</sup> Surfactants are often added to the PEDOT:PSS dispersion to enhance the wetting behavior on a hydrophobic surface for a better film formation.<sup>[26]</sup> The fluorosurfactant Zonyl® is often used for this purpose.<sup>[26]</sup> Crosslinkers are well known for their increased film and mechanical stability.<sup>[17,27]</sup> The use of crosslinkers reduces the ability to uptake water and reduces the swelling of the film.<sup>[17,27]</sup> 3-glycidoxypropyltrimethoxysilane (GOPS) is often used as a crosslinker in PEDOT:PSS films.<sup>[17]</sup> It has been reported that by the addition of GOPS, the film integrity and strong adhesion to the substrate is maintained when immersed in water, preventing dissolution and delamination.<sup>[28]</sup> For instance, it has been shown, that by aging PEDOT:PSS films in water leads to a loss of the PSS chains.<sup>[28]</sup> Crosslinkers have proven to minimize and slow down this phenomenon.<sup>[28]</sup> Despite the attractive properties as enhanced stability, the addition of a crosslinker lowers the conductivity and the ion mobility, which basically implies a trade-off and prevails to find the optimal condition.<sup>[27]</sup>

In addition to the excellent film forming properties and processability, PEDOT:PSS exhibits high transparency and thermal stability.<sup>[18]</sup> But principally, PEDOT:PSS is prominent for its high hole conductivity, maximized by the aid of additives and currently exceeding  $1000 \text{ S cm}^{-1}$ .<sup>[23]</sup> Furthermore, it is well-known for its high electrochemical stability in aqueous environments, including a broad range in pH, and biocompatibility.<sup>[15]</sup> This sets the premise for biological integration and combined with its excellent mixed conductivity, both ionic and electronic, makes PEDOT:PSS a prime candidate for biosensing applications.<sup>[14]</sup> The electronic conductivity of PEDOT:PSS films have been extensively studied under several aspects, involving additives, solvents, surfactants and processing methods.<sup>[23]</sup> In fact, various physical and chemical approaches, commonly defined as *Secondary Doping*, have been used to improve the electrical

conductivity of PEDOT:PSS.<sup>[23]</sup> In this way, the conductivity of commercially obtainable PEDOT:PSS films (pristine) of  $10^{-6}$ – $1 \text{ S cm}^{-1}$  can be increased several orders of magnitude, even reaching a maximum value of  $> 4000 \text{ S cm}^{-1}$ .<sup>[23]</sup> More explicable, *Secondary Doping* embraces techniques like light and thermal treatments<sup>[29–34]</sup>, as well as chemical methods like treatment with organic solvents and other compounds like ionic liquids, surfactants, salts and acids.<sup>[35–43]</sup> In fact, the organic solvent treatment to enhance PEDOT:PSS conductivity is the most prominent techniques and breaks down into different variants using polar organic solvents with high boiling points.<sup>[23]</sup> Further details about organic solvent treatment, in particular with dimethyl sulfoxide (DMSO), are described in *Chapter 3 – Effects of DMSO Solvent Treatments on the Performance of PEDOT:PSS-based Organic Electrochemical Transistors*.

The structure and morphology of PEDOT:PSS films have been extensively studied by a series of techniques including X-ray spectroscopy, atomic force microscopy, scanning tunneling microscopy and elemental and surface-sensitive scanning probes.<sup>[14,23,44–48]</sup> The structure consists of PEDOT:PSS-rich particles with a size of 20–25 nm in diameter, surrounded by PSS-rich lamellas in excess.<sup>[49]</sup> The composition is typically described as gel-like particles, embedded in PSS shells to stabilize the dispersion.<sup>[14]</sup> The morphology, often referred to as pancake-like, exhibits aggregates and crystallites, determined by  $\pi$ -stacking, and enhances the electronic transport.<sup>[14]</sup> The enhancement in PEDOT:PSS conductivity by *Secondary Doping* is induced by a structural rearrangement and loss of the excess, insulating PSS.<sup>[23,44,45,50,51]</sup> This will be further outlined in *Chapter 3 – Effects of DMSO Solvent Treatments on the Performance of PEDOT:PSS-based Organic Electrochemical Transistors*.

The development of polymers with high conductivity and transparency, acting as the charge injection layer or electrical active material in organic devices, has led to series of novel organic technologies such as light emitting diodes (OLEDs), solar cells, batteries and OFETs.<sup>[23,31,51,52]</sup> PEDOT:PSS has taken a remarkable place in these devices with great significance. Moreover, PEDOT has demonstrated being a promising alternative for indium tin oxide (ITO) as transparent electrodes.<sup>[50,53]</sup> In the field of bioelectronics, PEDOT:PSS has been used for a variety of biomedical applications.<sup>[5,15,17]</sup> PEDOT:PSS-coated electrodes or PEDOT:PSS-based organic electrochemical transistors (OECTs), have improved the performance in recordings and stimuli of electroactive cells and tissues.<sup>[2,12,16]</sup> Furthermore, PEDOT:PSS has been coated on soft and flexible substrates, for the development of implantable and cutaneous devices, designed for electrophysiological recordings.<sup>[12,16]</sup> Besides electrophysiology, PEDOT:PSS has demonstrated great potential in tissue engineering, biosensing and drug delivery.<sup>[2,5,12]</sup>

### 1.3. Organic Electrochemical Transistor

Novel organic technologies based on conductive polymers, leveraging the coupling of mixed electronic and ionic transport, are exploited in organic electrochemical transistors (OECTs).<sup>[5]</sup> The effective ion injection from an electrolyte into the conducting polymer to modulate its hole conductivity leads to a high transconductance as compared to FETs.<sup>[3]</sup>

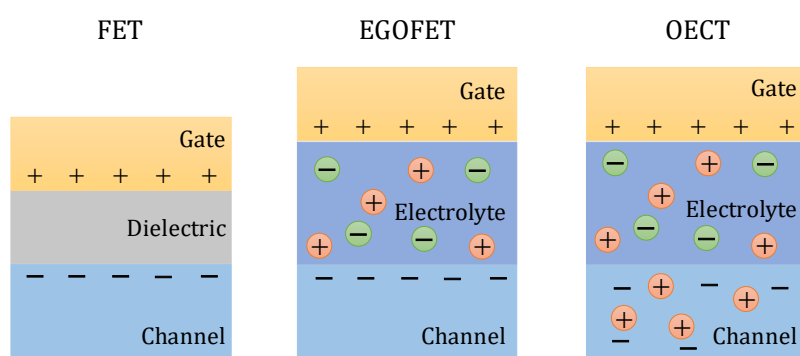


**FIGURE 1.5.** TRANSISTOR TECHNOLOGIES: Device structure and charge carrier accumulation in FETs, EGOFETs and OECTs. Compared to EGOFETs, the current modulation is induced by electrochemical reactions in the channel in OECTs.

A FET is assembled by a stacked structure of a semiconductor (channel), a thin layer of insulator (gate dielectric) and a metal electrode on top, serving as the gate (Figure 1.5).<sup>[5]</sup> The most prominent FET is the MOSFET, which is short for metal-oxide-semiconductor field-effect transistor.<sup>[54]</sup> The accumulation of mobile charge carriers near the interface with the dielectric upon applying a voltage is referred to as field-effect doping of the semiconductor (Figure 1.5).<sup>[54,55]</sup> Driven by the possible elimination and replacement of expensive metal oxides, the interest in developing a new class of materials has attracted enormous attention. The unique features of organic conjugated, semiconducting small molecules and polymers led to the development and recognition of OFETs.<sup>[56–58]</sup> Over the last three decades, this class of promising materials has established high mobilities and stability, compatibility with biological systems and the ease of tunable electronic properties.<sup>[2,16]</sup> Due to their many advantages, they offer a variety of applications including pixel drivers for displays, flexible transistors and sensitive biosensors.<sup>[12,16]</sup> Particularly in the field of sensing applications, the organic thin-film transistors (OTFTs) have been well established.<sup>[15]</sup> Due to the inherent signal amplification and allowance of small sample volumes, the OTFTs have successfully been used in sensing different essential biological analytes and ion concentrations.<sup>[15]</sup>

It was 1984, when the OECT was first introduced by Wrighton and his colleagues, as a new class of an electrolyte-gated organic field-effect transistors (EGOFETs, Figure 1.5).<sup>[59]</sup> The OECT is assembled by a semiconducting polymer, horizontally sandwiched between two metal electrodes

(Figure 1.5), acting as the source and the drain.<sup>[60]</sup> The application of a drain voltage  $V_D$  induces a current (drain current,  $I_D$ ), which flows from source to drain and is proportional to the number of mobile holes or electrons in the conducting channel.<sup>[60]</sup> The conducting polymer is in direct contact with an electrolyte, in which a gate electrode is immersed.<sup>[60]</sup> The key difference to EGFETs is the ion injection from the electrolyte into the conducting polymer upon applying a gate bias  $V_G$ , modifying its doping state, and thereby its bulk conductivity.<sup>[5]</sup> In this way, the  $V_G$  regulates the doping state of the conducting polymer, while the  $V_D$  probes the doping state of the channel.<sup>[5]</sup>

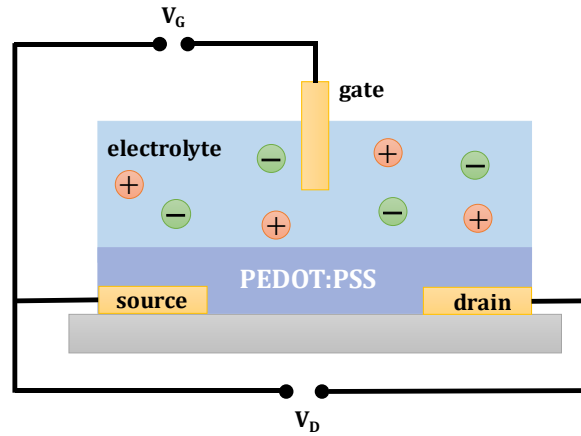
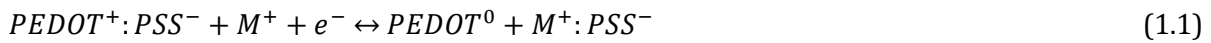


**FIGURE 1.6.** PEDOT:PSS-BASED OEFT: Typical device structure of an OEFT, consisting of a source, drain and a gate, which is immersed in an electrolyte.

PEDOT:PSS is by far the most commonly used active material in OEFTs.<sup>[17]</sup> It's a *p*-type semiconducting polymer, which leads to mobile holes, resulting in a hole current.<sup>[15]</sup> The PEDOT:PSS-based OEFT operates in the depletion mode (Figure 1.6)<sup>[60]</sup>. Driven by the electric field, caused by the gate electrode, cations of the electrolyte are able to penetrate the channel, due its soft and permeable design, and compensate the negative charges of the sulfonate groups of PSS.<sup>[17,60]</sup> This migration causes an electrochemical dedoping of PEDOT.<sup>[15,17]</sup> The highly conductive oxidized  $PEDOT^+$  will be reduced to the less conductive neutral state ( $PEDOT^0$ ), according to the following reversible electrochemical reaction<sup>[15]</sup>:



where  $M^+$  is a cation of the electrolyte and  $e^-$  an electron from the source. In other words, the number of mobile holes is replaced by immobile ions in the channel, which results in lowering of the hole current. The transistor is pushed into the off-state ( $I_D$  is decreased) due to the decreased hole density.<sup>[5]</sup> This process is reversible and recovers by ions drifting back to the electrolyte.<sup>[15]</sup> In contrast to traditional OTFTs, the drain current ( $I_D$ ) is regulated by electrochemical reactions in the channel.<sup>[5]</sup> This makes the OEFT an efficient ion-to electron transducer.<sup>[17]</sup> Like MOSFETs

and OFETs, OECTs operate as a switch and can be seen as an amplifier of electronic signals.<sup>[5]</sup> The gate voltage (input) controls the drain current (output), that symbolizes the switching between ON and OFF.<sup>[5]</sup> Furthermore, following the magnitude of an input signal on the way to the output, emphasizes the excellent non-invasive and label-free amplification properties of OECTs.<sup>[5]</sup> Indeed, the coupling of ionic and electronic charges throughout the entire volume of the channel is expressed in one of the highest transconductances among different types of transistors.<sup>[3,60]</sup> Defined as  $g_m = \partial I_D / \partial V_G$ , the transconductance is the first derivative of the transfer curve, highlighting the efficiency of the transduction of the input/output signal.<sup>[60]</sup> OECTs typically reach a transconductance in the range of millisiemens.<sup>[5,60]</sup>

Instead of using the traditional polyanion PSS as a *p*-type dopant, PEDOT has been doped with small molecules like tosylate (TOS) or with alternative anionic polyelectrolytes consisting of a styrenic or methacrylic backbone with (trifluoromethylsulfonyl)sulfonylimide side groups.<sup>[5,61,62]</sup> Besides using a dopant in form of polyanions or small molecules, the ionic group can be directly attached to the thiophene backbone through side chains.<sup>[5]</sup> For example, attaching sulfonate groups to the backbone of polythiophene with a hexyl chain (PTHS) designs a semiconductor, as the ion is compensated by a counter ion.<sup>[5]</sup> In comparison, by attaching a sulfonate group via a side chain to the backbone of PEDOT (PEDOT-S), the conjugating polyelectrolyte acts as a conductor, as the ion is compensated by an electronic charge on the conjugating backbone.<sup>[5]</sup> Alternative conjugated polymers with ion-transporting or hydrophilic side chains have been used as active channel materials in OECTs as well.<sup>[5]</sup> Overall, a broad variety of different materials have been used to fabricate OECTs and each material has its advantages and drawbacks, hence the choice of material often depends on the application and fabrication limitations.<sup>[5]</sup>

The electrical behavior of an OECT is represented by its current-voltage (*I*–*V*) characteristics.<sup>[15]</sup> The transfer characteristics (TC,  $I_D$ – $V_G$ ) in Figure 1.7(a), show the modulation of  $I_D$  according to the dedoping (forward sweep) and doping (backward sweep) process of the channel, regulated by  $V_G$ . It basically shows the dependence of  $I_D$  on  $V_G$ , while the steepness of the curve represents the magnitude of the transduction, expressed in the already mentioned transconductance.<sup>[15]</sup> Bernards *et al.* established a model on OECT device physics, which describes the steady-state and transient behavior of the OECT.<sup>[63]</sup> In principle, the model assumes the division of the device in an ionic and electronic circuit.<sup>[63]</sup> Bernard's model achieved a good fit for the output characteristics and estimates essential characteristics like the charge carrier mobility and density.<sup>[63]</sup> Depending on the applied gate and drain voltages, the OECT can operate in the linear or saturation regime.<sup>[63]</sup> In the output characteristics (OC, Figure 1.7(b)), the transition from linear to saturation is clearly displayed.<sup>[15]</sup> For lower  $V_D$ , the OECT operates in the linear regime, literally expressed by the linear relationship between  $I_D$  and  $V_D$ , and the dedoping is homogenous throughout the organic polymer.<sup>[63]</sup> By increasing  $V_D$ , the OECT is eventually operated in saturation region.<sup>[63]</sup> In saturation, the channel is completely dedoped close to the

drain side (pinched-off) and  $I_D$  is almost independent on  $V_D$ .<sup>[63]</sup> Further details about the device physics in OECTs will be outlined in *Chapter 3 – Effects of DMSO Solvent Treatments on the Performance of PEDOT:PSS-based Organic Electrochemical Transistors*.

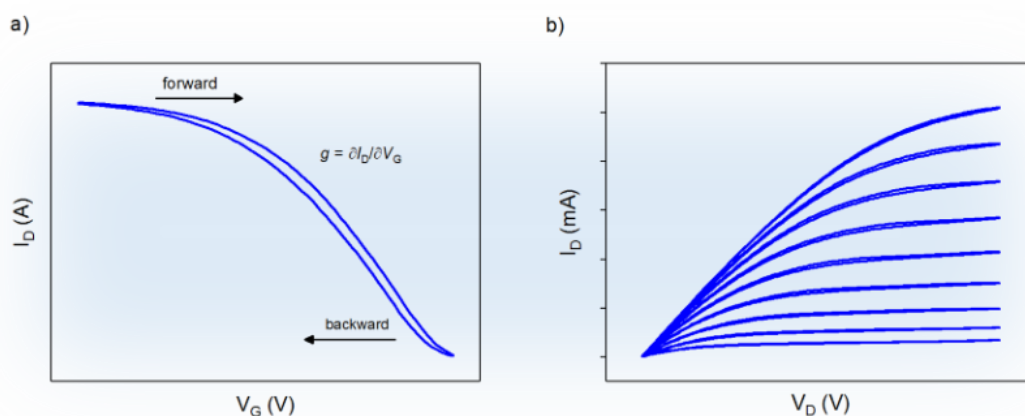


**FIGURE 1.7.** OECT CHARACTERISTICS: **a)** The transfer characteristics show the forward and backward sweep of  $I_D$  at a specific  $V_D$ , revealing the hysteresis of the device. **b)** Output characteristics for a series of  $V_G$ , displaying the transition from the linear to the saturation regime.

The many advantages of the OECT, combined with the development of highly efficient organic electronic materials and the variety of substrates, makes it an excellent candidate for organic electronic technologies.<sup>[2,5,12,16]</sup> Especially due to the very low operating voltages, its biocompatibility and the ease of fabrication, OECTs are suited for a broad range of applications, including logic circuits, memory and neuromorphic devices, and most of all bioelectronic devices.<sup>[5]</sup>

In particular, the latter has attracted enormous attention and amplified the rise of the OECT.<sup>[1,11]</sup> Due to the soft nature of the conducting polymer and development of soft, flexible and stretchable substrates, OECTs play a major role in bioelectronics for biomedical and healthcare related usage and show high potential towards its use in clinical applications (Figure 1.8).<sup>[5,11,64,65]</sup> High sensitivity and excellent signal-to-noise ratio provides the OECT with the ability to monitor cell activity when integrated with electrically active tissues and organs (Figure 1.8).<sup>[5,66,67]</sup> Implantable devices have been placed for example on the brain of a rat to record epileptic seizures.<sup>[68]</sup> Hence, OECTs are able to provide amplified recordings of electrophysiological signals from the brain, heart, and other organs.<sup>[5]</sup> For cutaneous application, it is possible to record electrocardiograms when placed in contact with the human skin.<sup>[69]</sup> In addition, the OECT can monitor action potential for electrogenic cells to provide a spatial map of the electrophysiological activity.<sup>[70]</sup> Furthermore, OECTs have been used for cell culture analysis, as well as cell membrane integrity for non-electrogenic cells, for both in vitro and in vivo applications (Figure 1.8).<sup>[6,7,71,72]</sup> The application as a biosensor, serving as a transducer, has been successfully used to detect different electrolytes and metabolites.<sup>[73–78]</sup> This particularly includes glucose and lactate, which

are important for human health, as lactate states the metastatic potential of tumor cells (Figure 1.8).<sup>[74,75,79]</sup> In addition to the detection of an analyte in a saline solution, sensing among others in breath, saliva, sweat and cell culture media has been accomplished.<sup>[65,80–82]</sup>

The OECT has been used in a variety of circuits like inverters or Wheatstone bridges, to convert an input signal to an output signal (Figure 1.8).<sup>[5,74,83,84]</sup> This not only expands the possibilities of using electrophysiological equipment as most of this equipment requires a voltage input, but most of all this amplifies the output voltage and, in this way, accomplishes enhanced sensitivity.<sup>[74]</sup> There is a great interest in developing networks for information processing and transmission, as well as recognition and storage, inspired by the inherent capability of the human brain to cope with this kind of signals.<sup>[5,16,85]</sup> Neuromorphic systems are devices that mimic the structure and function of biological neural networks, to be able to recognize temporary or permanent changes in electrical signals, and thereby simulating short-term or long-term memory.<sup>[85]</sup> The OECT has been used in a variety of neuromorphic and memory devices, especially due to its ability for low power consumption per switching event (Figure 1.8).<sup>[85–87]</sup>

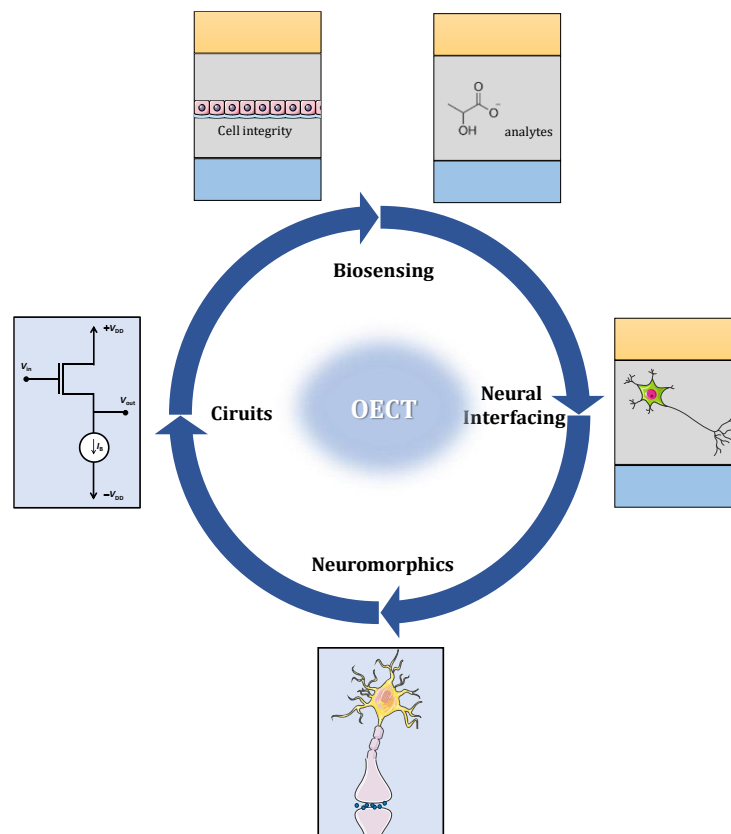


**FIGURE 1.8.** BIOELECTRONIC APPLICATIONS OF OECTS: The OECT has been used in biosensors as impedance sensors to monitor changes in the ion permeability by placing a cell layer between the gate and the channel. The OECT can be used to detect analytes in the electrolyte such as metabolites by functionalizing the gate. In electrophysiology, the OECT has been used to record electrical activity of cells like neuron cells. The OECT has been used in a variety of neuromorphic devices as well as in circuits, like the inverter configuration. Schema has been created by images of SMART.<sup>[13]</sup>



### 1.3 Epithelial Cells and Cell Junctions

Cells are the basic units of living organisms and are considered as the “buildings blocks of life”.<sup>[88,89]</sup> All cells consist of a cell membrane, embedding the cell’s interior water-based cytoplasm.<sup>[89]</sup> This liquid environment contains many functional and structural elements like nucleic acids, proteins, carbohydrates and lipids.<sup>[88]</sup> Cells can be differentiated in two major categories (Figure 1.9): Prokaryotes, containing the DNA within the cytoplasm, and eukaryotes, having the genome located in its own membrane-bound room, called the nucleus.<sup>[90]</sup>

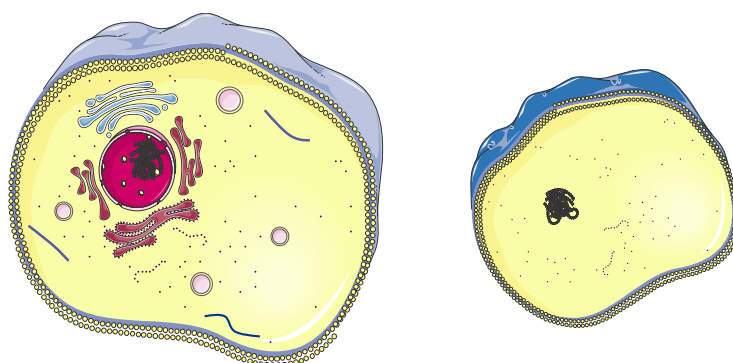


**FIGURE 1.9.** TWO TYPES OF CELLS: Eukaryotic cells (left) possess a membrane-enclosed DNA, called the nucleus. In addition, they also have membrane-bound organelles of different shapes and sizes. Prokaryotic cells (right) do not have a membrane-enclosed DNA nor organelles. The genome is located in cytoplasm. Cartoon has been created by images of SMART.<sup>[13]</sup>

Some cells are organisms by themselves and are unicellular, consisting of a single cell (e.g. bacteria).<sup>[88]</sup> Others are part of multicellular organisms, able to form tissues, organs or even entire organisms.<sup>[88]</sup> In multicellular organisms, cells are mostly assembled in complexes called tissues, such as the connective, muscle, nervous and epithelial tissue, present in vertebrates.<sup>[89]</sup> Figure 1.10 visualizes the relative scale of biological molecules and structures.<sup>[89]</sup>

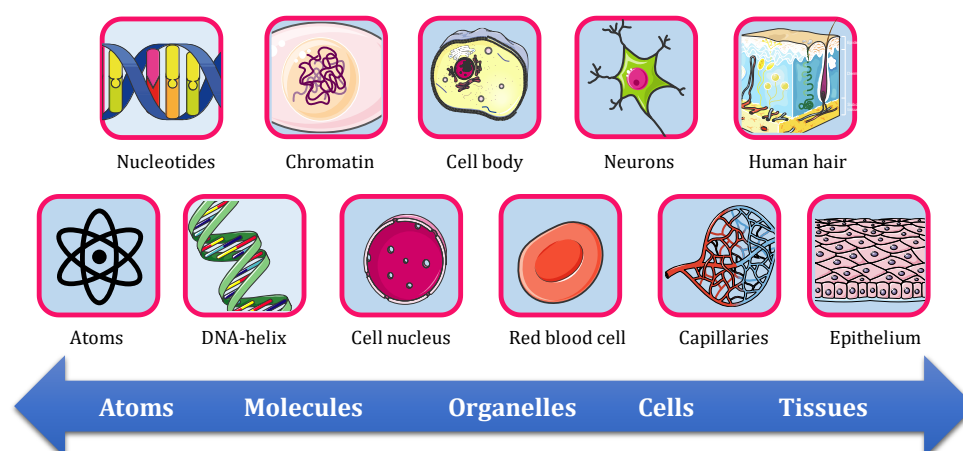


**FIGURE 1.10.** RELATIVE SCALE OF BIOMATERIAL: This scheme compares the size of a cell in relation to atoms, molecules, organelles and tissues. Cells vary between  $1\mu\text{m}$  and hundreds of  $\mu\text{m}$ . Cartoon has been created by images of SMART.<sup>[13]</sup>

In epithelial tissues, cells are tightly connected into sheets, called epithelia.<sup>[88,90]</sup> Typical arrangements are the epidermal covering of the skin and the lining of the respiratory, digestive, urinary, and reproductive tracts.<sup>[88,90]</sup> The main functions of epithelial cells involve secretion, selective absorption, protection, sensing and cellular transport.<sup>[88,90,91]</sup> Especially in the latter case, cell-cell junctions are highly relevant, which are the “glue” between epithelial cells.<sup>[6,72,90]</sup> In fact, the assembly of cell junctions and the cellular matrix plays a critical role in the function, organization and dynamics in multicellular organisms.<sup>[88]</sup> Disorders and defects in this assembly lead to a variety of diseases.<sup>[6,90]</sup> A typical environment of epithelial cells is illustrated in Figure 1.11, found in all animals.<sup>[90]</sup> A thin layer of extracellular matrix, mainly consists of the basement membrane (basal lamina), underlies the epithelial sheet. Compared to the underneath located connective tissue, where cells are sparsely embedded in the extracellular matrix, the basement membrane is less pronounced.<sup>[90]</sup>

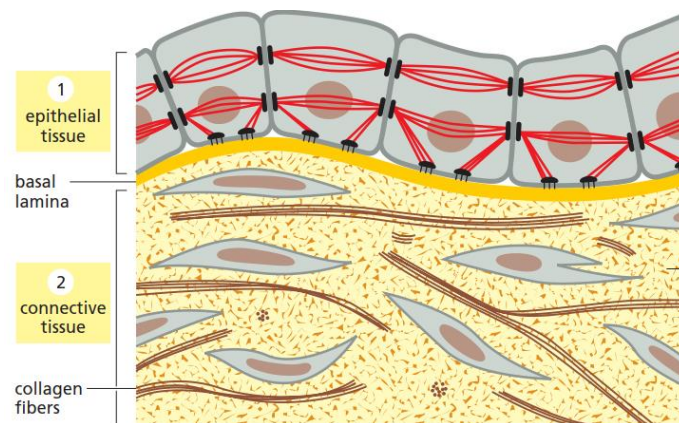


**FIGURE 1.11. TWO CATEGORIES OF TISSUES:** Epithelial cells are connected by basal lamina (extracellular matrix) to the connective tissue. Compared to the epithelial sheets, the cells are sparsely distributed in the extracellular matrix. Image adapted from reference.<sup>[90]</sup>

A closer view on epithelial cells, illustrated in Figure 1.12(a), reveals four main types of cell-cell junctions, next to the here neglecting cell-matrix junctions: Tight junctions, gap junctions, adherens junctions and desmosomes.<sup>[90]</sup> While the two latter cases belong to the types of anchoring junctions, linking the cytoskeleton of adjacent cells, the gap junctions are located at the basal side, allowing and regulating the passage of small molecules from cell to cell.<sup>[90]</sup> In contrast, tight junctions (TJs) have mainly two main functions: they hold neighboring cells together and seal the gap, and constrain the diffusion of macromolecules through the paracellular route.<sup>[9,92]</sup> Second, they act as a fence for apical and basolateral proteins to leak into the wrong plasma membrane domain as shown in Figure 1.12(b).<sup>[90]</sup> In epithelial cells certain plasma membrane proteins are confined to the apical side of the cell (protein A), whereas other proteins are confined to the basal and lateral (basolateral) surface of the cell (protein B).<sup>[90]</sup> This asymmetric distribution of membrane proteins is often of great importance for the function of epithelial

cells.<sup>[90]</sup> In the epithelium of the small intestine this “fence” ensures the natural transcellular transport of nutrients.<sup>[88,90]</sup> And for this transport to be effective, the sealing of the gaps between adjacent cells has to be tight, so that transported molecules do not diffuse back into the gut lumen.<sup>[90]</sup> TJs are located at the apical side and consists of a complex of transmembrane and cytoplasmic proteins.<sup>[92]</sup> The tightness of these intercellular junctional complexes can strongly vary.<sup>[9]</sup> While the brain and skin epithelium are subject to a very tight barrier, the colon and stomach junctional connection is of intermediate tightness.<sup>[9]</sup> In comparison, the small intestine exhibits a weak tightness and is considered as a leaky epithelial tissue.<sup>[9,92]</sup>

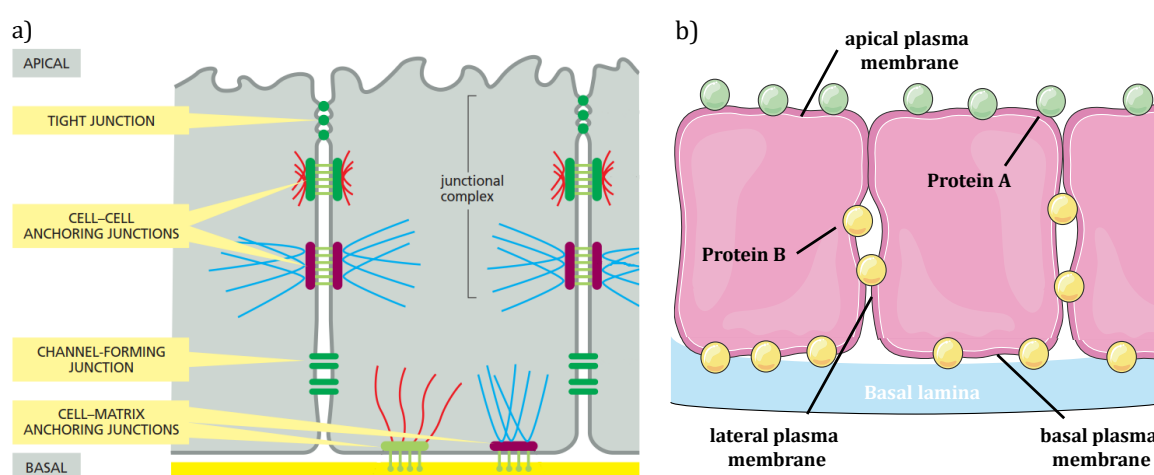


**FIGURE 1.12. CELL JUNCTIONS IN EPITHELIAL CELLS:** **a)** In the epithelium, cells are tightly connected by junctional complexes, classified in cell-cell and cell-matrix junctions. Each of these junctions are specifically located thorough the gap and are subjected to specific functions. Image adapted from reference.<sup>[90]</sup> **b)** Tight junctions serve as a belt to prevent mixing of apical and basolateral plasma membrane proteins. Cartoon has been created by images of SMART.<sup>[13]</sup>

The epithelium also acts as a barrier to infections.<sup>[6,8,90]</sup> The first encounter of infectious organisms are typically epithelial cells as they provide both physical and chemical barriers for pathogens and toxins.<sup>[6,90,93,94]</sup> As TJs control and regulate the passage of ions and molecules between adherent cells, the cell additionally produces substances in form of secretion to inhibit the attachment or entry of infectious compounds.<sup>[90]</sup> For example, fatty acids and lactic acids are secreted in the skin to discourage bacterial growth. Furthermore, epithelial cells in all tissues produce a secretion based on antimicrobial molecules, called defensins, which binds to and disrupt the membranes of many pathogens, including viruses, bacteria, fungi and parasites.<sup>[90]</sup>

In terms of drug delivery, epithelial and endothelial cells of the human body are subjected as major obstacles to the systemic circulation.<sup>[9]</sup> Several transport routes within these barriers exist, which can be exploited for drug absorption.<sup>[9,92]</sup> While the transcellular pathway involves transcytosis, the paracellular transport is restricted by junctional complexes, including TJs.<sup>[7]</sup> For that reason, it is not surprising that the small intestinal is the major place for drug absorption.<sup>[92]</sup> In addition, the oral route is the most convenient and comfortable method to take drugs.<sup>[92]</sup>

Nevertheless, the non-invasive transport of drugs to the systemic circulations or to target organs is still challenging, due to the high protection of those barriers.<sup>[9]</sup> The discovery of the transmembrane proteins of TJs in the last 25 years, was a great achievement in understanding how epithelial barriers work and how this knowledge can be used for drug discovery and targeting, and disease therapies.<sup>[9]</sup> The absorption of drugs across the epithelium is constrained by several factors, including the limited paracellular transport by intercellular junctions.<sup>[9,92]</sup> In the last decades several methods and molecules have been investigated to improve drug absorption and penetration.<sup>[9,92]</sup> This issue will be further intensified in *Chapter 6 – Monitoring of Cell Layer Integrity with a Current-Driven Organic Electrochemical Transistor* and in *Chapter 7 – Reversible Opening of Membranous Barriers by Tight Junction Modulators*.

# Chapter 2

## Experimental

This chapter contains device fabrication, biological preparation as well as characterization methods used in this work. The preparation and fabrication of organic electrochemical transistors (OECTs) devices is outlined in detail, comprising in particular the organic solvent treatments for PEDOT:PSS. The microfabrication of precisely PEDOT:PSS-coated electrodes involves photolithography and is extensively discussed. Cell preparation embraces culturing of different cell lines and preparation for biological experiments. Characterization of the devices is investigated by different techniques and concludes the experimental section.

## 2.1. Device Fabrication

In this section the fabrication of PEDOT:PSS-based OECTs and electrodes is described. OECTs are processed by thermal evaporating of metal contacts using shadow masks for patterned structures. The PEDOT:PSS-coated electrodes make use of photolithography to pattern the metal contacts as well as PEDOT:PSS. All cleaning and fabrication processes were conducted in a clean room and in gloveboxes, which are under an inert nitrogen atmosphere.

### 2.1.1. Fabrication of OECTs

PEDOT:PSS (Clevios PH 1000, Hereaus) was exclusively used as the active conducting material in the channel in OECTs. The PEDOT:PSS solution was premixed with the non-ionic fluorosurfactant Zonyl® FSO-100 (2 drops/10 mL) from DuPont to enhance the wetting behavior on a hydrophobic surfaces for film processing. If not otherwise stated, the additive dimethyl sulfoxide (DMSO, Merck KGaA) was used in a volume ratio of 10% for organic solvent treatments of PEDOT:PSS without further purification. The dispersion was stirred at least for 1 hour before further use.

Glass substrates (Corning®EAGLE XGTM AMLCD) or quartz substrates (Präzisions Glas & Optik GmbH) were used with a size of 30 × 30 mm. The substrates were manually scrubbed for 1 minute with a soap solution (Extran® MA 02, Merck KGaA) and rinsed thoroughly with deionized water, before immersing in a deionized water bath for 7 minutes. Afterwards the substrates were subsequently cleaned by sonication in acetone and isopropanol for 5 minutes and dried for 10 minutes at 140 °C. A UV-ozone treatment (UVOCS®) of 20 minutes was conducted to remove any organic residues on the surface. By using a shadow mask, gold source and drain electrodes and interconnects (100 nm) were thermally evaporated and patterned on the cleaned substrates. Chromium (5 nm) served as an adhesion layer between gold and the substrate material. Arrays of transistors were fabricated on the substrates with a channel width of 1000 μm and channel lengths varying between 1000–50 μm (Figure 2.3(a)). Other transistor dimensions than these will be noted in the relevant chapters. For a better adhesion, the glass surface was reactivated by a brief UV-ozone treatment of 10 minutes before film deposition. The PEDOT:PSS solution was spin-coated using the following recipe: 10 seconds at 1000 rpm (1000 acceleration), followed by the drying step of 50 seconds at 1500 rpm (1000 acceleration). The first step determines the thickness, in this case usually averaged 100 nm. The PEDOT:PSS channel was patterned with a wet cotton stick before annealing for 1 hour at 140 °C. After the final annealing samples were rinsed in deionized water and dried with nitrogen. A poly(methyl methacrylate)-well (PMMA) was placed on top for a defined volume of the electrolyte, using double-sided tape to prevent leakage.

In *Chapter 4*, an additional 1.8  $\mu\text{m}$  AZ1518 positive photoresist, purchased from Microchemicals GmbH, was spin-coated and photolithographically patterned on top of electrodes of the OECT. Sodium chloride (NaCl) and potassium chloride (KCl), purchased from Sigma-Aldrich, were simply dissolved in deionized water providing the electrolyte solutions. Various concentrations have been prepared by the means of serial dilutions.

For the *Solvent Additive* method (SA) the additive DMSO is simply premixed in different volume ratios to the PEDOT:PSS dispersion as already described above as the standard method. For the *Polar Solvent Vapor Annealing* (PSVA) and *Polar Solvent Post-Treatment* (PSPT) methods the aqueous dispersion of PEDOT:PSS was spin-coated without the additive. Solvent post-treated films were annealed for 10 minutes at 140 °C right after film deposition and patterning, before immersing and cooling in a DMSO bath for a duration varying from 1–30 minutes. For PSVA, the devices were placed in a specially designed PSVA-chamber, which can be flooded with pure nitrogen or DMSO-saturated nitrogen gas. The samples have been vapor-annealed for a duration of 30–240 minutes at a solvent temperature of 120 °C or at a set time of 2 hours for various DMSO temperatures, ranging from 25–120 °C. Before and after vapor annealing the chamber was flooded with pure dry nitrogen gas for 5 minutes. In order to have a DMSO-saturated gas in the whole PSVA setup, the procedure was started at least 1 hour in advance (with no samples inside) to make sure the setup including container and tubes were filled with saturated gas.

The ion-selective OECT (IS-OECT), used in *Chapter 4*, implies a  $\text{K}^+$ -selective membrane integrated with the OECT. As for that matter, the PVC-based membrane was synthesized by mixing high molecular weight PVC (36.5 wt.%, Fluka–Chemika) with potassium ionophore III (2.5 wt.%, Sigma-Aldrich), potassium tetrakis(4-chlorophenyl-)borate (0.5 wt.%, Sigma-Aldrich) and diisodecyl adipate (60.5 wt.%, Sigma-Aldrich) in tetrahydrofuran (THF, 500 mg/5 mL).<sup>[95]</sup> The solution was drop-casted onto a glass substrate in the center of a rubber ring to define its dimension as shown in Figure 2.1(a).<sup>[95]</sup> The membrane was dried overnight at room temperature. The rubber ring allows the necessary stability to transfer the membrane onto the OECT, illustrated in Figure 2.1(b).<sup>[95]</sup>

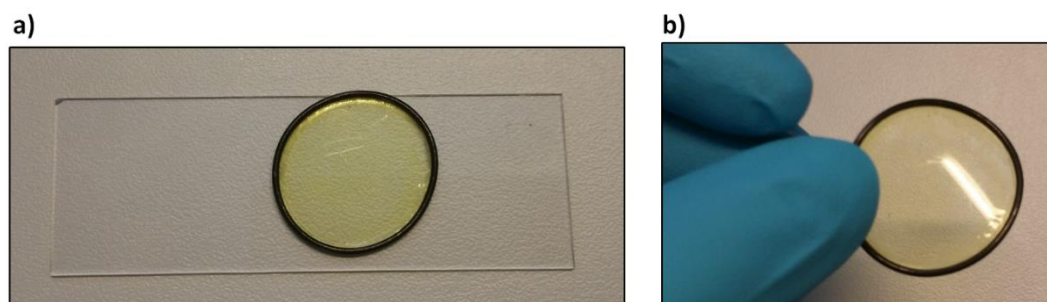


**FIGURE 2.1.** Ion-selective membrane: **a)** The THF solution was drop-casted on a glass slide, surrounded by a rubber ring. **b)** The rubber ring provided the necessary stability to transfer the membrane onto the OECT.

### 2.1.2. Microfabrication of Electrodes

Microscope slides in the dimension of  $26 \times 76$  mm were used for PEDOT:PSS-coated electrodes for the application in *Chapter 5*. The substrates were thoroughly cleaned first in a soap (Micro-90®, Sigma-Aldrich) and then in a 1:1 (vol/vol) solvent mixture of acetone/isopropanol sonication bath.

The following PEDOT:PSS formula was used: 38 mL of PEDOT:PSS aqueous dispersion (Clevios PH-1000), 2 mL of ethylene glycol (EG, Sigma-Aldrich), 50  $\mu$ L of 4-dodecylbenzenesulfonic acid (DBSA, Sigma-Aldrich) and 0.4 mL of 3-methacryloxypropyl-trimethoxysilane (GOPS, Sigma-Aldrich). Like DMSO, EG served as a conductivity enhancer. DBSA increases film formation, as GOPS promotes surface adhesion and polymer crosslinking.

The gold electrodes were patterned with the use of a photoresist (Microposit S1813, DOW) and an initial photolithography step, just before a double layer of Parylene C was employed to encapsulate the device. Between the two layers of Parylene C, soap solution (Micro-90®, 1% vol/vol in bidistilled water) served as an anti-adhesive layer facilitating a later peel-off step of the fabrication. On the other hand, silane, an anti-adhesive promoter, was deployed between the substrate and the first Parylene C layer in order for the adhesion to be enhanced. On top of the second Parylene C layer, a different photoresist (AZ 9260, Microchemicals, Cipeç Spécialités) was spun and a second photolithography step defined window openings on the photoresist above each electrode. Reactive Ion Etching (RIE) etching with  $O_2$  plasma was used to remove Parylene C under those window openings and to expose the active area of each one of them. PEDOT:PSS was afterwards spun, creating a thin film of a conducting polymer of around 100 nm on the device. A final peel-off step defined the active area of the conducting polymer-coated gold electrodes. The devices were subsequently soft baked for 1 hour at  $140^\circ\text{C}$  before placed in bidistilled water over night for the removal of the excess of any low molecular weight molecules.



## 2.2. Cell Preparation

In this work, two different cell lines were used to address different biological purposes. Caco-2 cells were used to study barrier tissue integrity, originating from a human colorectal carcinoma and being a well-known model for gastrointestinal barriers<sup>[6]</sup>. MDA-MB-231 cells in particular do not express E-cadherin<sup>[96]</sup>, leading to low cell-cell contacts, which allows the expression of photoswitchable proteins for light-induced cell-cell interactions. The two cell lines were routinely cultured according to standard procedures.<sup>[97]</sup>

### 2.2.1. Culturing of Caco-2 Cells

Caco-2 cells were cultured in EMEM (Eagle's Minimum Essential Medium, Lonza), supplemented with 10% FBS (fetal bovine serum, Thermo Fisher), 2 mM Glutamine (GlutaMax™-1, 100X, Thermo Fisher) and 1% Penicillin (10,000 U/mL) and Streptomycin (10,000 µg/mL) (Pen/strep, Thermo Fisher) at 37 °C in a humidified atmosphere with 5% CO<sub>2</sub> (CO<sub>2</sub> Incubator C200, Labotect). The cells were passaged when confluency reached approx. 80%. Consumed cell medium was discarded and the cells were washed in 10 mL Dulbecco's Phosphate Buffered Saline (PBS, Sigma-Aldrich). For detachment the cells were immersed in 10 mL trypsin-EDTA (Thermo Fisher, Gibco) for 15 minutes at 37 °C. Afterwards, 10 mL EMEM solution was added to the flask and pipette up and down to detach all cells. The cell suspension was centrifuged at 300 g (800 rpm) for 3 minutes. The supernatant medium was removed and the formed cell pellet was resuspended in 10 mL cell medium. For cell viability, the cell solution was mixed with a Trypan Blue solution (0.4%, Sigma-Aldrich) in a volume ratio of 1:1 (20 µL). The live count was determined by an automated Cell Counter (TC10, Bio-Rad).

For barrier tissue measurement, cells were seeded at  $1.5 \times 10^5$  cells/insert on a 12 mm Transwell filter with 0.4 µm pore polycarbonate membrane inserts. The medium was changed every 2–3 days. A closed cell layer was established after 14 days, confirmed with a TEER of 400–500 Ω cm<sup>2</sup>.

Caco-2 cells were purchased from Leibniz-Institut DSMZ – Deutsche Sammlung von Mikroorganismen und Zellkulturen GmbH.

### 2.2.2. Culturing of MDA Cells

Wildtype MDA cells and MDA cells, expressing photoswitchable proteins, were cultured in DMEM (Dulbecco's Modified Eagle Medium, Gibco) with 10% FBS, 1% Penicillin (10,000 U/mL) and Streptomycin (10,000 µg/mL) (Pen/strep), and Geneticin (G-418 Solution, 1.8 mg/mL, Roche) under similar conditions as in *Section 2.2.1*. For cell detachment, 10 mL Acctuase (Thermo Fisher, Gibco) was used for 3–5 minutes and the cell suspension was centrifuged at 500 g for 5 minutes.

Cells were seeded at  $5 \times 10^5$  cells/insert on Transwell filters (1.12 cm<sup>2</sup>, 0.4 µm), if not otherwise stated. The cell filters were usually used after 7–9 days in culture. For the light induced cell-cell interactions, it is crucial to use phenol red free medium as well as the cofactor Phycocyanobilin (PCB, 5 µM) for the cyanobacterial phytochrome 1 system (CPH-1) and flavin mononucleotide (FMN, 1:1000) for improved light-inducible dimer/Nano system (iLID/Nano) on the day of the measurements. The cofactor PCB was extracted from *Spirulina* (in house), while FMN was purchased from Sigma-Aldrich. For the light induced cell measurement the light system from flora LED<sup>s</sup> CLF Plant Climatics Germany was used.

MDA-MB-231 cells were purchased from European Collection of Authenticated Cell Cultures (ECACC).

### 2.2.3. Filter Preparation

For an increased cell layer resistance, the area was reduced to approx. 0.08 cm<sup>2</sup> by applying polydimethylsiloxane (PDMS) on the back side for the filter and curing at room temperature for 2 days, as displayed in Figure 2.2(a–c). The silicon elastomer from Dow Corning was processed by mixing Sylgard 184 with the current agent in a ratio of 1:10 and was kept for further use at –80 °C. For PDMS-modified Transwell filters an additional collagen-coating was implemented for improved cell attachment. The PDMS-modified Transwell filters were sterilized under UV-light for 60 minutes and washed twice with PBS before incubating the filters with 0.5 mL collagen (type 1 solution from rat tail, Sigma-Aldrich) overnight at 37 °C. The remaining solution was removed and the filters were dried under UV light. Before cells were seeded, the filters were carefully washed again with PBS.

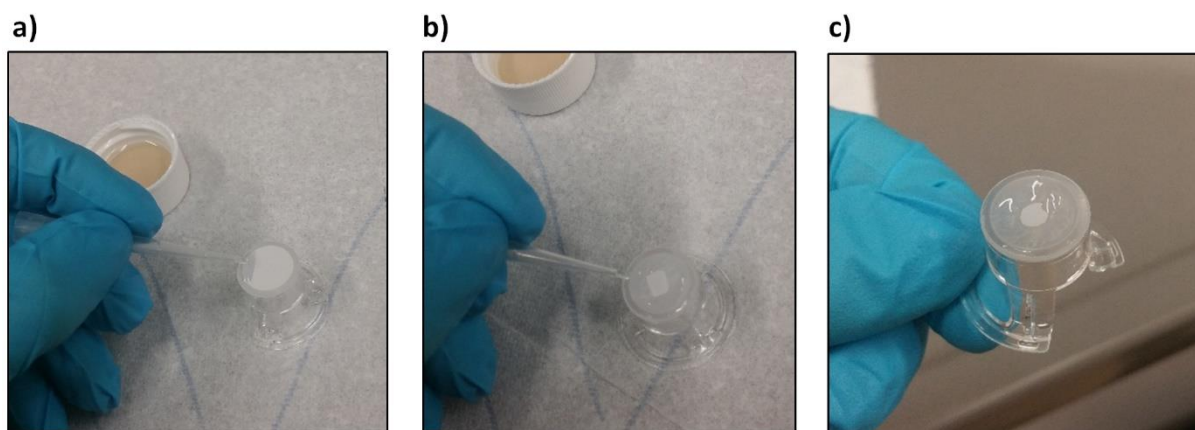


**FIGURE 2.2.** Filter Preparation: **a–c)** The viscous PDMS solution was applied with an Eppendorf tip on the back side of the Transwell filter to reduce the area by a factor of 8–10.

#### 2.2.4. Preparation of Tight Junction Modulators

Chitosan (oligosaccharide) with an average molecular weight  $M_n$  of 5,000 Da and poly-L-lysine (hydrobromide) with an average molecular weight  $M_n$  of 30,000–70,000 Da, were obtained from Sigma-Aldrich. The polymers were dissolved at a concentration of 1% and 10% in EMEM cell culture medium.

Taurocholic acid sodium salt (NaTC) and sodium caprate (C10), purchase from Sigma-Aldrich, were dissolved in EMEM cell culture medium at a concentration of 10 mM and 16 mM, respectively.

#### 2.2.5. Immunofluorescence Staining

Immunofluorescence staining was conducted on the cytoskeleton and the nucleus of cells to visualize cell layer coverage. In this procedure, the cell layers were fixed in 4% paraformaldehyde (PFA). The fixed cell layers were washed twice with PBS and permeabilized with 0.1% Triton-X-100 (Sigma-Aldrich) for 5 minutes at room temperature. After washing with PBS, Phalloidin (1:1000 in PBS,) was added to stain the cytoskeleton. The stained cell layers were uniformly mounted on slides by using a Mowiol 4-88 (Carl Roth) solution containing DAPI (1  $\mu\text{g}/\text{mL}$ , Sigma-Aldrich), to stain the nucleus. The microscope slides were dried overnight and examined under a confocal laser scanning microscope (cLSM).

## 2.3. Characterization Methods

In this section, all applied methods for characterization will be outlined. OECTs were in general analyzed by current-voltage measurements under ambient atmosphere with the assistance of a probe station. In addition, electrochemical impedance spectroscopy was conducted on OECTs and electrodes. Purely spin-coated PEDOT:PSS films were solely analyzed for morphological reasons by spectroscopical methods as XPS and GIWAXS. Biological samples were additionally examined with microscopy techniques.

### 2.3.1. Electrical Characterization

OECTs were characterized by using a Keithley 4200 – Semiconductor Characterization System and the recorded data was analyzed with OriginLab and MatLab software. The transistor samples were introduced to a probe station as shown in Figure 2.3(b). Positioned on a plate, movable in  $x$ -,  $y$ -,  $z$ -direction, the samples were fixed by a rough vacuum. Source and drain were contacted with probes as depicted in Figure 2.3(c), while a Ag/AgCl pellet (2 mm, Warner Instruments) was connected on top using a crocodile electrode as a gate. If not otherwise stated, an aqueous solution of NaCl in the standard concentration of 0.1 M was applied as an electrolyte.

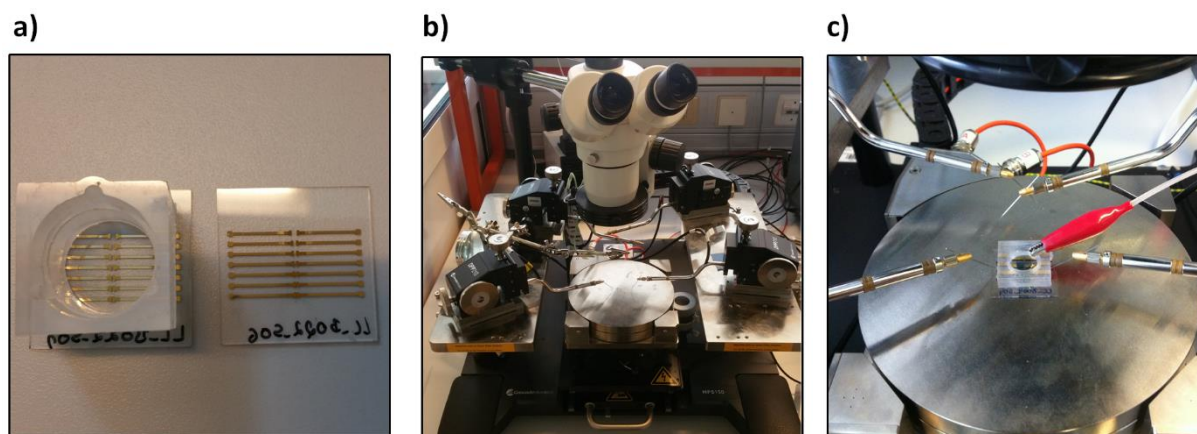


**FIGURE 2.3.** DEVICE STRUCTURE AND MEASURING SETUP: **a)** Image of an OECT device consisting of an array of transistors, with and without a PMMA well. **b)** Image of the probe station consisting of a movable plate, probes and a microscope. **c)** Image of a contacted OECT device within the probe station.

*Current-voltage measurements* were performed to analyze the electrical characteristics of OECTs. The maximum operating gate voltage was kept well below 1 V to avoid any water electrolysis and the over-degradation of the conducting polymer. The electrical characteristics are determined by the device dimensions, defined by the width ( $W$ ), length ( $L$ ) and the thickness ( $d$ ) of the channel. The output characteristics show the modulation of the drain current sweeping the drain voltage

at a constant gate voltage, exhibiting the linear and saturation operating regime. The transfer characteristics are demonstrated by sweeping the gate voltage at constant drain voltage. The corresponding transconductances is defined by the term  $g_m = dl_d/dV_g$ , quantifying the efficiency of the transducing signal.

*Resistance measurements* were performed by the two-point probe technique at dry conditions. Taking the channel's dimension into account, Equation (2.1) reveals the corresponding conductivity of the PEDOT:PSS film, given in the standard  $S\text{ cm}^{-1}$  unit. The thickness of the spin-coated films was measured with a surface profilometer (Bruker, DektakXT Stylus Profiler) at dry conditions.

$$\sigma = \frac{L}{W \cdot d} \cdot \frac{1}{R} \quad (2.1.)$$

For the IS-OECT a small PDMS-well contained the inner solution ( $10^{-2}$  M KCl) and additionally served as a mechanical support for the  $K^+$ -selective membrane. On top of the ion-selective membrane, a small chamber (Transwell filter,  $0.4\text{ }\mu\text{m}$ ) was placed with the analyte solution at various concentrations. A reference Ag/AgCl electrode was immersed into the analyte solution and used as gate electrode (1 mm pellet, Warner Instruments). The complete structure of the IS-OECT is displayed in Figure 2.4(a).

*Cell layer integrity experiments* were accomplished at ambient conditions in a time frame of 90 minutes to ensure cell viability. Transwell filters, providing the cells, were integrated between the gate and the channel as shown in Figure 2.4.(b). Instead of a saline solution, cell culture medium served as the electrolyte. Toxic compounds such as  $H_2O_2$  or tight junction modulators were added to the apical side of the cell filter.  $H_2O_2$  was added as an aqueous solution in a concentration of 1 mM or 5 mM in deionized water, without changing media. Tight junction modulators were added as a solution in cell culture medium in the respective concentration. The transient response was measured by pulsing the gate voltage  $V_G$  at 300 mV for 20 seconds at a drain voltage  $V_D = -0.1$  V. Its response time was determined by the Fourier Transform of the multi-exponential decay of the experimental transient response. The normalized response was calculated by  $\Delta\tau/\tau_0$ , which is the change of the response time by applying a gate voltage, divided by the response time when  $V_G$  is off. In the current-driven configuration the supply voltage was set to  $V_{DD} = 0.2$  V and the input voltage  $V_{in}$ , applied at the gate, was swept from  $-0.2$  V to  $+0.7$  V at a constant current bias  $I_B$ . The normalized response was obtained like  $\tau$  by  $\Delta I_D/I_0$ , which is the change of the drain current by applying a gate voltage, divided by the drain current when  $V_{in}$  is off.

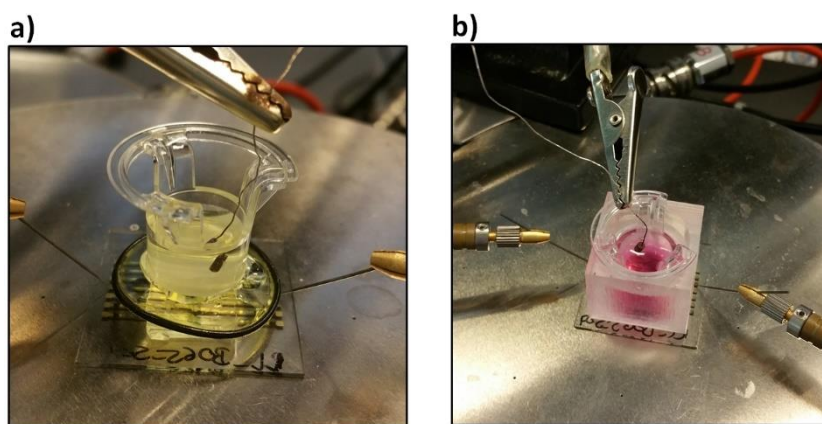


**FIGURE 2.4.** OECTS FOR DIFFERENT APPLICATIONS: **a)** Image of the IS-OECT composed of a small PDMS well, containing the inner solution, the ISM and the upper well, containing the analyte solution. **b)** Image of the cell layer integrated OECT. A Transwell filter with Caco-2 cells is introduced between the gate and the channel.

*Transepithelial electrical resistance measurements* (TEER) were realized with a handheld epithelial volt-ohm meter EVOM<sup>2</sup>™ from World Precision Instruments as depicted in Figure 2.5(a), evaluating the integrity of the cellular barrier by measuring the ohmic resistance. The EndOhm chamber consists of two concentric electrodes, incorporating a voltage-sensing Ag/AgCl pellet in the center and an annular current electrode. The current electrode is made of Ag and coated with AgCl. The top cap assembly consists of three components: the cap, the locking nut and the electrode. This assembly centers the electrode in the culture and fixes the height of the electrode. The complete setup is schematically depicted in Figure 2.5(b). By applying a small AC signal across two electrode plates, which are placed on both sides of a cell monolayer and measuring the voltage and current, the electrical resistance is calculated. The TEER is given in  $\Omega \text{ cm}^2$ , normalized on the area of the Transwell insert.

For the electrical monitoring of light-induced cell-cell interactions, the resistance measurements were performed under sterile conditions inside the hood and light illumination of the respective wavelength. For irradiation inside the hood, the entire room was darkened and a LED lamp served as the light source. For irradiation inside the incubator, the light system from flora LED<sup>s</sup> CLF Plant Climatics was used.

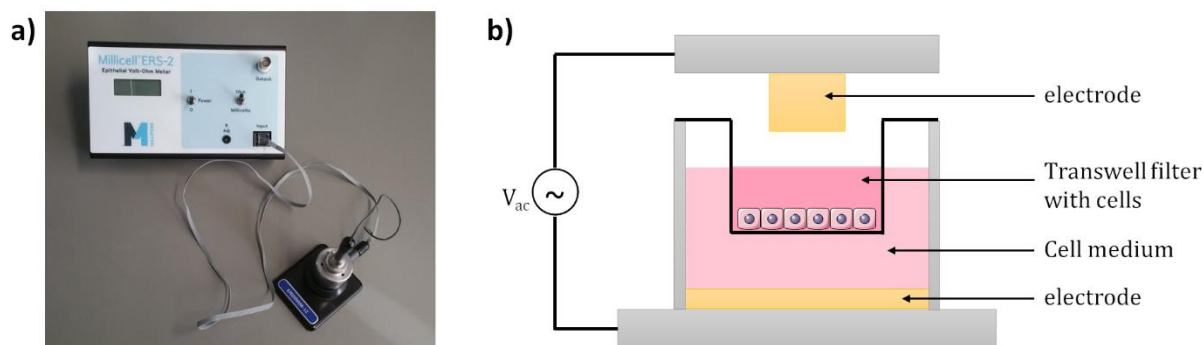


**FIGURE 2.5.** TEER VOLT-OHM METER: **a)** Image of the volt-ohm meter comprising of the measuring device EVOM and the EndOhm chamber. **b)** Schematic diagram of the EndOhm chamber in the open state with an integrated Transwell filter.

*Electrochemical impedance spectroscopy* (EIS) was realized in a three-electrode configuration at a potentiostat (FRA2  $\mu$ Autolab TYPE III). For the OECT measurements a 0.1 M NaCl solution was used. OECT's source and drain were shorted, serving as the working electrode, while Pt and Ag/AgCl electrodes were used as the counter and the reference electrode, respectively. For the frequency depended impedance properties of PEDOT:PSS-coated electrodes, Transwell filters were used to host the Caco-2 layer of cells above the recording sites. The PEDOT:PSS-coated electrodes served as the working electrode. At the working electrode a small voltage signal was applied, and the impedance was recorded as a function of frequency. A custom Labview software was subjected to control the equipment. The data were fitted with an equivalent R – C circuit to obtain capacitance and resistance values.

Only in *Chapter 4*, we used the National Instruments PXI-1042 system, equipped with a PXI-5421 arbitrary wave-function generator and a PXI-5112 oscilloscope, and two Ag/AgCl pellets served as the counter and reference electrode.

### 2.3.2. Spectroscopical Characterization

For XPS and GIWAXs samples, silicon oxide substrates with the size of  $10 \times 10$  mm were used. The substrates were cleaned in a similar way. A UV-ozone treatment of 20 minutes was conducted before spin coating the PEDOT:PSS solution. The respective organic solvent treatment with DMSO was implemented, before final annealing for 1 hour at  $140^\circ\text{C}$ .

*X-ray photoelectron spectroscopy* (XPS) was conducted using a Kratos Axis Ultra<sup>DLD</sup> spectrometer (Kratos, Manchester, England) utilizing an Al K $\alpha$  excitation source with a photon energy of 1487 eV. This strength of photon energy probes the top layer of about 8–10 nm. The hybrid mode was used to analyze using a  $0^\circ$  take-off angle, defined as the angle between the

surface normal and the axis of the analyzer lens. Employing a setting analyzer energy of 80 eV detailed region XPS spectra were collected, while for high resolution spectra 20 eV was used. A neutralizer was always used during spectra collection. The *relative PEDOT-to-PSS ratio* was defined as the ratio of the maximum of PEDOT to PSS signal of the spectrum in respect to the pristine ratio. For the depth profile, the PSPT-treated PEDOT:PSS films were etched using a RIE plasma etcher. The thickness was determined by a profilometer. The *relative PEDOT-to-PSS ratio* was defined as the ratio of the area of PEDOT and PSS in respect to the pristine ratio.

*Grazing incidence wide-angle X-ray scattering* (GIWAXS) was performed at the DELTA Synchrotron using beamline BL09 (1.0x0.2 mm) with a photon energy of 10 keV ( $\lambda = 1.239 \text{ \AA}$ ). The spin-coated silicon oxide samples were irradiated just below the critical angle for total reflection regarding the incoming X-ray beam ( $\sim 0.1^\circ$ ). A 2-D image plate (MAR-345) with a pixel size of  $150 \text{ }\mu\text{m}$  (2300x2300 pixels) was used as a detector and was placed 381 mm from the sample center. Silver behenate was used as a calibration standard to convert the raw detector image into reciprocal-space, which has rings at known  $2\theta$  positions. Scattering data are defined as a function of the scattering vector:  $Q = 4\pi/\lambda \sin(\theta)$ , where  $\theta$  is a half the scattering angle and  $\lambda = 1.239 \text{ \AA}$  is the wavelength of the incident radiation. All X-ray scattering measurements were conducted under vacuum ( $\sim 1 \text{ mbar}$ ) to reduce air scattering and beam damage to the sample. All GIWAXS data was analyzed with Datasqueeze software.

### 2.3.3. Microscopy Characterization

The confluency of Caco-2 cells as well for MDA cells was examined under the Inverted Microscope CKX41 from Olympus.

The visualization of the cell layer was employed by confocal laser scanning microscopy (cLSM). Microscopic slides, prepared by immunofluorescence staining, were examined on the LSM SP5 STED Leica Laser Scanning Confocal Microscope (Leica, Germany), consisting of an inverse fluorescence microscope DMI 6000CS equipped with a multi-laser combination using a HCX PL APO CS 63 x 1.4 oil objective.



# Chapter 3

## Effect of DMSO Solvent Treatments on the Performance of PEDOT:PSS-based Organic Electrochemical Transistors

The conductivity of poly(3,4-ethylenedioxythiophene):poly(styrene sulfonic acid) (PEDOT:PSS) can be strongly enhanced by treatment with high boiling solvents as dimethyl sulfoxide (DMSO). In this chapter we report on the effect of various DMSO solvent treatment methods on the performance of organic electrochemical transistors (OECTs) based on PEDOT:PSS. The treatments include mixing PEDOT:PSS with DMSO before film deposition, exposing a deposited PEDOT:PSS film to a saturated DMSO vapor and dipping a PEDOT:PSS film in a DMSO bath. Compared to dry PEDOT:PSS, operating in the OECT configuration causes a significant reduction of its conductivity for all treatments, due to the swelling of PEDOT:PSS by the direct contact of the conductive channel with the electrolyte. The dipping method gives rise to the highest OECT performance, reflected in the highest on/off ratio and transconductance. The improved conductivity and device performance after dipping arise from an enhanced charge carrier mobility due to enhanced structural order.\*

\*L. V. Lingstedt, M. Ghittorelli, H. Lu, D. A. Koutsouras, T. Marszalek, F. Torricelli, N. I. Crăciun, P. Gkoupidenis, P. W. M. Blom, *Adv. Electron. Mater.* **2019**, 26, 1800804.

### 3.1. Introduction

Bioelectronics has drawn huge attention in applications related to neural interfacing, chemical sensing, biosensing, drug delivery, e-plants, and chemical logic.<sup>[1,17]</sup> A key element of this field is the organic electrochemical transistor (OECT), belonging to the class of electrolyte-gated transistors.<sup>[15,59]</sup> The working principle of an OECT has been described in detail in the *Introduction* in *Chapter 1* and is shortly outlined here.<sup>[3,60,63]</sup> The OECT is assembled by the typical configuration of source and drain, comprising a conductive channel in direct contact with an electrolyte, in which a gate electrode is immersed. OECTs, operating with *p*-type semiconducting polymers as the active channel, work in the depletion mode. The essential is the ability of cation injection from the electrolyte into the channel upon a positive gate bias, modifying its hole conductivity. The transistor is pushed into the off-state (drain current is decreased) due to the decreased hole density. The non-invasive and label-free high amplification of signals makes OECTs attractive for sensing and monitoring of biological events.<sup>[3,4,61,83]</sup> OECTs have one of the highest transconductance among the different types of transistors ( $g_{m,max} > 1 \text{ mS}$  for micro-scale devices).<sup>[3,4]</sup>

The most frequently used conducting polymer in OECTs is PEDOT, doped with PSS, well combining mixed ionic and electronic conductivity and stability in aqueous environments over a wide pH range.<sup>[4,5,14,15,80,98]</sup> The conductivity strongly depends on the film morphology and its dopant.<sup>[15]</sup> Without special treatment typical conductivities of  $\sigma = 0.2\text{--}1 \text{ S cm}^{-1}$  are obtained for PEDOT:PSS, which are not sufficient for application in OECTs.<sup>[50,52]</sup>

Several techniques have been reported in literature to improve the electrical conductivity of PEDOT:PSS, commonly defined as *Secondary Doping* and has been briefly introduced in the *Introduction* in *Chapter 1*.<sup>[23]</sup> Examples are physical approaches like light and thermal treatment<sup>[23,29–34]</sup>, as well as chemical methods as treatment with organic solvents and other compounds like ionic liquids, surfactants, salts and acids.<sup>[23,35–43]</sup> The most common chemical technique to enhance PEDOT:PSS conductivity is using polar organic solvents with high boiling points as dimethyl sulfoxide (DMSO), ethylene glycol, N,N-dimethyl formamide, xylitol, tetrahydrofuran, sorbitol, glycerol, methoxyethanol, diethylene glycol, dimethyl sulfate and meso-erythritol.<sup>[23]</sup> Depending on the method and the solvent, a significant enhancement of the conductivity ranging from  $\sigma = 4\text{--}677 \text{ S cm}^{-1}$  can be achieved.<sup>[23,45,99–104]</sup> Typically, the high boiling solvent is added to the PEDOT:PSS dispersion before deposition and this approach is therefore termed *Solvent Additive* (SA) method.<sup>[23,45,101]</sup> By combining NEXAFS and X-ray scattering it was demonstrated that the addition of a solvent generates domain purification in form of PEDOT:PSS-rich domains, described as gel-like particles in a pancake-like morphology, surrounded by a PSS-rich matrix.<sup>[14]</sup> However, in OECTs the PEDOT:PSS is in direct contact with an electrolyte, typically leading to swelling.<sup>[105]</sup> Therefore, it is very relevant to understand if the conductivities measured

in solvent-treated dried PEDOT:PSS films are representative for the performance of PEDOT:PSS in OECT configuration. Furthermore, it is not clear which kind of solvent treatment leads to an optimized OECT performance in terms of on/off ratio and transconductance. In this study we focus on the electrical characteristics of OECTs based on PEDOT:PSS using various methods of organic solvent treatments. For the *Solvent Additive* (SA) method a solution of PEDOT:PSS is mixed with DMSO in various concentrations before deposition of the film. In the second approach, the *Polar Solvent Vapor Annealing* (PSVA) method, spin-coated PEDOT:PSS films are exposed to a saturated DMSO vapor. Finally, spin-coated PEDOT:PSS films were immersed in a DMSO bath, subsequently termed here as the *Polar Solvent Post-Treatment* (PSPT) method. Each treatment is investigated by varying the amount of organic solvent, which is equivalent for some treatments by the duration of procedure. A schematic overview of the different procedures is shown in Figure 3.1.

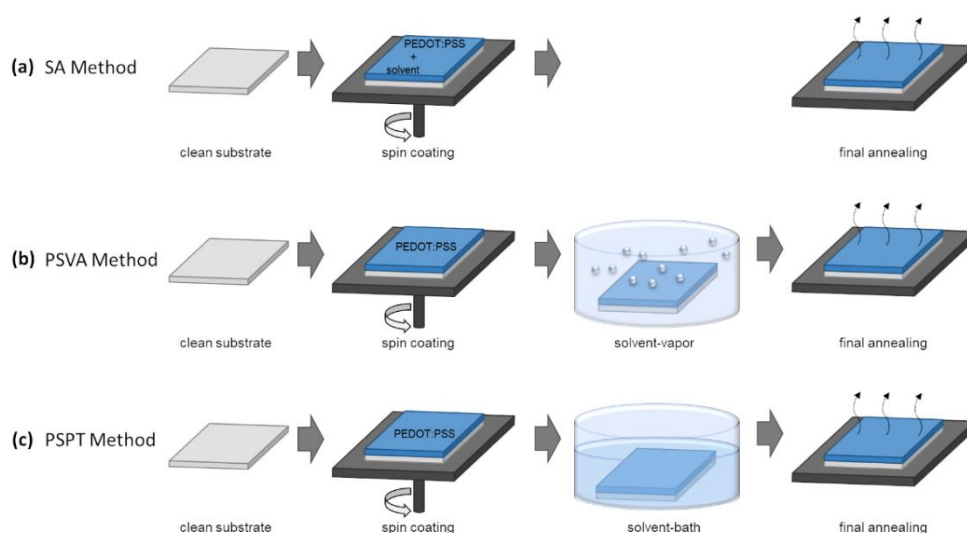


**FIGURE 3.1.** ORGANIC SOLVENT TREATMENTS: **a)** The *Solvent Additive* method (SA) uses premixed PEDOT:PSS dispersion with additives for spin-coating. **b)** Exposing solvent vapor to pure PEDOT:PSS films is applied by the *Polar Solvent Vapor Annealing* method. **c)** The *Polar Solvent Post-Treatment* method is carried out by immersing pure PEDOT:PSS films in a solvent bath.

## 3.2. Results and Discussion

As a reference we first investigate the conductivity  $\sigma_{\text{dry}}$  of PEDOT:PSS as function of solvent treatment procedure under dry conditions, meaning that there was no contact with the electrolyte involved. In the SA method the effect of doping can be controlled by the amount of the added DMSO solvent (Figure 3.1(a)).<sup>[23,44,99–101]</sup> We observe that  $\sigma_{\text{dry}}$  increases from 2.5 S cm<sup>-1</sup> for a pristine PEDOT:PSS film to 1233 S cm<sup>-1</sup> by the addition of 10 vol-% of DMSO (Table 3.1). A more detailed

study on the dependence of DMSO content on the conductivity of PEDOT:PSS is shown in Figure S3.1(a) in the *Supporting Information of Chapter 3*. For the PSVA method a special setup was constructed (Figure S3.2, *Supporting Information 3.4*), where the chamber can be either flooded with dry nitrogen gas or with solvent-enriched gas and both can be regulated by a gas flow control. Herein, the samples were treated with a DMSO-enriched gas for different durations at a specific solvent temperature. In the PSVA procedure the controlling factor for conductivity enhancement is the “exposure time” to the solvent vapor.<sup>[102]</sup> After a DMSO vapor treatment of 2 hours at 120 °C the conductivity increases to value of  $\sigma_{\text{dry}} = 1406 \text{ S cm}^{-1}$  (Table 3.1). The time and temperature dependence on the conductivity of PEDOT:PSS are displayed in Figure S3.1(b, c) in the *Supporting Information 3.4*. Treating PEDOT:PSS films with solvents in form of a solvent bath (Figure 3.1(c)) is a relatively simple way to reach enhanced conductivity.<sup>[51,52,103,106,107]</sup> Table 3.1 shows the effect on the dry conductivity of PEDOT:PSS, which has been dipped in a DMSO bath for a duration of 30 minutes. With an outstanding value of up to  $\sigma_{\text{dry}} = 2124 \text{ S cm}^{-1}$ , PSPT shows the highest enhancement in conductivity. The behavior of the conductivity as well as of the thickness as a function of the dipping duration is depicted in Figure S3.1(c) and Figure S3.3(a) in the *Supporting Information 3.4*, respectively. The morphology of pristine and solvent-treated PEDOT:PSS films were studied by X-ray photoelectron spectroscopy (XPS). The detailed XPS measurements of PEDOT:PSS films treated by the different organic solvent treatments are illustrated in Figure S3.4(a–c) in the *Supporting Information 3.4*. The *relative PEDOT-to-PSS ratio* for each treatment at the optimum condition, representative for the morphological change, is listed in Table 3.1 along with the corresponding enhancement in conductivity at dry conditions.

**Table 3.1.** OVERVIEW OF THE ELECTRICAL AND MORPHOLOGICAL CHANGES IN PEDOT:PSS according to the particular treatments at optimum conditions.  $\sigma_{\text{dry}}$  refers to conductivity values without involving an electrolyte. The *relative PEDOT-to-PSS ratios* were extracted from XPS experiments.

	Pristine	SA	PSVA	PSPT
		[10%]	[120 °C/2 h]	[30 min]
$\sigma_{\text{dry}} [\text{S cm}^{-1}]$	2.5	1233	1406	2124
<i>relative PEDOT-to-PSS ratio</i> [%]	0	6.0	–2.2	47.3

The increased *relative PEDOT-to-PSS ratio* is attributed to the previously described domain purification of high conductive PEDOT:PSS-rich domains surrounded by an insulating PSS matrix, and additionally in the case of PSPT the removal of excess PSS on the surface.<sup>[23,44,45,50,51]</sup> Furthermore, PSPT-treated films also exhibit enhanced structural order, given by an enhanced  $\pi$ -stacking scattered intensity at  $Q = 0.25 \text{ \AA}^{-1}$  in the wide-angle grazing incidence scattering

(GIWAXS, Figure S3.4(d), *Supporting Information 3.4*).<sup>[14,108]</sup> The reduced PEDOT-to-PSS ratio, shown by the “negative” *relative PEDOT-to-PSS ratio* for PSVA, implies a formally correct increased PSS amount, compared to PEDOT. Thus, for a better comparison for all three techniques, the *relative PEDOT-to-PSS ratio* was used. PSVA induces a vertical phase segregation between excess PSS and PEDOT:PSS domains, leading to an enriched PSS top layer as seen for PSVA.<sup>[102]</sup> As the XPS technique only provides spectroscopic assessment of the surface chemical composition, a depth profile was performed, to determine the composition of PEDOT:PSS throughout the whole film. Figure S3.5 in the *Supporting Information 3.4* displays the enhanced structural order at the surface as well as in the bulk of PSPT-treated PEDOT:PSS films, confirming the uniform distributed effect of solvent treatment in the entire film. Degradation measurements (Figure S3.6, *Supporting Information 3.4*) approve the structural integrity of pristine PEDOT and PSS repetition units over time. Additional atomic force microscopy (AFM) images of the pristine and solvent-treated films provided no further information on morphology changes upon solvent treatments.

To evaluate the effect of solvent treatment in PEDOT:PSS based OECTs two fundamental questions have to be answered. First, in how far are the conductivities obtained on dry PEDOT:PSS representative for the conductivity in OECT configuration, and second how do the various treatments affect the OECT performance. To study the effect of solvent treatments on the device performance, electrical characterization of OECTs with solvent-treated PEDOT:PSS films at their optimum (dry) condition were performed.

The typical device structure and wiring of the PEDOT:PSS-based OECT is displayed in Figure 3.2(a). In order to avoid Faradaic leakage currents due to electrolysis, the OECT operates in the water-stable operation regime with a gate voltage ( $V_G$ ) well below 1 V.<sup>[84]</sup> The electrical characteristics are depended on the device dimensions, defined by the width ( $W$ ), length ( $L$ ) and the thickness ( $d$ ) of the channel.<sup>[4]</sup> The output characteristics show the modulation of the drain current  $I_D$  in forward and backward sweeps for the different treatments at gate voltages  $V_G = -0.2$  V (Figure 3.2(b)). The linear and saturation operating regime are clearly displayed with small hysteresis. The transfer curves are demonstrated in Figure 3.2(c), showing forward sweeps at drain voltages  $V_D = -0.4$  V and their respective transconductances  $g_m = dI_D/dV_D$  as a function of  $V_G$  (Figure 3.2(c)) for each processing method. The conductivity enhancement affects mainly the on-current as the off-current is almost independent on the treatment. Thus, higher on/off ratio is mainly attributed to the on-current of the conductivity enhancement. The minimum current is about  $10^{-5}$  A, thus limiting the on/off ratio to  $10^2$  (Figure 3.2(d)).

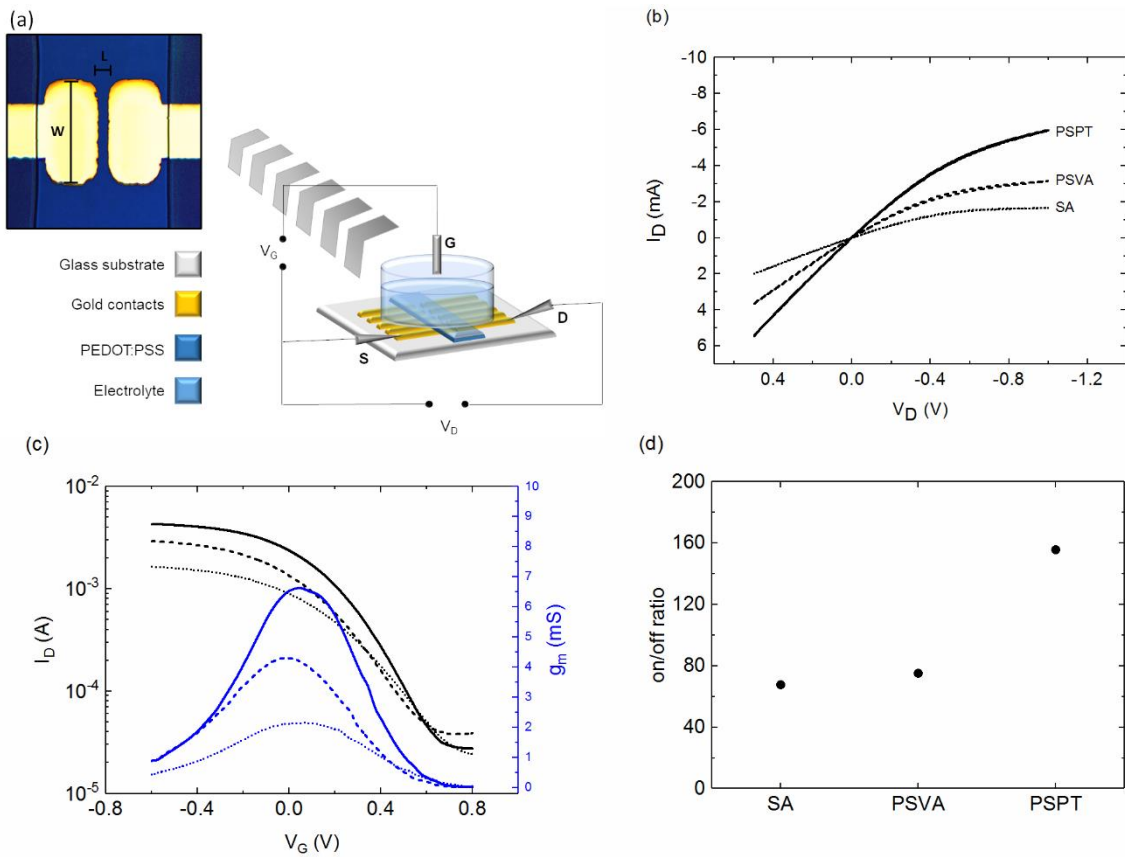


**FIGURE 3.2.** OECT ARCHITECTURE AND ITS ELECTRICAL CHARACTERISTICS: **a)** 3D-image of the cross-section and wiring of a PEDOT:PSS-based transistor with a micrograph of the dimensions. **b)** Output characteristics at  $V_g = -0.2$  V for PSPT-, PSVA- and SA-treated PEDOT:PSS films (solid, dashed and dotted line). **c)** Transfer characteristics (left y-axis) and transconductance (blue axis) at  $V_D = -0.4$  V for the PSPT-, PSVA- and SA method (solid, dashed and dotted line). **d)** on/off ratios for the different treatments, extracted from the corresponding transfer curves in c). The device geometries were  $L = 300$   $\mu\text{m}$ ,  $W = 1000$   $\mu\text{m}$ ,  $d = 69$  nm (SA), 100 nm (PSVA) and 110 nm (PSPT). The NaCl concentration in the aqueous solution amounts to 0.1 M and the gate electrode is an Ag/AgCl pellet.

The OECT on-current  $I_D$  agrees with the trend of the conductivity enhancement in dry PEDOT:PSS (Table 3.1). The PSPT method, showing the highest dry conductivity, exhibits in the OECT configuration the highest on-current and maximum transconductance ( $g_{m,\text{max}} \sim 7$  mS) as compared to the PSVA- and the SA method. As next step we investigate whether the measured dry conductivities are also quantitatively in agreement with the measured OECT currents. First, we monitor the  $I_D$ - $V_D$  characteristics of an OECT without applied gate bias upon addition of the electrolyte. We observe a significant decrease of the drain current when measuring in the OECT configuration with electrolyte, as shown in Figure S3.7 in the *Supporting Information 3.4*. The direct contact between the electrolyte and the channel, and the additional hygroscopic behavior of PSS, lead to water uptake in the PEDOT:PSS film, resulting in a swollen film<sup>[27,28,105]</sup>. The swelling of PEDOT:PSS changes the properties of the material and has a negative influence on the electrical conductivity.<sup>[105]</sup>

To quantitatively determine the PEDOT:PSS conductivity in contact with an electrolyte as well as the effect of the organic solvent treatment on the OECT electrical properties we apply the analytical device model by Bernardis *et al.* to fit the OECT characteristics.<sup>[63]</sup> The model describes the steady-state and transient behavior of OECTs and is shortly outlined here. Depending on the applied gate and drain voltages (the source is biased at 0 V), the OECT can operate in linear or saturation region. When the OECT is operated in linear region ( $|V_G - V_P| > |V_D|$ ) the dedoping is homogenous throughout the organic polymer and the drain current reads<sup>[63]</sup>:

$$I_D = G \left[ 1 - \frac{V_G - V_P}{V_P} \right] V_D \quad (3.1)$$

where  $G$  is the conductance and  $V_P$  the pinch-off voltage<sup>[63]</sup>.

When the OECT is operated in saturation region ( $|V_G - V_P| < |V_D|$ ) the channel is completely dedoped close to the drain side because the local density of injected cations is equal to the intrinsic dopant density of the organic polymer and the current reads<sup>[63]</sup>:

$$I_D = -\frac{G \cdot V_D^{sat2}}{2V_P} \quad (3.2)$$

These equations are used to model the experimental transfer characteristics. As shown in Figure 3.3 the model calculations provide an excellent fit to OECT characteristics for the three organic solvent treatments (Figure 3.3(a–c)). We note that mainly the linear operation regime was exploited. The applied model yields two essential OECT parameters,  $G$  and  $V_P$  which represent the electrical properties of PEDOT:PSS in the OECT configuration.

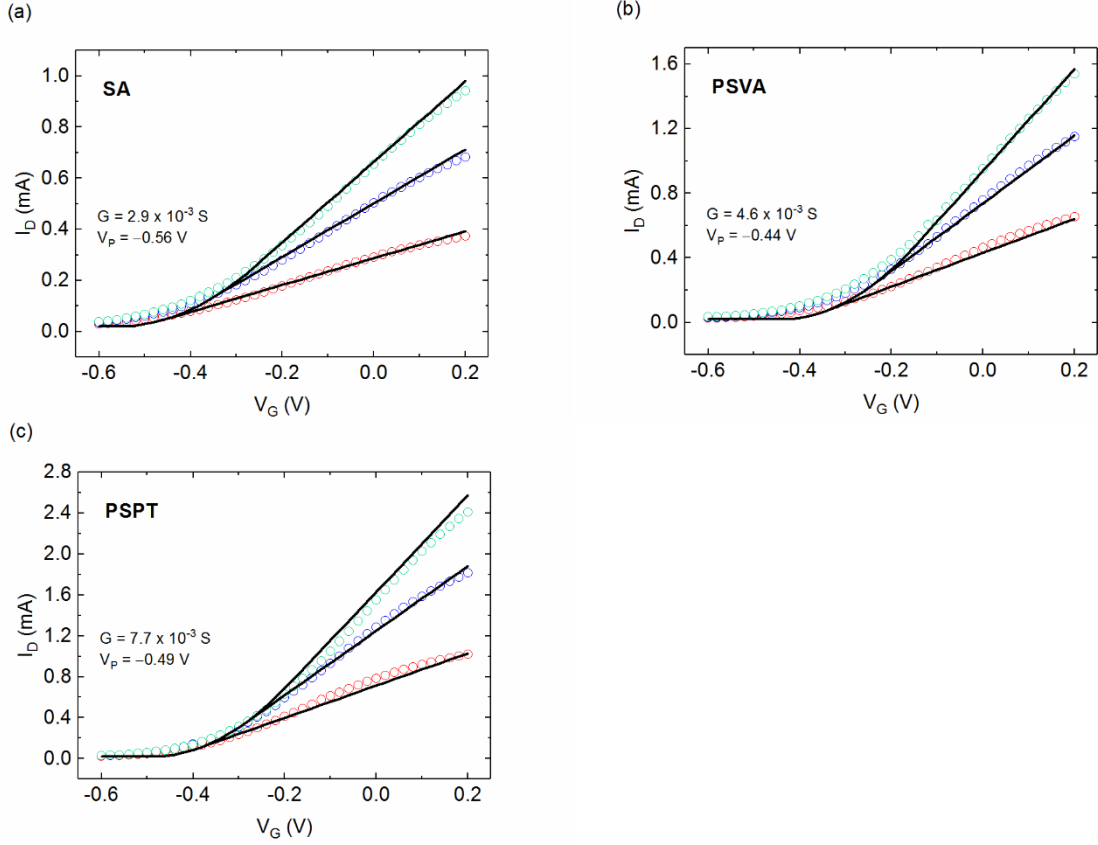


**FIGURE 3.3.** EXPERIMENTAL TRANSFER CHARACTERISTICS (data points) of an OECT fitted to the modeled linear regime of transfer characteristics (solid lines). By using drain voltages of  $V_D = -0.1$  V (red),  $-0.2$  V (blue) and  $-0.3$  V (green),  $G$  and  $V_P$  were extracted for SA **a)**, PSVA **b)** and PSPT **c)**. The device geometries were  $L = 300 \mu\text{m}$ ,  $W = 1000 \mu\text{m}$ ,  $d = 69$  nm (SA),  $100$  nm (PSVA) and  $110$  nm (PSPT). A NaCl solution with a concentration of  $0.1$  M was used as an electrolyte.

The conductance  $G$  reveals the conductivity of PEDOT:PSS by incorporating the dimensions of the OECT:

$$G = \sigma \frac{W \cdot d}{L} \text{ with } \sigma = q\mu p_0 \quad (3.3)$$

where  $q$  is the elementary charge,  $\mu$  is the charge carrier mobility and  $p_0$  is the initial charge carrier density.<sup>[63]</sup> As those parameters are extracted from measurements in the OECT configuration, we define this conductivity as  $\sigma_{\text{wet}}$ , indicating the presence of an electrolyte. The values for the conductivity at wet conditions show the same behavior as for dry conditions (Table 3.2): PSPT exhibiting the highest conductivity, compared to the PSVA- and SA method. However, the conductivities at wet conditions are decreased by one order of magnitude due to the swelling of the film.

The other parameter that is extracted from the fits is  $V_P$ , which defines the onset of saturation in the absence of a gate bias<sup>[63]</sup>:



$$V_P = \frac{qp_0d}{c_d} \quad (3.4)$$

with  $C_d$  the capacitance of the channel. From  $G$  and  $V_P$  only, it is not possible to independently extract the charge carrier density and mobility of PEDOT:PSS in OECT configuration. However, when the channel capacitance  $C_d$  is known, Equation (3.4) provides the free carrier density  $p_0$  which combined with Equation (3.3) then gives the carrier mobility  $\mu$ . To this end we have performed electrochemical impedance spectroscopy measurements (EIS) to determine the channel capacitance (Figure S3.8, *Supporting Information 3.4*). The resulting hole mobilities and densities are given in Table 3.2 and are in good agreement with previously reported values for PEDOT:PSS-based OECTs.<sup>[108]</sup> We observe that the dipping treatment (PSPT) with  $\mu = 0.437 \text{ cm}^2 \text{ V}^{-1} \text{ s}^{-1}$  gives rise to the highest mobility. This demonstrates that the observed conductivity enhancement in the OECT for the dipping treatment originates from an improved charge carrier mobility and not from an increased carrier density.

**Table 3.2.** OVERVIEW OF THE EXTRACTED VALUES by fitting experimental data to the modeled steady-state characteristics and by electrochemical impedance spectroscopy measurements. We refer to the values as wet, indicating the presence of an electrolyte.

	SA	PSVA	PSPT
$C_d$ [F]	$3.46 \cdot 10^{-5}$	$5.04 \cdot 10^{-5}$	$3.23 \cdot 10^{-5}$
$\sigma_{\text{wet}}$ [S cm <sup>-1</sup> ]	126	138	210
$\mu$ [cm <sup>2</sup> V <sup>-1</sup> s <sup>-1</sup> ]	0.131	0.185	0.437
$p_0$ [cm <sup>-3</sup> ]	$5.99 \cdot 10^{21}$	$4.66 \cdot 10^{21}$	$2.99 \cdot 10^{21}$

Focusing on the device performance, also cyclability is essential for the use of OECTs, especially in sensing applications. Strong hysteresis in the electrical characteristics makes the OECT output dependent on the read-out history. Therefore, we have also investigated how the OECT characteristics react on repeatedly scanning the device as function of the PEDOT:PSS processing methods. Figure 3.4(a) shows transfer characteristics for PSPT-treated PEDOT:PSS films for 120 consecutive cycles. An overview of the on-current in respect to the initial on-current for the different treatments for 120 cycles is displayed in Figure 3.4(b). PSPT-treated films are stable after 60 cycles and exhibit a higher operational stability compared to the other methods.

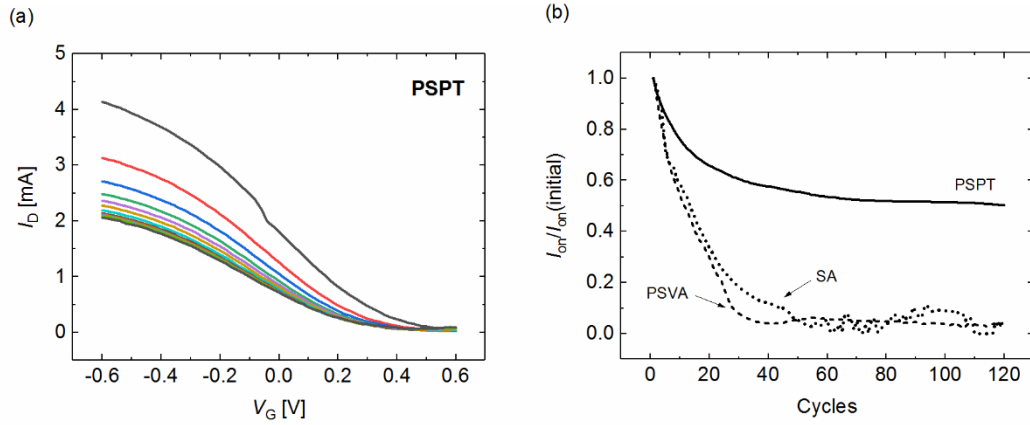


**FIGURE 3.4. CYCLABILITY: a)** Transfer characteristics for an OECT with a PSPT-treated PEDOT:PSS film after a dipping duration of 10 minutes. The device was measured for 120 consecutive cycles at  $V_D = -0.4$  V. Starting with the first cycle (black) every 10. cycle is depicted. The device geometries were:  $L = 500$   $\mu\text{m}$ ,  $W = 1000$   $\mu\text{m}$ ,  $d = 58$  nm. The NaCl concentration in the aqueous solution was 0.1 M and the gate electrode was an Ag/AgCl pellet. **b)** on-current in respect to the initial on-current for SA-, PSVA- and PSPT- treated PEDOT:PSS films (dotted-, dashed-, solid-line) for 120 cycles. The on-currents were extracted from transfer characteristics.

### 3.3. Summary of Chapter 3

In conclusion, we have investigated the effect of different organic solvent treatments on the performance of PEDOT:PSS-based OECTs. The results show that in dry conditions the *Solvent Additive* (SA), *Polar Solvent Vapor Annealing* (PSVA) and the *Polar Solvent Post-Treatment* (PSPT) method all lead to strongly enhanced conductivities. In OECT configuration the PEDOT:PSS conductivity is typically reduced by one order of magnitude by incorporation of an electrolyte due to swelling effects. The PSPT method gives rise to the highest transconductance and on/off ratio as compared to the PSVA- and SA method. The enhanced conductivity originates from an increased charge carrier mobility due to phase segregation in PEDOT:PSS-rich and PSS-rich domains and exhibit enhanced structural order.

### 3.4. Supporting Information of Chapter 3

For organic solvent treatments, the enhancement in the conductivity of PEDOT:PSS can be controlled by the amount of solvent.<sup>[23,45,99–101]</sup> In the SA method this is literally given by the solvent content, added to the PEDOT:PSS dispersion. The dependence of the DMSO amount on the conductivity is shown in Figure S3.1(a). In the PSVA treatment the controlling factor can be the exposure time of the solvent vapor, as seen in Figure S3.1(b) for DMSO at 120 °C. The conductivity increases with the duration of the treatment, especially within the first 120 minutes, till it reaches saturation. With a duration of 240 minutes it reaches its maximum conductivity of up to 1520 S cm<sup>-1</sup>. At room temperature, PSVA-treated PEDOT:PSS films show even after a treatment of 2 hours only a slight enhancement in conductivity ( $\sigma_{\text{dry}} \approx 170 \text{ S cm}^{-1}$ ). The reason is the not sufficiently saturated nitrogen gas with DMSO due to its low vapor pressure of 0.55 hPa (at 20°C).<sup>[109]</sup> By increasing the temperature of DMSO, the gas becomes more saturated, and the exposure has a stronger effect on the conductivity of PEDOT:PSS. Figure S3.1(c) shows the enhancement in conductivity by increasing the DMSO temperature due to higher saturation of the vapor. The time dependence of the dipping duration for the PSPT method is depicted in Figure S3.1(d). Already after 1 minute the conductivity reaches an almost steady value with no further evidence of time dependence.

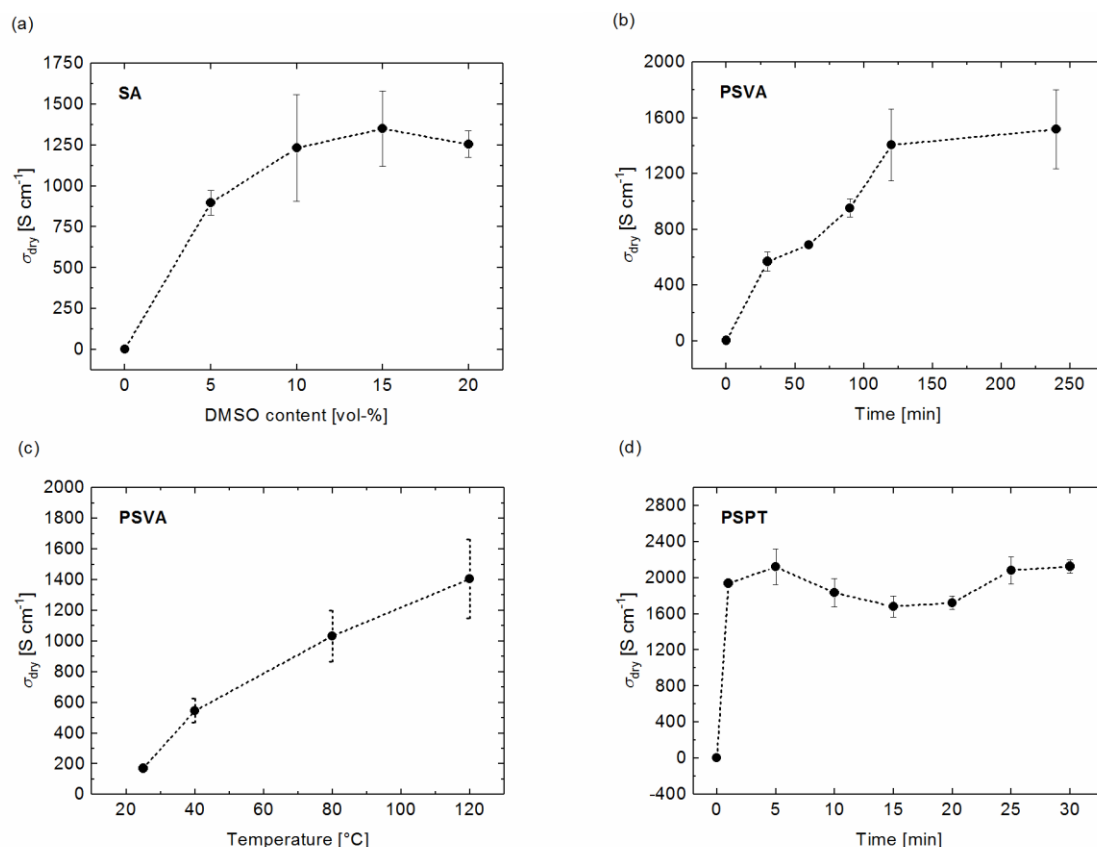


**FIGURE S3.1.** CONDUCTIVITY BEHAVIOR OF PEDOT:PSS FILMS FOR DIFFERENT ORGANIC SOLVENT TREATMENTS: Conductivity as a function of **a)** the DMSO amount (SA), **b)** time at a DMSO temperature of 120 °C (PSVA), **c)** temperature at a duration of 2 hours (PSVA) and **d)** the dipping duration in a DMSO bath (PSPT method). The error bars are calculated by standard deviation of the average of five measured conductivities, varying the channel length per sample.

Conducting the PSVA treatment in a closed glass jar in an oven, resulted in solvent condensation on the PEDOT:PSS layer. This led to uneven films and in worst cases even to a wash-off of the PEDOT:PSS. Furthermore, placing the glass jar on a hotplate caused an uneven heat distribution. To have a controlled solvent vapor and preventing condensation issues, a special setup for the PSVA was constructed as seen in Figure S3.2. The PSVA chamber can be either filled with dry nitrogen gas or with solvent-enriched gas. The flow can be regulated by a gas flow control. The solvent is placed in a wash bottle and the temperature of the solvent can be adjusted. To avoid condensation, the samples are generally cooled and dried with pure nitrogen gas after the treatment.

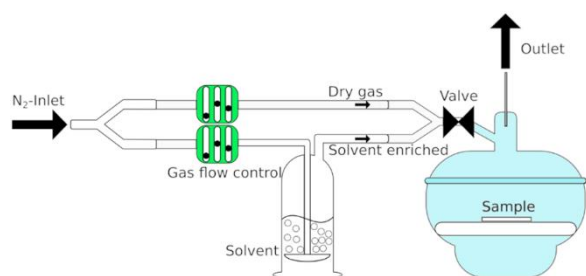


**FIGURE S3.2.** SETUP FOR THE PSVA METHOD: The PSVA chamber with a flow control system of nitrogen gas and solvent-enriched gas.

Even after a short soft bake of 10 minutes at 140 °C, some of the polymer layer gets washed-off during the PSPT treatment. The thickness behavior over time including the corresponding percentage of the wash-off is displayed in Figure S3.3. Thickness measurements confirm a wash-off of 30–45% of the PEDOT:PSS films depending on the duration of the dipping procedure, whereas most it is washed off within the first few minutes.

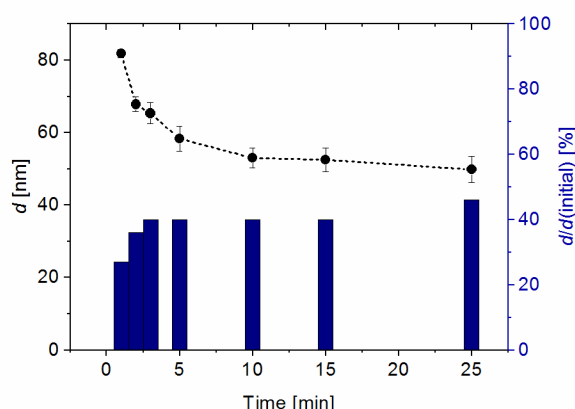


**FIGURE S3.3.** THICKNESS AND WASH-OFF BEHAVIOR OF PSPT-TREATED PEDOT:PSS: Thickness dependence of PEDOT:PSS films as a function of the dipping duration in a DMSO bath. The wash-off effect of PSPT has been investigated by measuring the initial- and post-treated thickness.

By detecting the electronic state of elements, XPS gives information about the surface chemical composition of a material. PEDOT and PSS both contain sulfur atoms in their chemical structure. The sulfur atom in PEDOT is imbedded in a thiophen ring, whereas the sulfur atom in PSS belongs to the sulfonate group. The chemical environment of the S (2p) electrons differs from each other leading to different binding energies in the S (2p) XPS spectra and this enables us to determine the composition of PEDOT:PSS at the surface with respect to a possible morphological change caused by different treatments.<sup>[44]</sup>

Figure S3.4(a) shows the sulfur (S) 2p XPS spectra of pristine and SA-treated PEDOT:PSS films. The sulfur-signals of PSS appear at higher binding energies (168.8 and 167.7 eV), as the lower binding energy peaks of 165.7 and 163.8 eV are assigned to PEDOT.<sup>[44]</sup> For a better visualization

the spectra have been normalized to the PSS signal. The *relative PEDOT-to-PSS ratio* has been defined by using the area of the particular peaks in respect to the pristine PEDOT-to-PSS ratio. This directly shows the change in composition of PEDOT:PSS at the surface after SA treatment with different DMSO content (Figure S3.4(a), inset). The increased *relative PEDOT-to-PSS ratio* by adding DMSO is attributed to the previously described phase segregation of PEDOT and PSS resulting in more PEDOT:PSS-rich phases. However, it should be noted that the change in the PEDOT-to-PSS ratio caused by the SA treatment is relatively small compared to earlier reported results.<sup>[23,44,45]</sup>

The S(2p) XPS spectra of the PSVA-treated PEDOT:PSS films is shown in Figure S3.4(b) for different durations. The *relative PEDOT-to-PSS ratio* is reduced compared to the pristine film, noticeable by a “negative” value, pointing out the increased PSS amount compared to PEDOT. In contrast to the previous results, this indicates a PSS-rich phase on the top surface. Corresponding with Na *et al.*, PSVA induces a vertical phase segregation between excess PSS and PEDOT:PSS domains, leading to an enriched PSS top layer.<sup>[23,101]</sup>

Figure S3.4(c) shows the S(2p) XPS spectra of the PEDOT:PSS films treated by PSPT as a function of the dipping duration with the corresponding *relative PEDOT-to-PSS ratio*. Independent of time, the dipping procedure causes an increase of the *relative PEDOT-to-PSS ratio* of about 35–50% compared to the pristine ratio. Such a strong increase of conductivity as well as *relative PEDOT-to-PSS ratio* is an indication for the previous described domain purification of high conductive PEDOT:PSS-rich domains surrounded by an insulating PSS matrix and the removal of excess PSS on the surface.<sup>[23,50,106]</sup>

The enhancement in electronic transport can be additionally evoked by aggregation and or crystallization.<sup>[14]</sup> The molecular packing of PEDOT:PSS can be further investigated using GIWAXS. Due to the limiting X-ray scattering contrast of PEDOT and PSS and relatively disordered film microstructure the investigation of the multi-scale microstructure of PEDOT:PSS films is challenging.<sup>[14]</sup> PSPT-treated PEDOT:PSS films exhibit an enhanced  $\pi$ -stacking scattered intensity at  $Q = 0.25 \text{ \AA}^{-1}$  (Figure S3.4(d)).<sup>[108]</sup> In contrast, SA- and PSVA-treated PEDOT:PSS films did not show enhanced  $\pi$ -stacking, indicative of only small structural changes. As a result, the high conductivity obtained after dipping is not only a result of domain purification but is also due to enhanced structural order.

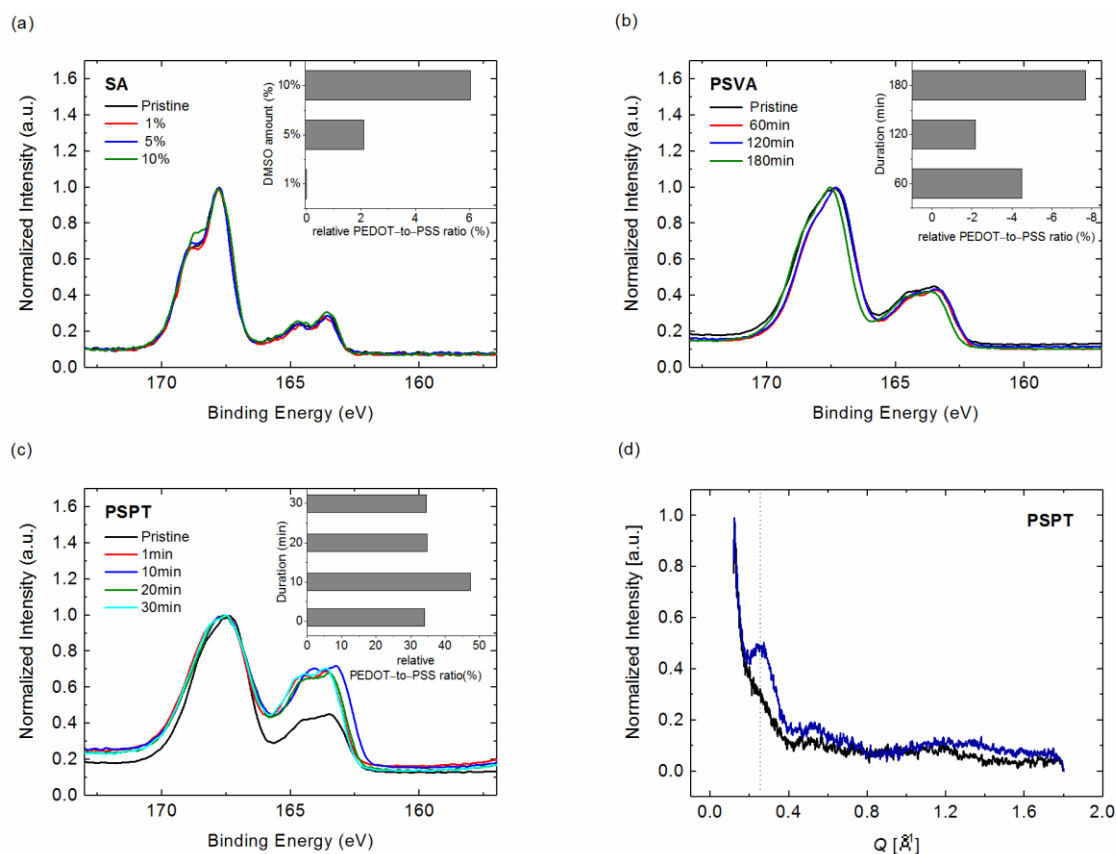


**FIGURE S4.4.** SPECTROSCOPICAL STUDY OF PEDOT:PSS FILMS TREATED WITH DIFFERENT ORGANIC SOLVENT TREATMENTS: S(2p) XPS spectra of PEDOT:PSS films **a)** as a function of the DMSO amount (SA), **b)** modified by DMSO vapor for different durations (PSVA) and **c)** exposed to a DMSO bath for different durations (PSPT). The insets display the relative increase of PEDOT-to-PSS ratio in respect to the pristine ratio. **d)** GIWAXS of a pristine (black) and PSPT-treated PEDOT:PSS film after a dipping duration of 30 minutes (blue). The dotted line is the position of the relative PEDOT:PSS  $\pi$ -stacking scattered intensity.<sup>[108]</sup>

Based on the fact, that XPS only examines the surface (about 8–10nm deep), additional XPS spectra were taken at the bulk of the film, providing a depth profile of the solvent-treated PEDOT:PSS films. For that reason, solvent-treated PEDOT:PSS films, after a DMSO post-treatment of 10 minutes, were measured at different thicknesses, achieved by partial removing of PEDOT:PSS by plasma etching. Figure S3.5 confirms, that the enhanced structural order is uniformly distributed through the whole film due to the constant PEDOT/PSS area ratio.

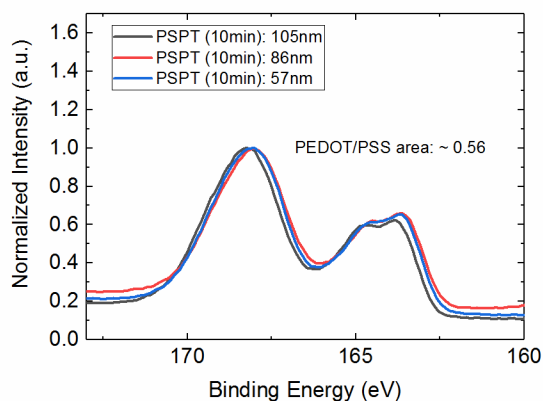


**FIGURE S3.5.** XPS DEPTH PROFILE OF A POST-TREATED PEDOT:PSS FILM: XPS spectra were taken from PSPT-treated films at several thicknesses, realized by various plasma etching steps.

In terms of possible degradation of PSS, in form of eventually losing sulfo-moieties, the pristine PEDOT:PSS film was measured again after several months. Figure S3.6 shows the XPS spectrum of a pristine PEDOT:PSS film, that has been aged for 9 months, exhibiting a constant PEDOT/PSS area ratio and stating its stability over time.

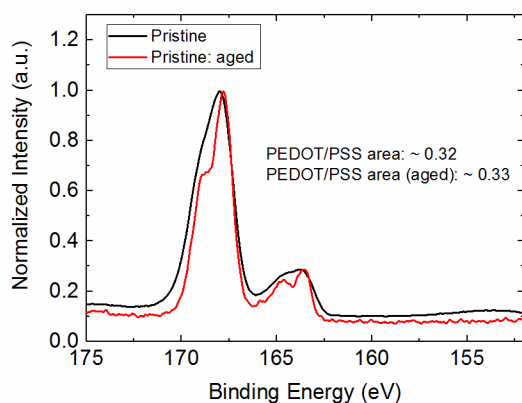


**FIGURE S3.6.** DEGRADATION OF PEDOT:PSS: XPS spectrum of a pristine film, that has been aged for 9 months to examine the stability of PEDOT and PSS moieties.

A simple test confirming the assumption that the PEDOT:PSS conductivity decreases in contact with an electrolyte due to swelling is to monitor the drain current, as shown in Figure S3.7.<sup>[27,105]</sup> The  $I$ – $V$  was measured first in absence of an electrolyte at dry conditions. After immersing the device in a NaCl solution for about 30 minutes, the drain current shows a significant drop, which refers to a change in the resistance from 40  $\Omega$  to 110  $\Omega$ .



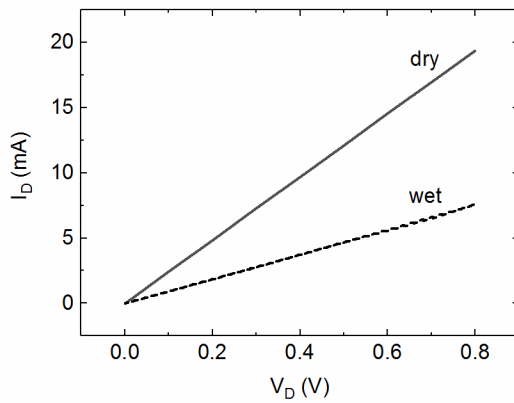


**FIGURE S3.7.**  $I$ – $V$  MEASUREMENT of an PEDOT:PSS-based OECT without an electrolyte (solid line) and with an electrolyte after 30 minutes (dashed line). The device geometries were:  $L = 400 \mu\text{m}$ ,  $W = 1000 \mu\text{m}$ ,  $d = 500 \text{ nm}$ . A NaCl aqueous solution with a concentration of 0.1 M was used.

In order to investigate the effect of the secondary doping of PEDOT:PSS on the electrical properties,  $c_d$  was needed to calculate the  $\mu$  and  $p_0$ . By using EIS measurements the capacitance has been extracted by fitting the experimental data to an R – C equivalent circuit as a reference (Figure S3.8).

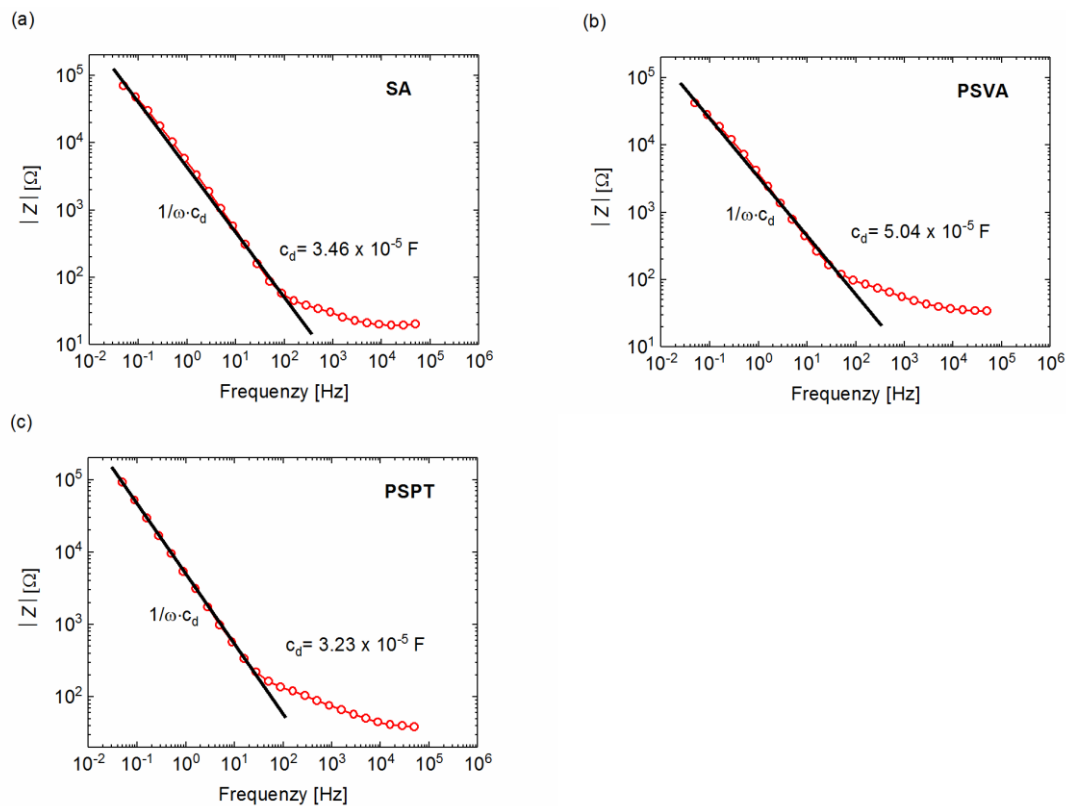


**FIGURE S3.8.** ELECTROCHEMICAL IMPEDANCE SPECTROSCOPY MEASUREMENTS OF PEDOT:PSS-BASED OECTS: The experimental impedance measurements (data points) for the **a)** SA-, **b)** PSVA- and **c)** PSPT method are fitted to an R – C equivalent circuit (solid black line). The dimensions of the device were  $L = 300 \mu\text{m}$ ,  $W = 1000 \mu\text{m}$ ,  $d = 110 \text{ nm}$  (PSPT),  $100 \text{ nm}$  (PSVA) and  $69 \text{ nm}$  (SA).



# Chapter 4

## High-Sensitivity Ion Detection at Low Voltages with Current-Driven Organic Electrochemical Transistors

Ions dissolved in aqueous media play a fundamental role in plants, animals, and humans. Therefore, the in situ quantification of the ion concentration in aqueous media is gathering relevant interest in several fields including biomedical diagnostics, environmental monitoring, healthcare products, water and food test and control, agriculture industry and security. The fundamental limitation of the state-of-art transistor-based approaches is the intrinsic trade-off between sensitivity, ion concentration range and operating voltage. In this chapter we show a current-driven configuration based on organic electrochemical transistors that overcomes this fundamental limit. The measured ion sensitivity exceeds by one order of magnitude the Nernst limit at an operating voltage of few hundred millivolts. The ion sensitivity normalized to the supply voltage is larger than  $1200 \text{ mV V}^{-1} \text{ dec}^{-1}$ , which is the largest value ever reported for ion-sensitive transistors. The proposed approach is general and can be extended to any transistor technology, thus opening opportunities for high-performance bioelectronics.\*

\* M. Ghittorelli, L. Lingstedt, P. Romele, N. I. Crăciun, Z. M. Kovács-Vajna, P. W. M. Blom, F. Torricelli, *Nat. Commun.* **2018**, 9, 1441-1450.

## 4.1. Introduction

Ions dissolved in aqueous media play a fundamental role in plants, animals, and humans. Ions regulate the biological processes at the single cell scale, enable the propagation of electronic signals and maintain a suitable balance between the fluids of the extracellular and intracellular environments, which is extremely important for several processes including nerve impulses, hydration, muscle function, and the regulation of pH level.<sup>[110–114,114,115]</sup> The in situ quantification of the ion concentration in aqueous media is thus gaining significant interest in several emerging fields including biomedical diagnostics, environmental monitoring, healthcare products, water and food test and control, agriculture industry and security.<sup>[11,12,116–123]</sup>

Ion-sensitive field-effect transistors (ISFETs) are one of the most studied sensor-platforms for ion detection. In ISFETs the electrolyte solution is in contact with the insulator and the reference electrode acts as the gate.<sup>[116,124–126]</sup> The first ISFETs were fabricated using single-crystal silicon technology while, more recently, emerging technologies based on graphene, zinc oxide, silicon-nanowires, amorphous-oxides, and organics have been investigated.<sup>[124,125,127–131]</sup> Among them, organic technologies have triggered a great deal of interest because they are compatible with flexible large-area substrates, require simple processing, as for example spin coating or printing, allow simple functionalization through synthetic chemical modification, and the materials can be biocompatible, which is an essential prerequisite for in-vivo applications.

A fundamental challenge in applying organic transistors as ion sensors in aqueous solution is the stability, inherently due to the electrolysis. In order to avoid Faradaic leakage currents due to electrolysis, the maximum operating voltage has to be well below 1 V.<sup>[84,123]</sup> Low-voltage operation can be achieved by removing the insulating layer between the electrolyte and the organic semiconductor (OSC). Depending on the permeability of the OSC to the ions, two different classes of organic transistors can be obtained.<sup>[123]</sup> Ion-impermeable OSCs yield electrolyte-gated organic FETs (EGOFETs). In EGOFETs ions are compensated by charges (electrons or holes) accumulated into the OSC at the electrolyte–OSC interface, and an electric double-layer (EDL) is formed. The EDL capacitance is of the order of micro-Farads, ensuring a water-stable operation window.<sup>[123,124,127,132]</sup> On the other hand, ion-permeable OSCs yield organic electrochemical transistors (OECTs). In OECTs ions can drift into the OSC and compensate the induced charge carriers.<sup>[3,4,60]</sup> The electrochemical doping and dedoping processes modulate the conductivity of the OSC and are reversible.<sup>[3,4,60]</sup> Compared to EGOFETs, in OECTs the corresponding transconductance  $g_m = \Delta I_D / \Delta V_G$  is extremely large because the interaction between ions and electronic charges takes place through the bulk of the OSC and not only at the electrolyte–OSC interface. Micro-scale OECTs show  $g_m > 10^{-3}$  S at very low gate bias, making them ideal ion-to-electron transducers.<sup>[3,60,64,133]</sup>

State-of-art OECTs show a current ion sensitivity of the order of tens  $\mu\text{A dec}^{-1}$ ,<sup>[95,134]</sup> that is one order of magnitude larger than that obtained with EGOFETs. The current variation is then converted into a voltage variation that, in turn, is related to the ion concentration by means of the Nernst equation.<sup>[58,95,124]</sup> When the current variation is converted into a voltage variation both OECTs and EGOFETs show comparable voltage ion sensitivity of the order of the Nernst limit, viz. 59 mV  $\text{dec}^{-1}$  at room temperature.<sup>[58,95]</sup> To improve the voltage ion sensitivity a possible approach is to increase the ratio between the electrolyte–OSC ( $C_d$ ) and gate–electrolyte ( $C_g$ ) capacitances ( $C_d/C_g$ ) by reducing  $C_g$ .<sup>[134]</sup> Another approach relies on the use of a load resistor ( $R_L$ ) to directly convert the drain current  $I_D$  into an output voltage resulting in an amplification  $A = g_m R_L$ .<sup>[84]</sup> Although in principle large  $g_m$  and  $R_L$  result in a large sensitivity, the output voltage should be compatible with the aqueous environment in the whole range of physiological ion concentration. The fundamental limitation of the aforementioned approaches is thus the stringent trade-off between the sensitivity, the operating range and the operating voltage.

Here we show low-voltage high-sensitivity ion detection with OECTs used in a current-driven inverter-like configuration. In the proposed approach the bias current  $I_B$  sets the operating range of ion concentration and the sensitivity is not limited by the supply voltage  $V_{DD}$ , thus overcoming the fundamental limitation of state-of-art approaches. The measured voltage ion sensitivity exceeds by about one order of magnitude the Nernst limit in the case of  $V_{DD} = 0.4$  V, while it shows a five-fold increase in the case of  $V_{DD} = 0.2$  V in the ion concentration range  $10^{-4}$ – $10^0$  M. The ion sensitivity normalized with respect  $V_{DD}$  is larger than 1200 mV  $\text{V}^{-1} \text{dec}^{-1}$ , which is more than one order of magnitude larger than the largest value ever reported for ion-sensitive transistors including ISFETs, EGOFETs, and OECTs. As relevant application example, a low-voltage ion-selective current-driven OECT with a voltage-normalized sensitivity as high as 1035 mV  $\text{V}^{-1} \text{dec}^{-1}$  is eventually demonstrated.

## 4.2. Results

### 4.2.1. Device Structure and Measurements

The typical device structure of the OECTs is shown in Figure 4.1(a), comprising the ion-permeable conducting polymer PEDOT:PSS as the active material in the channel, defined by length  $L$  and width  $W$ . The deposited PEDOT:PSS films have thicknesses ( $d$ ) ranging from 25 to 100 nm. A 1.8  $\mu\text{m}$  thick photoresist, deposited by spin coating and patterned photolithographically, insulates the gold electrodes from the electrolyte solution.

As electrolyte, we used an aqueous solution of NaCl or KCl since sodium, potassium, and chloride are very relevant for biological processes. For example, they preserve suitable pressure and balance of various body fluids inside and between cells, as well as blood. Moreover, they are essential for maintaining suitable acidity into the body, passively balancing out the ions of tissue, blood, and organs.<sup>[110,111,113,135,136]</sup> A tungsten foil or Ag/AgCl pellet is immersed into the electrolyte and used as gate electrode. The former is a polarizable electrode, viz. it forms an EDL with the electrolyte, while the latter is a non-polarizable quasi-reference electrode. Further details on the transistor fabrication are provided in the *Experimental in Chapter 2*. The transfer and output characteristics of a typical OECT are shown in Figure 4.1(b, c). The measurements show that the OECT operates in the water-stable operation window ( $|V_G| < 1$  V), the minimum current is about  $10^{-6}$  A and the on/off current ratio is larger than  $10^3$ . The linear and saturation operating regions are clearly displayed in the output characteristics of Figure 4.1(c). Figure 4.1(d) shows the measured transconductance  $g_m = dI_D/dV_G$  as a function of  $V_G$ . The maximum  $g_m$  is about 3 mS at  $V_G = -0.1$  V and  $V_D = -0.4$  V, which agrees with state-of-art OECTs.<sup>[3,4,60]</sup> Figure 4.1(e) shows the measured output resistance  $r_o = (dI_D/dV_D)^{-1}$  as a function of  $V_D$ . The maximum  $r_o$  is about 70 k $\Omega$  at  $V_D = -0.7$  V and  $V_G = 0.2$  V and it reduces to about 10 k $\Omega$  at  $V_G = -0.2$  V.

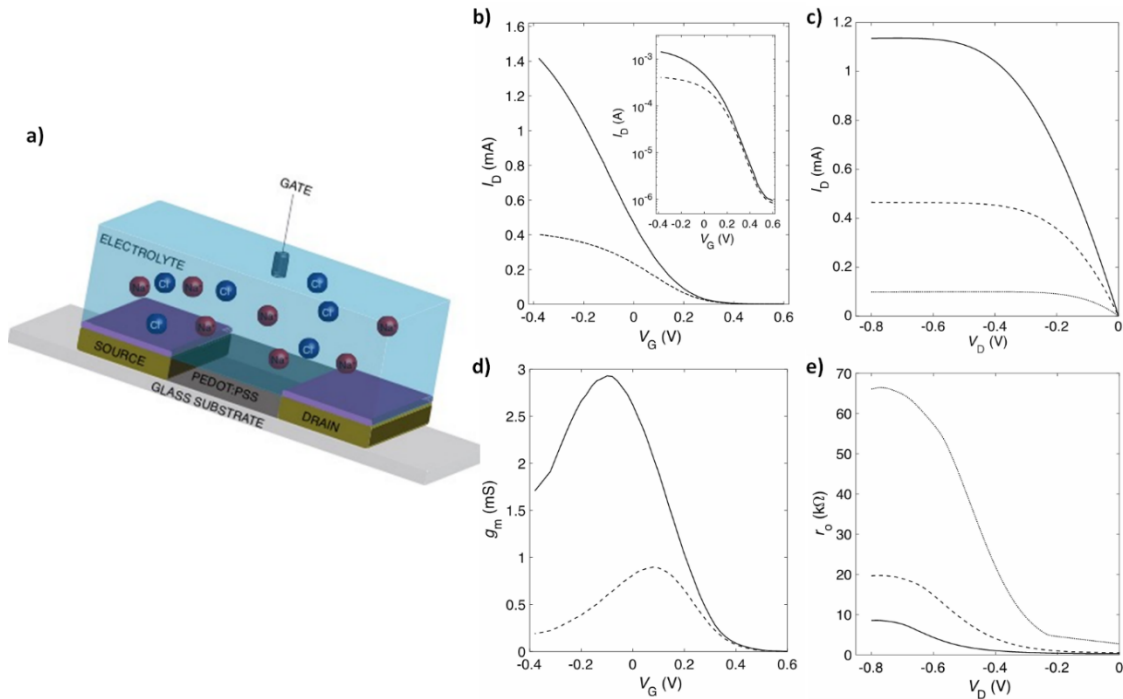


**FIGURE 4.1.** TRANSISTOR ARCHITECTURE AND ELECTRICAL CHARACTERISTICS: **a)** Schematic structure of the fabricated OECTs. **b)** Transfer characteristics at  $V_D = -0.1$  V (dashed line) and  $V_D = -0.4$  V (full line). The gate current is lower than 1  $\mu$ A. **c)** Output characteristics at  $V_G = 0.2$  V (dotted line),  $V_G = 0$  V (dashed line), and  $V_G = -0.2$  V (full line). **d)** Transconductance at  $V_D = -0.1$  V (dashed line) and  $V_D = -0.4$  V (full line). **e)** Output resistance at  $V_G = 0.2$  V (dotted line),  $V_G = 0$  V (dashed line), and  $V_G = -0.2$  V (full line). The gate is an Ag/AgCl pellet and the OECTs geometries are:  $W = 1000$   $\mu$ m,  $L = 50$   $\mu$ m,  $d = 50$  nm. The NaCl concentration is 1 M.

### 4.2.2. Current-Driven OECT Configuration

The proposed current-driven OECT configuration is shown in Figure 4.2(a). The OECT is connected in series with a current generator resembling an inverter topology, as schematically depicted in Figure 4.2(b). The input voltage ( $V_{in}$ ) is applied to the gate ( $V_G = V_{in}$ ) while the output voltage ( $V_{out}$ ) is measured at the drain ( $V_D = V_{out}$ ). The bias current  $I_B$  is set by the current generator and the topology gives  $I_D = I_B$ . A typical transfer characteristic ( $V_{out} - V_{in}$ ) with  $I_B = 1.25$  mA is displayed in Figure 4.2(c). When the current-driven OECT is biased at negative  $V_{in}$  (e.g.,  $V_{in} = -V_{DD}$ ), anions are injected into the PEDOT:PSS, the polymer is doped, and the OECT operates in linear region. The OECT output resistance  $r_o$  is small (Figure 4.1(e)) and  $V_{out} = V_{DD} - I_B r_o \approx V_{DD}$ . By increasing  $V_{in}$  anions are progressively extracted from the polymer and cations injected. Therefore, the polymer is dedoped,  $r_o$  increases,  $V_{out}$  lowers, and the OECT is eventually operated in saturation region. In the transfer characteristics  $V_{out} - V_{in}$  the transition between the linear and the saturation region takes place when  $V_{in} - V_{out} = V_P$ , where  $V_P$  is the pinch-off voltage. As an example, in Figure 4.2(c) the OECT saturation condition is achieved at  $V_{in} = +0.22$  V where  $V_{out} = -0.05$  V and hence  $V_{in} - V_{out} = +0.27$  V which, as readily visible in Figure 4.1(b), is equal to the pinch-off voltage  $V_P = +0.27$  V. In saturation, the transistor is pinched-off at the drain (output contact),  $I_D$  is almost independent of  $V_D$ ,  $r_o$  increases by more than one order of magnitude (Figure 4.1(e)), and, as a consequence,  $V_{out}$  sharply drops to the minimum supply voltage  $-V_{DD}$ . This is analogous to the zero- $V_{GS}$  inverter topology.<sup>[137]</sup> Here the OECT is the driver and the current generator is the zero- $V_{GS}$  load. When  $V_{in}$  is low the OECT operates in linear region and pulls  $V_{out}$  towards  $V_{DD}$ . By increasing  $V_{in}$  the OECT becomes less conductive,  $V_{out}$  lowers and, in the case of Figure 4.2(c), at  $V_{in} \geq 0.22$  V the OECT is eventually operated in saturation, where  $r_o$  is large and  $V_{out}$  drops to  $-V_{DD}$ . It is worth noting that the minimum supply voltage ( $-V_{DD}$ ) is set by means of the voltage-compliance of the current generator. We define the switching voltage  $V_{SW}$  as the minimum  $V_{in}$  required to operate the OECT in saturation. The switching voltage provides meaningful information on the OECT parameters and can be analytically calculated as follows. The OECT current in the saturation regime reads<sup>[4,63]</sup>:

$$I_D = \beta(V_S + V_P - V_G)^2 \quad (4.1)$$

where  $\beta = W \mu C_v d (2 L)^{-1}$ ,  $\mu$  is the charge carrier mobility,  $C_v$  is the volumetric capacitance,  $V_S$  is the source voltage,  $V_P = q p_0 C_v^{-1}$  is the pinch-off voltage,  $q$  is the elementary charge, and  $p_0$  is the initial charge carrier density in the conductive polymer before the application of the gate voltage. When the OECT is connected in the current-driven configuration  $V_S = V_{DD}$ ,  $I_D = I_B$ ,  $V_G = V_{in}$ . Since the OECT starts to operate in saturation when  $V_{in} = V_{SW}$ , the switching voltage can be analytically calculated by substituting  $V_G = V_{SW}$  in Equation (4.1) and results:

$$V_{SW} = V_D + V_P - \left( I_B / \beta \right)^{1/2} \quad (4.2)$$

Equation (4.2) shows that  $V_{SW}$  depends on the main parameters of the current-driven configuration, i.e. the OECT physical and geometrical parameters ( $V_P$ ,  $\beta$ ), the supply voltage  $V_{DD}$  and the bias current  $I_B$ . Figure 4.2(d) shows the transfer characteristics  $V_{out}-V_{in}$  of the current-driven OECT for several current biases  $I_B$ . According with Equation (4.2), by increasing  $I_B$  the switching voltage shifts to lower  $V_{in}$ . This is because  $V_{out}$  gets lower at larger  $I_B$  and thus the OECT saturation occurs at a lower input voltage (i.e.,  $V_{SW}$  reduces). Furthermore, Equation (4.2) shows that  $V_{SW}$  also depends on the OECT parameters (viz.  $V_P$  and  $\beta$ ) that, in turn, are related to the transistor geometry (namely  $W$ ,  $L$ ,  $d$ ) and to the physical parameters of the conductive polymer and the electrolyte solution (namely  $\mu$ ,  $C_v$ , and  $p_0$ ).

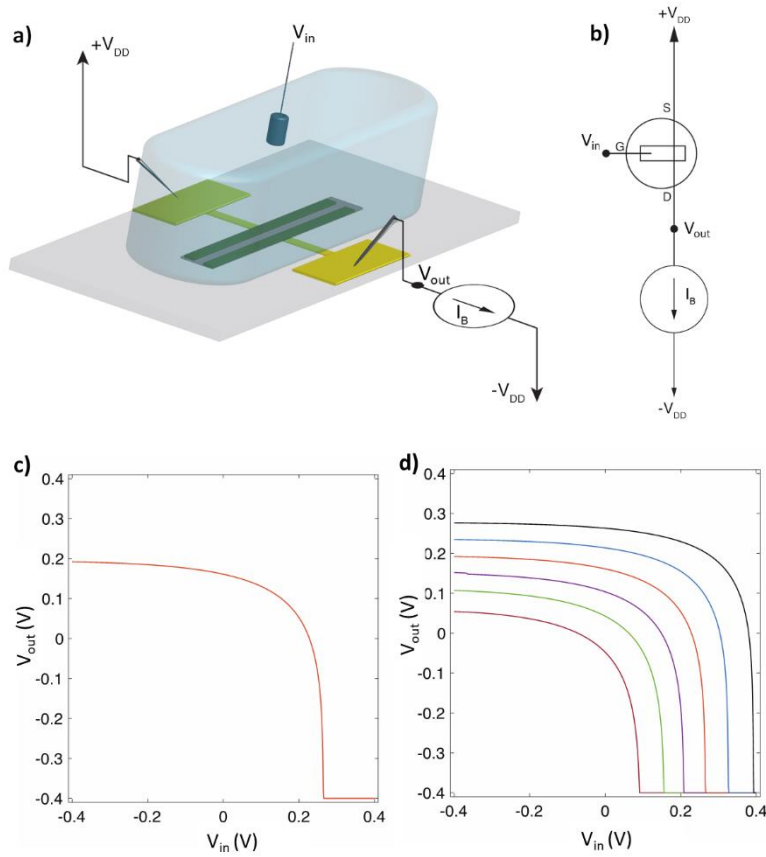


**FIGURE 4.2.** CURRENT-DRIVEN OECT ARCHITECTURE AND ELECTRICAL CHARACTERISTICS: **a)** Current-driven OECT configuration. **b)** Schematic of the current-driven OECT. **c)** Measured transfer characteristic of a current-driven OECT at  $I_B = 1.25$  mA and  $V_{DD} = 0.4$  V. **d)** Measured transfer characteristics of a current-driven OECT by varying the bias current from  $I_B = 2.0$  mA (brown curve) to  $I_B = 0.75$  mA (black curve) with a step of  $-0.25$  mA,  $V_{DD} = 0.4$  V. The gate is a Ag/AgCl pellet and the OECTs geometries are:  $W = 1000$   $\mu\text{m}$ ,  $L = 50$   $\mu\text{m}$ ,  $d = 50$  nm. The NaCl concentration is 1 M.



### 4.2.3. Impact of the Ion Concentration

In order to investigate the impact of the ion concentration on the electrical characteristics of the current-driven OECT, Figures 4.3(a–d) show the measured  $V_{\text{out}}-V_{\text{in}}$  as a function of the ion concentration. More in detail, Figure 4.3(a) shows the  $V_{\text{out}}-V_{\text{in}}$  characteristics of a current-driven OECT operated with a current bias  $I_B = 0.4$  mA. When the ion concentration is  $c = 10^0$  M, the switching voltage is close to 0 V. By decreasing the ion concentration,  $V_{\text{SW}}$  shifts towards positive voltage. We found  $V_{\text{SW}} = 0.17$  V and  $V_{\text{SW}} = 0.38$  V with  $c = 5 \times 10^{-1}$  M and  $c = 2 \times 10^{-1}$  M, respectively.

By further decreasing  $c$ , the switching voltage exceeds the supply voltage ( $V_{\text{DD}} = 0.4$  V), and cannot be detected anymore since we sweep  $V_{\text{in}}$  in the range  $|V_{\text{in}}| \leq |V_{\text{DD}}|$ . As shown in Equation (4.2), by increasing the current bias  $I_B$  it is possible to shift  $V_{\text{SW}}$  back within the supply voltage range. This is confirmed in Figure 4.3(b) which shows that the  $V_{\text{out}}-V_{\text{in}}$  characteristic obtained at  $c = 2 \cdot 10^{-1}$  M is restored to  $V_{\text{SW}} \approx 0.1$  V. Consequently, the ion concentration can be decreased to  $c = 10^{-1}$  M resulting in a shift of the switching voltage to  $V_{\text{SW}} = 0.27$  V. When  $c$  is further decreased to  $c = 5 \cdot 10^{-2}$  M,  $V_{\text{SW}}$  cannot be detected anymore (Figure 4.3(b), dashed green line), and has to be restored within the supply voltage range by increasing  $I_B$ . Similar considerations hold for the cases  $I_B = 1$  mA (Figure 4.3(c)) and  $I_B = 1.8$  mA (Figure 4.3(d)).

It is worth to note that the current bias drives the OECT operation and sets  $V_{\text{SW}}$  within a given range of ion concentration, while the variation of the switching voltage is inherently related to the variation of the ion concentration. In other words, the ion concentration range is set by selecting  $I_B$  while  $V_{\text{SW}}$  is related to the value of  $c$ .

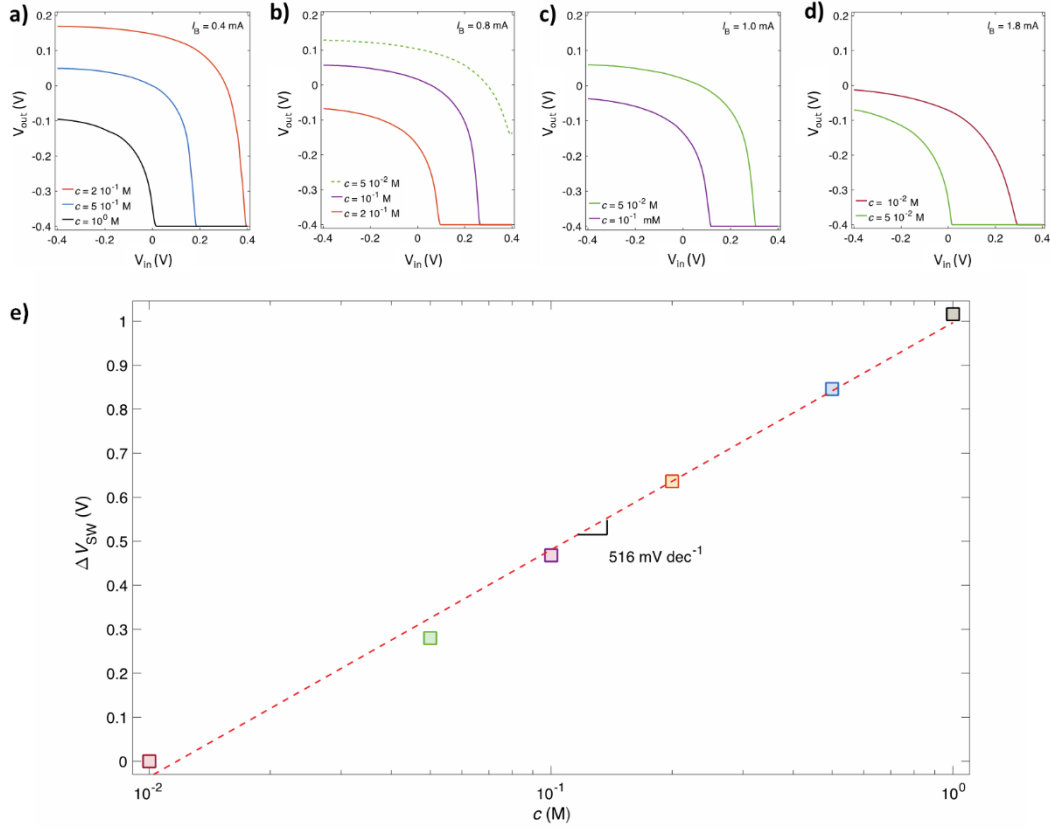


**FIGURE 4.3.** CURRENT-DRIVEN OECT USED AS ION SENSOR: **a–d)** Measured transfer characteristics of a current-driven OECT at several NaCl concentration  $c$ ,  $V_{DD} = 0.4$  V. **a)**  $I_B = 0.4$  mA, **b)**  $I_B = 0.8$  mA, **c)**  $I_B = 1.0$  mA, **d)**  $I_B = 1.8$  mA. **e)** Cumulative switching voltage variation  $\Delta V_{SWi+1} = \Delta V_{SWi} + (V_{SWi+1} - V_{SWi})$  as a function of ion concentration. The average sensitivity calculated by last-square linear approximation is of 516 mV dec $^{-1}$ . The gate is a tungsten foil and the OECTs geometries are:  $W = 1000$   $\mu$ m,  $L = 300$   $\mu$ m,  $d = 25$  nm.

#### 4.2.4. Investigation of the Ion Sensitivity

In order to quantitatively assess the ion sensitivity of the proposed current-driven OECTs, we calculate the cumulative shift of the switching voltage, defined as  $\Delta V_{SWi+1} = \Delta V_{SWi} + (V_{SWi+1} - V_{SWi})$ , where  $i$  is the  $i$ -th ion concentration. Figure 4.3(e) shows  $\Delta V_{SW}$  as a function of the ion concentration. The least-square linear approximation of the measured  $\Delta V_{SW}$  (red dashed line) gives an average sensitivity of 516 mV dec $^{-1}$  at a supply voltage of 0.4 V, that is about one order of magnitude larger than the theoretical Nernstian sensitivity of 59.16 mV dec $^{-1}$ . It is worth to note that the measured ion sensitivity of the current-driven OECT is almost constant in the whole range of ion concentration (Figure 4.3(e)). For a given  $I_B$ , a certain range of ion concentrations can be assessed, ensuring at the same time that the measured  $V_{SW}$  lies within the supply voltage. This condition can be achieved for any ion concentration and thus the sensitivity is not limited by the

supply voltage. The possibility of selecting the ion concentration range by means of  $I_B$  enables to operate the current-driven OECT at extremely low supply voltages – fundamental to prevent Faradaic leakage currents due to water electrolysis – while maintaining at the same time a high ion concentration sensitivity ( $\Delta V_{SW}/\Delta c$ ). From Equation (4.2), the ion concentration sensitivity can be calculated as follows:

$$V_{SW}/\Delta c = +\Delta V_P/\Delta c + [(I_B/\beta^3)^{1/2}/2] \times \Delta\beta/\Delta c \quad (4.3)$$

Equation (4.3) shows that the ion concentration sensitivity depends on the OECT parameters sensitivity, viz.  $\Delta V_P/\Delta c$  and  $\Delta\beta/\Delta c$ .

To gain more insight on the origin of the high ion sensitivity of the current-driven OECT configuration, it is crucial to estimate the OECT parameters sensitivity. Figures 4.4(a, b) show the measured transfer characteristics and transconductances as a function of the ion concentration, ranging from  $10^{-2}$  to  $10^0$  M, at  $V_D = -0.4$  V. The measured transfer characteristics shift toward negative voltages and the transconductances get lower by increasing the ion concentration. By reproducing the measurements with the model proposed by Bernardis and Malliaras (Equation (4.1)),<sup>[4,63]</sup> we estimated the OECT parameters  $V_P$  and  $\beta$  at several ion concentrations. Figure 4.4(c, d) show that both  $V_P$  and  $\beta$  linearly depend on the logarithm of the ion concentration and we found  $\Delta V_P/\Delta c = -135$  mV dec<sup>-1</sup> and  $\Delta\beta/\Delta c = -0.9$  mS V<sup>-1</sup> dec<sup>-1</sup>. It is worth noting that  $\Delta V_P/\Delta c$  agrees with state-of-art OECTs operated with polarizable gate electrode (e.g., tungsten).

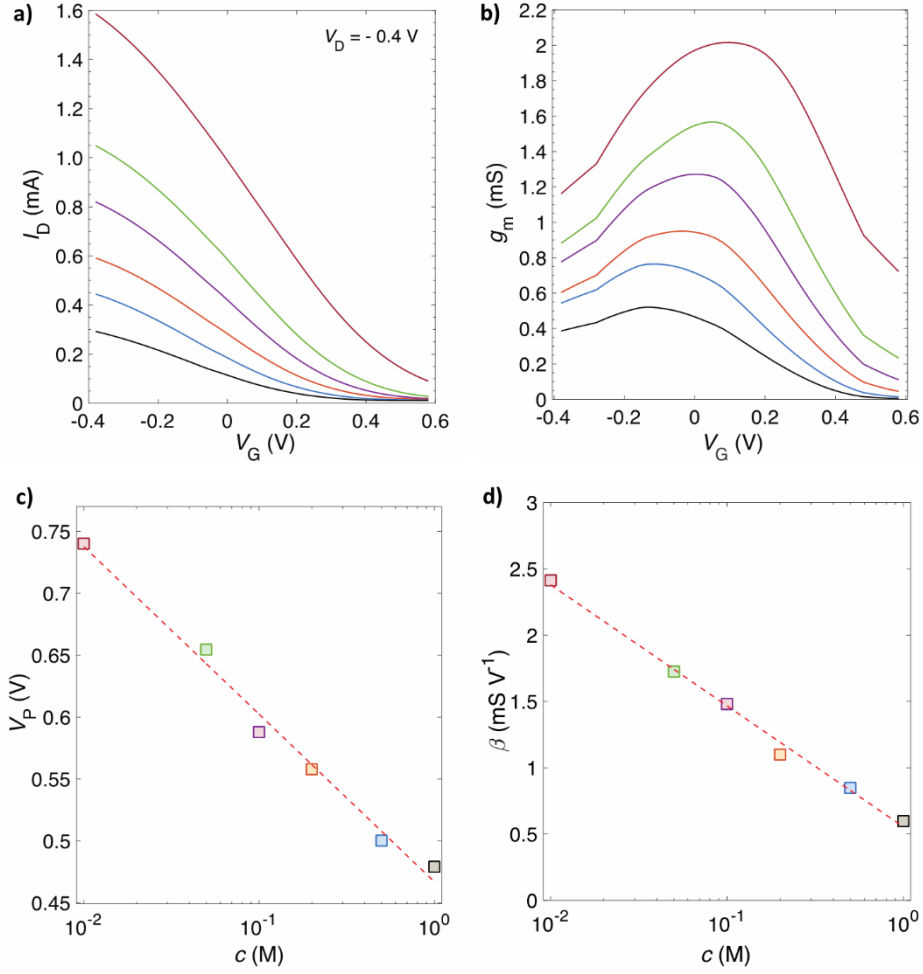


**FIGURE 4.4.** OECT CHARACTERISTICS AND PARAMETERS AS A FUNCTION OF THE ION CONCENTRATION: **a)** Measured transfer characteristics of an OECT at several NaCl concentrations  $c$ ,  $V_D = 0.4$  V and **b)** corresponding transconductance ( $g_m$ ). **c)** Pinch-off voltage  $V_P$  as a function of the ion concentration.  $V_P$  is extracted by fitting the  $I_D$ – $V_G$  with the model<sup>[4,63]</sup>:  $I_D = 2\beta(-V_G + V_P + V_D/2)V_D$ . The crossing point (named  $V_X$ ) between the linear least square approximation of  $I_D$  and the  $V_G$ -axis provides  $V_P = V_X - V_D/2$ . The average sensitivity is  $\Delta V_P/\Delta c = -135$  mV dec<sup>-1</sup>. **d)** Current prefactor  $\beta$  as a function of the ion concentration. The average sensitivity is  $\Delta\beta/\Delta c = -0.9$  mS V<sup>-1</sup> dec<sup>-1</sup>. The gate is a tungsten foil and the OECTs geometries are:  $W = 1000$   $\mu$ m,  $L = 300$   $\mu$ m,  $d = 25$  nm.

#### 4.2.5. Low-Voltage Operation

In order to evaluate the effectiveness of the proposed approach at lower voltage, we investigated current-driven OECTs operated at a supply voltage as low as  $V_{DD} = 0.2$  V. We note that this operating voltage is significantly lower than that typically used for OECTs<sup>[3,60,134]</sup>, OECT-based ion sensors<sup>[95]</sup> and voltage amplifiers<sup>[84]</sup>. To optimize the operation at low voltages, we replaced the tungsten gate with a Ag/AgCl gate electrode. This minimizes the voltage drop at the gate electrode/electrolyte interface at the expense of a slightly reduction of  $\Delta V_P/\Delta c$ . Moreover, the

OECT geometries have been optimized to warrant the detection of one order of magnitude of concentration for a given current bias  $I_B$ .

Figure 4.5(a–d) show the measured  $V_{out}-V_{in}$  of the ultra-low voltage current-driven OECT as a function of the ion concentration. More in detail, Figure 4.5(a) shows the  $V_{out}-V_{in}$  characteristics of a current-driven OECT operated with a current bias  $I_B = 0.2$  mA. When the ion concentration is  $c = 10^0$  M, the switching voltage is close to 0 V. By decreasing the ion concentration,  $V_{SW}$  shifts towards positive voltages. We found  $V_{SW} = 0.15$  V with  $c = 10^{-1}$  M. Further decreasing  $c$ , the switching voltage exceeds the supply voltage ( $V_{DD} = 0.2$  V), and cannot be detected anymore. By increasing the current bias  $I_B$  it is possible to shift  $V_{SW}$  back within the supply voltage range. Figure 4.5(b) shows the  $V_{out}-V_{in}$  characteristics of a current-driven OECT operated with a current bias  $I_B = 0.3$  mA. When the ion concentration is  $c = 10^{-1}$  M, the switching voltage is restored to  $V_{SW} \approx 0$  V. Consequently, the ion concentration can be decreased to  $c = 10^{-2}$  M resulting in a shift of the switching voltage to  $V_{SW} = 0.17$  V. Similar considerations hold for the cases  $I_B = 0.5$  mA (Figure 4.5(c)) and  $I_B = 0.8$  mA (Figure 4.5(d)).

To quantitatively assess the ion sensitivity of the ultra-low voltage current-driven OECTs, Figure 4.5(e) shows  $\Delta V_{SW}$  as a function of the ion concentration in the range  $10^{-4}$ – $10^0$  M. The linear least-square approximation of the measured  $\Delta V_{SW}$  (red dashed line) gives an average sensitivity of  $243$  mV dec $^{-1}$  in the ion concentration range  $10^{-4}$ – $10^{-2}$  M and of  $144$  mV dec $^{-1}$  in the range  $10^{-2}$  to  $10^0$  M, at a supply voltage as low as 0.2 V.

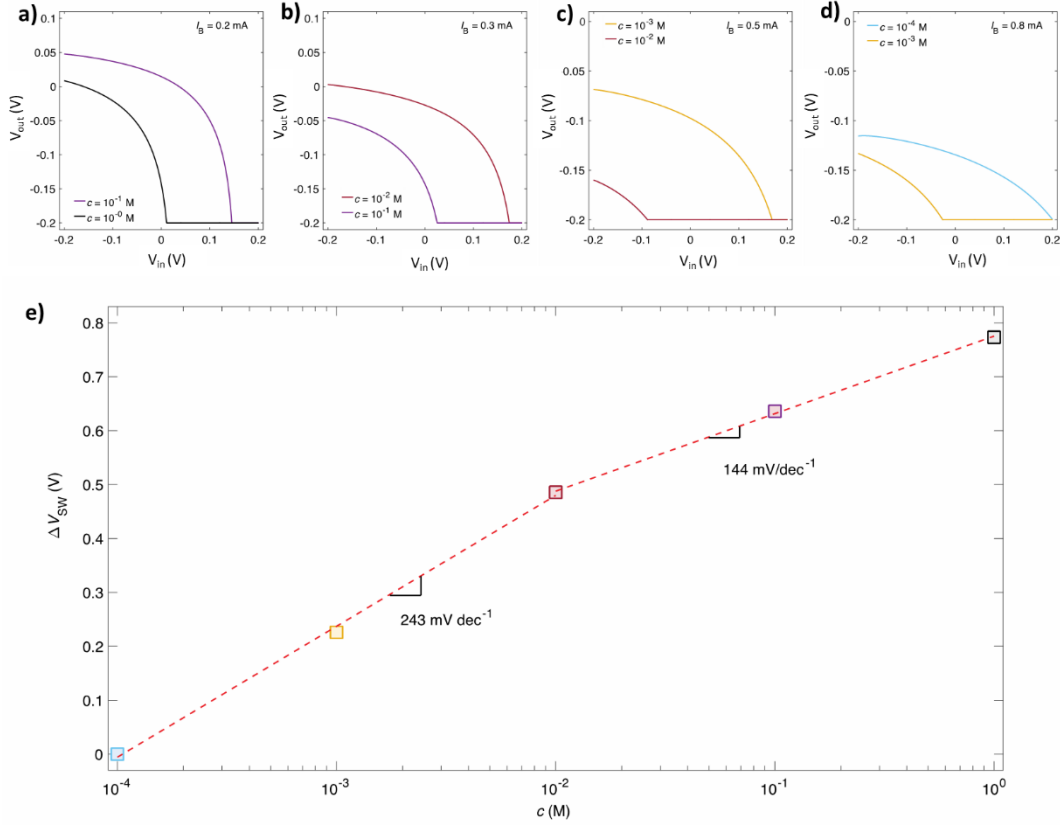


**FIGURE 2.5.** ULTRA-LOW VOLTAGE CURRENT-DRIVEN OECT: **a-d**) Measured transfer characteristics of the current-driven OECT at several NaCl concentration  $c$ ,  $V_{DD} = 0.2$  V. **a)**  $I_B = 0.2$  mA, **b)**  $I_B = 0.3$  mA, **c)**  $I_B = 0.5$  mA, **d)**  $I_B = 0.8$  mA. **e)** Cumulative switching voltage variation  $\Delta V_{SWi+1} = \Delta V_{SWi} + (V_{SWi+1} - V_{SWi})$  as a function of the ion concentration. The average sensitivity is of 144 mV dec $^{-1}$  in the range  $10^{-2}$ – $10^0$  M and 243 mV dec $^{-1}$  in the range  $10^{-4}$ – $10^{-2}$  M. The gate is a Ag/AgCl pellet and the OECTs geometries are:  $W = 1000$   $\mu$ m,  $L = 100$   $\mu$ m,  $d = 50$  nm.

#### 4.2.6. Ion-Selective Operation

As a relevant application example, high-sensitivity ion-selective detection is demonstrated by endowing the current-driven OECT with an ion-selective membrane. According with previous works<sup>[58,95]</sup> an ion-selective membrane is fabricated and used to separate an inner electrolyte in direct contact with the OECT from the analyte. The inner and the analyte electrolytes are confined in two wells, one stacked on the top of the other, and separated by the ion-selective membrane. Further details are provided in the *Experimental in Chapter 2*. To directly compare the current-driven approach with state-of-art ion-selective OECTs, a Ag/AgCl pellet is used as gate electrode, and a membrane selective to  $K^+$  ions is fabricated as described in<sup>[95]</sup>. A  $10^{-2}$  M KCl electrolyte is used as inner filling solution while KCl or NaCl at several concentrations are used as analyte solution.

Figure 4.6(a–d) show the measured  $V_{\text{out}}-V_{\text{in}}$  of an ion-selective current-driven OEET as a function of the ion concentration. According with the previous analysis,  $V_{\text{SW}}$  shifts to more positive voltages when the ion concentration is reduced and it is possible to shift  $V_{\text{SW}}$  back within the supply voltage range by increasing the current bias  $I_B$ . This ensures, at the same time, both high-sensitivity and low-voltage operation. To evaluate the ion sensitivity of ion-selective current driven OEETs, Figure 4.6(e) shows  $\Delta V_{\text{SW}}$  as a function of the ion concentration. The linear least-square approximation of the measured  $\Delta V_{\text{SW}}$  (red dashed line) gives an average sensitivity of  $414 \text{ mV dec}^{-1}$  at a supply voltage equal to 0.4 V, which is more than 8-fold larger than the ion sensitivity obtained by using an OEET<sup>[95]</sup>. Moreover, it is worth to note that the sensitivity obtained with the ion-selective membrane is close to the value obtained without the ion-selective membrane.

Finally, the selectivity is investigated by using NaCl as analyte solution. Figures S4.1(a, b) in the *Supporting Information of Chapter 4* show the measured  $V_{\text{out}}-V_{\text{in}}$  as a function of the ion concentration and at several  $I_B$ . Independently of the NaCl concentration  $V_{\text{out}}$  is almost constant in the supply voltage range and no switching occurs. This confirms that the membrane is selective to  $\text{K}^+$  ions, and the current-driven OEET configuration can be successfully used for high sensitivity and selective ion detection.

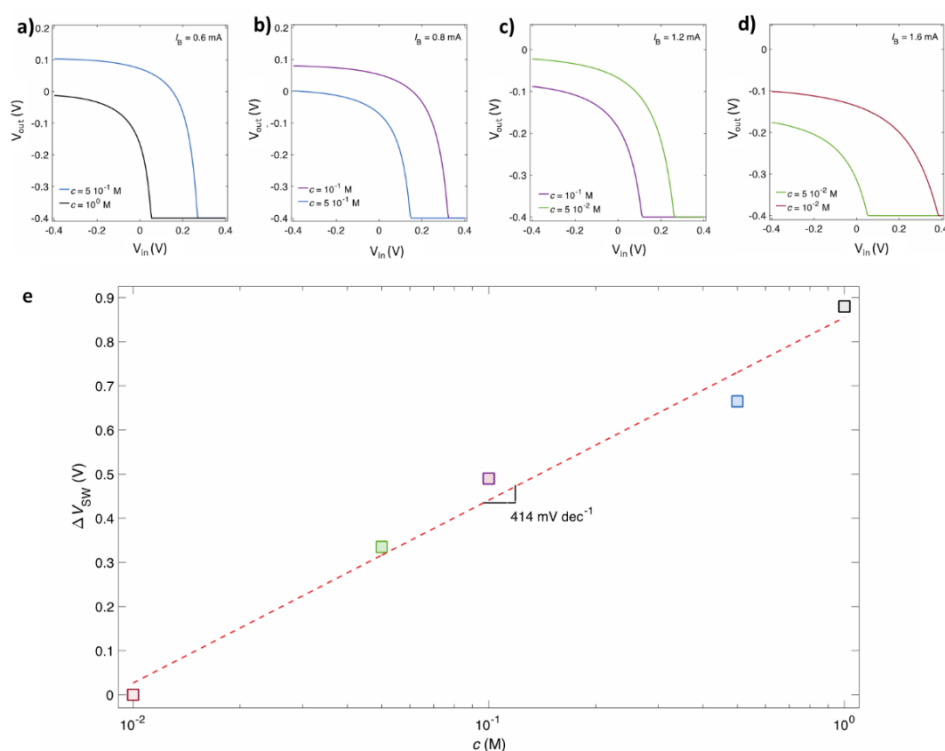


**FIGURE 2.6. ION-SELECTIVE CURRENT-DRIVEN OEET: a–d)** Measured transfer characteristics of an ion-selective current-driven OEET at several KCl concentrations  $c$ ,  $V_{\text{DD}} = 0.4 \text{ V}$ . **a)**  $I_B = 0.6 \text{ mA}$ , **b)**  $I_B = 0.8 \text{ mA}$ , **c)**  $I_B = 1.2 \text{ mA}$ , **d)**  $I_B = 1.6 \text{ mA}$ . **e)** Cumulative switching voltage variation  $\Delta V_{\text{SW}i+1} = \Delta V_{\text{SW}i} + (V_{\text{SW}i+1} - V_{\text{SW}i})$  as a function of the ion concentration. The average sensitivity is  $414 \text{ mV dec}^{-1}$ . The gate is a Ag/AgCl pellet, the membrane is selective to  $\text{K}^+$  ions, and the OEETs geometries are:  $W = 1000 \text{ }\mu\text{m}$ ,  $L = 300 \text{ }\mu\text{m}$ ,  $d = 100 \text{ nm}$ .

### 4.2.7. Discussion

The current-driven OECT configuration provides, at the same time, low-voltage operation and high sensitivity. The sensitivity,  $\Delta V_{sw}/\Delta c$ , depends on the sum of two contributions (Equation (4.3)), i.e.,  $\Delta V_{sw}/\Delta c = \Delta V_p/\Delta c + \Delta V_\beta/\Delta c$ , where  $\Delta V_\beta/\Delta c = k \times \Delta\beta/\Delta c$  and  $k = (I_B/\beta^3)^{1/2}/2$ . Since in the current-driven OECT configuration both  $V_p$  and  $\beta$  decrease by increasing the ion concentration, the terms  $\Delta V_\beta/\Delta c$  and  $\Delta V_p/\Delta c$  sum up resulting in an improved voltage ion sensitivity with respect to that obtained with conventional OECT operation, where the voltage sensitivity is limited to only  $\Delta V_p/\Delta c$ <sup>[134]</sup>.

The current-driven OECTs overcome these fundamental limitations by adding a very relevant contribution to the voltage ion sensitivity, i.e.  $\Delta V_\beta/\Delta c = k \times \Delta\beta/\Delta c$ , that can be enhanced by means of the OECT design parameters, viz. channel width and length, semiconductor thickness, mobility, and volumetric capacitance. For example, the results presented in Figures 4.3 and 4.4 show that current-driven OECTs operated at  $I_B = 0.8$  mA and at  $c = 2 \times 10^{-1}$  M gives  $k \approx 400$  and therefore  $\Delta V_\beta/\Delta c \approx 360$  mV dec<sup>-1</sup>, which yield  $\Delta V_\beta/\Delta c \approx 3 \times \Delta V_p/\Delta c$ .

Interestingly, ultra-low voltage current-driven OECTs show a voltage ion sensitivity  $\Delta V_{sw}/\Delta c = \Delta V_p/\Delta c + \Delta V_\beta/\Delta c$  larger at smaller concentrations (Figure 4.5(e)). This can be explained as follows. Figures S4.2(c) in the *Supporting Information 4.4* shows that  $V_p$  linearly depends on the logarithm of the ion concentration while Figure S4.2(d) in the *Supporting Information 4.4* shows that  $\beta$  has a double linear dependence on the logarithm of the ion concentration. We found that  $\Delta V_p/\Delta c = -98$  mV dec<sup>-1</sup> in the whole concentration range, while  $\Delta\beta/\Delta c = -0.28$  mS V<sup>-1</sup> dec<sup>-1</sup> in the concentration range  $10^{-4}$ – $10^{-2}$  M and  $\Delta\beta/\Delta c = -0.10$  mS V<sup>-1</sup> dec<sup>-1</sup> in the range  $10^{-2}$ – $10^0$  M. Consequently,  $\Delta V_\beta/\Delta c = k \times \Delta\beta/\Delta c$  is larger in the concentration range  $10^{-4}$ – $10^{-2}$  M, and this explains the larger ion sensitivity at smaller concentrations. The variation of  $\beta$  as a function of the ion concentration  $c$  could be related to a variation of  $C_v$  and/or  $\mu$ . To investigate this point, we extracted  $C_v$  and  $\mu$  as a function of the ion concentration. Taking advantage of electrochemical impedance spectroscopy measurements (Figure S4.3, *Supporting Information 4.4*) we found that  $C_v$  is independent of  $c$  and results  $C_v = 39.38 \pm 1.76$  F cm<sup>-3</sup>, in good agreement with state-of-art PEDOT-PSS OECTs<sup>[3,4,60]</sup>. Then, we extracted  $\mu$  as a function of  $c$  from the measured  $I_D$ – $V_G$  (Figure S4.4, *Supporting Information 4.4*). We found that  $\mu$  decreases by increasing  $c$ , thus explaining the  $\beta$ – $c$  characteristic displayed in Figure S4.2(d) in the *Supporting Information 4.4*.

The proposed approach is compared with several ion-sensitive transistor technologies in Table 4.1. The voltage ion sensitivity of the current-driven OECT configuration outperforms silicon, metal-oxide and electrolyte-gated organic field-effect transistors. It is only surpassed by ZnO double gate transistors<sup>[124,127,138]</sup>, which require a more complex multi-layer fabrication and a quite large supply voltage (up to 20 V) inherently related to the small gate capacitance. In order to fairly compare the different transistor technologies, the voltage ion sensitivity is normalized



with respect to the supply voltage. As shown in Table 4.1, the normalized voltage ion sensitivity  $A_{VI} = (\Delta V_{SW}/\Delta c)/V_{DD}$  obtained with current-driven OECTs at  $V_{DD} = 0.2$  V and  $V_{DD} = 0.4$  V results  $A_{VI} = 1215$  mV V<sup>-1</sup> dec<sup>-1</sup> and  $A_{VI} = 1290$  mV V<sup>-1</sup> dec<sup>-1</sup>, respectively. These values are more than one order of magnitude larger than those reported for state-of-art ion-sensitive transistors including Si ISFETs, ZnO single and double gate FETs, a-IGZO double gate FETs, Si nanowire FETs, graphene FETs, EGOFETs, and OECTs.

The current-driven OECT approach ensures, at the same time, low-voltage operation and high sensitivity in a wide range of ion concentrations. In contrast to state-of-art ion sensors where the input ion concentration is converted in an output voltage<sup>[84]</sup>, the current-driven OECT configuration is based on the reading of the switching voltage, which is positioned inside the supply voltage range by properly selecting the bias current. Therefore, the current-driven OECT approach exploits the large transconductance of OECTs in a completely different fashion with respect to standard voltage amplifier configurations<sup>[84]</sup> and breaks the intrinsic trade-off between sensitivity and operating voltage.

**TABLE 4.1. SENSITIVITY COMPARISON:** The table compares several technologies by considering the type of ion, the current sensitivity ( $\Delta I/\Delta c$ ), the voltage sensitivity ( $\Delta V/\Delta c$ ), the supply voltage ( $V_{DD}$ ), and the supply voltage-normalized voltage sensitivity  $A_{VI} = (\Delta V/\Delta c)/V_{DD}$ .

Technology	Ion	$\Delta I/\Delta c$ ( $\mu A$ dec <sup>-1</sup> )	$\Delta V/\Delta c$ (mV dec <sup>-1</sup> )	$V_{DD}$ (V)	$A_{VI}$ (mV V <sup>-1</sup> dec <sup>-1</sup> )	Ref.
Si ISFET	pH	60	53	2.5	21.2	[128]
ZnO–single gate	pH	90	55	2	27.5	[128]
ZnO–double gate	pH	0.012	2250	20	112.5	[124,127,138]
a-IGZO–double gate	pH		160	5	32.0	[130]
Si NanoWire	pH	1		40		[129]
Si NanoWire–double gate	pH		220	7	31.43	[125]
Graphene FET	pH		49	0.4	122.5	[131]
Ion-selective P3HT EGOFET	Na <sup>+</sup>	0.5	62	0.5	124.0	[58]
Ion-selective OECT	K <sup>+</sup>	47	48	0.4	120.0	[95]
OECT	Na <sup>+</sup> K <sup>+</sup> H <sup>+</sup>	20	135	1.25	108.0	[134]
OECT	Na <sup>+</sup>	780	135	0.4	337.5	This work
OECT	Na <sup>+</sup>	270	98	0.4	245.0	This work
Current-drive OECT	Na <sup>+</sup>		516	0.4	1290.0	This work
Current-drive OECT	Na <sup>+</sup>		243	0.2	1215.0	This work
IS-current-driven OECT	K <sup>+</sup>		414	0.4	1035.0	This work

### 4.3. Summary of Chapter 4

In summary, the current-driven OECT approach shows that it is possible to dramatically enhance the ion sensitivity of OECTs while maintaining a low-voltage operation. The key ingredients are the large transistor transconductance that reflects in the large amplification and the bias current that enables to select the operating range and ensures the low-voltage operation.

The measured voltage ion sensitivity exceeds by about one order of magnitude the Nernst limit in the case of supply voltage of 0.4 V, while it shows a five-fold increase in the case of supply voltage of 0.2 V. The ion sensitivity normalized with respect to the supply voltage is larger than  $1200 \text{ mV V}^{-1} \text{ dec}^{-1}$ , which is the largest value ever reported for ion-sensitive transistors.

The proposed approach is general and could be extended to other electrochemical and field-effect transistor technologies. In addition, current-driven OECTs allow simple and low-cost fabrication on flexible substrates, opening new opportunities for high-performance conformable and widespread organic bioelectronics.

## 4.4. Supporting Information of Chapter 4

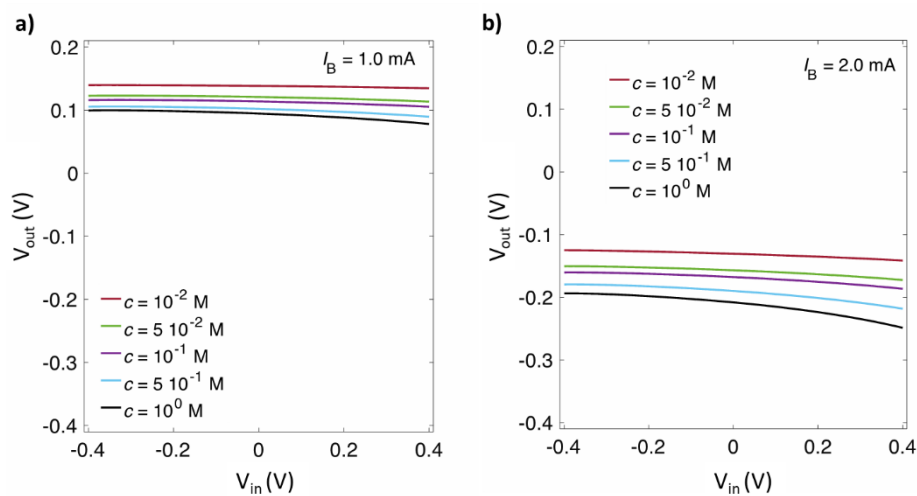


**FIGURE S4.1.** MEASURED TRANSFER CHARACTERISTICS ( $V_{\text{out}}-V_{\text{in}}$ ) of the current-driven OECT at several NaCl concentration  $c$ ,  $V_{\text{DD}} = 0.4$  V. **a)**  $I_{\text{B}} = 1$  mA, and **b)**  $I_{\text{B}} = 2.0$  mA. The membrane, placed in between the inner and the analyte solutions, is selective to  $\text{K}^+$  ions. Independently of the NaCl concentration  $V_{\text{out}}$  is almost constant and no switching is displayed. The gate is a Ag/AgCl pellet and the OECTs geometries are:  $W = 1000$   $\mu\text{m}$ ,  $L = 300$   $\mu\text{m}$ ,  $d = 100$  nm.

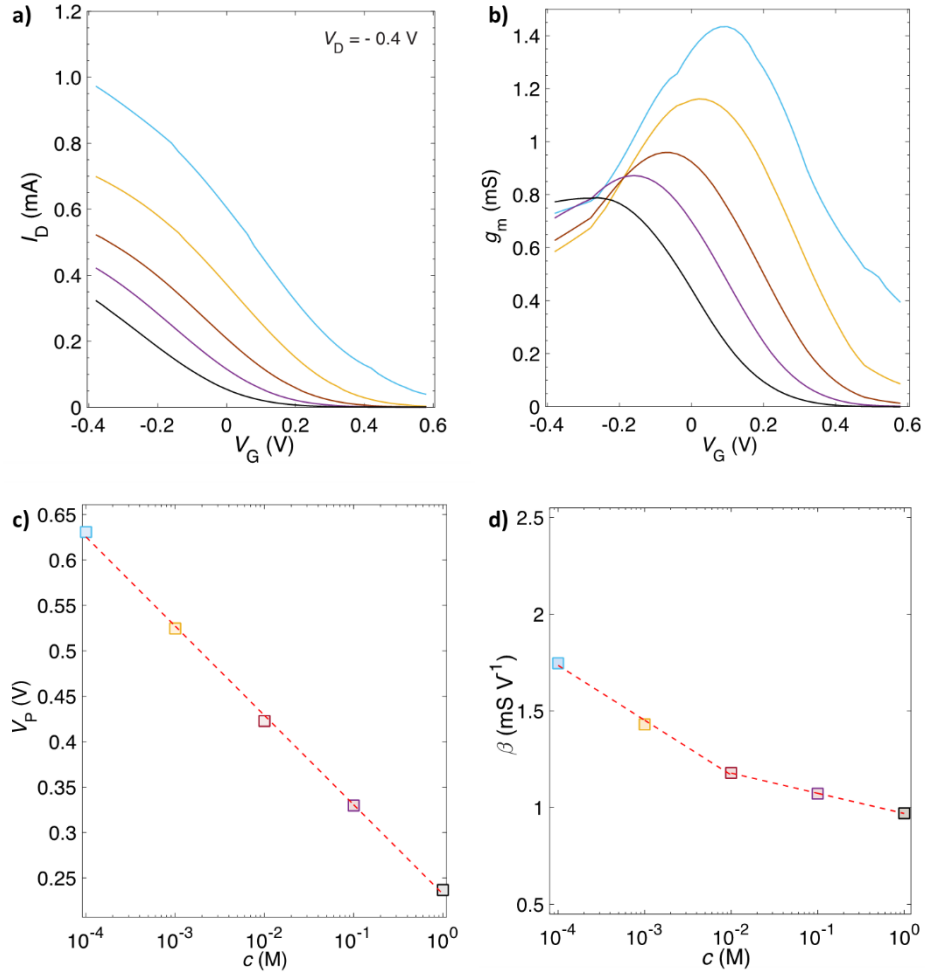


**FIGURE S4.2.** CHARACTERISTICS AND PARAMETERS OF OECS OPERATED AT ULTRA-LOW VOLTAGE: **a)** Measured transfer characteristics of the OECS at several ion concentrations,  $V_D = -0.4$  V and **b)** corresponding transconductance ( $g_m$ ). **c)** Pinch-off voltage  $V_P$  as a function of the ion concentration. The average sensitivity is  $\Delta V_P / \Delta c = -98$  mV dec<sup>-1</sup>. **d)** Current prefactor  $\beta$  as a function of the ion concentration. The average sensitivity is  $\Delta \beta / \Delta c = -0.28$  mS V<sup>-1</sup> dec<sup>-1</sup> in the concentration range  $10^{-4}$  to  $10^{-2}$  M and  $\Delta \beta / \Delta c = -0.10$  mS V<sup>-1</sup> dec<sup>-1</sup> in the range  $10^{-2}$  to  $10^0$  M. The gate is a Ag/AgCl pellet and the OECS geometries are:  $W = 1000$   $\mu$ m,  $L = 100$   $\mu$ m,  $d = 50$  nm.

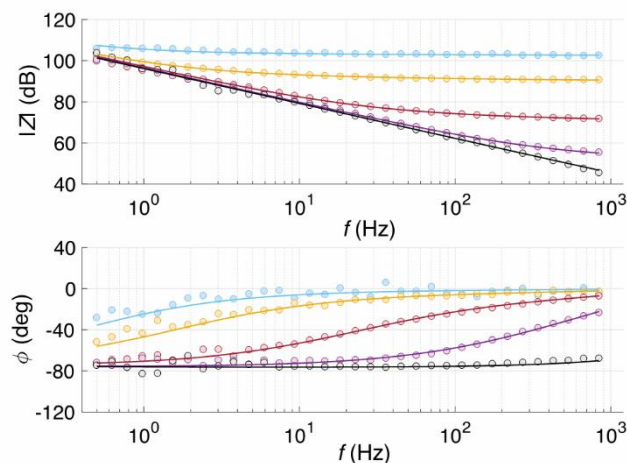


**FIGURE S4.3.** OECT IMPEDANCE SPECTRA AS A FUNCTION OF ION CONCENTRATION  $c = [10^{-4} \ 10^{-3} \ 10^{-2} \ 10^{-1} \ 10^0] \text{ M}$ . In order to extract the volumetric capacitance  $C_v$ , for each ion concentration we modelled the measured impedance as a function of the frequency with the Randles equivalent circuit. According with Ref. X<sup>[4]</sup>, in the case of an OECT the Randles circuit is composed by a series resistor  $R_s$ , and a parallel of a resistor  $R_p$  and a capacitor  $C$ . In this model,  $R_s$  is the electrolyte resistance,  $R_p$  depends on the Faradaic reactions at the working electrode, and  $C$  is the capacitance. The OECT volumetric capacitance is then calculated as  $C_v = C v^{-1}$  where  $v = W L d$  is the total volume of PEDOT:PSS. In the case of analysis  $W = 1000 \ \mu\text{m}$ ,  $L = 800 \ \mu\text{m}$ , and  $d = 100 \text{ nm}$ . We reproduced the measurements (symbols) with the model (full line) and we found that for all ion concentrations  $R_p > 5 \text{ M}\Omega$ ,  $R_s$  is proportional to the inverse of the ion concentration, in agreement with the Debye-Hückel-Onsager theory<sup>[63]</sup>, and the volumetric capacitance is independent of the ion concentration and results  $C_v = 39.38 \pm 1.76 \text{ F cm}^{-3}$ .

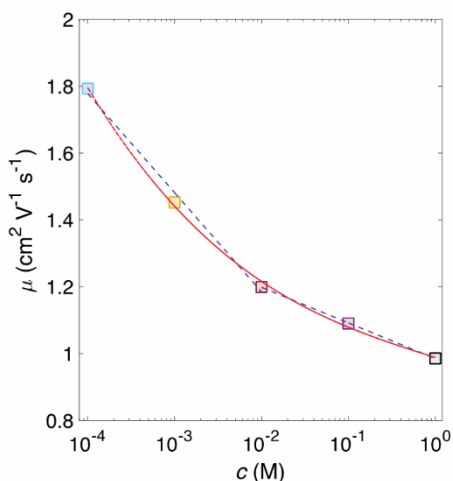


**FIGURE S4.4.** MOBILITY AS A FUNCTION OF THE ION CONCENTRATION: Symbols are calculated from the measurements, dashed blue line is a simple double logarithmic approximation and red line is a third-order approximation. Lines are used only as guides for eyes. According with the model proposed by Bernardis and Malliaras<sup>[4,63]</sup>, when the transistor is operated in the linear regime the mobility can be extracted from the transfer characteristics as follows  $\mu(c) = g_m^* L (W C_V d V_D)^{-1}$  where  $g_m^* = \max(\Delta I_D / \Delta V_G)$  is the maximum transconductance. The mobility decreases by increasing the ion concentration. This could be interpreted as follows. In PEDOT:PSS the charge transport takes place in PEDOT nanocrystals surrounded by an amorphous PEDOT:PSS matrix<sup>[139]</sup>. Ions easily penetrate the amorphous phase of PEDOT:PSS and interacts with the PEDOT nanocrystals<sup>[14,140]</sup>. This situation is analogous to the case where ions enter a semicrystalline organic semiconductor. In this case, it has been found that the overall semiconductor mobility gets lower by increasing the ion concentration because the highly oriented fraction of the semiconducting polymer reduces<sup>[141]</sup>.

# Chapter 5

## **Probing the Impedance of a Biological Tissue with PEDOT:PSS-Coated Metal Electrodes: *Effect of Electrode Size on Sensing Efficiency***

Conducting polymers are promising to revolutionize the world of bioelectronics due to their unique set of features. Especially, in the field of biosensing, PEDOT:PSS devices have been widely integrated with biological cell layers for barrier tissue integrity measurements and for high sensitivity biosensors realization with applications both in basic research and in diagnostics. Despite its great importance, a systematic experimental study of the correlation between tissue integrity and impedance of the sensing device has not yet been conducted. In this chapter, with the use of electrochemical impedance spectroscopy, we investigate the way that the impedance ratio of the biological tissue to the recording device, affects the recording ability of the latter. PEDOT:PSS-coated electrodes of various dimensions were employed and the effect of their size to their sensing efficiency is examined. The biotic/abiotic ensemble is modeled with a simple equivalent circuit and an analytical expression of the total impedance as a function of frequency is extracted. The results reveal a critical impedance ratio of the biological tissue to the sensor which allows for efficient sensing of the tissue integrity. The results provide the ground rules for improved impedance-based biosensors with optimized sensitivity.\*

\*D. A. Koutsouras, L. V. Lingstedt, J. Reinholz, R. M. Owens, V. Mailänder, P. W. M. Blom and P. Gkoupidenis, **2019**, *in preparation*.

## 5.1. Introduction

Organic electronic materials are currently the most promising candidates to revolutionize the field of bioelectronics. This view is justified by the unique set of features they possess and which allows them to interact with biological systems in an extremely effective way<sup>[2,11,117]</sup>. Conducting polymers in particular, have been widely exploited lately in biological driven applications as electrode coatings as well as the channel material of organic-based transistors<sup>[68,142–144]</sup>. The reason behind that is their characteristic to improve the tissue/recording site interaction in-vitro and also in-vivo, by lowering the overall device impedance<sup>[20,145]</sup>. This is mainly due to their ability to conduct both ions and electrons, a fact which delivers extremely high capacitance values<sup>[146]</sup>. The above attributes have already resulted in a variety of applications spanning from neural interfacing<sup>[147,148]</sup>, biosensing<sup>[149]</sup> and drug delivering<sup>[150]</sup> to the materialization of neuromorphic devices<sup>[86,151]</sup> and electronic plants<sup>[152]</sup>. In addition they offer a biocompatible substrate, which favors the biotic/abiotic interplay<sup>[153,154]</sup> and the facile/cost effective fabrication process that comes hand to hand with their solution-based manipulation. More than that, features like the above, have also been widely exploited in the past for examining the integrity state of various types of tissue layers.

Indeed, a lot of studies have already, focused on ion transport through lipid bilayers and barrier tissues with the use of PEDOT:PSS as the active material in the measuring device<sup>[6,155]</sup>. In general, epithelial and endothelial cells form layers by accomplishing intercellular junctions between them and separating the apical (luminal) from the basolateral (abluminal) domain<sup>[156]</sup>. Most importantly, they are able to form a functional barrier among different compartments by controlling the passage of chemical compounds, nutrition ingredients, water molecules and even cells through them<sup>[157]</sup>. This control can take place either along the formed tight junctions (TJs, paracellular pathway) or via transport through the cell cytoplasm (intracellular pathway<sup>[156]</sup>). The integrity of the barrier monolayer is, therefore, essential for guaranteeing the physiological function of different compartments, and its loss signifies pathophysiological issues serving at the same time as a disease indicator. In addition, being able to accurately, fast and easily monitor the level of this integrity is of great importance now more than ever. Namely, it allows for reliable tests on drug toxicity in in vitro models, especially since the 3Rs (Replacement, Reduction, Refinement) principle has become a necessity<sup>[158]</sup>. In practice, in order for the above integrity to be studied, the response of the tissue is usually tested taking under consideration the two ways that ions, molecules and ingredients can pass through a biological cell layer, the intercellular and the paracellular pathway<sup>[157]</sup>.

Regarding the intercellular pathway, the cell membrane permeability is typically assessed by radiolabeled markers or nonradioactive fluorescence labeled proteins<sup>[159]</sup>. The paracellular one on the other hand, is commonly studied via transepithelial electrical resistance measurements



(TEER)<sup>[159]</sup>. However, the former technique suffers from tracer compounds/barrier interferences, while the latter comes along with temporal resolution and reproducibility issues, in addition to a destructive effect on both the cells and the electrodes.

Consequently, alternative, non-invasive, ways to check tissue integrity have been developed. Impedance spectroscopy (IS), in particular, is an automated and reliable way to improve TEER measurements. It is based on defining the impedance (magnitude  $|Z|$  and phase  $\phi$ ) of the tissue by sweeping a small AC voltage signal over frequency and recording the resulting AC current signal. Importantly, it allows for a system to be properly modeled due to the fact that except from the resistance provides information regarding the capacitance of the cell layer over a frequency range. Conducting polymers have proved to be a valuable asset in this task as their unique features allow the fabrication of state-of-the-art passive electrode devices. Notably, they can be used as electrode coatings facilitating the electrolyte/recording site interface throughout the measurements.

Organic electrochemical transistors (OECTs), on the other hand, are devices that consist of a degenerated doped conducting polymer film channel in contact with an electrolyte<sup>[63]</sup>. The swelling of the channel material yields high transconductance values for low operation voltages. As shown in previous studies<sup>[6,8,93]</sup>, the presence of the tissue layer in a suspended filter (Transwell) affects the way the current in the channel is modulated by the gate electrode. As a result, the device constitutes not only a low-cost biosensor but also a candidate for the fabrication of diagnostic tools with high sensitivity and with the advantage of high temporal resolution. Interestingly, in these experiments the study of the cell layer integrity was facilitated by the decrease in the tissue area or equivalently by an increase of the tissue impedance compared to the one of the measuring device<sup>[6]</sup>. In a following theoretical study, the biological barrier layer-functionalized OECT was modeled<sup>[160]</sup>. The result showed that the barrier-to-device area ratio is an important parameter in order to tune the device sensitivity and to define the detection limit. Later on, in a different study, the scaling of the impedance of conducting polymer-coated electrodes as a function of area, film thickness and electrolyte concentration was examined revealing a universal scaling rule for the above mentioned parameters<sup>[161]</sup>. Nevertheless, up to now, there is no systematic experimental investigation of the device efficiency to sense the tissue integrity, as a function of the ratio between the impedance of the tissue and that of the measuring device.

Here, we examine the effect of the impedance ratio  $\lambda$  of a tissue cell layer to the measuring electrode in the sensing ability of the later, by means of frequency domain electrochemical impedance spectroscopy. The study is conducted by systematically changing the area of the electrode a fact projected on its impedance spectrum. The results show that for a specific ratio  $\lambda$ , a well-documented in literature plateau appears<sup>[160,162]</sup>. This plateau is attributed to the impedance of the tissue layer. By changing  $\lambda$ , the plateau disappears confirming that there is a

critical value above which we can achieve sensing. The total biotic/abiotic ensemble can be described by a simple four element circuit which leads to the extraction of analytical formulas for the frequency depended impedance  $Z$  as a function of geometrical characteristics. Since the study targets the PEDOT:PSS film features, its outcome is valid for both conducting polymer-coated electrodes and OECTs, as the extrapolation from the former device to the latter is straightforward. Our results pave the way for better understanding the necessary conditions for device optimization for biosensing, in order to minimize the mismatch between electronics and biological tissue.

## 5.2. Results and Discussion

Figure 5.1(a) represents the experimental set up. A poly(methyl methacrylate) (PMMA) chamber was initial constructed and then glued on the electrode device in order to encompass its active area. A compartment is thus created to host a Transwell filter on which the Caco-2 cells were cultured (see also experimental part). The chamber is filled with Eagle's Minimum Essential Medium (EMEM), a culture medium that establishes an ionic connection between the recording sites (electrodes) and the biological tissue. A useful way to study the ensemble is to represent the impedance spectrum of the system as an equivalent electrical circuit like the one presented in Figure 5.2(b) and which has been widely used throughout literature<sup>[156]</sup>. The electrode is simulated by a basic  $R_s - C_{EL}$  circuit in series with a basic  $R_{MEM} // C_{MEM}$  circuit (Figure 5.2(b)).  $C_{EL}$  represents the capacitor created at the electrode interface with the electrolyte and  $R_s$  the spreading resistance which depends on the electrode's size<sup>[163]</sup>.  $R_{MEM}$  on the other hand expresses the ohmic resistance of the paracellular pathway due to the presence of tight junctional proteins connecting the cells. This is the ohmic resistance that can also be obtained via TEER measurements. Finally,  $C_{MEM}$  is the electrical capacitance at the biological membrane.

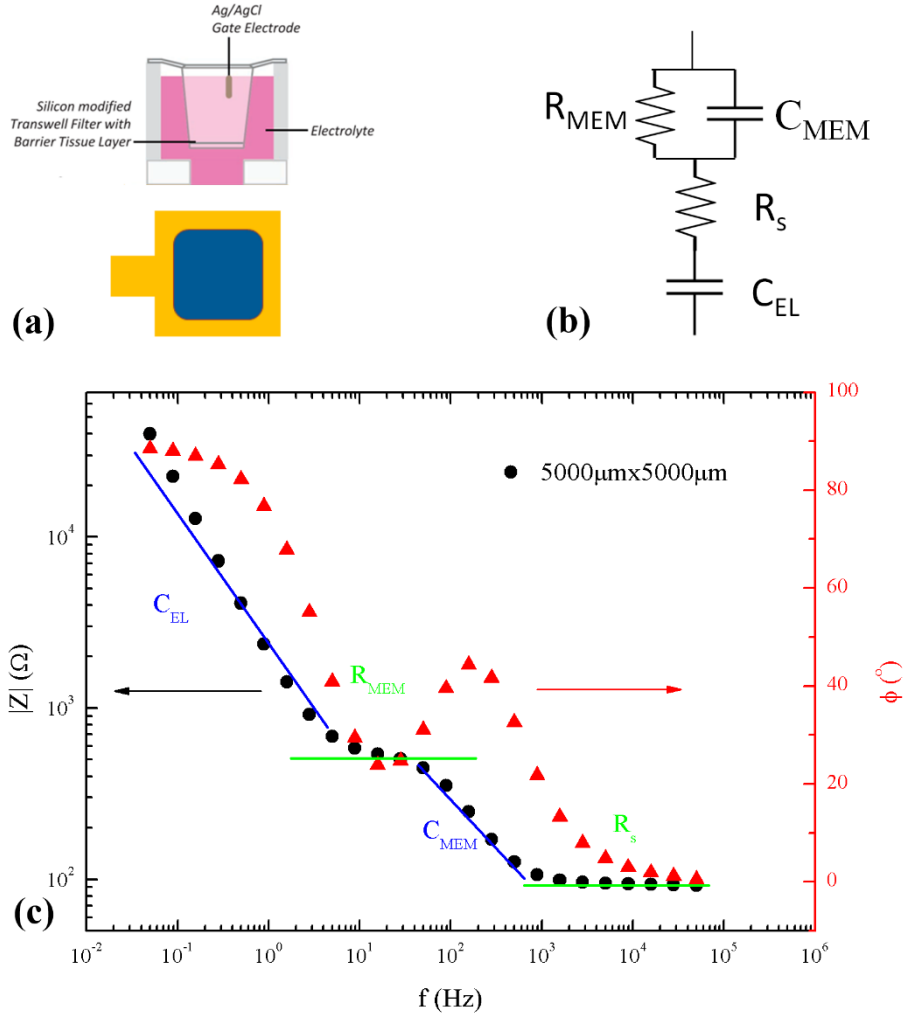


**FIGURE 5.1.** EXPERIMENTAL SET UP AND ELECTRODE IMPEDANCE SPECTRUM: **a)** Schematic that represents the Transwell filter on top of the PEDOT:PSS-coated gold electrode. The filter hosts the Caco-2 cell layer allowing for electrochemical impedance measurements to take place. **b)** The equivalent circuit models the system taking into account a  $R_{EL} - C_{EL}$  circuit which corresponds to the electrode and a  $R_{MEM} // C_{MEM}$  circuit which corresponds to the tissue layer. **c)** Electrode impedance spectrum: The modeled resistors and capacitors used in the equivalent circuit are present in the impedance spectrum of the  $5000\mu\text{m} \times 5000\mu\text{m}$  electrode (Bode magnitude  $|Z|$  and phase  $\phi$  plots).  $C$  and  $R$  notations are used to signify the capacitive and resistive nature of the impedance at those frequency regions.

In Figure 5.1(c), a reference example of the impedance spectroscopy spectrum of a  $5000\mu\text{m} \times 5000\mu\text{m}$  electrode under the presence of the cell layer is shown. On the plot, four distinctive regions are clearly presented. At very high frequencies, the system exhibits a resistive behavior with a constant  $R_s$  value over frequency. For smaller frequencies ( $10^2$ – $10^3$  Hz), a capacitive part becomes dominant corresponding to the capacitance of the tissue  $C_{MEM}$ , followed by a second resistive part  $R_{MEM}$  from 1 to  $10^2$  Hz due to the paracellular resistance this time. For this particular Caco-2 cell barrier the fitted  $R_{MEM}$  value equals to  $400\Omega$  which is close to the experimentally measured TEER value of  $425\Omega$ . It is worth noticing here, that the  $R_{MEM} // C_{MEM}$

combination of the equivalent circuit represents the biological part of the system. Most importantly, its footprint on the spectrum, with the form of a plateau, validates the ability of the electrode to sense the tissue barrier presence. Finally, below 1 Hz we return to a capacitive regime having the formed capacitor  $C_{EL}$  at the medium/coated electrode interface being the dominant circuit element. In the same figure, the corresponding phase is also presented. Studying the data from a complementary perspective, the resistive nature of the system is clear through the zero phase  $\varphi$  value at high frequencies. The presence of the tissue capacitance becomes apparent with the phase peak between  $10^2$ – $10^3$  Hz, while the tissue resistance emerges from 1 to  $10^2$  Hz. Below that frequency, the capacitance of the electrode dominates with a phase value  $\varphi$  that approaches  $-90^\circ$ .

The above described impedance features of the interaction between the tissue and the electrode are better depicted in Figure 5.2. Figure 5.2(a) illustrates typical impedance spectra of electrodes (reference experiment) with various areas and Figure 5.2(b) presents the corresponding phase. The resistive part at the higher frequencies and the capacitive part at the lower ones are clearly portrayed for every electrode. Briefly, it can be concluded that a change on the electrode area alters the position of the corresponding curve in the impedance magnitude  $|Z|$  –  $f$  plane, leaving yet, unchanged its overall shape. This scaling behavior is in agreement with previous work<sup>[161]</sup>. Nonetheless, the presence of the Caco-2 barrier tissue layer modifies the electrical characteristics of the system, a fact reflected on the impedance spectra presented in Figure 5.2(c). While a change is unseen for the smaller electrodes (sizes  $1000\ \mu\text{m} \times 1000\ \mu\text{m}$  and below), it is apparent for the larger ones (sizes  $10000\ \mu\text{m} \times 10000\ \mu\text{m}$  and  $5000\ \mu\text{m} \times 5000\ \mu\text{m}$ ). Moreover, there seems to be a transition electrode size separating the two extreme cases (no-sensing and sensing electrodes). This observation implies a connection between the recording site area, and consequently its impedance, and its ability to sense the presence of the cell layer above it<sup>[160]</sup>. During the measurement, a small amplitude AC signal is applied at the Ag/AgCl reference electrode which creates an ionic current that is measured by the working electrode (PEDOT:PSS-coated electrode). Naturally, the presence of the tissue barrier impedes the ionic charge movement. Whether the electrical fingerprint of the tissue will eventually be recorded, or not, depends on the relationship between the impedance attributed to the layer and the one attributed to the electrode. Larger electrodes are better in capturing the transmitted signal due to their small impedance compared to the cell layer one. This fact is depicted on the plateau shown for frequencies below 100 Hz for these electrodes. Similarly, regarding the impedance phase  $\varphi$  spectra, peaks are also observed for them in Figure 5.2(d). These peaks denote the capacitive contribution due to the presence of the cell membrane.

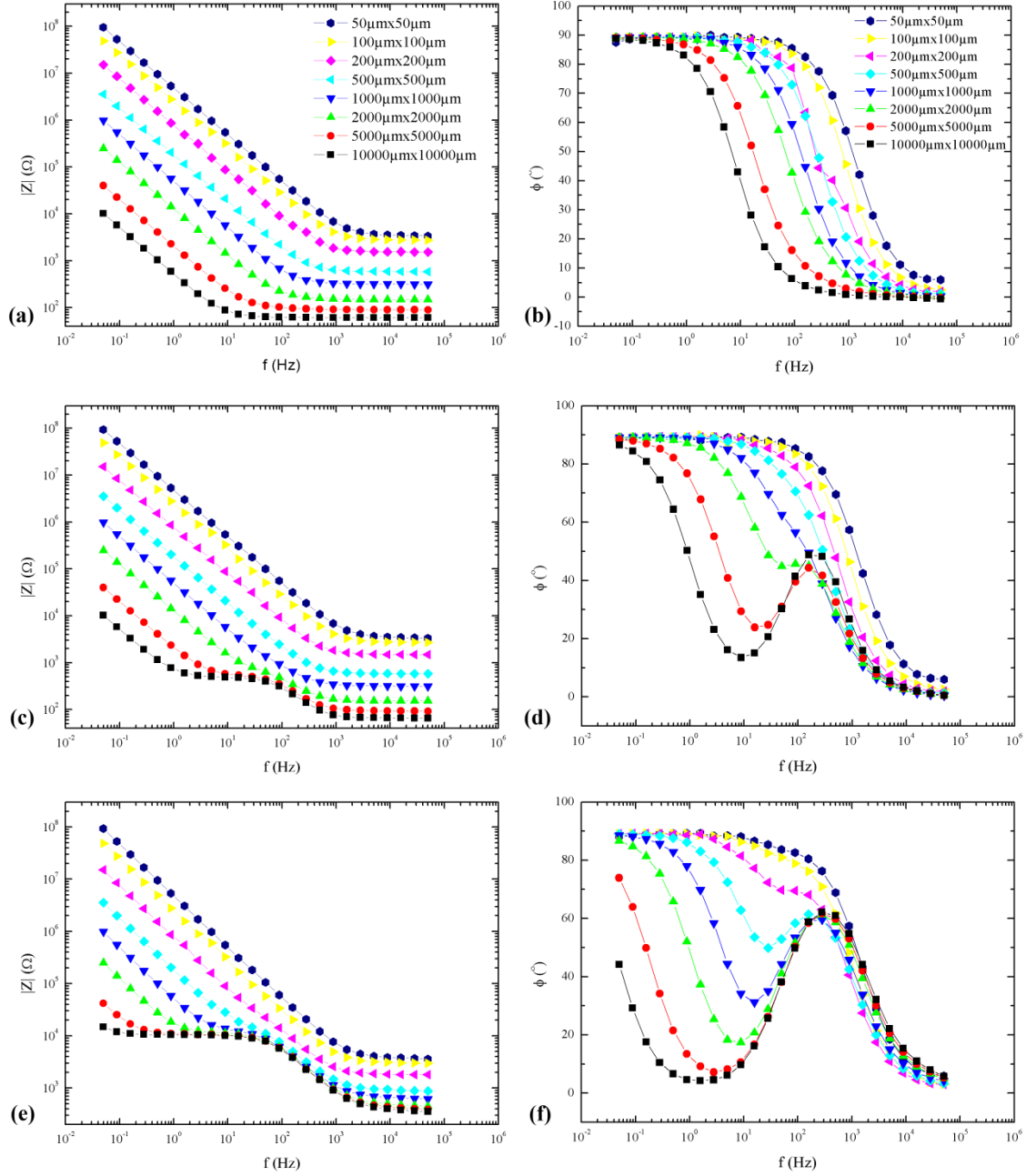


**FIGURE 5.2.** BODE MAGNITUDE AND PHASE SPECTRA OF ELECTRODES OF VARIOUS SIZES WITH AND WITHOUT CELLS: **a) , b)** Panel (a) and panel (b) show impedance plots (Bode magnitude  $|Z|$  and phase  $\phi$  respectively) of PEDOT:PSS-coated gold electrodes of various sizes. **c) , d)** The presence of the cell barrier in panel (c) and panel (d) alters the shape of the spectra with the appearance of a plateau in the Bode magnitude and a peak in the phase plots of the electrodes with the smaller impedance (greater sized electrodes). **e) , f)** By changing the effective area of the cell barrier tissue (with the use of PDMS) even smaller sized electrodes can be recruited to sense the presence of the biological tissue.

Having the above in mind, it can be concluded that the impedance spectrum is affected by the values of the electric components of the equivalent circuit. What that means is that if we are to change the values of either  $R_s$ ,  $C_{EL}$  that correspond to the electrode or  $R_{MEM}$ ,  $C_{MEM}$  that correspond to the biological tissue, different traces will be obtained<sup>[156]</sup>. This is illustrated in Figure 5.2(e)

where polydimethylsiloxane (PDMS) was used on the filter in order to reduce its size before Caco-2 cells were cultured on it. In terms of the electric circuit components, that results to an increased  $R_{MEM}$  value with a simultaneous decreased capacitance  $C_{MEM}$  leading to an overall impedance increment of the  $R_{MEM} // C_{MEM}$  part of the circuit. As a result, more electrodes of the used electrode set will be able to sense the presence of the cell layer leading to the conclusion that the ratio  $\lambda$  of  $|Z_{MEM}|$  to  $|Z_{EL}|$  plays a crucial role in the biosensing abilities of the device. Indeed, Figure 5.2(e) depicts the increase in the number of electrodes that present the impedance magnitude plateau attributed to the cell presence. Similarly, Figure 5.2(f) shows the phase spectra with more electrodes presenting a peak due to the existence of the tissue layer.

Most importantly, there seems to be a critical impedance ratio value  $|Z_{MEM}| / |Z_{EL}|$  that signifies the transition from the non-sensing regime (that corresponds to the smallest electrode, size  $50 \mu\text{m} \times 50 \mu\text{m}$ ) to the sensing regime (that corresponds to the largest electrode, size  $10000 \mu\text{m} \times 10000 \mu\text{m}$ ). In particular, Figure 5.3(a) reveals that for the  $50 \mu\text{m} \times 50 \mu\text{m}$  electrode (non-sensing regime) there is no obvious difference between the impedance spectrum with and without the presence of cells. This implies that the biological tissue is literally invisible to the biosensor. Figure 5.3(b) on the other hand, illustrates that for the  $10000 \mu\text{m} \times 10000 \mu\text{m}$  electrode (sensing regime) the situation changes drastically since the presence of the tissue dramatically alters the electrode's spectrum.

In order to determine the transition requirement, an analytical formula for estimating the impedance magnitude  $|Z|$  as a function of frequency  $f$  was derived based on the four-element equivalent circuit presented in Figure 5.1(b). The formula provides the impedance magnitude  $|Z|$  and the corresponding phase  $\varphi$  for different electrode sizes  $\alpha$  and different PEDOT:PSS thicknesses  $d$  (*Supporting Information of Chapter 5*). For the impedance magnitude  $|Z|$ :

$$|Z| = \sqrt{\left(\left(\frac{\rho \ln 4}{\pi \alpha}\right)^2 + \frac{R_{MEM}}{1 + (2\pi f R_{MEM} C_{MEM})^2}\right)^2 + \left(\frac{1}{2\pi f C^* \alpha^2 d} + \frac{2\pi f R_{MEM}^2 C_{MEM}}{1 + (2\pi f R_{MEM} C_{MEM})^2}\right)^2} \quad (5.1)$$

while the phase  $\varphi$  is:

$$\varphi = \tan^{-1} \left( \frac{\frac{1}{2\pi f C^* \alpha^2 d} + \frac{\omega R_{MEM}^2 C_{MEM}}{1 + (R_{MEM} C_{MEM} 2\pi f)^2}}{\frac{\rho \ln 4}{\pi \alpha} + \frac{R_{MEM}}{1 + (R_{MEM} C_{MEM} 2\pi f)^2}} \right) \quad (5.2)$$

where  $\rho$  is the solution resistivity,  $\alpha$  the side of the square electrode,  $d$  the film thickness,  $f$  the frequency,  $C^*$  the capacitance per volume of the conducting polymer (for PEDOT:PSS in our case),  $R_{MEM}$  the ohmic resistance of the tissue layer and  $C_{MEM}$  the capacitance at the of tissue cell layer. For this particular study (i.e., for a given tissue), the degrees of freedom can be narrowed down to

two, that is the electrode side  $\alpha$  and the film thickness  $t$ , since for Caco-2 cell layers the values for the resistance and the capacitance are  $R_{MEM} = 400 \Omega$  and  $C_{MEM} = 5 \times 10^{-6} \text{ F}$ , respectively, as obtained from fitting to experimental measurements as well as from data in the literature<sup>[159]</sup>. The capacitance per volume  $C^*$  of PEDOT:PSS has already been estimated to  $39 \text{ F cm}^{-3}$ <sup>[160]</sup>. Therefore Figure 5.3(c) plots the impedance magnitude  $|Z| - f$  for different electrode dimensions based on Equation (5.1). The PEDOT:PSS film thickness was kept fixed at  $d = 100 \text{ nm}$ . The simulated results show that there is a curve (signified by the red stars) which divides the  $|Z| - f$  plane in two regimes. In the upper regime where  $|Z_{MEM}| < |Z_{EL}|$  the curves resemble the typical curves of PEDOT:PSS electrodes in an electrolyte solution. In particular, a high frequency resistive part and a lower frequency capacitive part constitute the plot with no evidence of the tissue shown. In the lower regime though, where  $|Z_{MEM}| > |Z_{EL}|$ , the curves exhibit a characteristic plateau which corresponds to the presence of the Caco-2 layer. In addition, the transition between these regions takes place for an electrode with impedance magnitude value similar to the one of the biological tissue barrier  $|Z_{MEM}| \approx |Z_{EL}|$ .

Consequently, the necessary condition for tuning the device sensing ability should be:

$$|Z_{MEM}| \geq |Z_{EL}| \quad (5.3)$$

$$\lambda = \frac{|Z_{MEM}|}{|Z_{EL}|} \geq 1 \quad (5.4)$$

For the under-study system, the function of the absolute difference between the impedance magnitude of the tissue and the electrode  $||Z_{MEM}| - |Z_{EL}||$  presents a minimum value in a logarithmic plot and for a size of  $\sim 1800 \mu\text{m}$  (Figure S5.1, *Supporting information 5.4*). Greater sized electrodes are able to successfully sense the biological tissue while smaller ones are not. The above conditions are further supported by the experimental measurements in Figure 5.3(d). The impedance spectra of electrodes of different sizes, and consequently of different impedance magnitude values, are presented showing that the ratio  $\lambda$  should be greater than 1 in order for the electrode to be able to record. In particular, when  $|Z_{MEM}| < |Z_{EL}|$  ( $1000 \mu\text{m} \times 1000 \mu\text{m}$  electrode) the tissue barrier layer is not detectable. A critical point appears for the  $2000 \mu\text{m} \times 2000 \mu\text{m}$  electrode due to the fact that for this size  $|Z_{MEM}| \approx |Z_{EL}|$ . Finally, for  $|Z_{MEM}| > |Z_{EL}|$  ( $5000 \mu\text{m} \times 5000 \mu\text{m}$  electrode) the system is properly tuned and consequently able to sense the presence of the cells.

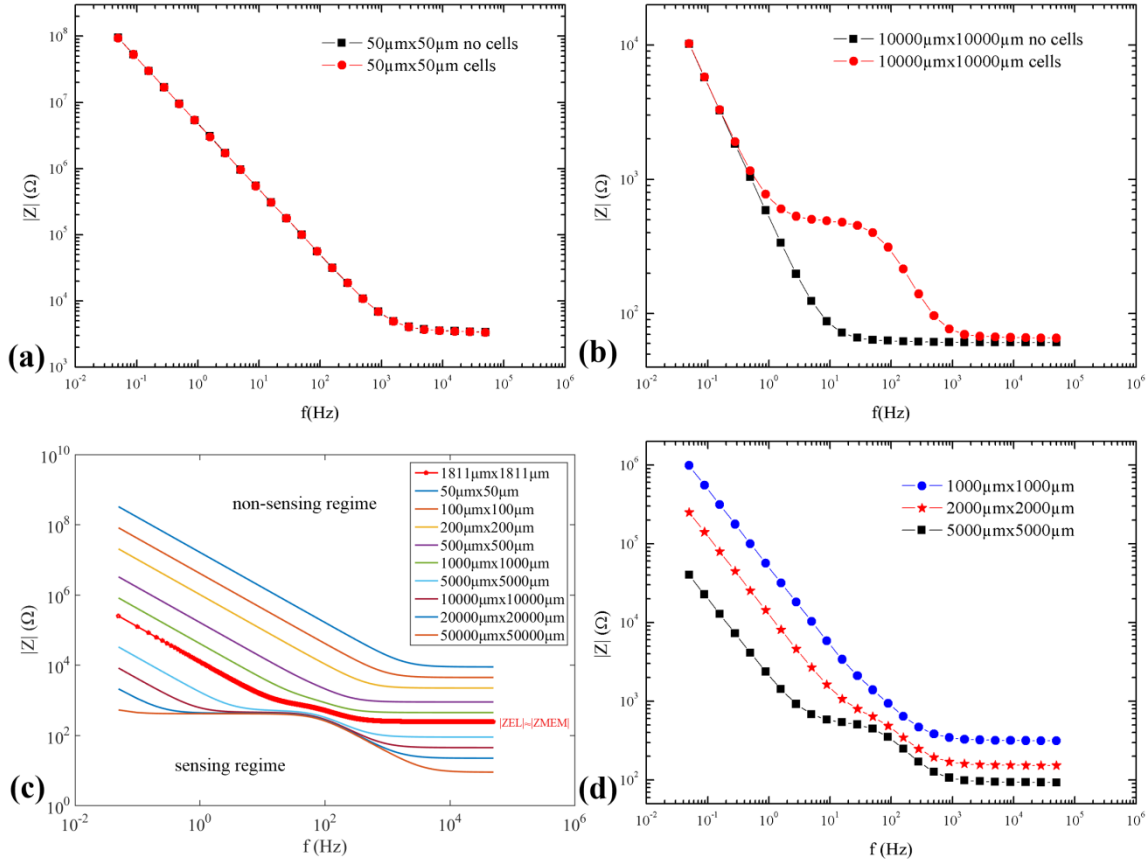


**FIGURE 5.3.** EXPERIMENTAL MEASUREMENTS AND SIMULATION OF THE IMPEDANCE MAGNITUDE  $|Z|$  OF VARIOUS SIZED ELECTRODES OVER FREQUENCY: **a)** The impedance spectrum of the smallest used electrode ( $50\mu\text{m} \times 50\mu\text{m}$ ) remains virtually unaffected by the presence of the cell layer. **b)** Nevertheless, the presence of the tissue has an obvious effect on the greatest used electrode ( $10000\mu\text{m} \times 10000\mu\text{m}$ ) as it alters noticeably its impedance spectrum. **c)** Simulation of the impedance spectra of the tissue barrier/electrode ensemble for various electrode sizes with the use of Equation (5.1). While the impedance magnitude of the electrode  $|Z_{EL}|$  is greater than that of the tissue barrier  $|Z_{MEM}|$  the latter is virtually invisible to the former. For  $|Z_{EL}|$  smaller than  $|Z_{MEM}|$  a plateau emerges. The value of this plateau corresponds to the TEER obtained cell resistance  $R_{MEM}$ . The transition from the non-sensing to the sensing regime goes through an electrode size with impedance value  $|Z_{EL}|$  almost equal to  $|Z_{MEM}|$  (transition electrode size). The estimated value of the electrode size that satisfies this equality is about  $1800\mu\text{m}$  (Supporting Information 5.4). **d)** Experimental data that support the above. The  $2000\mu\text{m} \times 2000\mu\text{m}$  electrode has a size that satisfies the impedance ratio requirement ( $\lambda \approx 1$ ) for the transition from the non-sensing ( $1000\mu\text{m} \times 1000\mu\text{m}$ ) to the sensing ( $5000\mu\text{m} \times 5000\mu\text{m}$ ) electrode.



### 5.3. Summary of Chapter 5

In conclusion, in this chapter we demonstrated how the impedance ratio,  $\lambda = |Z_{\text{MEM}}| / |Z_{\text{EL}}|$ , between a biological tissue and an electrode biosensor affects the sensing ability of the latter. The analysis was conducted with the help of IS while the impedance of the sensing device was systematically changed by varying its size. The presence of the tissue barrier was confirmed with the appearance of a plateau as expected by the literature. A simple four element circuit  $R_s - C_{\text{EL}} - R_{\text{MEM}} // C_{\text{MEM}}$  was proved adequate to model the system resulting into an analytical formula for the impedance as a function of frequency. The impedance magnitude for different electrode areas was simulated over frequency and revealed a transition from a non-sensing to a sensing regime. Critical parameter for this transition is the ratio  $\lambda$  as it turned out that for values of the electrode impedance  $|Z_{\text{EL}}|$  greater than the values of the tissue layer impedance  $|Z_{\text{MEM}}|$  the electrodes did not present any biosensing competence. As  $|Z_{\text{EL}}|$  decreased, due to the increase of their area, the electrodes disclosed their recording ability exactly when their impedance became smaller than the one of the tissue cell barrier. Therefore a  $\lambda$  value greater than 1 should be targeted for improved biosensing efficiency. Importantly, as the  $R_s - C_{\text{EL}}$  equivalent circuit models both PEDOT:PSS-coated electrodes and OECTs of the same film thickness, this conclusion is valid for both of these devices. The results of this work provide guidelines for the design of impedance-based sensors and for the optimization of their sensing ability.

## 5.4. Supporting Information of Chapter 5

### Analytical Formula

R – C circuit:

For the R – C circuit that models the complex impedance  $Z$  of an electrode in an electrolyte is given by Equation (S5.1):

$$Z_{EL} = R_s + \frac{1}{i\omega C_{EL}} = R_s - i \frac{1}{\omega C_{EL}} = R_s - i \frac{1}{2\pi f C_{EL}} \quad (S5.1)$$

where  $R_s$  is the solution spreading resistance ( $\Omega$ ),  $\omega$  the angular frequency (rad/s),  $f$  the frequency (Hz) and  $C_{EL}$  the capacitance at the electrode/electrolyte interface (F).

R // C circuit:

For the R // C circuit that models the tissue barrier the complex impedance  $Z$  is given by Equation (S5.2):

$$\begin{aligned} \frac{1}{Z_{MEM}} &= \frac{1}{R_{MEM}} + \frac{1}{\frac{1}{i\omega C_{MEM}}} = \frac{1}{R_{MEM}} + i\omega C_{MEM} \\ \frac{1}{Z_{MEM}} &= \frac{1 + i\omega R_{MEM} C_{MEM}}{R_{MEM}} \\ Z_{MEM} &= \frac{R_{MEM}}{1 + iR_{MEM} C_{MEM} \omega} \\ Z_{MEM} &= \frac{R_{MEM}(1 - iR_{MEM} C_{MEM} \omega)}{1^2 + (R_{MEM} C_{MEM} \omega)^2} \\ Z_{MEM} &= \frac{R_{MEM}}{1 + (R_{MEM} C_{MEM} \omega)^2} - i \frac{\omega R_{MEM}^2 C_{MEM}}{1 + (R_{MEM} C_{MEM} \omega)^2} \\ Z_{MEM} &= \frac{R_{MEM}}{1 + (R_{MEM} C_{MEM} 2\pi f)^2} - i \frac{\omega R_{MEM}^2 C_{MEM}}{1 + (R_{MEM} C_{MEM} 2\pi f)^2} \end{aligned} \quad (S5.2)$$

where  $R_{MEM}$  is ohmic resistance of tissue layer (e.g., Caco-2 cell layer in this work) ( $\Omega$ ),  $\omega$  the angular frequency (rad/s),  $f$  the frequency (Hz) and  $C_{MEM}$  the capacitance at the of the tissue layer (F).

R – C – R // C circuit:

The total impedance of the electrode/ Caco-2 cell layer ensemble is then given by:

$$Z = Z_{EL} + Z_{MEM}$$

$$Z = R_s - i \frac{1}{2\pi f C_{EL}} + \frac{R_{MEM}}{1 + (R_{MEM} C_{MEM} 2\pi f)^2} - i \frac{\omega R_{MEM}^2 C_{MEM}}{1 + (R_{MEM} C_{MEM} 2\pi f)^2}$$

$$Z = R_s + \frac{R_{MEM}}{1 + (R_{MEM} C_{MEM} 2\pi f)^2} - i \left( \frac{1}{2\pi f C_{EL}} + \frac{\omega R_{MEM}^2 C_{MEM}}{1 + (R_{MEM} C_{MEM} 2\pi f)^2} \right) \quad (S5.3)$$

The impedance magnitude  $|Z|$  is given by the equation:

$$|Z| = \sqrt{\left( R_s + \frac{R_{MEM}}{1 + (R_{MEM} C_{MEM} 2\pi f)^2} \right)^2 + \left( \frac{1}{2\pi f C_{EL}} + \frac{\omega R_{MEM}^2 C_{MEM}}{1 + (R_{MEM} C_{MEM} 2\pi f)^2} \right)^2} \quad (S5.4)$$

As shown before for a square electrode of side  $\alpha$  the spreading resistance  $R_s$  is<sup>[163]</sup>:

$$R_s = \frac{\rho \ln 4}{\pi \alpha} \quad (S5.5)$$

where  $\rho$  is the solution resistivity. For 0.1 M NaCl solution  $\rho = 100 \Omega \cdot \text{cm}$ .

Furthermore, Rivnay *et. al.* have previously shown that the capacitance per volume  $C^*$  for PEDOT:PSS films is equal to<sup>[4]</sup>:

$$C^* = 39 \text{ F/cm}^3$$

By definition capacitance per volume  $C^*$  is:

$$C^* = \frac{C}{V}$$

and therefore for a square electrode of side  $\alpha$ ,  $C$  equals to:

$$C = C^* V = C^* \alpha^2 d \quad (S5.6)$$

where  $d$  is the film thickness.

Combining (S5.4), (S5.5) and (S5.6) we get for the impedance magnitude of a square electrode with side  $\alpha$ :

$$|Z| = \sqrt{\left(\frac{\rho \ln 4}{\pi a} + \frac{R_{MEM}}{1 + (R_{MEM} C_{MEM} 2\pi f)^2}\right)^2 + \left(\frac{1}{2\pi f C^* a^2 d} + \frac{\omega R_{MEM}^2 C_{MEM}}{1 + (R_{MEM} C_{MEM} 2\pi f)^2}\right)^2} \quad (S5.7)$$

Where  $\alpha$  is the electrode side,  $R_{MEM}$  the ohmic resistance of the tissue layer ( $\Omega$ ),  $f$  the frequency (Hz),  $C_{MEM}$  the capacitance at the of the tissue layer (F), and  $C^*$  the capacitance per volume (F/m<sup>3</sup>).

Equation (S5.7) provides the impedance magnitude  $|Z|$  of the conducting polymer-coated gold electrode/Caco-2 layer ensemble. In the case of PEDOT:PSS film by using  $C^* = 39 \text{ F/cm}^3$  we have:

$$|Z| = \sqrt{\left(\frac{\rho \ln 4}{\pi a} + \frac{R_{MEM}}{1 + (R_{MEM} C_{MEM} 2\pi f)^2}\right)^2 + \left(\frac{1}{2\pi f 39 a^2 d} + \frac{\omega R_{MEM}^2 C_{MEM}}{1 + (R_{MEM} C_{MEM} 2\pi f)^2}\right)^2} \quad (S5.8)$$

Concerning the Bode phase  $\varphi$  we have:

$$\varphi = \tan^{-1} \left( \frac{Z_{im}}{Z_{real}} \right) \quad (S5.9)$$

Equations (S5.3), (S5.5) and (S5.9) yield:

$$\varphi = \tan^{-1} \left( \frac{\frac{1}{2\pi f C^* a^2 d} + \frac{\omega R_{MEM}^2 C_{MEM}}{1 + (R_{MEM} C_{MEM} 2\pi f)^2}}{\frac{\rho \ln 4}{\pi a} + \frac{R_{MEM}}{1 + (R_{MEM} C_{MEM} 2\pi f)^2}} \right) \quad (S5.10)$$

where  $\alpha$  is the electrode side,  $\rho$  is the solution resistivity,  $C^*$  the capacitance per volume of the PEDOT:PSS film,  $R_{MEM}$  the ohmic resistance of the tissue layer ( $\Omega$ ),  $f$  the frequency (Hz) and  $C_{MEM}$  the capacitance at the of tissue cell layer (F).

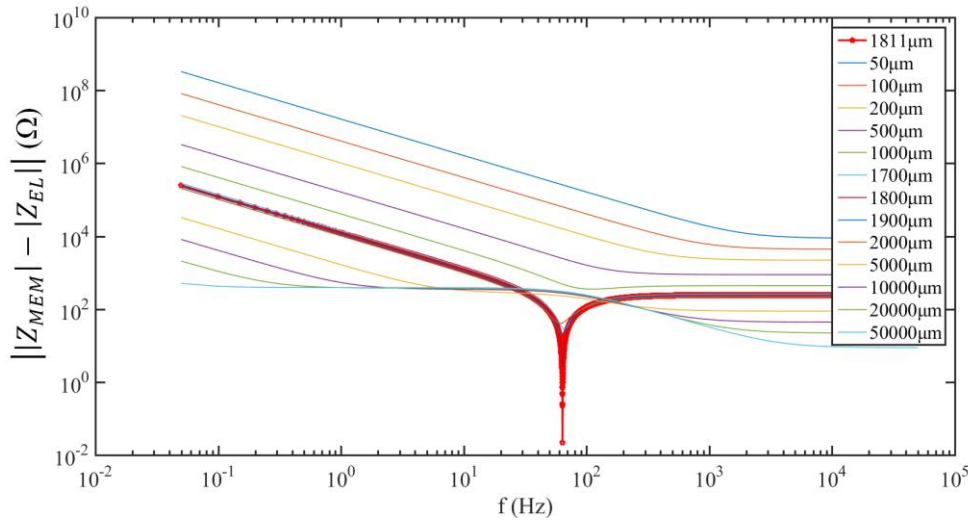


**FIGURE S5.1.** MAGNITUDE OF THE ABSOLUTE DIFFERENCE BETWEEN THE IMPEDANCE OF THE CELL LAYER MINUS THE IMPEDANCE OF ELECTRODES OF VARIOUS SIZES.

Figure S5.1 presents the magnitude of the absolute difference between the impedance magnitude  $||Z_{MEM}| - |Z_{EL}||$ . From the plot it can be extracted that the function  $||Z_{MEM}| - |Z_{EL}||$  presents a minimum value for an electrode size  $\sim 1800 \mu\text{m}$ . This is the point where the two impedances have almost the same value and consequently it is the point of transition from the non-sensing to the sensing regime. When the value of the electrode impedance becomes clearly greater than the value of the membrane impedance a plateau becomes apparent a fact indicative of the presence of the cell layer.



# Chapter 6

## Monitoring of Cell Layer Integrity with a Current-Driven Organic Electrochemical Transistor

The integrity of CaCo-2 cell barriers is investigated by organic electrochemical transistors (OECTs) in a current-driven configuration. Ion transport through cellular barriers via the paracellular pathway is blocked by tight junctions between adjacent cells. Rupturing its integrity by  $\text{H}_2\text{O}_2$  has been monitored by the change of the output voltage in the transfer characteristics. In this chapter, we demonstrate that by operating the OECT in a current-driven configuration, the sensitive and temporal resolution for monitoring the cell barrier integrity is strongly enhanced as compared to the OECT transient response measurement. As a result, current-driven OECTs are a useful tool to assess dynamic and critical changes in tight junctions, relevant for clinical applications as drug targeting and screening.

## 6.1. Introduction

Epithelial cells consist of a packed monolayer of cells and thereby provide a physical barrier to separate the organism from the external environment<sup>[9]</sup>. Several transport routes within these barriers exist.<sup>[9,92]</sup> As thoroughly described in the *Introduction* in *Chapter 1*, the paracellular pathway is limited by specialized complexes between adjacent cells, most of all by the tight junctions (TJs).<sup>[9,92]</sup> TJs consist are located at the apical domain of neighboring epithelial cells and regulate the paracellular passage of ions and small molecules as shown in Figure 6.1.<sup>[92]</sup> These transport routes within these barriers can be exploited for drug delivery for instance.<sup>[9,92]</sup> In the body a number of different barriers are present differing from each other by the tightness of the paracellular barrier.<sup>[92]</sup> The lower parts of the small intestine are determined as the leaky epithelial tissue due to a weak connection of the TJs.<sup>[92]</sup> Hence, the small intestine is considered as the major place for drug absorptions<sup>[92]</sup>, but also for points of application of pathogens and toxins, since barrier tissues can be disrupted by vicious organisms and compounds.<sup>[6,93,94]</sup> One possible way of disruption is targeting the TJs or other junctions between adjacent cells as shown in Figure 6.1. <sup>[6,9]</sup>This leads to an uncontrolled diffusion of ions, macromolecules and other cells, which can take up nutrients and electrolytes and harm the body.<sup>[6]</sup> Hence, the state of the cell barrier integrity acts as a precursor to dysfunction and disease, as well as can be used for a model for toxicological studies.<sup>[6,93,94]</sup> Furthermore, it can be exploited for drug delivery and drug targeting, as in the last decades the safe and reversible opening of these junctions for a controlled drug absorption and penetration has been thoroughly studied.<sup>[9,92]</sup> An efficient method for barrier tissue characterization will help to conceive models for a better understanding of how epithelial and endothelial barriers work and how to use this knowledge in drug testing and drug targeting, aiming among others for the replacement for animal testing in toxicological profiling.<sup>[6,9]</sup>

The tightness of the intercellular junctional complex is reflected on the transepithelial electrical resistance (TEER), measuring the paracellular ion flow.<sup>[6,9,92]</sup> TEER can be measured with an epithelial volt-ohm meter.<sup>[6]</sup> This measurement is easy to perform but suffers from slow temporal resolution and reproducibility.<sup>[6,8]</sup> A more optimized approach is the use of impedance spectroscopy to measure the resistance (= TEER) and capacitance ( $C_{MEM}$ ) of the cell membrane.<sup>[164,165]</sup> Despite its high validity, this method requires expensive equipment and is still limited by temporal resolution and sensitivity.<sup>[8,164,165]</sup> Other traditional techniques to assess the integrity of the cellular barrier are immunofluorescence and permeability assay.<sup>[8,92]</sup> Nevertheless, these methods identify themselves with high expenses in costs and time.<sup>[8,92]</sup> The organic electrochemical transistor (OECT) provides a unique platform for the integration of electronics and biological systems.<sup>[5]</sup> With the ability to conduct both electronic and ionic carriers, OECTs play a major role in health care and biomedical diagnostics.<sup>[5,14]</sup> In particular, using the OECT for assessing cell barrier integrity has been proven to be an attractive method in comparison to



traditional techniques.<sup>[6–8,166]</sup> By integrating the OECT with epithelial cells, minute variations in paracellular ion flow, caused by toxic compounds, has been detected.<sup>[7,93,94]</sup> A further enhancement of the sensitivity level of the OECTs would enable real-time detection of the integrity of TJs during disease and treatment. As shown in *Chapter 4 – High-Sensitivity Ion Detection at Low-Voltages with Current-Driven Organic Electrochemical Transistors*, the sensitivity in ion detection of aqueous electrolytes can be further enhanced and reaching the highest value ever reported so far for ion-sensitive transistors by using the OECT in the current-driven configuration.<sup>[83]</sup>

Here, we show the integration of epithelial cells with the OECT in the current-driven configuration to further enhance the sensitivity in monitoring the cell barrier integrity. The process of incorporating a healthy cell layer and rupturing its integrity by  $H_2O_2$ , has been monitored by the change of the output voltage in the transfer characteristics. For sensitivity, different peroxide concentrations have been used to evaluate the effect on the transfer characteristics as well as on the response times, in reference to the earlier stated OECT transient response method. Our approach has been optimized to allow higher sensitivity in direct comparison, emphasizing the OECT as a competitive measuring tool for cell barrier assessment in respect to the conventional methods.

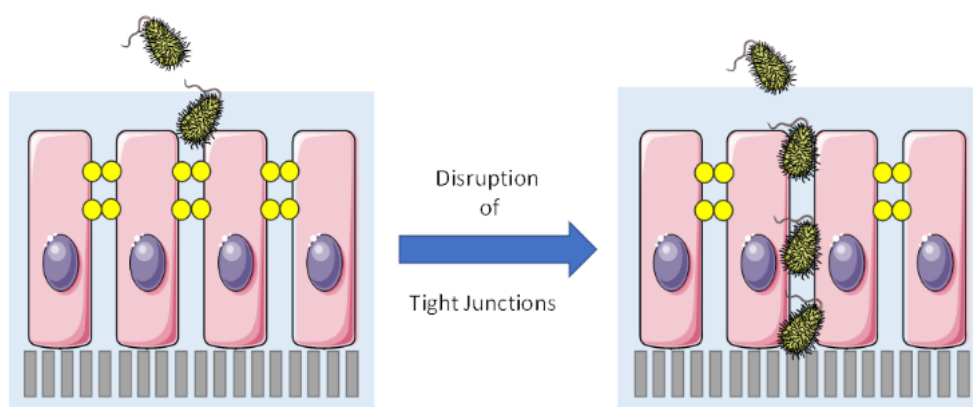


**FIGURE 6.1.** CARTOON OF A PACKED LAYER OF EPITHELIAL CELLS, CONNECTED BY TIGHT JUNCTIONS: TJ disruption can be the result of toxins and pathogens, here symbolized by bacterial components. Cartoon has been created by images of SMART.<sup>[13]</sup>

## 6.2. Results and Discussion

The OECT device structure with an integrated cell layer is shown in Figure 6.2(a) and resembles the typical 3-terminal transistor configuration of source, drain and gate. In the current-driven OECT, the device is connected in series with a current generator, as illustrated in Figure 6.2(b).<sup>[83,167]</sup> Analogous to *Chapter 4*, the input voltage  $V_{in}$  is applied at the gate and this

gives us the topology of  $V_{in} = V_G$ , enabling the control of the channel doping. The output voltage  $V_{out}$  is measured at the drain ( $V_{out} = V_D$ ).<sup>[83]</sup> By using the current generator, we force a current bias  $I_B$  ( $I_B = I_D$ ), and as a result we measure  $V_{out}$ .<sup>[83]</sup> Thus, the configuration can also be described as a voltage divider of the supply voltage  $V_{DD}$  of the transistor, defined by  $V_{out} = V_{DD} - I_B \cdot r_o$ .<sup>[84]</sup> Figure 6.2(c) shows typical transfer characteristics ( $V_{out}-V_{in}$ ) of a current-driven OEET for a series of  $I_B$ . By sweeping  $V_{in}$  from  $-0.2$  V to  $+0.7$  V,  $r_o$  increases due to the dedoping process of PEDOT:PSS. Starting with  $V_{out}$  close to  $+V_{DD}$ ,  $V_{out}$  eventually approaches the minimum supply voltage of  $-V_{DD}$ , as a consequence of the increased  $r_o$  at saturation. The minimum supply voltage of  $-0.4$  V is limited by the voltage-compliance of the current generator.

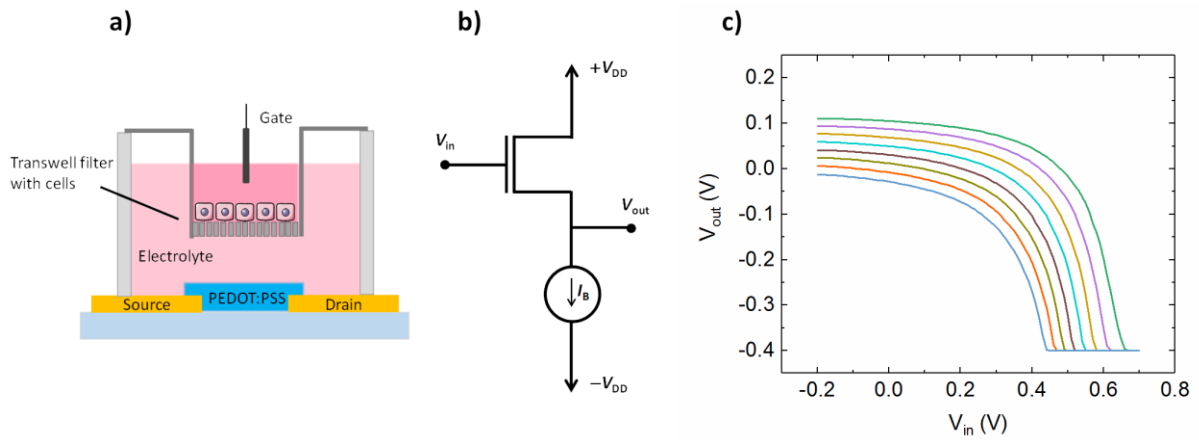


**FIGURE 6.2.** OEET AS A SENSOR FOR CELL BARRIER INTEGRITY: **a)** Device structure with an integrated Transwell filter with cells.<sup>[13]</sup> **b)** Schematic circuit of the current-driven configuration. **c)** Measured transfer characteristics of a current-driven OEET for  $I_B$  ranging from  $-0.7$  till  $-1.4$  mA (top to bottom) at  $V_{DD} = 0.2$  V. Device dimension were  $W = 2$  mm,  $L = 1$  mm. A Ag/AgCl gate electrode and EMEM cell culture medium as an electrolyte was used.

Here, we demonstrate the OEET in the current-driven configuration as a sensor for cell layer integrity using the Caco-2 cell line, a well-known model for the gastrointestinal barrier.<sup>[7,168]</sup> Incorporating a cell layer between the gate and the channel creates a barrier for passing ions that impedes the ion flow.<sup>[6]</sup> Figure 6.3(a) shows the integration of an intact layer of cells, which are tightly connected by TJs (depicted in yellow). This causes a shift of the ( $V_{out}-V_{in}$ )-transfer curve toward higher  $V_{out}$ . The high cell resistance  $R_{MEM}$  (= TEER) induces a low ionic flux and consequently higher  $V_{in}$  are needed to dedope the channel. Reactive oxygen species are known for their irreversible effect on TJs, inducing a disruption of the cell layer.<sup>[8,9]</sup> Thus, the addition of toxic compounds in the form of hydrogen peroxide ( $H_2O_2$ ), damages the TJs and finally leads to a cell layer opening<sup>[6,8]</sup>: TEER decreases and thereby lowers  $V_{out}$ , pulling the ( $V_{out}-V_{in}$ )-curve towards the starting condition, meaning the absence of cells (Figure 6.3(a)). For a better cell viability cell culture medium was used as the electrolyte.<sup>[168]</sup> Adding an aqueous  $H_2O_2$  solution dilutes the cell

culture medium, meaning changing the electrolyte's concentration and so its resistance  $R_{\text{MED}}$ . The current-driven OECT is highly sensitive to changes in the ion concentration, thus a very small shift of the  $(V_{\text{out}}-V_{\text{in}})$ -transfer curve according to the change in the switching voltage is observed in Figure 6.3(b).<sup>[83]</sup> Noting, that we define the switching voltage as the minimum  $V_{\text{in}}$  required to operate the OECT in saturation. No further shift over a period of 60 minutes is observed (Figure 6.3(b)), therefore this configuration is a reliable measuring method for assessing the cell barrier integrity.

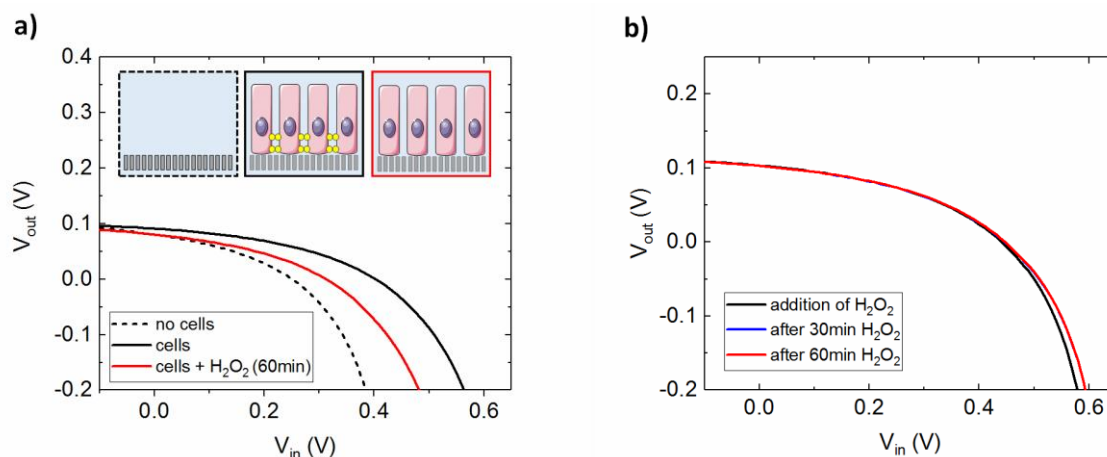


**FIGURE 6.3.** TRANSFER CHARACTERISTICS of the current-driven configured OECT monitoring the addition of 1 mM  $\text{H}_2\text{O}_2$  **a)** in the presence and **b)** absence of epithelial cells (control experiment). The inset in panel a) shows the Transwell filter in the absence of a cell layer (black dashed frame), a healthy cell layer with TJs (yellow, black frame) and a ruptured cell layer (red frame). The inset has been created by images of SMART.<sup>[13]</sup>

The most obvious and straightforward way to validate the sensitivity of the proposed method is the direct comparison with a similar method as a reference, published by Owens *et al.* in 2012.<sup>[6]</sup> In this particular work the transient response of the OECT was measured by pulsing  $V_G$ . Integrating the OECT with epithelial cells changes the paracellular ion flow and this has been affecting the speed of the transistor response till it reaches steady state, in the end resembled in the transient response. By using toxic compounds, the integrity of cellular barriers has been detected.<sup>[6]</sup> Hence, both methods were conducted using the same devices under the same conditions. Figure 6.4(a) demonstrates the cell layer disruption by using a rather high concentration of 5 mM of  $\text{H}_2\text{O}_2$  using the current-driven OECT: as shown before a significant shift of the  $(V_{\text{out}}-V_{\text{in}})$ -transfer curve is seen when the cell layer is integrated. An almost completely opening of the cell layer is achieved with  $\text{H}_2\text{O}_2$ , as the initial state of the characteristic curve is nearly reached after 60 minutes. In the reference method the transient response is measured. In this time the channel is dedoped, resembled in a modulation of  $I_D$  in Figure 6.4(b). The integration of a cell layer decreases the ion flux, in other words slows down the transistor response till it reaches steady state. A smaller modulation of  $I_D$  in the same pulse duration as before is the result

(Figure 6.4(b)). Adding  $\text{H}_2\text{O}_2$  in a concentration of 5 mM increases again the ion flow through the membrane, and therefore the modulation of  $I_D$ , reaching towards the initial modulation in the absence of cells. Figure 6.4(c, d) show the results for a lower concentration of 1 mM  $\text{H}_2\text{O}_2$ . While a smaller but still detectable shift in the  $(V_{\text{out}}-V_{\text{in}})$ -transfer curve is obtained with the current-driven OECT, no changes are visible with the reference method. Control experiments with  $\text{H}_2\text{O}_2$  are shown in Figure S6.1 in the *Supporting Information of Chapter 6*, to confirm that no damage of the reactive oxygen species has occurred with neither the gate electrode nor the conductive polymer.

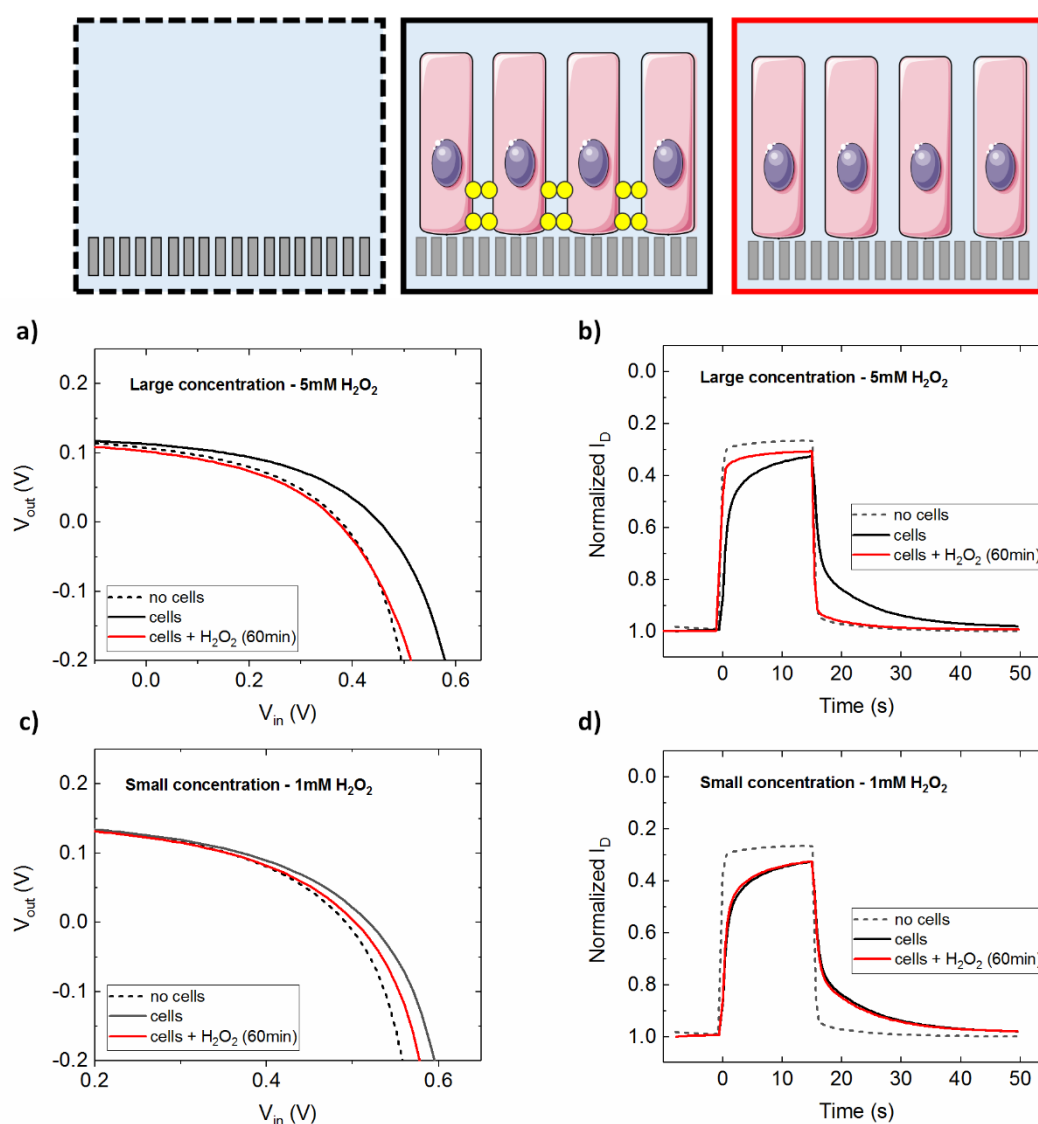


**FIGURE 6.4.** OECT AS A CELL BARRIER INTEGRITY SENSOR FOR  $\text{H}_2\text{O}_2$ : The cartoon shows the Transwell filter in the absence of a cell layer (black dashed frame) and the condition of the cell layer (black and red frame). The integrity of the cellular barrier is symbolized by the presence and absence of TJs (yellow). The OECT response in the **a)** current-driven and **b)** in the standard configuration in the absence and presence of cells adding 5 mM  $\text{H}_2\text{O}_2$ . The transfer characteristics in the current-driven configuration with and without cells adding 1 mM  $\text{H}_2\text{O}_2$  is shown in **c)**, while the analogues transient response in the reference method is seen in **d)**. The inset has been created by images of SMART.<sup>[13]</sup>

In the current driven OECT, we defined the characteristic response by  $V_{in}$  at  $V_{out} = -0.2$  V in small time intervals. For the reference method, the response time or the time constant of the system was defined by fitting the output current  $I_D$  with a two exponential decay function (mathematical derivation is described in the *Supporting Information 6.4* and Figure S6.2). For or both techniques the extracted responses were normalized for comparison purposes.

For the higher concentration (5 mM  $H_2O_2$ ) a cell barrier rupture is observed in both cases, revealing an abrupt cell opening. This is quantified as a change of 80–90% of the normalized device response (Figure 6.5(a)). While the current-driven configuration shows already after 5 minutes a significant effect of 60% by adding  $H_2O_2$  and reaching after only 10 minutes a steady state of 80% ruptured layer, the reference method shows a delay of 10 minutes before reaching after 30 minutes the final state of 90% cell opening (Figure 6.5(a)). For lower concentration (1 mM  $H_2O_2$ ) this picture completely changes. While in the reference method no change is detected, two concurrently processes can be detected in the current-driven configuration. Due to the slow cell opening process, the dilution of the electrolyte is eventually revealed. Increasing the electrolyte's resistance, higher  $V_{in}$  are needed to dedope the channel, leading to a shift of the  $(V_{out}-V_{in})$ -curve to the right. This is resembled by a decreased normalized response. After 10 minutes the rupture of the TJs slowly progresses. Destroying the TJs and decreasing TEER, affects the  $(V_{out}-V_{in})$ -curves by continually shifting to the left. In Figure 6.5(b), this is expressed by an increasing normalized response, eventually reaching 60% cell opening, highlighting the partial cell opening. Overall, for low  $H_2O_2$  concentrations no detectable change in response time is observed, while lower concentrations emphasize the higher sensitivity that only achieved in the current-driven configuration. The OECTs measurements were amended by simple TEER measurements by a handheld epithelial volt-ohm meter. Figure S6.3 in the *Supporting Information 6.4* states overall the same trend in the normalized response for both cases.

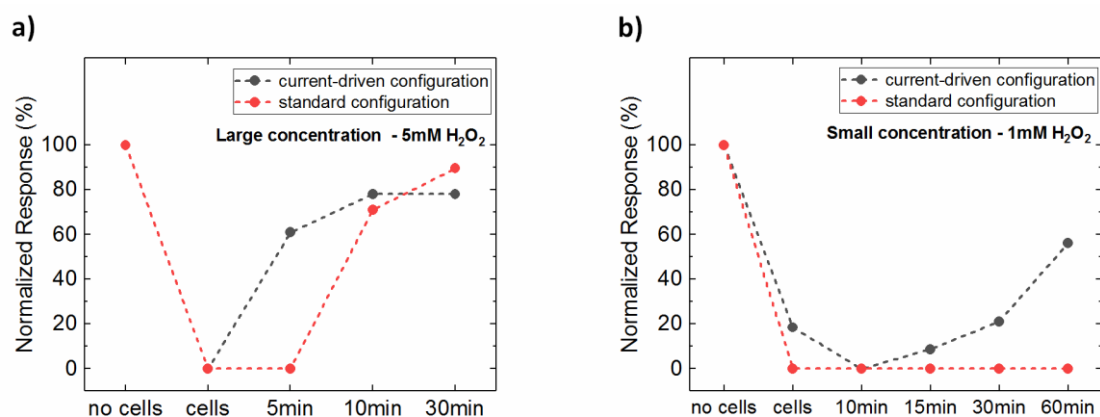


**FIGURE 6.5.** THE CORRESPONDING NORMALIZED RESPONSE of the OECT in the standard (response time of the OECT) and current-driven configuration (shift of input voltage  $V_{in}$ ) after the addition of  $H_2O_2$  for **a)** 5 mM and **b)** 1 mM. The response in the standard configuration is defined as the time constant of the output current  $I_D$ . The response of the current-driven OECT is defined by the shift of  $V_{in}$  at  $V_{out} = -0.2$  V, while the dielectric relaxation time is used for the transient response in the reference method.

It should be noted, that one requirement for using the reference OECT method as a sensor for cell barrier integrity is the need to increase the effective cell layer resistance of the Transwell filter.<sup>[6,160]</sup> Expressed in an equivalent circuit, the integration of a cell layer is represented in an additional resistor  $R_{MEM}$  (= TEER) and capacitor  $C_{MEM}$  in parallel, which are connected in series with the capacitor of the channel  $C_d$  and the resistor of the electrolyte medium  $R_{MEM}$ .<sup>[6,160]</sup> By decreasing the cell filter area with polydimethylsiloxane (PDMS), the effective cell layer resistance can be increased. In this way the change in resistance caused by the cell layer disruption is amplified and after all detectable. This requirement is not necessary for the current-driven configuration as shown in Figure S6.4 in the *Supporting Information 6.4*. Modifying the cell filter with PDMS is time consuming, causes a higher risk for contamination and errors, and thus lowers reproducibility. Overall, the current-driven configuration not only enhances the sensitivity with higher temporal resolution than the reference method, but also has advantages in terms of fabrication and execution in measuring the barrier integrity.

TJs are of dynamic nature, changing and adjusting rapidly their structure according to physiological stimuli. Thus conventional measurement techniques have been limited by their invasive, elaborate and slow method.<sup>[6,8]</sup> That is why the key advantage of the OECT is the ability to dynamically assess the barrier properties in a very sensitive matter and depth.<sup>[6]</sup> Providing a label-free and non-invasive detection of toxic compound and pathogens, OECT are believed to have a strong potential for toxicological purposes and clinical applications.<sup>[5,6,64]</sup> The reversible opening of epithelial TJs and enhancing paracellular permeation by TJ modulators (e.g. chitosan) have been shown great potential in improving drug delivery.<sup>[9,92]</sup> Conventional methods like immunofluorescence staining and microscopic TEM have successfully yielded detailed structural information but are strongly limited by temporal resolution.<sup>[8,92]</sup> OECT would offer a fast and

sensitive way to monitor cellular barrier dynamics, which could promote in combination with other measurements technologies the understanding and optimization of TJ modulators and how to exploit them for disease therapies and drug delivery.

### **6.3. Summary of Chapter 6**

In summary, OECTs have been shown as suitable sensors for cell barrier integrity, differentiating from other traditional techniques due to their low cost, temporal resolution and sensitivity. Using the OECT in the current-driven configuration has already demonstrated to have the highest sensitivity in ion detection at low voltages. Here, by combining the current-driven transistor configuration with an integrated cell layer, has indeed achieved higher sensitivity and temporal resolution in detecting disruption in barrier function. The process of the cell opening can be detected in detail as a variation of the output voltage. We believe that by tuning the device towards greater sensitivity, this method will have high potential for fundamental research, as well as applications in biosensing. The current-driven OECT is a useful method to assess dynamic and critical changes in TJs, achieving a depth of information, useful for clinical applications as drug targeting and screening.

## 6.4. Supporting Information of Chapter 6

Control experiments were conducted with different  $\text{H}_2\text{O}_2$  concentrations to evaluate possible parasitic effects of the reactive oxygen species on the channel or the gate electrode. Figure S6.1(a, b) show the transient response of the OECT in the standard configuration after the addition of 1 mM and 5 mM of an aqueous solution of  $\text{H}_2\text{O}_2$ , observing no noticeable effect. In the current-driven OECT a small change in the transfer curve are observed for both concentrations at the beginning, resembling the small dilution of the electrolyte, affecting the electrolyte's resistance (Figure S6.1(c, d)). Despite the adjustment of the change in the electrolyte's resistance, no further shifts occurred, confirming the negligible effect of  $\text{H}_2\text{O}_2$  on the device behavior (reference experiments).

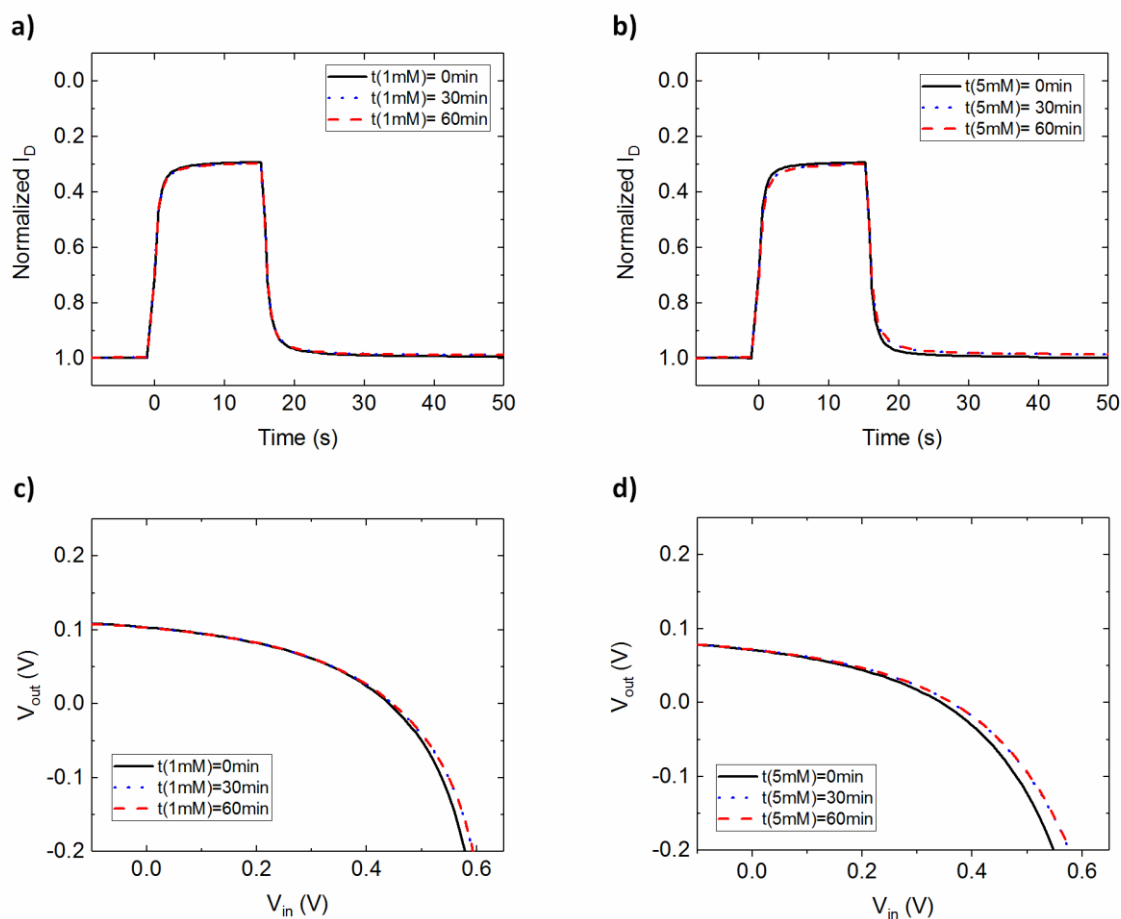


**FIGURE S6.1.** CONTROL EXPERIMENTS WITH  $\text{H}_2\text{O}_2$ : OECT transient response in the standard configuration with **a)** 1 mM and **b)** 5 mM  $\text{H}_2\text{O}_2$ . Transfer Characteristics of a current-driven OECT with the addition of **c)** 1 mM and **d)** 5 mM  $\text{H}_2\text{O}_2$ . Device dimension were  $W = 2\text{ mm}$ ,  $L = 1\text{ mm}$ . A Ag/AgCl gate electrode and EMEM cell culture medium as an electrolyte was used.



To extract the response time of the output, drain current  $I_D$  in the standard OECT configuration, we performed fitting of the  $I_D$  vs time characteristic with a double exponential decay (Equation (S6.1)). In Equation (S6.1),  $t$  is time,  $t_n$  the time constant of the  $n$ -th exponential decay,  $A_n$  the pre-exponential factor and  $y_0$  an offset that expresses the background current response (here, a series of two exponential decays is used). The Fourier Transform  $FT[y]$  of the multi-exponential response  $y$  of Equation (S6.1) in frequency domain is given by Equation (S6.2), with  $\omega$  the radial frequency and the  $i$  the imaginary unit. The imaginary part of Equation (S6.2), expresses the losses of the system, and from the peak of the imaginary part as a function of time,  $FT[y]''$  vs  $t$ , the response time of the output  $I_D$  is defined (Figure S6.2).<sup>[169]</sup>

$$y = \sum_n A_n e^{-\frac{t}{t_n}} + y_0 \quad (S6.1)$$

$$FT[y] = \sum_n \frac{A_n}{(\frac{1}{t_n} + i\omega)} \quad (S6.2)$$

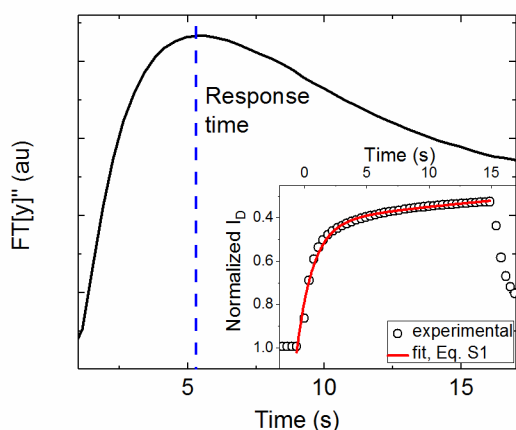


**FIGURE S6.2.** RESPONSE TIME OF THE OECT: the extracted response time of the OECT when integrating a cell layer. The dashed blue line defines the response time which corresponds to the maximum of the  $FT[y]''$  function. The inset shows the transient response to a  $V_G$  pulse of 300 mV at  $V_D = -0.1$  V with an integrating cell layer. Device dimension were  $W = 2$  mm,  $L = 1$  mm. A Ag/AgCl gate electrode and EMEM cell culture medium as an electrolyte was used.

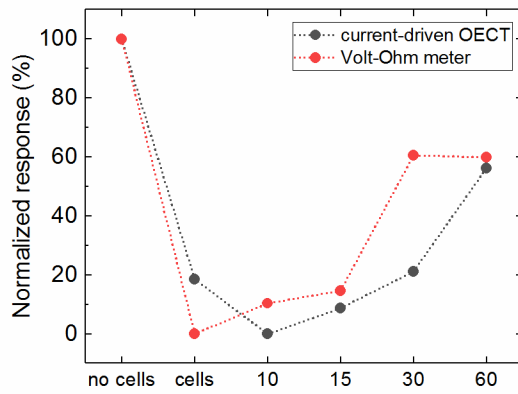


**FIGURE S6.3.** NORMALIZED RESPONSE of the TJ disruption by  $\text{H}_2\text{O}_2$ , measured with a current-driven OECT and a handheld epithelial volt-ohm meter. The cell layer integrity was ruptured by adding 1 mM of  $\text{H}_2\text{O}_2$  and measured over time.

Integrating a cell layer and opening the cell layer influences the effective cell layer resistance  $R_{\text{MEM}}$  (=TEER). In order to detect such changes,  $R_{\text{MEM}}$  has to be high in relation to  $R_{\text{MED}}$  and  $R_{\text{d}}$ .<sup>[6,160]</sup> For an increased  $R_{\text{MEM}}$ , the cell area of the Transwell filter can be decreased with PDMS. Measuring the transient response with an unmodified Transwell filter, shows no detectable change, not even when integrating the cell layer (Figure S6.(4)a). In the current-driven OECT the presence of cells can be observed by a significant shift in the transfer curve, as well as for the TJ disruption, despite an unmodified  $R_{\text{MEM}}$  (Figure S6.4(b)).

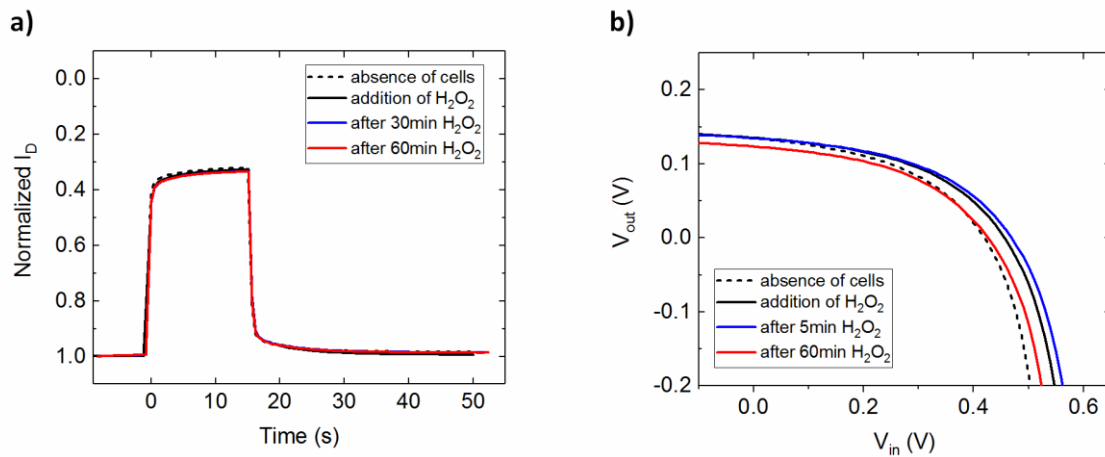


**FIGURE S6.4.** EFFECT OF A NON-INCREASED EFFECTIVE CELL LAYER RESISTANCE: **a)** Transient response in the standard configuration and **b)** current-driven transfer characteristics of an unmodified Transwell filter with cells before and after adding 1 mM  $\text{H}_2\text{O}_2$ .

# Chapter 7

## Reversible Opening of Membranous Barriers by Tight Junction Modulators

Novel tight junction (TJ) modulators can directly target TJ proteins and reversibly enhance their paracellular permeability with less toxicity, expanding the possibilities of drug delivery across the epithelial barrier. The temporary effect on the TJ assembly of gastrointestinal Caco-2 cells, induced by TJ modulators, is investigated by the organic electrochemical transistor (OECT). As TJs regulate the passage of ions across the cellular barrier and influence the ion permeability, the rupture of its integrity has been directly monitored by the change in the transient response of the OECT, since the ion flow is reflected in the output current. Here, we show the concentration-dependent reversible opening of TJs upon the addition of modulator poly-L-lysine, monitored with greater sensitivity and temporal resolution compared to traditional techniques. As a result, the OECT holds great potential as a useful tool to assess the dynamic changes of cell layer integrity, relevant for improved drug delivery systems across epithelial barriers.

## 7.1. Introduction

The emerging number of new drug types, like peptides drugs, has triggered the demand of novel drug delivery systems.<sup>[170]</sup> Traditional systems have to cope with the metabolism of many drugs in the gastrointestinal tract or during first-pass hepatic metabolism.<sup>[170]</sup> The development of new transepithelial drug delivery routes may increase the availability of the new generation of peptide drugs.<sup>[170]</sup> The ideal drug delivery system should be capable to penetrate through various biological barriers, release the drug in a controlled way at the target place of its therapeutic relevance and subsequently safely degrade.<sup>[171]</sup> Furthermore, it should be biocompatible, biodegradable and non-immunogenic.<sup>[171]</sup>

The paracellular permeability of epithelial and endothelial barriers is the most critical factor in drug transport.<sup>[9]</sup> The penetration of biological barriers is restricted or completely blocked by junctional complexes.<sup>[9,92,171]</sup> Tight junctions (TJs), one group of the junctional complexes in epithelial and endothelial cells, seal the paracellular gap between adjacent cells and regulate the controlled passage of ions and small molecules through this barrier.<sup>[90]</sup> TJ modulators are able to modify the intercellular junctions and paracellular permeability of various epithelial and endothelial barriers, including the gastrointestinal tract, the airway epithelium, skin, and the blood-brain barrier, pointing out the major barriers for drug delivery.<sup>[9]</sup> TJ modulators developed in the last 40 years reacted rather in an unspecific and uncontrolled way with effective doses close to toxicity.<sup>[9]</sup> The discovery of the transmembrane proteins of TJs and their signaling pathways regulating TJ functions in the last 25 years, has not only led to the improved knowledge of how epithelial barriers work, but also to the development of novel TJ modulators.<sup>[9]</sup> These modulators can be potentially used to safely and reversible open TJs to increase paracellular transport and drug delivery of hydrophilic compounds and biopharmaceuticals with less toxicity than previous examples, defining the long-time goal in pharmaceutical and biomedical research.<sup>[9,92]</sup>

More precisely, TJs consist of a complex of transmembrane (e.g. occludin, , tricellulin, claudin and JAMs) and cytoplasmic (e.g. ZO-1, ZO-2, ZO-3) proteins, which can be potential targets of TJ modulators.<sup>[9,92,170]</sup> TJs and their proteins are depicted at the apical side of the image in Figure 7.1. Modulators can also target transmembrane adherent junction proteins.<sup>[9]</sup> Like TJs, adherens junctions (AJ) are also part of the junctional complexes in epithelial and endothelial barriers, which regulate cell-cell contacts as well as barrier permeability.<sup>[90]</sup> Furthermore, TJ modulators can target signaling pathways that regulate TJ functions, as well as lipid rafts and membrane microdomains.<sup>[9]</sup>

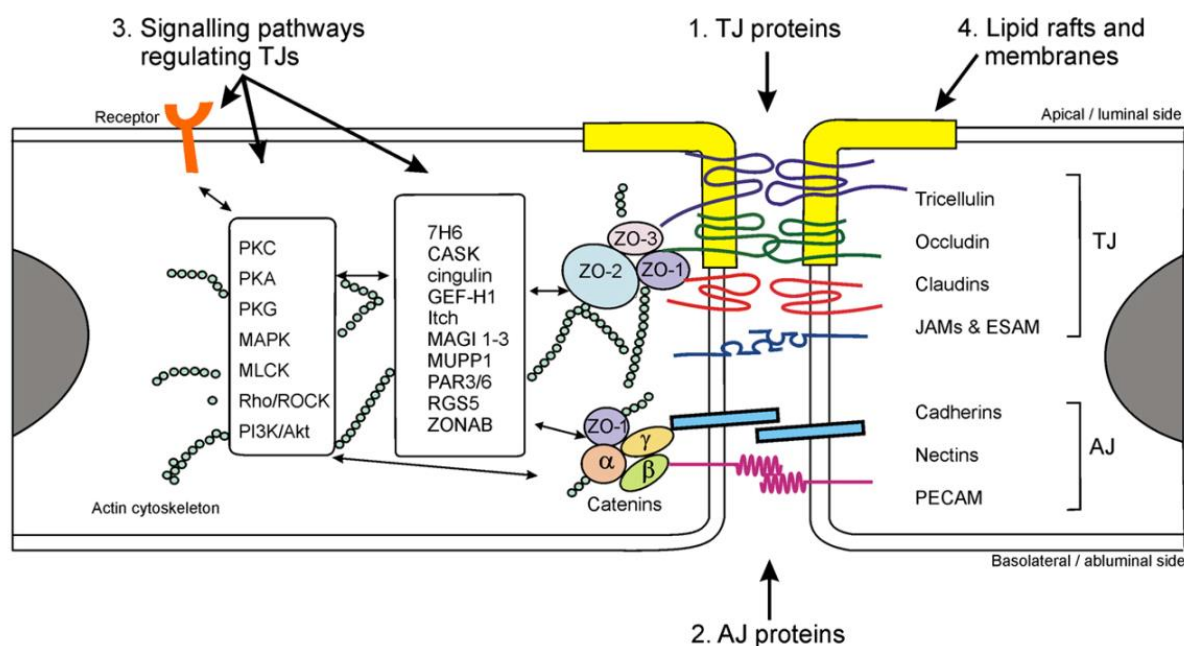


**FIGURE 7.1.** TIGHT JUNCTION MODULATORS AND THEIR TARGETS: Schematic model of TJs and AJs, including their proteins, as well as signaling pathways regulating TJs, and lipid rafts and membranes. Image adapted from reference.<sup>[9]</sup>

One possible way of TJ modulators to interfere, is the directly and specifically acting on extracellular loops of TJ proteins and TJ-associated membrane microdomains.<sup>[9]</sup> These modulator substances are peptides, enzymes or lipids and can be subjected to the safe and reversible opening of TJs for drug delivery.<sup>[9]</sup>

Yet another way of TJ modulating can be induced by absorption enhancers (AEs) and paracellular permeability enhancers (PPEs), to reversibly open cell layers in a controlled way to enhance drug delivery.<sup>[9]</sup> AEs and PPEs used to react in a rather unspecific way, due to the small knowledge of the molecular composition and functions of TJs.<sup>[9]</sup> Now there is a variety of AEs and PPEs used for the opening of TJs in epithelial barriers of peripheral organs or even at the blood–brain barrier.<sup>[9]</sup> Nevertheless, the effective doses of AEs are still close to toxicity.<sup>[9]</sup> Due to different morphological and molecular structures of barriers, AEs can be effective in one barrier, but non-effective in the other, or the local action can be different.<sup>[9]</sup> The list of studied modulator substances, involving test studies on organs/tissues/cells not only in epithelial barriers of peripheral organs but also on the blood–brain barriers is long and involves substances such as chelators, fatty acids (including modified fatty acids and phosphate esters), surfactants, cationic polymers, cyclodextrins and nitric oxide donors.<sup>[9]</sup>

However, Table 7.1 illustrates a number of promising modulators substances and their possible target and mechanisms. Thereby we particularly focused on studies on Caco-2 cells, a cell line, which has been thoroughly used as a well-known model for gastrointestinal epithelial tissues in this work.

**TABLE 7.1. TARGETS AND MODE OF ACTION OF MODULATORS IN EPITHELIAL BARRIERS:** The different TJ modulators haven been classified in chelators, fatty acids, cationic polymers and surfactants.<sup>[9]</sup>

Modulator	Possible Target	Studies	Tracer
<b>Chelators</b>			
EDTA /EGTA	Ca↓, PKC, AJ and TJ disassembly		
EDTA		In-vitro, Caco-2	carboxyfluorescein, PEG 4000, furosemid, FITC-dextran
<b>Fatty acids</b>			
Oleic acid	Lipid rafts, PKC, gap junction	In-vitro, Caco-2	TEER↓ mannitol
Sodium caprate	PLC, PI3, redistribution of TJ proteins	In-vitro, Caco-2	mannitol
<b>Cationic Polymers</b>			
Poly-L-Lysine	PKC, phospholipase D	In-vitro, Caco-2	TEER↓ inulin
Chitosan	PKC-α, redistribution of actin, occludin, ZO-1	In-vitro, Caco-2	TEER↓ inulin
<b>Surfactants</b>			
SDS	Actin reorganization, Ca↑, AP-1 and NF-Kb	In-vitro, Caco-2	TEER↓ mannitol
Bile salts	Ca↑, F-actin reorganization	In-vitro, Caco-2	TEER↓ mannitol, PEG

Chitosan (CS) and poly-L-lysine (PLL), belonging to the class of cationic polymers, have shown great potential in reversible opening of TJs in epithelial cell models.<sup>[9,92,170–174]</sup> Conventionally, CS has been used as food supplements to control overweight and hyperlipidemia.<sup>[172]</sup> Studies confirm the reduction of fat absorption in the intestine by binding fatty acids, triglycerides and bile acids.<sup>[172]</sup> CS and derivatives have been extensively investigated for drug delivery systems across dermal, gastrointestinal, nasal and pulmonary epithelial barriers, most of all due to the mucoadhesive properties, but as well due to their low toxicity and good water solubility.<sup>[9,171,172]</sup> CS induces a reversible TJ permeability by redistributing occludin, ZO-1 and the actin-cytoskeleton, involving the activation of Protein kinase C-α (PKC-α) in Caco-2 cells.<sup>[9]</sup> This effect has been monitored by transepithelial electrical resistance (TEER) and inulin as a marker for paracellular routes.<sup>[9]</sup> Furthermore, it has been shown that the non-toxic, soft-tissue compatible polysaccharide CS is involved in the translocation of transmembrane protein JAM-1, inducing a reversible TJ opening as well.<sup>[92]</sup> Though, the width of the opening is limited.<sup>[92]</sup> The passage of insoluble CS aggregates has shown to be restricted, as the transport of soluble excipients such as insulin is possible.<sup>[92]</sup> Based on the excellent modulating effect, CS derivatives are considered as promising candidates for enhanced drug delivery systems for clinical applications.<sup>[9]</sup>

Like CS, PLL has the ability to increase paracellular permeability on TJs as well, showing a temporary and reversible effect upon concentration dependency.<sup>[172,173]</sup> The effect is associated with a drop in TEER, induced by the redistribution of the F-actin cytoskeleton, as well as in the localization of tight junctional proteins.<sup>[9,172]</sup>

EDTA (ethylenediamine-N,N,N',N'-tetraacetic acid) and EGTA (ethylene glycol-bis(beta-aminoethyl ether)-N,N,N',N'-tetra-acetic acid) are the most well-known and commonly used chelators in chemistry and biology, and have demonstrated excellent properties for reversible cell opening in epithelial barriers.<sup>[9,174,175]</sup> Triggered by chelation of calcium, the paracellular permeability is increased by the activation of PKC, accomplishing reversible TJ and AJ disruption.<sup>[9]</sup> For example, EDTA has been used for Caco-2 monolayers for transferring polyethylene glycol, furosemide, carboxyfluorescein, and FITC-dextran without any serious signs of cytotoxicity.<sup>[9]</sup>

For fatty acids, the oleic acid plays by far the most important role in transdermal drug delivery systems.<sup>[9]</sup> Due to the modifying effect of membrane structures, oleic acids have been used in reversible permeability studies for epithelial barriers, for instance, in the mannitol flux in Caco-2 cells, accompanied by a decrease in TEER.<sup>[9]</sup> The effect of oleic acid is not limited to epithelial barriers, further studies show increased paracellular permeability of dermal, gastrointestinal, alveolar and blood-brain barriers as well.<sup>[9]</sup> Next to oleic acid, sodium caprate, a medium chain fatty acid is as well used for absorption enhancing in clinical applications.<sup>[9]</sup> Not only exhibits sodium caprate increased permeability in Caco-2 cells for mannitol by redistribution of the cytoskeleton and the TJ proteins ZO-1 and occludin, resulting in TJ opening, but also shows reversible mucosal damage after exposure.<sup>[9,176]</sup>

Unlike fatty acids, surfactants are soluble and allow the application via oral, injectable and nasal absorption. Various anionic, non-ionic surfactants and bile salts have been used to increase paracellular permeability in epithelial barriers.<sup>[9,177]</sup> Sodium dodecyl sulfate (SDS), the parade example for an anionic surfactant, as well as bile salts such as sodium cholate, sodium taurocholate and sodium taurodeoxycholate, exhibit all a concentration-dependent effect on the paracellular permeability.<sup>[9]</sup> They lead to a decreased TEER, an increased intracellular calcium level, accompanied with TJ opening.<sup>[9]</sup> While short-term incubation induces a reversible effect on the paracellular permeability, long-term exposure has shown from irreversible changes via membrane damages through to cellular toxicity.<sup>[9]</sup>

The aforementioned investigations on TJ modulators like CS, PLL and various bile salts, have provided direct evidence of increased paracellular permeability in TJs, resulting in safe and controlled opening of epithelial barriers. In-vitro results in Caco-2 cell monolayers and TEER measurements demonstrate that reversible effects on the permeability still often rely on concentrations and exposure times. Hence, the main goal of this investigation is to examine the temporary and reversible opening of TJs via modulators with the in-vitro model of Caco-2 cells

using the organic electrochemical transistor (OECT) as a sensor. The OECT has proven in several occasions as an enhanced measuring tool for barrier tissue integrity with higher sensitivity and temporal resolution compared to conventional techniques. Here, we show the TJ paracellular expansion effects of CS, PLL and other TJ modulators in Caco-2 cell monolayers by continuously monitoring the current transient response in OECTs in time. Extracting the response time by an exponential fit of the transient response reveals the immediate effect of modulators upon its addition, while the desired temporary effect is revealed after removing of the modulator and additional washing (Figure 7.2).

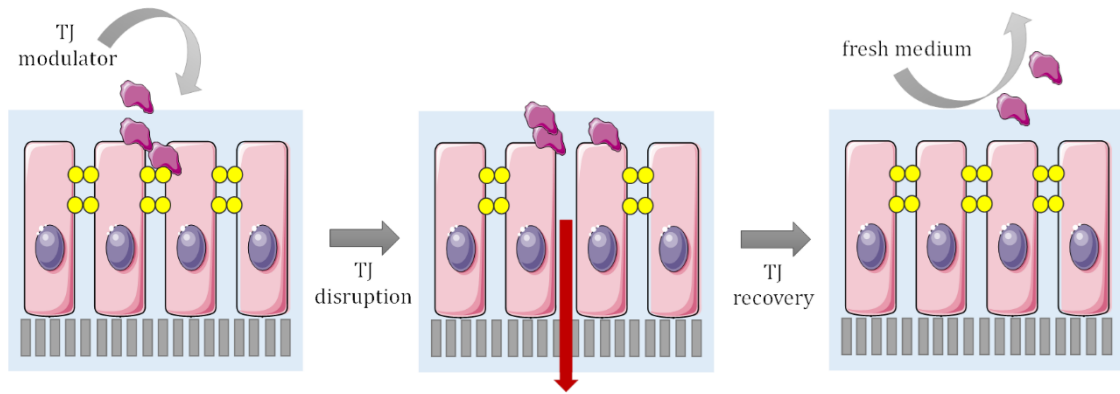


**FIGURE 7.2.** CARTOON OF THE EFFECT OF TIGHT JUNCTION MODULATORS: The addition of TJ modulators implies a TJ disruption, which is ideally only of temporary nature. Upon its removal and washing with fresh medium TJ assembly can be regained. Cartoon has been created by images of SMART.<sup>[13]</sup>

## 7.2. Results and Discussion

The OECT device structure with an integrated Transwell filter, cultured with Caco-2 cells, is shown in Figure 7.3(a). The typical 3-terminal configuration is depicted by the gold source and drain contacts, embedding the highly conductive PEDOT:PSS channel. The *p*-type semiconductor is in direct contact with an electrolyte, in this case cell culture medium, in which a gate electrode is immersed. Upon positive gate bias  $V_G$ , cations of the cell culture medium are injected into the PEDOT:PSS channel, and modify its conductivity by electrochemical reactions in form of dedoping, inducing a modulation of the drain current  $I_D$ . At steady state,  $I_D$  is linearly proportional to the number of injected ions, and the transistor response time is depended on the ion flow till it reaches steady state.

In this experiment we pulse  $V_G$  for 30 seconds with 180 seconds off-time, and monitor the modulation of  $I_D$ . The continuous square voltage pulse and its  $I_D$  response in the absence of cells is displayed in Figure 7.3(b). The integration of a cell layer, changes the ion permeability, and influences the ion flux in the OECT system, which is portrayed in  $I_D$ . The presence of the cells leads



to a smaller modulation of  $I_D$ , induced by the decrease in ion flux as seen in Figure 7.3(c). In other words, the incorporation of a cell layer slows down the transistors response till it reaches steady state.

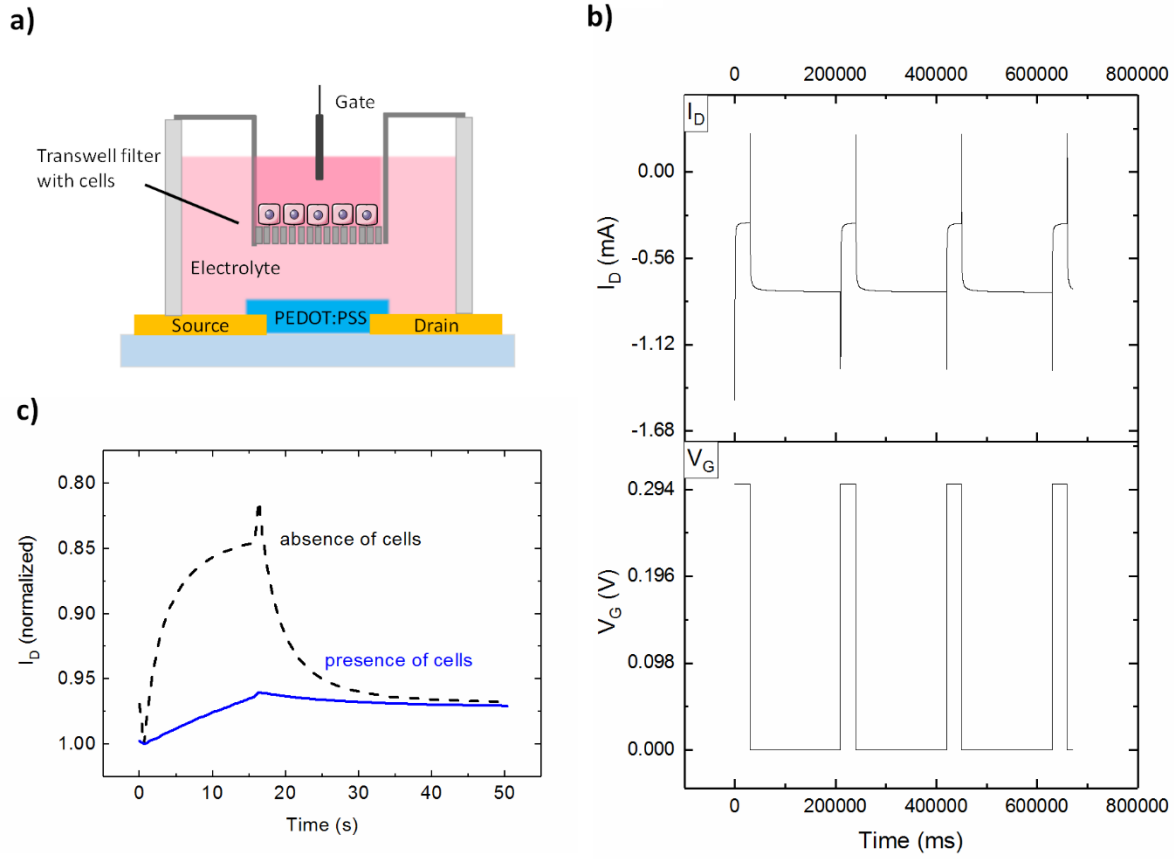


**FIGURE 7.3. CELL LAYER INTEGRITY: a)** Cross-section of the OECT device structure, including a Transwell filter for the integration of a cell membrane. **b)** The OECT  $I_D$  response to a square  $V_G$  pulse of 300 mV with 30 seconds on and 180 seconds off at  $V_D = -0.1$  V. **c)** Normalized  $I_D$  response of a  $V_G$  pulse in the absence and presence of cells.

With reference to *Chapter 5 – Probing the Impedance of a Biological Tissue with PEDOT:PSS-Coated Metal Electrodes*, the critical factor of the transition from a non-sensing to a sensing capability is given by the ratio  $\lambda = \frac{|Z_{MEM}|}{|Z_{EL}|}$ , which reveals that the impedance of the tissue layer  $|Z_{MEM}|$  has to be greater than the impedance of the electrodes  $|Z_{EL}|$ . Based on this declaration, we used on the one hand relatively large channel dimensions of  $10 \times 15$  mm ( $W \times L$ ) to effectively decrease  $|Z_{EL}|$ , in addition we decreased the cell area by applying polydimethylsiloxane (PDMS) on the back of the Transwell filters to increase the effective cell layer resistance, as in  $|Z_{MEM}|$ . For an effective cell layer resistance, a uniform coverage of a closed monolayer of cells is necessary. Caco-2 cells obtain generally after 14 days a closed cell layer, demonstrated by a TEER of  $400\text{--}500 \Omega \text{ cm}^2$  and visualized by confocal laser scanning microscopic (cLSM) images. Caco-2 cell monolayers were

immunofluorescently stained for the cytoskeleton and the nucleus, to monitor a closed and uniform cell coverage, as shown in Figure 7.4.

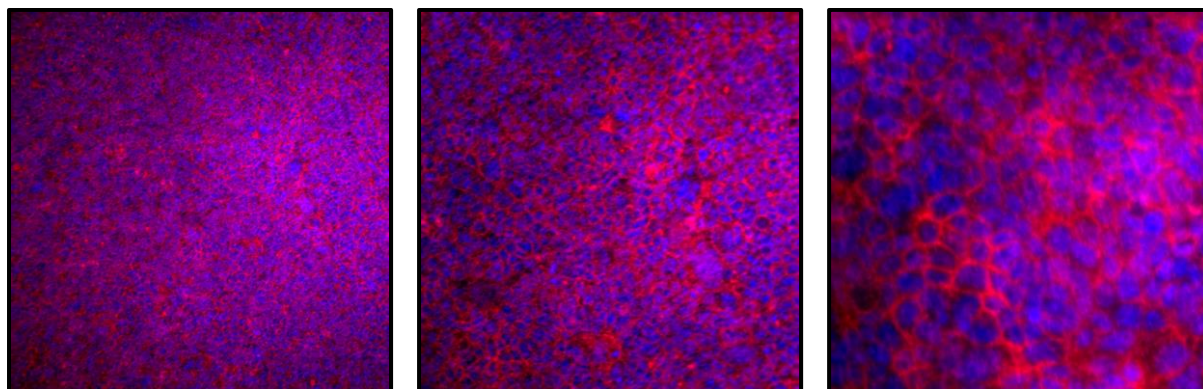


**FIGURE 7.4.** CLSM IMAGES OF CACO-2 CELL LAYERS: Microscopic images of immunofluorescently stained Caco-2 cells in the magnification of 5x, 10x and 20x, respectively.

The effect on the paracellular permeability of TJs caused by modulators in form of cationic polymers is demonstrated for CS in Figure 7.5(a). The recorded  $I_D$  was used to extract the response time of the OECT by the exponential fit of the transient response, serving as the finger print of the transistor speed. The fact that the increased response time after integrating the cells significantly lowers upon addition of CS (exposure time of 1 hour), assembles the effect of increased paracellular expansion of the TJs. The desired reversible effect of the cell opening could not be observed, outlined by the unchanged response time after removing CS and washing the filters with fresh medium, including an additional hour for recovery. Probing a concentration-dependent effect on the temporary influence of CS, Figure 7.5(b) reveals that even with a lower concentration of CS of 1%, the favored recovery and closing of the TJs could not be achieved once again. Despite the non-occurred recovery, it should be noted that by lowering the CS concentration from 10% to 1%, the resulted change in the response times decreases as well. Figure 7.5 (a, b) notices a change from 20% to 16%. Control experiments with CS at different concentrations (Figure S7.1, *Supporting Information of Chapter 7*), even confirm an increasing effect on the response time of the OECT, outlining that CS itself changes the resistance of the medium. This effect underlies the fact, that the OECT is highly sensitivity to any changes in the ion concentration in the electrolyte medium, which is directly reflected in the output current.

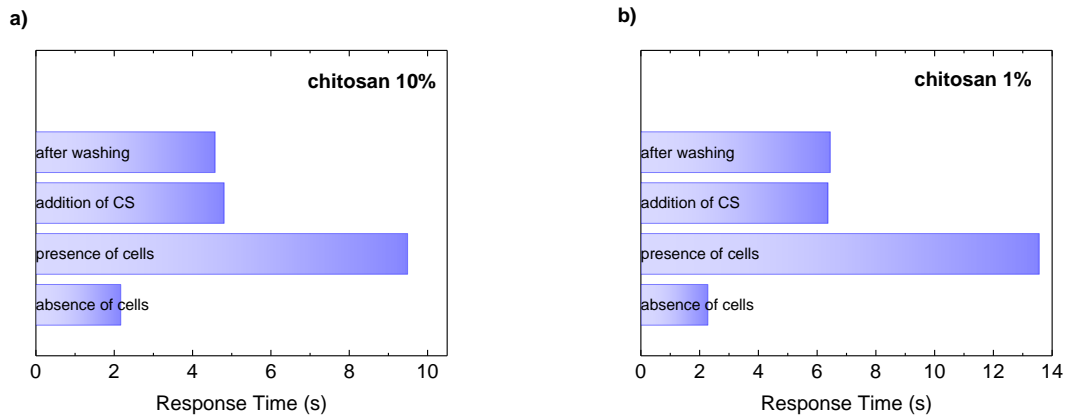


**FIGURE 7.5.** EFFECT OF CHITOSAN ON TIGHT JUNCTIONS: OECT response time before and after the addition of CS in the concentration of **a)** 10% and **b)** 1%. After 1 hour, CS was removed and filters were washed with fresh medium for recovery. Last measurements were taken after 1 hour after replacing the medium.

Next to CS, another promising representative of cationic polymers for TJ modulators is PLL. Starting with a rather large concentration of 10%, the addition of PLL provokes a cell opening of the barrier by TJ disruption, traceable via a decrease in the response time of the OECT in Figure 7.6(a). Again, the effect is not reversible by replacing the medium. However, lowering the PLL doses to 1%, imitates not only an immediate paracellular expansion of the TJs, but also shows the desired reversible effect of the paracellular permeability of the TJs (Figure 7.6.(b)). The induced cell opening of the TJs is relatively seen small, but an almost full recovery has been accomplished. Again, the resulted change in the response times lowers, in this case from 12% to 5%, when changing the PLL doses from 10% to 1% (Figure 7.6(a, b)). Control experiments exhibits the same concentration-dependent effect of the medium, as for CS (Figure S7.1(c, d), *Supporting Information 7.4*).

Additional studies with different TJ modulators as in sodium taurocholic acid (NaTC), a representative for a bile salt, and sodium caprate (C10), a medium chain fatty acid did not even show a change in the response time of the OECT upon the addition of the TJ modulator, even at relatively large concentrations (Figure S7.2, *Supporting Information 7.4*).

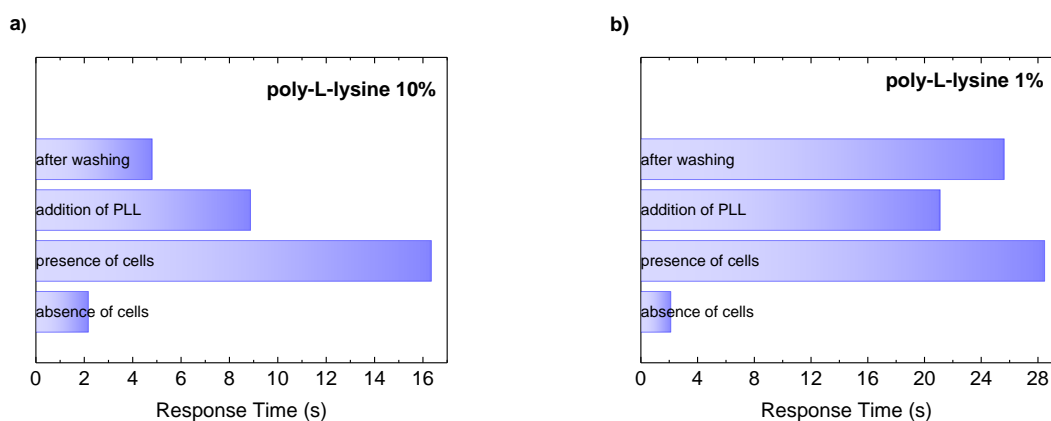


**FIGURE 7.6.** EFFECT OF POLY-L-LYSINE ON TIGHT JUNCTIONS: The transistor response time before and after the addition of PLL in the concentration of **a)** 10% and **b)** 1%. After an exposure time of PLL of 1 hour, the medium was replaced with fresh medium, allowing 1 hour of recovery.

### 7.3. Summary and Outlook of Chapter 7

In conclusion, the OECT has demonstrated, upon the integration of human cells, to be a promising method for cell barrier integrity. The label-free and non-invasive sensing device not only protrudes by its low-cost manufacturing and tuneability, but particularly by high sensitivity and temporal resolution compared to other traditional techniques. Increased paracellular permeability of TJs in form of cell opening can be detected in high sensitivity as a change in the output current of the OECT. The discovery of TJ transmembrane proteins and the urgent need of novel drug delivery systems has led to the development of optimized TJ modulators, which can directly target TJ proteins, to reversible enhance paracellular transport for drug delivery with less toxicity than previous absorption enhancers. Here, by combining the OECT with TJ modulators, the temporary TJ disassembly can be assessed in more detail and high sensitivity. This investigation embraced the use of various TJ modulators including cationic polymers, surfactants and fatty acids. Overall, CS and PLL, which are widely used as food supplements, have shown an immediate effect on the paracellular permeability of the TJs, but only PLL achieved the favored reversible effect of the TJ assembly. The doses-dependent effect of PLL has only accomplished a recovery of a small damage in the TJ assembly so far. Higher PLL concentrations led to greater but permanent TJ damages, as seen for CS.

We believe that with further investigations focusing on the doses and exposure times, especially of cationic polymers, the reversible effect on the cell layer opening can be further enhanced. Using the OECT in the current-driven configuration has not only led to the highest sensitivity in ion detection at low voltages, but also achieved higher sensitivity and temporal resolution in detecting disruption in barrier functions. By tuning the device toward greater

sensitivity and using the current-driven OECT, this method has high potential to be used as a complementary sensor for cell barrier integrity, applicable for pharmaceutical excipients to improve drug delivery across epithelial barriers.

## 7.4 Supporting Information of Chapter 7

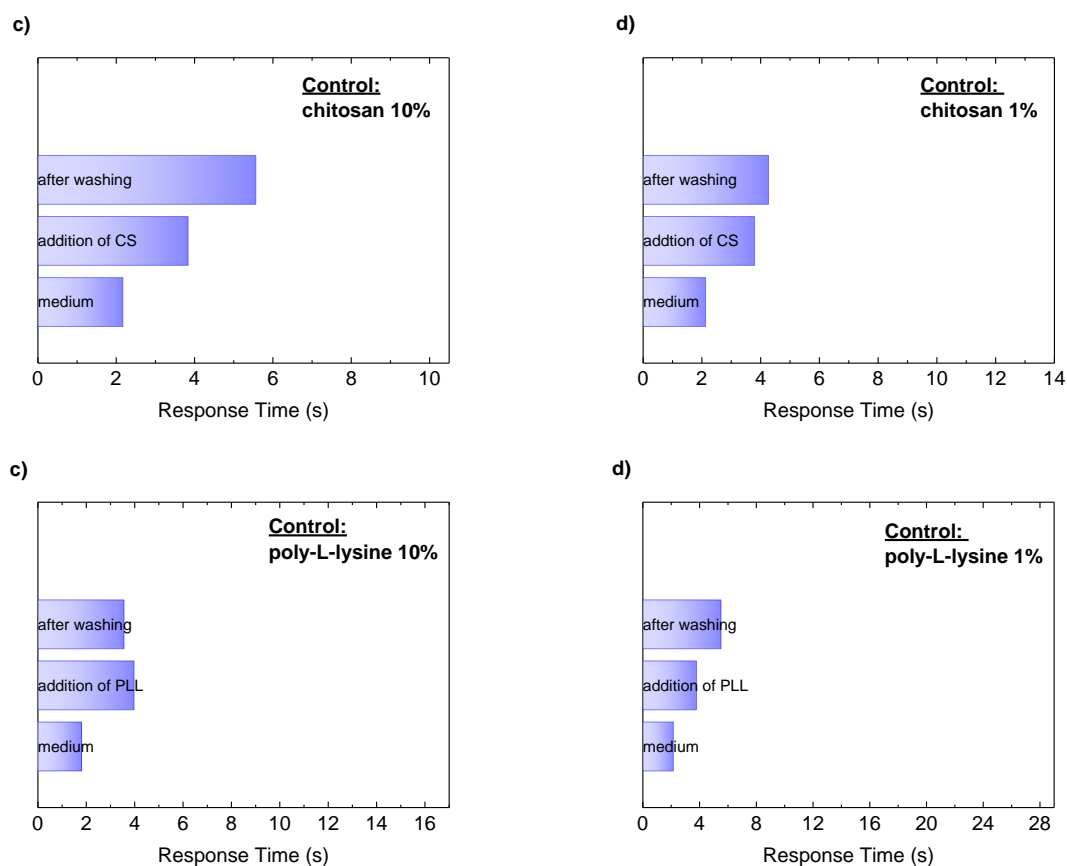


**FIGURE S7.1.** CONTROL EXPERIMENTS OF CATIONIC POLYMERS: The OECT response time before and after the addition of **a)** 10% CS, **b)** 1% CS, **c)** 10% PLL and **d)** 1% PLL in the absence of cells. After 1 hour the modulator was removed and the filters were washed with fresh medium for recovery (1 hour).

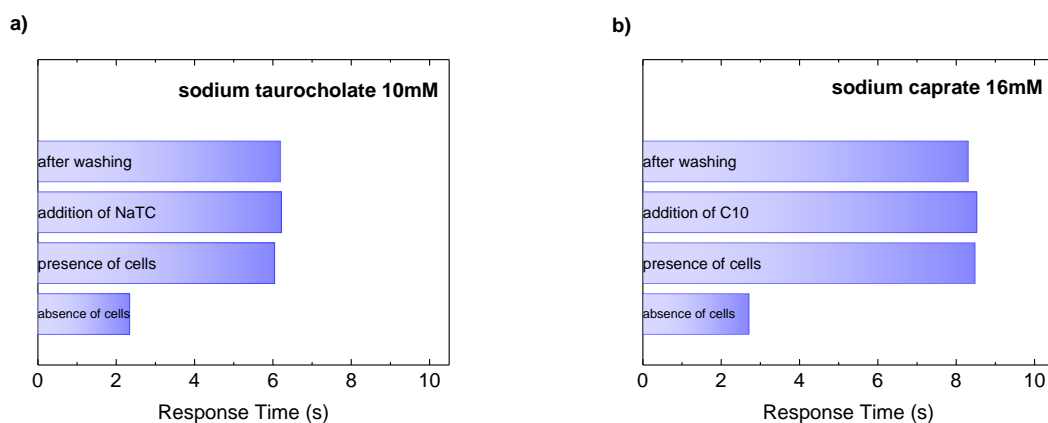


**FIGURE S7.2.** EFFECT OF TIGHT JUNCTION MODULATORS: **a)** OECT response time before and after the addition of **a)** sodium taurocholate (NaTC) and **b)** sodium caprate (C10). After 1 hour the modulator was removed and the filters were washed with fresh medium for recovery. Last measurements were taken after 1 hour after replacing the medium.

# Chapter 8

## Electrical Monitoring of Light-Induced Cell-Cell Interactions

Manipulating signal transduction by the use of light is the focus of optogenetics. Expanding this concept by the employment of photoswitchable proteins, expressed on the surface of cells, allows the control of reversible light-induced cell clustering. Activation and inactivation of cell clustering, resembling cell barrier integrity, has been electrically monitored for the first time. In the frame of pre-examination, the organic electrochemical transistor (OECT) has been exchanged with a simple volt-ohm meter to detect changes in the transepithelial electrical resistance (TEER) upon light illumination of cells, modified with different photosensitive proteins. Especially the homodimer system cyanobacterial phytochrome 1 (CPH-1), has demonstrated promising changes in TEER of cell-cell interactions. Further investigations, including additional measurement techniques and minimizing the probe size, is believed to further enhance the observed effects, thereby eliminating artefacts and other cell processes next to cell clustering. The use of electrical devices with higher sensitivity increases their potential for application towards tissue healing with light stimuli.

## 8.1. Introduction

The field of synthetic biology is a fast growing field, where biology and engineering meet and strengthen each other.<sup>[178,179]</sup> It is considered to be the promising future of biotechnology, holding great potential in developing artificial biological systems for basic research and medical applications.<sup>[178]</sup> Synthetic biology can traditionally be approached in two ways.<sup>[178]</sup> Rearranging of already existing biological systems is considered as top-down synthetic biology.<sup>[178]</sup> Using metabolic and genetic engineering techniques aspires to imply new functions in living organisms.<sup>[180]</sup> Contrary, bottom-up synthetic biology involves the designed and constructing of biological systems of non-living components.<sup>[178,179]</sup> The complexity of living organisms has led to the quest of much simpler and more predictable systems.<sup>[178]</sup> In fact, such minimized systems would for example offer a more efficient model for processes as energy conversion and production of drugs.<sup>[178]</sup> The concept of “minimal cells” originated from this hypothesis and has been the center of synthetic biology for many years.<sup>[178]</sup>

Cell communication is essential for cellular processes like cell division, growth and metabolism, protein synthesis and cell motility.<sup>[181,182]</sup> Each cell receives external signals and individually processes and gives appropriate responses.<sup>[182]</sup> This has provided a complex signal transduction network, based on highly dynamic processes, consisting of exact spatial and temporal resolution of events.<sup>[182]</sup> Defects in this cell communication can lead to uncontrolled cell growth and carcinomas.<sup>[181]</sup> Hence, the manipulation and control of cell-cell interactions, would provide essential knowledge in cell behavior and concurrently benefit its research, as well as offers a synthetic biological method for cell-based therapy.<sup>[181,182]</sup>

This approach has yielded a number of different methods, for instance using molecular biological techniques to genetically engineer cells, as well as using non-genetic methods or cell-surface engineering.<sup>[181,182]</sup> The combination of genetically encoded mutant proteins and chemicals has led, over the years, to a variety of techniques to regulate intercellular contacts, using systems responsive to temperature, enzymolysis, redox potential and chemical stimuli.<sup>[181]</sup> Despite their promising results, these systems still lack from deficits in spatial and temporal resolution, as well as reversibility and biocompatibility.<sup>[181]</sup>

Light provides a promising solution, as it can be easily applied in high precision and offers minimal invasiveness.<sup>[182]</sup> Optogenetics, which is based on genetically encoded light-responsive proteins, exploits this approach to manipulate signaling processes.<sup>[182]</sup> Using light as the sole activator, one of the first optogenetic applications has been the control of neuronal activity, even considered to be the breakthrough for optogenetics.<sup>[182]</sup> Subsequently, optogenetics has been applied to other areas in biology as well.<sup>[182]</sup>



While conventional techniques like genetic and chemical methods, only provide poor spatiotemporal resolution, the use of photoswitchable proteins offers remote control of micrometer spatial resolution and seconds of temporal resolution with visible light (Figure 8.1). On top, it's a biocompatible method, featuring reversibility and sustainability.<sup>[182]</sup>

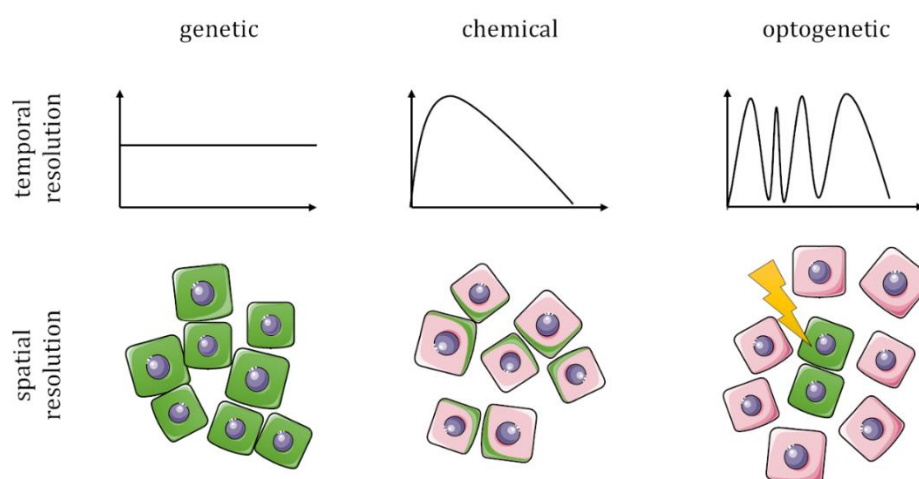


**FIGURE 8.1.** METHODS TO CONTROL CELL-CELL INTERACTIONS: Comparison of cell lines, expressing genetic, chemical and optogenetic tools in regard of spatiotemporal resolution. Part of the scheme, contain images, created by SMART.<sup>[13]</sup>

A variety of photosensitive proteins have been developed, addressing various processes inside a cell like gene activation, protein localization, enzyme activity, protein clustering using visible light.<sup>[183]</sup> Recently, photoswitchable proteins have been reported to control motility in minimal synthetic cells<sup>[184]</sup>, for social self-sorting of colloidal cell-mimics<sup>[183]</sup> and even for bacterial adhesion as a key step towards the design of biofilms.<sup>[185]</sup> Table 8.1 provides an overview of light-responsive proteins commonly applied in optogenetic signal transduction studies, differentiating by the activation light wavelength, activation/inactivation time and mechanism.<sup>[182]</sup>

**TABLE 8.1.** OVERVIEW OF COMMONLY APPLIED OPTOGENETIC PROTEINS: Photoswitchable proteins grouped by their respective peak absorbance in the red and blue light responsive systems.

Light	Photoswitchable Protein	Partner	Cofactor	Mechanism	Activation/inactivation
Red/Farred	CPH-1		PCB	homodimerization	milliseconds/milliseconds
Blue/dark	Vivid		FAD	homodimerization	Seconds/hours
Blue/dark	iLID	Nano	FMN	heterodimerization	Seconds/minutes
Blue/dark	nMag	pMag	FAD	heterodimerization	Seconds/minutes

The aim of this study is to electrically monitor the light-induced phenomenon of cell-cell interactions with bioelectronic devices. By expressing photoswitchable proteins on the surface of the cells, cell clustering can be activated and inactivated by light. In view of cell barrier integrity, this would assemble an open and closed cell layer, traceable by a change in the resistance, when integrated between two electrodes. For simplicity, we consulted transepithelial electrical resistance measurements (TEER) as a pre-stage before using the organic electrochemical transistor (OECT). For the photoactivated cell clustering we used two different photoswitchable protein systems: First, the heterodimer system of iLID (improved light-inducible dimer), which interacts with Nano upon blue light illumination and dissociates from it in the dark (Figure 8.2). Second, CPH-1 (cyanobacterial phytochrome 1) as a homodimer system, that undergoes photoactivation by irradiation with red and inactivation in far-red light (Figure 8.2).<sup>[182]</sup>

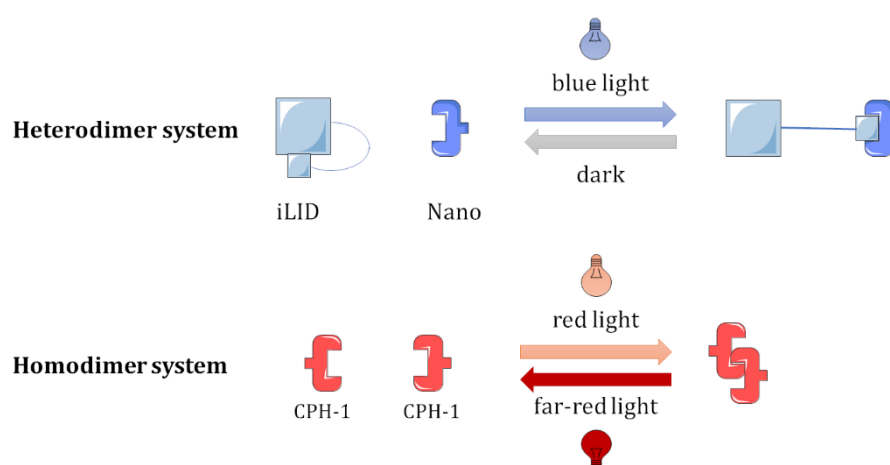


**FIGURE 8.2.** INTERACTION IN PHOTOSWITCHABLE PROTEINS: The proteins iLID and Nano connect as heterodimers under blue light and dissociate in the dark. CPH-1 forms homodimers upon red light exposure, while the inactivation takes place in far-red light. Scheme has been designed by images of SMART.<sup>[13]</sup>

## 8.2. Results and Discussion

Photosensitive proteins have been previously used to control various processes with light in cells.<sup>[183]</sup> However, they have not yet been used to mediate cell clustering as a matter of cell layer integrity, assessed by electrical measurements. We began by investigating photoswitchable proteins of different mechanisms, starting with the blue light-dependent heterodimer pair iLID/Nano. The iLID system, is the engineered version of the LOV2 (light-oxygen-voltage-sensing) domain from *Avena sativa*, which can be found in plants, fungi and prokaryotes. Upon blue light irradiation ( $\lambda = 480$  nm), iLID forms an adduct with flavin mononucleotide (FMN), a chromophore

which is added as a cofactor to the cell medium, leading to a conformational change of the iLID domain. As a consequence, iLID is able to reversibly bind to Nano in seconds and dissociates in the dark within seconds to minutes. Expressing the photoswitchable protein pair on the surface of cells, induces cell-cell interactions in form of clustering (Figure 8.4(a)).<sup>[183,184,186,187]</sup> For this purpose, we utilized especially MDA-MB-231 cells. This cell line does not express the transmembrane glycoprotein E-cadherin, which affects cell-cell interactions, leading to low cell-cell contacts.<sup>[96]</sup>

The OECT has shown to be an excellent tool for monitoring cell layer integrity.<sup>[6,8]</sup> However, we approached the electrical monitoring of light-induced cell clustering by simple and fast TEER measurements as a pre-step, to investigate the ideal photoswitchable protein candidate and its optimal condition. A handheld epithelial volt-ohm meter, consisting of two concentric electrode plates with voltage-sensing Ag/AgCl pellets, was subjected for TEER measurements, as its setup is shown in Figure 8.3. The device applies a small voltage signal between the electrodes, that holds a cell layer in between, and yields the vertical resistance. Inactivated cells resembling an open cell layer, imply a low resistance, while contrary activated cells induce cell clustering, reflecting a high resistance for a closed cell layer.<sup>[159,188,189]</sup> For an increased effective cell layer resistance, Transwell filters were upfront modified with polydimethylsiloxane (PDMS) to decrease the cell area of 1.12 cm<sup>2</sup> by a factor of approx. 8. Due to the unprecise area of the filters, TEER values can only be estimated and therefore, the cell layer integrity is mainly expressed in resistance.

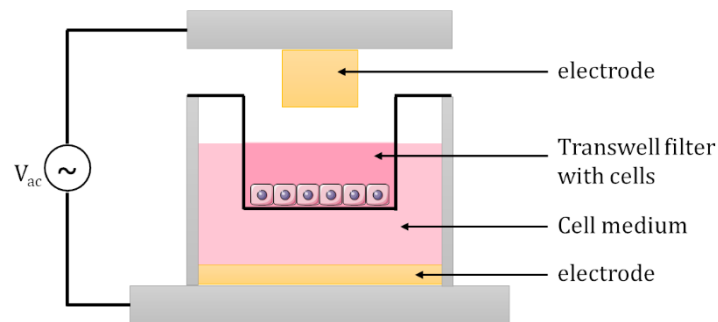


**FIGURE 8.3. VOLT-OHM METER CHAMBER:** Schematic cross-section of the EndOhm chamber from World Precision Instruments, consisting of two concentric electrode plates, one located at the bottom and the other one at the lid of the chamber. A Transwell filter can be integrated in between to measure TEER of tissue cultures.

iLID/Nano-expressed MDA cells, seeded on Transwell filters ( $6.5 \times 10^5$  cells/insert) and allowed to form a uniform monolayer of cells within 7 days, were exposed to blue light for 4 hours in the incubator to form a closed cell layer. Figure 8.4(b) shows resistance measurements monitoring the proposed cell opening by exposure to the dark. MDA cells are able to form only very low cell-cell contacts due to the absence of E-cadherin<sup>[96]</sup>, which is indeed crucial for the investigation. But that also implies no reference TEER values of a closed MDA cell layer can be applied. Consulting

other barrier tissue cells, such as Caco-2, demonstrates a TEER of  $400\text{--}500\ \Omega\ \text{cm}^2$ <sup>[6]</sup>, whereas MDCK I cells are known to have a low TEER of only  $150\ \Omega\ \text{cm}^2$ <sup>[7]</sup>. The low starting value of  $240\ \Omega$ , meaning a TEER of approx.  $34\ \Omega\ \text{cm}^2$ , most likely indicates an incomplete closing of the cell layer. Indeed, further cell tests and microscopical images (Figure S8.1, *Supporting Information of Chapter 8*), confirmed poor cell attachment of MDA cells on PDMS-modified Transwell filters. The small observed decrease in resistance in Figure 8.4(b) could suggest a light-induced dissociation of the cells, but due to the low value of TEER, this phenomenon is rather subjected to cell migration or even cell degradation. Furthermore, the heterodimer system appears to be rather unfavourable, as it additionally increases the chances of “holes” in the cell layer, in the case when two equal cell components happen to be next to each other, unable to cluster.

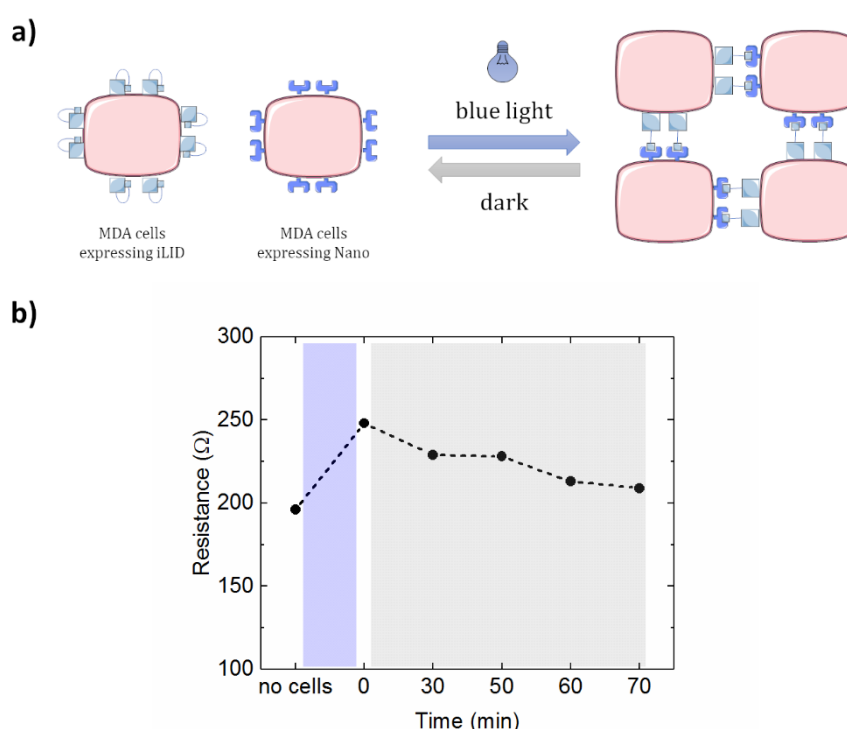


**FIGURE 8.4.** ILID/NANO FOR LIGHT-INDUCED CELL CLUSTERING: **a)** Scheme of MDA cells, expressing iLID and Nano on the cell surface, cluster and dissociate under blue light and in the dark, respectively. **b)** Resistance measurements of the light-induced cell dissociation in the dark over period of time. iLID/Nano expressing MDA cells were seeded on Transwell filter at  $6.5 \times 10^5$  cells/insert. Cartoon was created by images of SMART.<sup>[13]</sup>

The photosensitive protein CPH-1, not only offers favourable homodimerization, but also a controlled reverse interaction. The active and inactive conformation of CPH-1 can be interchanged by irradiation with red ( $\lambda = 650\ \text{nm}$ ) and respective far-red light ( $\lambda = 750\ \text{nm}$ ) in the presence of the chromophore phycocyanobillin (PCB) as a cofactor.<sup>[182]</sup> Collagen coating improved cell layer attachment and growing, though uniform cell layers of modified- and wildtype-MDA cells still remained delicate in many cases. But nevertheless, confocal laser scanning microscopic (cLMS)

images of immunofluorescently stained CPH-1 cells for actin and nucleus in Figure 8.5 point out the uniform distributed cell coverage.

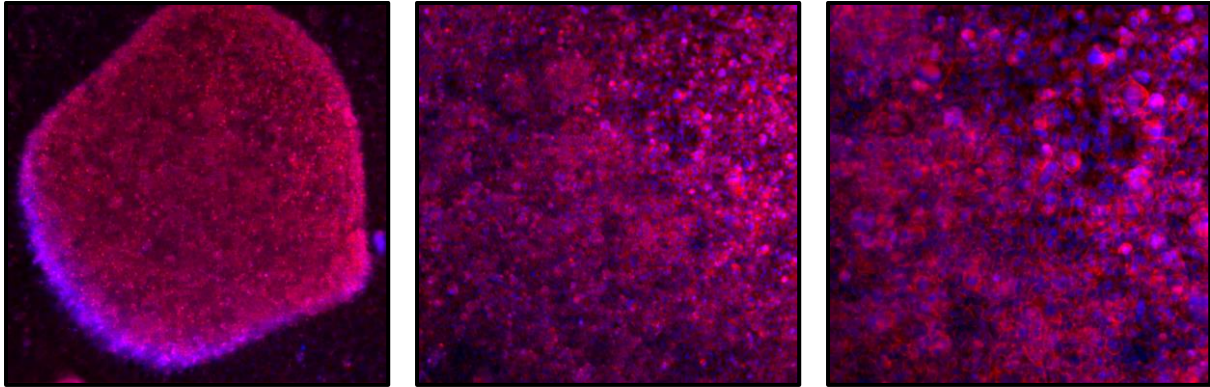


**FIGURE 8.5. MICROSCOPIC IMAGES OF MDA CELLS EXPRESSING CPH-1:** Immunofluorescently stained MDA cells for actin and nucleus, examined by cLMS, in the magnification of 5x, 10x and 20x, respectively. Cells were seeded on collagen-coated Transwell filter, modified with PDMS ( $5 \times 10^4$  cells/insert, after 9 days)

After an incubation time of 9 days to allow complete confluency on collage-coated Transwell filters and additional 5 hours in red light, CPH-1-expressed MDA cells were exposed to far-red for 5 hours to reverse the protein interaction (Figure 8.6(a)). Figure 8.6(b) states first of all a closed cell layer (roughly a TEER of  $370 \Omega \text{ cm}^2$ ), as well as a decrease of 24% in resistance, arguing in favour for the desired phenomenon of light induced cell opening. In principle, starting from a closed cell layer (red light) to induce dissociations in the dimers in form of “holes” (far-red) is easier to approach, although a decrease in resistance could be also the reason for cell degradation. A following reverse reaction is able to exclude this possibility.

On that account, CPH-1-expressing cells and wildtype-MDA cells as a reference were exposed to far-red light for 3 hours (Figure 8.6(c)), after a starting incubation time in red light for 2 hours. CPH-1-modified cells experience a decrease of 19% in resistance upon far-red light illumination, but no increase in resistance is observed for a subsequently irradiation of red light for 2 hours for the reversed interaction. In fact, they even show a further decrease in resistance. The activation and inactivation of CPH-1 proteins itself is reported to be within milliseconds<sup>[182]</sup>, but it may differ if expressed on the surface of cells. Therefore, the reverse interaction may take longer than the applied 2 hours of red light exposure. The estimated TEER of  $150 \Omega \text{ cm}^2$  ( $1035 \Omega$  respectively) at the beginning most likely implies a cell layer of only low integrity. However, reference MDA cells show almost no effect on the resistance upon light irradiation, neither in red nor in far-red light.

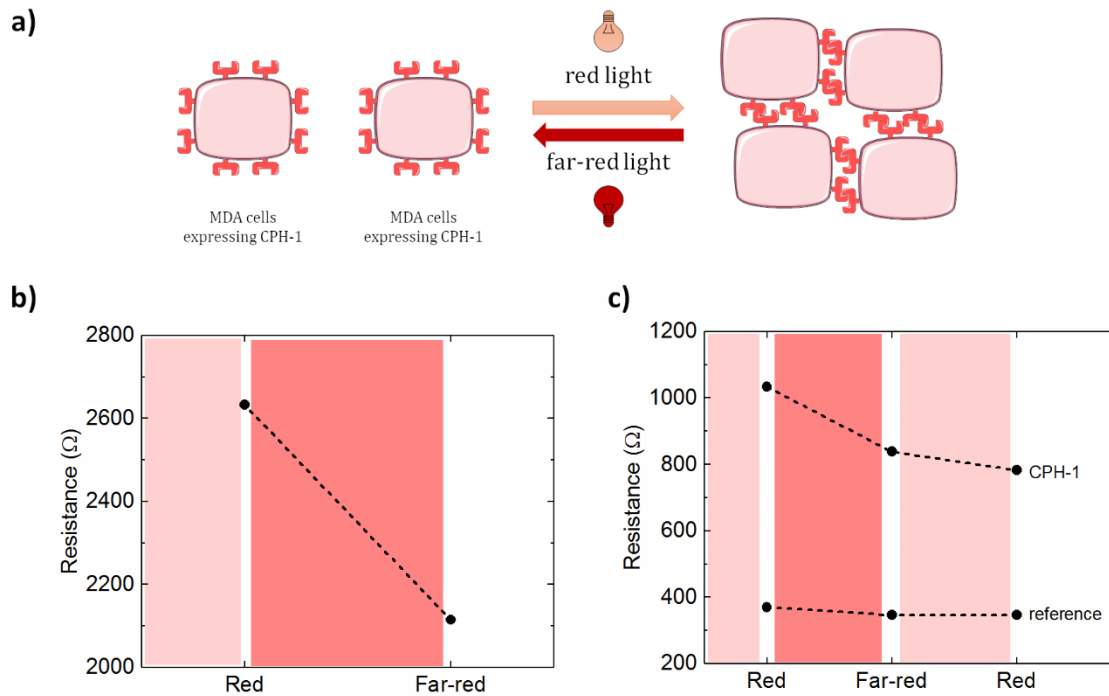


**FIGURE 8.6.** CPH-1 FOR LIGHT-INDUCED CELL-CELL INTERACTIONS: **a)** Scheme of CPH-1-expressing MDA cells, that cluster in red light and detach in far-red light. **b)** Resistance measurement of the light-induced cell opening in CPH-1 cells. Cells were seeded on PDMS-modified Transwell filters ( $1 \times 10^5$  cells/insert). **c)** Resistance of CPH-1 and reference cells upon far-red light and subsequently red light illumination ( $5 \times 10^4$  cells/insert). The Cartoon was designed by using images of SMART.<sup>[13]</sup>

This brought us back to the deliberation of starting from dissociated to clustered cells upon activation with red light. Although this approach may seem more difficult, considering that a completely closed cell layer is necessary to see a significant effect in TEER, it would imply an increase in TEER, which can be more easily associated with cell clustering.

CPH-1-expressing cells were incubated in the dark for 8 days on collagen-coated Transwell filters to allow uniform cell coverage. The change in resistance upon red light exposure for a total duration of 10 hours is displayed in Figure 8.7(a). After 4 hours an increase of 17% in resistance is achieved, which raises to 27% after 10 hours. This led to an estimated end TEER value of  $162 \Omega \text{ cm}^2$  (in this case cell area was only reduced by a factor of 5), suggesting a closed cell layer of low integrity though. A control measurement was performed on CPH-1-expressing MDA cells, without adding the necessary cofactor PCB for the light-induced photoactivation of the protein. Almost no effect upon red light irradiation is noticed for the reference system (Figure 8.7(b)). The latest observation provides promising results regarding light-induced cell clustering. However, the low TEER value and the small change in resistance can not only be subject to cell clustering, but also to other processes such as cell migration. Scaling down to microscopic sizes and consulting additional techniques is necessary to support the hypothesis and to exclude artefacts.

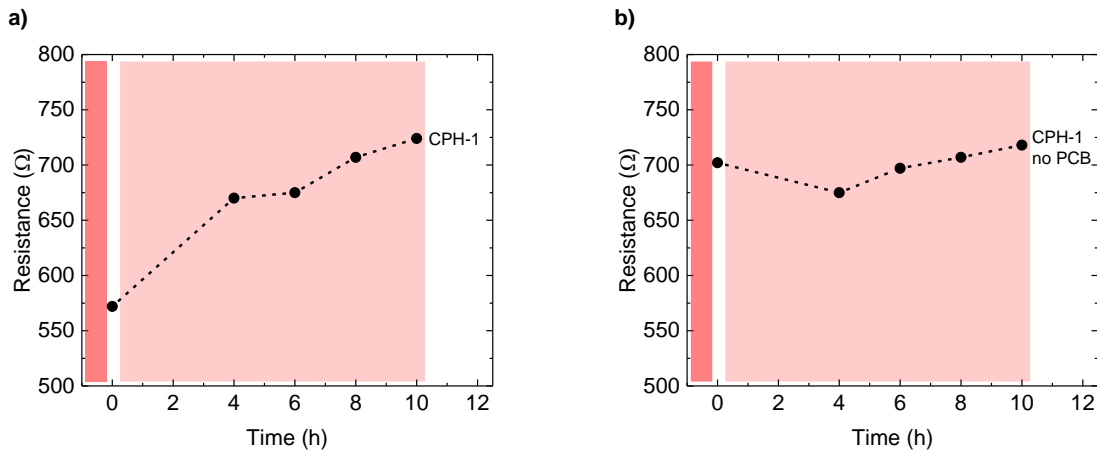


**FIGURE 8.7.** LIGHT-INDUCED CELL CLUSTERING USING CPH-1: Resistance measurements upon red light exposure on MDA cells expressing CPH-1 in the **a)** presence and **b)** absence of the cofactor PCB (reference). Cells were seeded on PDMS-modified Transwell filters with collagen coating ( $5 \times 10^4$  cells/insert).

### 8.3. Summary and Outlook of Chapter 8

In summary, the use of light-responsive proteins in the field of optogenetics has been successfully applied in various biological systems to control signal transduction in higher spatial and temporal resolution, compared to analogues genetic and chemical approaches. Expressing photoswitchable proteins on the surface of a cell, has the potential to manipulate cell-cell interactions, such as cell clustering in time and space with light. To electrically monitor the proposed change in the integrity of the cell barrier, the OECT has been shown in many occasions as a suitable candidate. For simplicity, with the aid of an epithelial volt-ohm-meter as a pre-examination, electrically monitoring of light-induced activation and inactivation of cell clustering has been investigated by means of a change in TEER. Especially, on the grounds of the photosensitive homodimer CPH-1, promising achievements have been made towards a light-induced changes in TEER upon cell clustering. Despite its promising indication of light-induced cell-cell interactions, other cell processes like cell migration or cell degradation could not be excluded at this stage, causing similar observations.

We believe that by scaling down to microscopic probe sizes and consulting of additional microscopic techniques, the phenomenon of light-induced cell clustering can be electrically monitored. The space and temporal control of cell-cell reversible interactions using photoswitchable proteins is believed to be further enhanced by using OECTs, offering higher sensitivity in assessing cell barrier integrity compared to conventional techniques. The combination of the OECT and optogenetics, demonstrated great potential in applications towards tissue healing with light stimuli and developing synthetic biological systems for cell-based therapy.



## 8.4 Supporting Information of Chapter 8

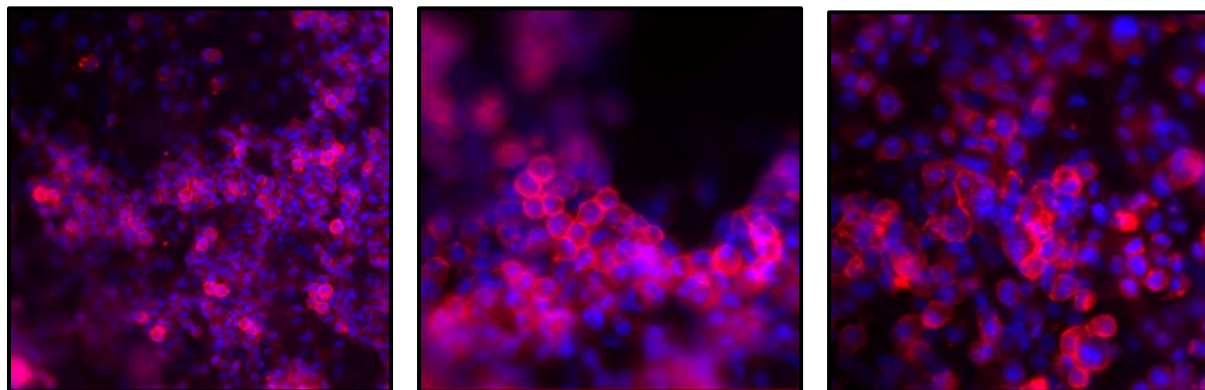


**FIGURE S8.1.** MICROSCOPIC IMAGES OF MDA CELLS ON TRANSWELL FILTERS: Immunofluorescently stained MDA cells for actin and nucleus, examined by cLMS, in the magnification of 20x, 40x and 40x, respectively. MDA cells were seeded on PDMS-modified Transwell-filters ( $1 \times 10^5$  cells/insert, after 14 days).



# Conclusion

The strongly emerging field of bioelectronics has produced many promising devices for biomedical applications. Among these is the organic electrochemical transistor (OECT) as the showpiece of high signal amplification and excellent biocompatibility at low cost and time manufacturing. In this thesis, the development of high-performance and highly sensitive OECTs has been investigated with the aim of the biosensing application of improved assessment of cell layer integrity in a label-free and non-invasive manner.

To that end, the establishment of improved OECT performances in terms of efficiency has been examined on the grounds of the optimization of the conducting polymer PEDOT:PSS as the active material. The conductivity of PEDOT:PSS can be further increased as a matter of *Secondary Doping* by treatments with high boiling solvents. In **Chapter 3** several organic solvent treatments with DMSO, including mixing PEDOT:PSS with dimethyl sulfoxide (DMSO) before film deposition, exposing a deposited PEDOT:PSS film to a saturated DMSO vapor and dipping a PEDOT:PSS film in a DMSO bath have been studied and evaluated by its effect on the performance of the OECT. In particular the dipping method leads to a strongly enhanced conductivity with a maximum value above  $2100 \text{ S cm}^{-1}$ , giving rise to the highest transconductance and on/off ratio. The improved OECT performance is the result of an increased charge carrier mobility, induced by a phase segregation in highly conductive PEDOT:PSS-rich and PSS-rich domains, and an enhanced structural order. Notifying, in OECT configuration the PEDOT:PSS conductivity is typically reduced by one order of magnitude by incorporation of an electrolyte due to swelling effects in PEDOT:PSS.

The achieved large transistor transconductance enables enhanced ion sensitivity, even many times more pronounced with the aid of the current-driven transistor configuration. **Chapter 4** outlines the overcome of the fundamental Nernst limitation by about one order of magnitude in ion sensitivity by connecting the OECT in series with a current generator. Exhibiting ion sensitivity, normalized with respect to the supply voltage, larger than  $1200 \text{ mV V}^{-1} \text{ dec}^{-1}$ , has

reached the largest value for voltage ion sensitivity ever reported for ion-sensitive transistors. The current-driven OECT shows that it is possible to dramatically enhance the ion sensitivity of OECTs while maintaining a low-voltage operation, due to the fact that the bias current sets the operating range of ion concentration and that in this way the sensitivity is not limited by the supply voltage. The significantly enhanced ion sensitivity is retained by using an ion-selective membrane, thus opening the opportunities in high-performance biosensing.

**Chapter 5** takes up this issue by finally interface biological input with organic bioelectronics. The classic approach of an array of electrodes has compiled a directive for minimized impedance mismatch in sensing platforms and sets the course for more efficient biosensing. Impedance spectroscopy of PEDOT:PSS-coated gold electrodes of various sizes has revealed the impact of the impedance differentiation on the sensing ability of electrodes in an electrode/cell barrier system. A four-element  $R_s - C_{EL} - R_{MEM} // C_{MEM}$  circuit is used to model this system and implies an electrode-area dependent transition from a non-sensing to sensing regime. The determinant is the ratio of  $\lambda = \frac{|Z_{MEM}|}{|Z_{EL}|}$ , defining the requirement for the biosensing capability by means of a greater value for the cell layer impedance  $|Z_{MEM}|$  than the electrode impedance  $|Z_{EL}|$ .

The up to this point achieved findings have been appointed to biosensing applications with the active element OECT. As a matter of assessment of cell layer integrity,  $H_2O_2$  as a model for toxins and pathogen, implies a permanent disruption of the cell layer barrier, which tightness is mainly supported by complexes of proteins called tight junctions (TJs). In **Chapter 6**, the promising combination of a current-driven OECT with an integrated cell layer has strongly enhanced the detection of barrier function disruption in terms of sensitive and temporal resolution compared to conventional traditional techniques. The process of the induced cell opening can be detected in detail as a variation of the output voltage, keeping the sensing regime by carefully chosen channel dimensions of the OECT.

Biosensing of cell layer integrity has been further intensified in **Chapter 7** by the use of TJ modulators to control its integrity by chemical modulation. Their temporary effect on the assembly of TJs between adherent cells has been exploited for reversible opening of membranous barriers, expanding the potential for improving drug delivery across epithelial barriers. A concentration-dependent control of reversible opening of TJs has been demonstrated for poly-L-lysine, a cationic polymer candidate of TJ modulators, by monitoring the change in the transient response of the OECT. This opens the window for time- and doses-dependent investigations of cationic polymers and other TJ modulator systems, to gain greater sensitivity and temporal resolution, most notably by using the OECT in the current-driven configuration.

One step further of controlling the ability of cells to form barriers by external stimuli, provides the application of optogenetic tools, representing the phenomenon of light-induced cell-cell interactions. Expressing photoswitchable proteins on the surface of the cells, allows the optical

stimulated activation and inactivation of cell clustering upon the precise and non-invasive use of light. The resembled change in cell barrier integrity has been electrically monitored for the first time by resistance measurements in **Chapter 8**. The red/far-red photosensitive protein CPH-1 has demonstrated, upon homodimerization, promising changes in resistance, arguing in favor for cell clustering. At this stage, other cell processes like cell migration and cell degradation could not be excluded so far. This triggers the demand for further investigation, including downscaling to microscopic probe sizes and consulting of additional microscopy techniques.

In summary, the first part of this work embraces material and device developments in OECTs. On the one hand, this has been achieved by improving transport properties of the benchmark conducting polymer for bioelectronics, which is directly reflected in the OECT performance. On the other hand, by defining new configurations of measuring OECTs, –the sensitivity in a biological relevant environment can be improved. The second part of this thesis directly encounters the field of bioelectronics. By defining the optimal regime for impedance-based sensors, the impedance mismatch between measuring devices and biological tissues can be minimized. New configurations of the measuring OECT have been evaluated by studying its sensitivity on the barrier tissue integrity. And finally, the manipulation of tissue integrity has been studied with external stimuli as in chemicals and light.



# Zusammenfassung

Das stark aufstrebende Gebiet der Bioelektronik hat eine Reihe von vielversprechenden Bauteilen für biomedizinische Anwendungen hervorgebracht. Dazu gehört der organische elektrochemische Transistor (OECT) als Vorzeigemodell für hohe Signalverstärkung und ausgezeichnete Biokompatibilität bei geringer kosten- und zeitintensiver Fabrikation. Mittelpunkt dieser Arbeit ist die Entwicklung von leistungsstarken und hochempfindlichen OECTs für die Biosensorik, mit dem Ziel die Beurteilung von Zellschichtintegrität auf einer labelfreien und nicht-invasiven Art und Weise zu verbessern.

Zu diesem Zweck wurde die Etablierung verbesserter OECT-Leistungen in Bezug auf die Effizienz angestrebt, im Hinblick auf die Optimierung des leitfähigen Polymers PEDOT:PSS als aktives Material. Die Leitfähigkeit von PEDOT:PSS kann durch das Verfahren *Sekundärdotierung* mit Behandlungen hochsiedender Lösungsmittel weiter gesteigert werden. In **Kapitel 3** wurden mehrere organischen Lösungsmittelbehandlungen mit Dimethylsulfoxid (DMSO) untersucht und dessen Einfluss auf die OECT-Leistung bewertet. Hierbei wurden folgende Behandlungen angewendet: Mischen von PEDOT:PSS mit DMSO vor der Filmbeschichtung, das Aussetzen von einem PEDOT:PSS-Film einem gesättigten DMSO-Dampf und das Eintauchen eines PEDOT:PSS-Films in ein DMSO-Bad. Insbesondere das Eintauchverfahren führt zu einer stark verbesserten Leitfähigkeit mit einem Maximalwert über  $2100 \text{ S cm}^{-1}$ , welches zu höchster Transkonduktanz und Ein-/Aus-Verhältnis führt. Die verbesserte OECT-Leistung ist das Ergebnis einer erhöhten Ladungsträger-Mobilität, die durch eine Phasentrennung in hochleitfähigen PEDOT:PSS-reichen und PSS-reichen Domänen und eine verbesserte strukturelle Ordnung hervorgerufen wird. In der OECT-Konfiguration wird die Leitfähigkeit von PEDOT:PSS typischerweise um eine Größenordnung reduziert, aufgrund von Quellungseffekten in PEDOT:PSS bei Kontakt mit dem

Elektrolyten.

Die erzielte große Transistor-Transkonduktanz ermöglicht eine noch höhere Ionenempfindlichkeit, die mit Hilfe der stromgesteuerten Transistorkonfiguration noch um ein Vielfaches erhöht wird. **Kapitel 4** beschreibt die Überwindung der grundlegenden Nernst-Begrenzung um etwa eine Größenordnung in der Ionenempfindlichkeit durch die Reihenschaltung des OECT mit einem Stromgenerator. Die Ionenempfindlichkeit, normiert auf die Versorgungsspannung, größer als  $1200 \text{ mV V}^{-1} \text{ dec}^{-1}$ , hat den größten Wert für die Spannungsionenempfindlichkeit erreicht, der jemals für ionensensitive Transistoren berichtet wurde. Der stromgesteuerte OECT zeigt, dass es möglich ist, die Ionenempfindlichkeit von OECTs bei gleichzeitigem Niederspannungsbetrieb drastisch zu erhöhen, da der Strom den Betriebsbereich der Ionenkonzentration festlegt und somit die Empfindlichkeit nicht durch die Versorgungsspannung begrenzt wird. Die deutlich erhöhte Ionenempfindlichkeit wird durch den Einsatz einer ionenselektiven Membran beibehalten und gewährt den Einsatz als Hochleistungsbiosensor.

**Kapitel 5** greift dieses Thema weiter auf, indem es biologisches Material mit der organischen Bioelektronik schlussendlich verbindet. Der klassische Ansatz von Elektroden hat eine Richtlinie zur Minimierung von Impedanzfehlanpassungen von Messplattformen erarbeitet und stellt die Weichen für eine effizientere Biosensorik. Die Impedanzspektroskopie von PEDOT:PSS-beschichteten Goldelektroden verschiedener Größen hat den Einfluss der Impedanzdifferenzierung auf das Erfassungsvermögen von Elektroden in einem Elektroden/Zellmembran System gezeigt. Eine Vier-Elemente-Schaltung  $R_s - C_{EL} - R_{MEM} // C_{MEM}$  dient zur Modellierung dieses Systems und impliziert einen elektrodenflächenabhängigen Übergang von einem Nicht-Erfassungs- zu einem Erfassungsregime. Der entscheidende Faktor für die Biosensorfähigkeit ist das Verhältnis von  $\lambda = \frac{|Z_{MEM}|}{|Z_{EL}|}$ , welches einen höheren Wert für die Zellschichtimpedanz  $|Z_{MEM}|$  als die Elektrodenimpedanz  $|Z_{EL}|$  fordert.

Die bis zu diesem Zeitpunkt gewonnenen Erkenntnisse wurden nun auf das aktive Element OECT für Biosensorik-Anwendungen umgesetzt. Wasserstoffperoxid als Modell für Toxine und Krankheitserreger impliziert eine permanente Schädigung der Zellschichtbarriere, die vor allem durch Proteinkomplexe, sogenannter Tight Junctions (TJs), unterstützt wird. Die vielversprechende Kombination eines stromgesteuerten OECT mit einer integrierten Zellschicht hat die Erkennung von Barrierefunktionsstörungen in Bezug auf Empfindlichkeit und Zeitauflösung im Vergleich zu herkömmlichen traditionellen Techniken stark verbessert (**Kapitel 6**). Der Prozess der induzierten Zellöffnung kann im Detail als Variation der Ausgangsspannung erkannt werden, wobei das Erfassungsregime durch sorgfältig ausgewählte Dimension des OECT eingehalten wird.

Die Biosensorik der Zellschichtintegrität wurde in **Kapitel 7** durch den Einsatz von TJ-Modulatoren als Beispiel für chemische Impulse weiter intensiviert. Die temporäre Wirkung von TJ Modulatoren auf den Zusammenhalt von TJs zwischen benachbarten Zellen wurde auf Reversibilität der Membranbarriereöffnung genutzt, welches großes Potenzial für eine verbesserte Wirkstofffreisetzung über epitheliale Barrieren besitzt. Eine konzentrationsabhängige Kontrolle der reversiblen Öffnung von TJs wurde für Poly-L-lysin, einen kationischen Polymerkandidaten von TJ-Modulatoren, durch die Änderung des Einschwingverhaltens des OECT detektiert. Dies öffnet die Türen für zeit- und dosisabhängige Untersuchungen von kationischen Polymeren und anderen TJ-Modulatorsystemen, um eine höhere Empfindlichkeit und zeitliche Auflösung zu erreichen, insbesondere durch den Einsatz des OECT in der stromgetriebenen Konfiguration.

Ein weiterer Schritt zur Kontrolle der Fähigkeit von Zellen, Barrieren durch äußere Reize zu bilden, ist die Anwendung optogenetischer Hilfsmittel, die das Phänomen der lichtinduzierten Zell-Zell-Interaktionen darstellt. Die Expression photoschaltbarer Proteine auf der Zelloberfläche ermöglicht die optisch-stimulierte Aktivierung und Inaktivierung von Zellgruppierung durch die präzise und nicht-invasive Verwendung von Licht. Die Änderung der Integrität in der Zellbarriere wurde erstmals durch Widerstandsmessungen in **Kapitel 8** elektrisch aufgenommen. Das rot-farblose lichtempfindliche Protein CPH-1 hat nach der Homodimerisierung vielversprechende Widerstandsänderungen gezeigt, die für eine positive Zellgruppierung sprechen. Andere Zellprozesse wie Zellmigration und Zellabbau konnten zu diesem Zeitpunkt jedoch bisher nicht ausgeschlossen werden. Dies löst den Bedarf an weiteren Untersuchungen aus, einschließlich der Verkleinerung der Probengröße auf mikroskopische Dimensionen und des Heranziehens zusätzlicher Mikroskopietechniken.

Zusammenfassend beinhaltet der erste Teil dieser Arbeit die Material- und Bauteilentwicklung in OECTs. Einerseits wurde dies durch die Verbesserung der Transporteigenschaften des Benchmark-Leitpolymers für die Bioelektronik erreicht, welches sich direkt in der OECT-Leistung widerspiegelt. Andererseits kann durch die Definition neuer Konfigurationen der Messung von OECTs die Empfindlichkeit in einer biologisch relevanten Umgebung verbessert werden. Der zweite Teil dieser Arbeit umfasst sich direkt mit dem Bereich der Bioelektronik. Durch die Definition des optimalen Regimes für impedanzbasierte Sensoren kann die Impedanz-Fehlanpassung zwischen Messgeräten und biologischen Geweben minimiert werden. Neue Konfigurationen der OECT-Messung wurden in Hinblick auf seine Empfindlichkeit für die Untersuchung der Zellschichtintegrität evaluiert. Abschließend wurde die Manipulation der Zellschichtintegrität mit äußeren Reizen wie z.B. mit Chemikalien und Licht untersucht.





# References

- [1] R. M. Owens, G. G. Malliaras, *MRS Bull.* **2010**, 35, 449.
- [2] M. Berggren, A. Richter-Dahlfors, *Adv. Mater.* **2007**, 19, 3201.
- [3] D. Khodagholy, J. Rivnay, M. Sessolo, M. Gurfinkel, P. Leleux, L. H. Jimison, E. Stavrinidou, T. Herve, S. Sanaur, R. M. Owens, G. G. Malliaras, *Nat. Commun.* **2013**, 4, 2133.
- [4] J. Rivnay, P. Leleux, M. Ferro, M. Sessolo, A. Williamson, D. A. Koutsouras, D. Khodagholy, M. Ramuz, X. Strakosas, R. M. Owens, C. Benar, J.-M. Badier, C. Bernard, G. G. Malliaras, *Sci. Adv.* **2015**, 1, e1400251.
- [5] J. Rivnay, S. Inal, A. Salleo, R. M. Owens, M. Berggren, G. G. Malliaras, *Nat. Rev. Mater.* **2018**, 3, 17086.
- [6] L. H. Jimison, S. A. Tria, D. Khodagholy, M. Gurfinkel, E. Lanzarini, A. Hama, G. G. Malliaras, R. M. Owens, *Adv. Mater.* **2012**, 24, 5919.
- [7] M. Ramuz, A. Hama, J. Rivnay, P. Leleux, R. M. Owens, *J. Mater. Chem. B* **2015**, 3, 5971.
- [8] S. A. Tria, L. H. Jimison, A. Hama, M. Bongo, R. M. Owens, *Biochim. Biophys. Acta* **2013**, 1830, 4381.
- [9] M. A. Deli, *Biochim. Biophys. Acta* **2009**, 1788, 892.
- [10] I. Willner, E. Katz, *Bioelectronics: From theory to applications*, Wiley-VCH, Weinheim **2005**.
- [11] J. Rivnay, R. M. Owens, G. G. Malliaras, *Chem. Mater.* **2014**, 26, 679.
- [12] D. T. Simon, E. O. Gabrielsson, K. Tybrandt, M. Berggren, *Chem. Rev.* **2016**, 116, 13009.
- [13] Servier Medical Art by Servier, licensed under a Creative Commons Attribution 3.0 Unported License, <https://creativecommons.org/licenses/by/3.0/>.

- [14] J. Rivnay, S. Inal, B. A. Collins, M. Sessolo, E. Stavrinidou, X. Strakosas, C. Tassone, D. M. Delongchamp, G. G. Malliaras, *Nat. Commun.* **2016**, *7*, 11287.
- [15] M. Nikolou, G. G. Malliaras, *Chem. Rec.* **2008**, *8*, 13.
- [16] M. Berggren, X. Crispin, S. Fabiano, M. P. Jonsson, D. T. Simon, E. Stavrinidou, K. Tybrandt, I. Zozoulenko, *Adv. Mater.* **2019**.
- [17] X. Strakosas, M. Bongo, R. M. Owens, *J. Appl. Polym. Sci.* **2015**, *132*, 41735.
- [18] L. Groenendaal, F. Jonas, D. Freitag, H. Pielartzik, J. R. Reynolds, *Adv. Mater.* **2000**, *12*, 481.
- [19] M. Lefebvre, Z. Qi, D. Rana, P. G. Pickup, *Chem. Mater.* **1999**, *11*, 262.
- [20] X. Cui, D. C. Martin, *Sens. Actuators, B* **2003**, *89*, 92.
- [21] A. Elschner, *PEDOT: Principles and applications of an intrinsically conductive polymer*, CRC Press, Boca Raton, FL **2011**.
- [22] Hereaus Deutschland GmbH & Co. KG, Leverkusen, *Production Sheet CLEVIOS™ PH 1000*.
- [23] H. Shi, C. Liu, Q. Jiang, J. Xu, *Adv. Electron. Mater.* **2015**, *1*, 1500017.
- [24] Hereaus Deutschland GmbH & Co. KG, Leverkusen, *Production Sheet CLEVIOS™ P VP AI 4083*.
- [25] F. Zabihi, Y. Xie, S. Gao, M. Eslamian, *Appl. Surf. Sci.* **2015**, *338*, 163.
- [26] C. M. Palumbiny, J. Schlipf, A. Hexemer, C. Wang, P. Müller-Buschbaum, *Adv. Electron. Mater.* **2016**, *2*, 1500377.
- [27] E. Stavrinidou, P. Leleux, H. Rajaona, D. Khodagholy, J. Rivnay, M. Lindau, S. Sanaur, G. G. Malliaras, *Adv. Mater.* **2013**, *25*, 4488.
- [28] C. Duc, A. Vlandas, G. G. Malliaras, V. Senez, *Soft Matter* **2016**, *12*, 5146.
- [29] A. Moujoud, S. H. Oh, H. S. Shin, H. J. Kim, *Phys. Stat. Sol. (a)* **2010**, *207*, 1704.
- [30] Y.-J. Lin, F.-M. Yang, C.-Y. Huang, W.-Y. Chou, J. Chang, Y.-C. Lien, *Appl. Phys. Lett.* **2007**, *91*, 92127.
- [31] A. Benor, S.-y. Takizawa, C. Pérez-Bolívar, P. Anzenbacher, *Org. Electron.* **2010**, *11*, 938.
- [32] J. Huang, P. F. Miller, J. S. Wilson, A. J. de Mello, J. C. de Mello, D. D. C. Bradley, *Adv. Funct. Mater.* **2005**, *15*, 290.
- [33] B. Friedel, P. E. Keivanidis, T. J. K. Brenner, A. Abrusci, C. R. McNeill, R. H. Friend, N. C. Greenham, *Macromolecules* **2009**, *42*, 6741.
- [34] Y. Kim, A. Ballanyne, J. Nelson, D. Bradley, *Org. Electron.* **2009**, *10*, 205.
- [35] C. Badre, L. Marquant, A. M. Alsayed, L. A. Hough, *Adv. Funct. Mater.* **2012**, *22*, 2723.
- [36] J. Y. Oh, M. Shin, J. B. Lee, J.-H. Ahn, H. K. Baik, U. Jeong, *ACS Appl. Mater. Interfaces* **2014**, *6*, 6954.
- [37] Y. Xia, J. Ouyang, *Macromolecules* **2009**, *42*, 4141.
- [38] I. Cruz-Cruz, M. Reyes-Reyes, R. López-Sandoval, *Thin Solid Films* **2013**, *531*, 385.
- [39] L. Tan, H. Zhou, T. Ji, L. Huang, Y. Chen, *Org. Electron.* **2016**, *33*, 316.

- [40] Z. Fan, P. Li, D. Du, J. Ouyang, *Adv. Energy Mater.* **2017**, 7, 1602116.
- [41] A. K. K. Kyaw, T. A. Yemata, X. Wang, S. L. Lim, W. S. Chin, K. Hippalgaonkar, J. Xu, *Macromol. Mater. Eng.* **2018**, 303, 1700429.
- [42] X. Wang, A. K. K. Kyaw, C. Yin, F. Wang, Q. Zhu, T. Tang, P. I. Yee, J. Xu, *RSC Adv.* **2018**, 8, 18334.
- [43] N. Kim, S. Kee, S. H. Lee, B. H. Lee, Y. H. Kahng, Y.-R. Jo, B.-J. Kim, K. Lee, *Adv. Mater.* **2014**, 26, 2268.
- [44] X. Crispin, S. Marciniak, W. Osikowicz, G. Zotti, Gon, A. W. Denier van der, F. Louwet, M. Fahlman, L. Groenendaal, F. de Schryver, W. R. Salaneck, *J. Polym. Sci. Part B: Polym. Phys.* **2003**, 41, 2561.
- [45] X. Crispin, F. L. E. Jakobsson, A. Crispin, P. C. M. Grim, P. Andersson, A. Volodin, C. van Haesendonck, M. Van der Auweraer, W. R. Salaneck, M. Berggren, *Chem. Mater.* **2006**, 18, 4354.
- [46] D. Alemu Mengistie, P.-C. Wang, C.-W. Chu, *J. Mater. Chem. A* **2013**, 1, 9907.
- [47] C. M. Palumbiny, C. Heller, C. J. Schaffer, V. Körstgens, G. Santoro, S. V. Roth, P. Müller-Buschbaum, *J. Phys. Chem. C* **2014**, 118, 13598.
- [48] S. Timpanaro, M. Kemerink, F. J. Touwslager, M. M. de Kok, S. Schrader, *Chem. Phys. Lett.* **2004**, 394, 339.
- [49] A. M. Nardes, M. Kemerink, R. A. J. Janssen, J. A. M. Bastiaansen, N. M. M. Kiggen, B. M. W. Langeveld, A. J. J. M. van Breemen, M. M. de Kok, *Adv. Mater.* **2007**, 19, 1196.
- [50] Y. H. Kim, C. Sachse, M. L. Machala, C. May, L. Müller-Meskamp, K. Leo, *Adv. Funct. Mater.* **2011**, 21, 1076.
- [51] T.-R. Chou, S.-H. Chen, Y.-T. Chiang, T.-T. Chang, C.-W. Lin, C.-Y. Chao, *Org. Electron.* **2017**, 48, 223.
- [52] D. Alemu, H.-Y. Wei, K.-C. Ho, C.-W. Chu, *Energy Environ. Sci.* **2012**, 5, 9662.
- [53] S.-I. Na, S.-S. Kim, J. Jo, D.-Y. Kim, *Adv. Mater.* **2008**, 20, 4061.
- [54] H. Göbel, *Einführung in die Halbleiter-Schaltungstechnik: [mit dem interaktiven Lehr- und Lernprogramm S.m.i.L.E.]*, Springer, Berlin [u.a.] **2011**.
- [55] J. Zaumseil, H. Sirringhaus, *Chem. Rev.* **2007**, 107, 1296.
- [56] D. A. Bernards, R. M. Owens, G. G. Malliaras, *Organic semiconductors in sensor applications*, Springer, Berlin **2008**.
- [57] L. Torsi, M. Magliulo, K. Manoli, G. Palazzo, *Chem. Soc. Rev.* **2013**, 42, 8612.
- [58] K. Schmoltner, J. Kofler, A. Klug, E. J. W. List-Kratochvil, *Adv. Mater.* **2013**, 25, 6895.
- [59] H. S. White, G. P. Kittleson, M. S. Wrighton, *J. Am. Chem. Soc.* **1984**, 106, 5375.
- [60] J. Rivnay, P. Leleux, M. Sessolo, D. Khodagholy, T. Hervé, M. Fiocchi, G. G. Malliaras, *Adv. Mater.* **2013**, 25, 7010.
- [61] S. Inal, J. Rivnay, A. I. Hofmann, I. Uguz, M. Mumtaz, D. Katsigiannopoulos, C. Brochon, E. Cloutet, G. Hadziioannou, G. G. Malliaras, *J. Polym. Sci. Part B: Polym. Phys.* **2016**, 54, 147.

- [62] A.-M. Pappa, S. Inal, K. Roy, Y. Zhang, C. Pitsalidis, A. Hama, J. Pas, G. G. Malliaras, R. M. Owens, *ACS Appl. Mater. Interfaces* **2017**, 9, 10427.
- [63] D. A. Bernardis, G. G. Malliaras, *Adv. Funct. Mater.* **2007**, 17, 3538.
- [64] P. Leleux, J. Rivnay, T. Lonjaret, J.-M. Badier, C. Bénar, T. Hervé, P. Chauvel, G. G. Malliaras, *Adv. Healthcare Mater.* **2015**, 4, 142.
- [65] C. Liao, C. Mak, M. Zhang, H. L. W. Chan, F. Yan, *Adv. Mater.* **2015**, 27, 676.
- [66] A. Williamson, M. Ferro, P. Leleux, E. Ismailova, A. Kaszas, T. Doublet, P. Quilichini, J. Rivnay, B. Rózsa, G. Katona, C. Bernard, G. G. Malliaras, *Adv. Mater.* **2015**, 27, 4405.
- [67] C. Yao, Q. Li, J. Guo, F. Yan, I.-M. Hsing, *Adv. Healthcare Mater.* **2015**, 4, 528.
- [68] D. Khodagholy, T. Doublet, P. Quilichini, M. Gurfinkel, P. Leleux, A. Ghestem, E. Ismailova, T. Hervé, S. Sanaur, C. Bernard, G. G. Malliaras, *Nat. Commun.* **2013**, 4, 1575.
- [69] A. Campana, T. Cramer, D. T. Simon, M. Berggren, F. Biscarini, *Adv. Mater.* **2014**, 26, 3874.
- [70] X. Gu, C. Yao, Y. Liu, I.-M. Hsing, *Adv. Healthcare Mater.* **2016**, 5, 2345.
- [71] M. Ramuz, K. Margita, A. Hama, P. Leleux, J. Rivnay, I. Bazin, R. M. Owens, *Chem. Phys. Chem.* **2015**, 16, 1210.
- [72] J. Rivnay, P. Leleux, A. Hama, M. Ramuz, M. Huerta, G. G. Malliaras, R. M. Owens, *Sci. Rep.* **2015**, 5, 11613.
- [73] D. A. Bernardis, D. J. Macaya, M. Nikolou, J. A. DeFranco, S. Takamatsu, G. G. Malliaras, *J. Mater. Chem.* **2008**, 18, 116.
- [74] M. Braendlein, A.-M. Pappa, M. Ferro, A. Lopresti, C. Acquaviva, E. Mamessier, G. G. Malliaras, R. M. Owens, *Adv. Mater.* **2017**, 29.
- [75] D. Khodagholy, V. F. Curto, K. J. Fraser, M. Gurfinkel, R. Byrne, D. Diamond, G. G. Malliaras, F. Benito-Lopez, R. M. Owens, *J. Mater. Chem.* **2012**, 22, 4440.
- [76] S. Casalini, F. Leonardi, T. Cramer, F. Biscarini, *Org. Electron.* **2013**, 14, 156.
- [77] G. Scheiblin, A. Aliane, R. Coppard, R. M. Owens, P. Mailley, G. G. Malliaras, in *Proc. SPIE*, Vol. 95681, p. 95681.
- [78] H. Tang, P. Lin, H. L. W. Chan, F. Yan, *Biosens. Bioelectron.* **2011**, 26, 4559.
- [79] Y. Kim, J. Do, J. Kim, S. Y. Yang, G. G. Malliaras, C. K. Ober, E. Kim, *Jpn. J. Appl. Phys.* **2010**, 49, 1.
- [80] A.-M. Pappa, V. F. Curto, M. Braendlein, X. Strakosas, M. J. Donahue, M. Fiocchi, G. G. Malliaras, R. M. Owens, *Adv. Healthcare Mater.* **2016**, 5, 2295.
- [81] E. Bihar, Y. Deng, T. Miyake, M. Saadaoui, G. G. Malliaras, M. Rolandi, *Sci. Rep.* **2016**, 6, 27582.
- [82] G. Scheiblin, R. Coppard, R. M. Owens, P. Mailley, G. G. Malliaras, *Adv. Mater. Technol.* **2017**, 2, 1600141.
- [83] M. Ghittorelli, L. Lingstedt, P. Romele, N. I. Crăciun, Z. M. Kovács-Vajna, P. W. M. Blom, F. Torricelli, *Nat. Commun.* **2018**, 9, 1441.
- [84] M. Braendlein, T. Lonjaret, P. Leleux, J.-M. Badier, G. G. Malliaras, *Adv. Sci.* **2017**, 4, 1600247.

- [85] P. Gkoupidenis, N. Schaefer, X. Strakosas, J. A. Fairfield, G. G. Malliaras, *Appl. Phys. Lett.* **2015**, *107*, 263302.
- [86] P. Gkoupidenis, N. Schaefer, B. Garlan, G. G. Malliaras, *Adv. Mater.* **2015**, *27*, 7176.
- [87] Y. van de Burgt, E. Lubberman, E. J. Fuller, S. T. Keene, G. C. Faria, S. Agarwal, M. J. Marinella, A. Alec Talin, A. Salleo, *Nat. Mater.* **2017**, *16*, 414.
- [88] B. Alberts, D. Bray, K. Hopkin, A. D. Johnson, J. Lewis, M. Raff, K. Roberts, P. Walter, *Essential Cell Biology*, CRC Press **2015**.
- [89] C. O'Connor, J. U. Adams, *Essentials of Cell Biology* **2014**, <https://www.nature.com/scitable>.
- [90] B. Alberts, *Molecular biology of the cell*, Garland Science, New York, NY **2015**.
- [91] S. A. Tria, M. Ramuz, M. Huerta, P. Leleux, J. Rivnay, L. H. Jimison, A. Hama, G. G. Malliaras, R. M. Owens, *Adv. Healthcare Mater.* **2014**, *3*, 1053.
- [92] K. Sonaje, E.-Y. Chuang, K.-J. Lin, T.-C. Yen, F.-Y. Su, M. T. Tseng, H.-W. Sung, *Mol. Pharmaceutics* **2012**, *9*, 1271.
- [93] S. Tria, L. Jimison, A. Hama, M. Bongo, R. M. Owens, *Biosensors* **2013**, *3*, 44.
- [94] S. A. Tria, M. Ramuz, L. H. Jimison, A. Hama, R. M. Owens, *J. Visualized Exp.* **2014**.
- [95] M. Sessolo, J. Rivnay, E. Bandiello, G. G. Malliaras, H. J. Bolink, *Adv. Mater.* **2014**, *26*, 4803.
- [96] M. T. Nieman, R. S. Prudoff, K. R. Johnson, M. J. Wheelock, *J Cell Biol* **1999**, *147*, 631.
- [97] G. Gstraunthaler, T. Lindl, *Zell- und Gewebekultur*, Springer Berlin Heidelberg, Berlin, Heidelberg **2013**.
- [98] Y. Zhang, S. Inal, C.-Y. Hsia, M. Ferro, M. Ferro, S. Daniel, R. M. Owens, *Adv. Funct. Mater.* **2016**, *26*, 7304.
- [99] I. Lee, G. W. Kim, M. Yang, T.-S. Kim, *ACS Appl. Mater. Interfaces* **2016**, *8*, 302.
- [100] J. Ouyang, Q. Xu, C.-W. Chu, Y. Yang, G. Li, J. Shinar, *Polymer* **2004**, *45*, 8443.
- [101] S.-I. Na, G. Wang, S.-S. Kim, T.-W. Kim, S.-H. Oh, B.-K. Yu, T. Lee, D.-Y. Kim, *J. Mater. Chem.* **2009**, *19*, 9045.
- [102] J.-S. Yeo, J.-M. Yun, D.-Y. Kim, S. Park, S.-S. Kim, M.-H. Yoon, T.-W. Kim, S.-I. Na, *ACS Appl. Mater. Interfaces* **2012**, *4*, 2551.
- [103] J. Luo, D. Billep, T. Waechtler, T. Otto, M. Toader, O. Gordan, E. Sheremet, J. Martin, M. Hietschold, D. R. T. Zahn, T. Gessner, *J. Mater. Chem. A* **2013**, *1*, 7576.
- [104] Q. Jiang, C. Liu, H. Song, H. Shi, Y. Yao, J. Xu, G. Zhang, B. Lu, *J Mater Sci: Mater Electron* **2013**, *24*, 4240.
- [105] L. Bießmann, L. P. Kreuzer, T. Widmann, N. Hohn, J.-F. Moulin, P. Müller-Buschbaum, *ACS Appl. Mater. Interfaces* **2018**, *10*, 9865.
- [106] H. Okuzaki, Y. Harashina, H. Yan, *Eur. Polym. J.* **2009**, *45*, 256.
- [107] D. McGillivray, J. P. Thomas, M. Abd-Ellah, N. F. Heinig, K. T. Leung, *ACS Appl. Mater. Interfaces* **2016**, *8*, 34303.
- [108] Q. Wei, M. Mukaida, Y. Naitoh, T. Ishida, *Adv. Mater.* **2013**, *25*, 2831.

- [109] Sigma-Aldrich, *Safety Data Sheet Sheet of dimethyl sulfoxide* **2016**.
- [110] N. A. Campbell, J. B. Reece, *Biology*, Pearson/Cummings, San Francisco, Calif. **2008**.
- [111] P. M. Quinton, *Nature* **1983**, 301.
- [112] N. U. Sulzer, M. P. Schweltnus, T. U. Noakes, *Med. Sci. Sports Exercise* **2005**, 37, 1081.
- [113] B. O. Tayo, A. Luke, C. A. McKenzie, H. Kramer, G. Cao, R. Durazo-Arvizu, T. Forrester, A. A. Adeyemo, R. S. Cooper, *J. Hum. Hypertens.* **2012**, 26, 315.
- [114] S. A.M. Marzouk, R. P. Buck, L. A. Dunlap, T. A. Johnson, W. E. Cascio, *Anal. Biochem.* **2002**, 308, 52.
- [115] A. Gholizadeh, D. Voiry, C. Weisel, A. Gow, R. Laumbach, H. Kipen, M. Chhowalla, M. Javanmard, *Microsyst. Nanoeng.* **2017**, 3, 17022.
- [116] A. Bratov, N. Abramova, A. Ipatov, *Anal. Chim. Acta* **2010**, 678, 149.
- [117] T. Someya, Z. Bao, G. G. Malliaras, *Nature* **2016**, 540, 379.
- [118] Y. T. Yew, A. Ambrosi, M. Pumera, *Sci. Rep.* **2016**, 6, 33276.
- [119] J. D. Yuen, S. A. Walper, B. J. Melde, M. A. Daniele, D. A. Stenger, *Sci. Rep.* **2017**, 7, 40867.
- [120] W. Gao, S. Emaminejad, H. Y. Y. Nyein, S. Challa, K. Chen, A. Peck, H. M. Fahad, H. Ota, H. Shiraki, D. Kiriya, D.-H. Lien, G. A. Brooks, R. W. Davis, A. Javey, *Nature* **2016**, 529, 509.
- [121] O. Knopfmacher, M. L. Hammock, A. L. Appleton, G. Schwartz, J. Mei, T. Lei, J. Pei, Z. Bao, *Nat. Commun.* **2014**, 5, 2954.
- [122] S. Imani, A. J. Bandodkar, A. M. V. Mohan, R. Kumar, S. Yu, J. Wang, P. P. Mercier, *Nat. Commun.* **2016**, 7, 11650.
- [123] S. H. Kim, K. Hong, W. Xie, K. H. Lee, S. Zhang, T. P. Lodge, C. D. Frisbie, *Adv. Mater.* **2013**, 25, 1822.
- [124] M. Spijkman, E. C. P. Smits, J. F. M. Cillessen, F. Biscarini, P. W. M. Blom, D. M. de Leeuw, *Appl. Phys. Lett.* **2011**, 98, 43502.
- [125] O. Knopfmacher, A. Tarasov, W. Fu, M. Wipf, B. Niesen, M. Calame, C. Schönenberger, *Nano Lett.* **2010**, 10, 2268.
- [126] T. Ji, P. Rai, S. Jung, V. K. Varadan, *Appl. Phys. Lett.* **2008**, 92, 233304.
- [127] M.-J. Spijkman, J. J. Brondijk, T. C. T. Geuns, E. C. P. Smits, T. Cramer, F. Zerbetto, P. Stolar, F. Biscarini, P. W. M. Blom, D. M. de Leeuw, *Adv. Funct. Mater.* **2010**, 20, 898.
- [128] M. Yano, K. Koike, K. Mukai, T. Onaka, Y. Hirofuji, K.-i. Ogata, S. Omatu, T. Maemoto, S. Sasa, *Phys. Stat. Sol. (a)* **2014**, 211, 2098.
- [129] E. Stern, J. F. Klemic, D. A. Routenberg, P. N. Wyrembak, D. B. Turner-Evans, A. D. Hamilton, D. A. LaVan, T. M. Fahmy, M. A. Reed, *Nature* **2007**, 445, 519.
- [130] N. Kumar, J. Kumar, S. Panda, *IEEE Electron Device Lett.* **2016**, 37, 500.
- [131] W. Fu, C. Nef, A. Tarasov, M. Wipf, R. Stoop, O. Knopfmacher, M. Weiss, M. Calame, C. Schöneberger, *Nanoscale* **2013**, 5, 12104.
- [132] F. Buth, D. Kumar, M. Stutzmann, J. A. Garrido, *Appl. Phys. Lett.* **2011**, 98, 153302.

- [133] K. Tybrandt, R. Forchheimer, M. Berggren, *Nat. Commun.* **2012**, *3*, 871.
- [134] P. Lin, F. Yan, H. L. W. Chan, *ACS Appl. Mater. Interfaces* **2010**, *2*, 1637.
- [135] W. B. Guggino, B. A. Stanton, *Nat. Rev. Mol. Cell Biol.* **2006**, *7*, 426.
- [136] S. Park, S. H. Baek, S. W. Lee, A. Lee, H. J. Chin, K. Y. Na, Y. S. Kim, D.-W. Chae, J. S. Han, S. Kim, *Sci. Rep.* **2017**, *7*, 2402.
- [137] E. Cantatore, T. C. T. Geuns, G. H. Gelinck, E. van Veenendaal, A. F. A. Gruijthuijsen, L. Schrijnemakers, S. Drews, D. M. de Leeuw, *IEEE J. Solid-State Circuits* **2007**, *42*, 84.
- [138] M.-J. Spijkman, K. Myny, E. C. P. Smits, P. Heremans, P. W. M. Blom, D. M. de Leeuw, *Adv. Mater.* **2011**, *23*, 3231.
- [139] Y. Honma, K. Itoh, H. Masunaga, A. Fujiwara, T. Nishizaki, S. Iguchi, T. Sasaki, *Adv. Electron. Mater.* **2018**, *4*, 1700490.
- [140] S. Inal, G. G. Malliaras, J. Rivnay, *J. Mater. Chem. C* **2016**, *4*, 3942.
- [141] J. O. Guardado, A. Salleo, *Adv. Funct. Mater.* **2017**, *27*, 1701791.
- [142] G. Wallace, G. Spinks, *Soft Matter* **2007**, *3*, 665.
- [143] A. Blau, A. Murr, S. Wolff, E. Sernagor, P. Medini, G. Iurilli, C. Ziegler, F. Benfenati, *Biomaterials* **2011**, *32*, 1778.
- [144] D. C. Martin, *MRC* **2015**, *5*, 131.
- [145] R. Green, M. R. Abidian, *Adv. Mater.* **2015**, *27*, 7620.
- [146] D. C. Martin, G. G. Malliaras, *Chem. Electro. Chem.* **2016**, *3*, 686.
- [147] D. A. Koutsouras, A. Hama, J. Pas, P. Gkoupidenis, B. Hivert, C. Faivre-Sarrailh, E. Di Pasquale, R. M. Owens, G. G. Malliaras, *MRC* **2017**, *7*, 259.
- [148] J. Pas, C. Pitsalidis, D. A. Koutsouras, P. P. Quilichini, F. Santoro, B. Cui, L. Gallais, R. P. O'Connor, G. G. Malliaras, R. M. Owens, *Adv. Biosys.* **2018**, *2*, 1700164.
- [149] N. Y. Shim, D. A. Bernards, D. J. Macaya, J. A. DeFranco, M. Nikolou, R. M. Owens, G. G. Malliaras, *Sensors* **2009**, *9*, 9896.
- [150] D. T. Simon, S. Kurup, K. C. Larsson, R. Hori, K. Tybrandt, M. Goiny, E. W. H. Jager, M. Berggren, B. Canlon, A. Richter-Dahlfors, *Nat. Mater.* **2009**, *8*, 742.
- [151] P. Gkoupidenis, D. A. Koutsouras, G. G. Malliaras, *Nat. Commun.* **2017**, *8*, 15448.
- [152] E. Stavrinidou, R. Gabrielsson, E. Gomez, X. Crispin, O. Nilsson, D. T. Simon, M. Berggren, *Sci. Adv.* **2015**, *1*, e1501136.
- [153] R. T. Richardson, B. Thompson, S. Moulton, C. Newbold, M. G. Lum, A. Cameron, G. Wallace, R. Kapsa, G. Clark, S. O'Leary, *Biomaterials* **2007**, *28*, 513.
- [154] M. R. Abidian, J. M. Corey, D. R. Kipke, D. C. Martin, *Small* **2010**, *6*, 421.
- [155] D. A. Bernards, G. G. Malliaras, G. E. S. Toombes, S. M. Gruner, *Appl. Phys. Lett.* **2006**, *89*, 53505.
- [156] K. Benson, S. Cramer, H.-J. Galla, *Fluids Barriers CNS* **2013**, *10*, 5.

- [157] M. S. Balda, J. A. Whitney, C. Flores, S. Gonzalez, M. Cereijido, K. Matter, *J. Cell Biol.* **1996**, 134.
- [158] V. Y. Soldatow, E. L. Lecluyse, L. G. Griffith, I. Rusyn, *Toxicol. Res.* **2013**, 2, 23.
- [159] B. Srinivasan, A. R. Kolli, M. B. Esch, H. E. Abaci, M. L. Shuler, J. J. Hickman, *J. Lab. Autom.* **2015**, 20, 107.
- [160] G. C. Faria, D. T. Duong, A. Salleo, C. A. Polyzoidis, S. Logothetidis, J. Rivnay, R. Owens, G. G. Malliaras, *MRC* **2014**, 4, 189.
- [161] D. A. Koutsouras, P. Gkoupidenis, C. Stolz, V. Subramanian, G. G. Malliaras, D. C. Martin, *Chem. Electro. Chem.* **2017**, 5, 131.
- [162] J. Rivnay, M. Ramuz, P. Leleux, A. Hama, M. Huerta, R. M. Owens, *Appl. Phys. Lett.* **2015**, 106, 43301.
- [163] J. Newman, *J. Electrochem. Soc.* **1966**, 113, 501.
- [164] J. Wegener, D. Abrams, W. Willenbrink, H.-J. Galla, A. Janshoff, *Bio. Techniques* **2004**, 37, 590.
- [165] J. Wegener, C. R. Keese, I. Giaever, *Exp. Cell Res.* **2000**, 259, 158.
- [166] M. Ramuz, A. Hama, M. Huerta, J. Rivnay, P. Leleux, R. M. Owens, *Adv. Mater.* **2014**, 26, 7083.
- [167] X. Wu, A. Surendran, J. Ko, O. Filonik, E. M. Herzig, P. Müller-Buschbaum, W. L. Leong, *Adv. Mater.* **2018**.
- [168] D. A. Volpe, *J. Pharm. Sci.* **2008**, 97, 712.
- [169] A. K. Jonscher, *J. Phys. D: Appl. Phys.* **1999**, 32, 57.
- [170] J. M. Smith, M. Dornish, E. J. Wood, *Biomaterials* **2005**, 26, 3269.
- [171] A. A. Zubareva, E. V. Svirshchevskaya, *Appl. Biochem. Microbiol.* **2016**, 52, 465.
- [172] G. Ranaldi, I. Marigliano, I. Vespignani, G. Perozzi, Y. Sambuy, *J. Nutr. Biochem.* **2002**, 13, 157.
- [173] G. T.A. McEwan, M. A. Jepson, B. H. Hirst, N. L. Simmons, *Biochim. Biophys. Acta* **1993**, 1148, 51.
- [174] A. Merzlikine, C. Rotter, B. Rago, J. Poe, C. Christoffersen, V. H. Thomas, M. Troutman, A. El-Kattan, *Drug Dev. Ind. Pharm.* **2009**, 35, 1082.
- [175] M. Tomita, M. Hayashi, S. Awazu, *J. Pharm. Sci.* **1996**, 85, 608.
- [176] E. K. Anderberg, T. Lindmark, P. Artursson, *Pharm. Res.* **1993**, 10, 857.
- [177] H. Lin, M. Gebhardt, S. Bian, K. A. Kwon, C.-K. Shim, S.-J. Chung, D.-D. Kim, *Int. J. Pharm.* **2007**, 330, 23.
- [178] P. Schwille, J. Spatz, K. Landfester, E. Bodenschatz, S. Herminghaus, V. Sourjik, T. J. Erb, P. Bastiaens, R. Lipowsky, A. Hyman, P. Dabrock, J.-C. Baret, T. Vidakovic-Koch, P. Bieling, R. Dimova, H. Mutschler, T. Robinson, T.-Y. D. Tang, S. Wegner, K. Sundmacher, *Angew. Chem.* **2018**, 57, 13382.
- [179] P. Schwille, *Science* **2011**, 333, 1252.



- [180] T. Nakano, *Molecular communication*, Cambridge University Press, Cambridge **2013**.
- [181] P. Shi, E. Ju, Z. Yan, N. Gao, J. Wang, J. Hou, Y. Zhang, J. Ren, X. Qu, *Nat. Commun.* **2016**, *7*, 13088.
- [182] W. W. D. Mühlhäuser, A. Fischer, W. Weber, G. Radziwill, *Biochim. Biophys. Acta* **2017**, *1864*, 280.
- [183] E. Chervyachkova, S. V. Wegner, *ACS Synth. Biol.* **2018**, *7*, 1817.
- [184] S. M. Bartelt, J. Steinkühler, R. Dimova, S. V. Wegner, *Nano Lett.* **2018**, *18*, 7268.
- [185] F. Chen, S. V. Wegner, *ACS Synth. Biol.* **2017**, *6*, 2170.
- [186] S. M. Bartelt, E. Chervyachkova, J. Steinkühler, J. Ricken, R. Wieneke, R. Tampé, R. Dimova, S. V. Wegner, *Chem. Commun.* **2018**, *54*, 948.
- [187] G. Guntas, R. A. Hallett, S. P. Zimmerman, T. Williams, H. Yumerefendi, J. E. Bear, B. Kuhlman, *Proc. Natl. Acad. Sci. U.S.A.* **2015**, *112*, 112.
- [188] S. Chen, R. Einspanier, J. Schoen, *Histochem. Cell Biol.* **2015**, *144*, 509.
- [189] J. Hickman, *J. Rare Dis. Res. Treat.* **2016**, *1*, 46.



# Appendix

## Declaration

I hereby declare that I wrote the dissertation submitted without any unauthorized external assistance and used only sources acknowledged in this work. All textual passages which are appropriate verbatim or paraphrased from published and unpublished texts, as well as all information obtained from oral sources, are duly indicated and listed in accordance with bibliographical rules. In carrying out this research, I complied with the rules of standard scientific practice as formulated in the statutes of Johannes Gutenberg-University Mainz to insure standard scientific practice.

.....  
(Leona Lingstedt)

## List of Publications

1. D. A. Koutsouras, **L. V. Lingstedt**, J. Reinholz, R. M. Owens, V. Mailänder, P. W. M. Blom, P. Gkoupidenis **2019**, *in preparation*.
2. **L. V. Lingstedt**, M. Ghittorelli, J. Reinholz, N. I. Crăciun, F. Torricelli, V. Mailänder, P. Gkoupidenis, P. W. M. Blom, Monitoring of cell layer integrity with a current-driven organic electrochemical transistor, *Adv. Healthcare Mater.* **2019**, *submitted*.
3. **L. V. Lingstedt**, M. Ghittorelli, H. Lu, D. A. Koutsouras, T. Marszalek, F. Torricelli, N. I. Crăciun, P. Gkoupidenis, P. W. M. Blom, Effect of DMSO solvent treatments on the performance of PEDOT:PSS-based organic electrochemical transistors, Journal article in the submission process, *Adv. Electron. Mater.* **2018**, 26, 1800804.
4. M. Ghittorelli, **L. Lingstedt**, P. Romele, N. I. Crăciun, Z. M. Kovács-Vajna, P. W. M. Blom, F. Torricelli, High-sensitivity ion detection at low voltages with current-driven organic electrochemical transistors, *Nat. Commun.* **2018**, 9, 1441.

## Conference Contributions

1. **L. V. Lingstedt**, M. Ghittorelli, V. Mailänder, P. Gkoupidenis, P. W. M. Blom, Low Voltage Current-Driven Organic Electrochemical Transistor for Biomedical Applications, Oral Presentation at the MRS Fall Meeting 2018, Boston, United States of America.
2. **L. V. Lingstedt**, M. Ghittorelli, V. Mailänder, P. Gkoupidenis, P. W. M. Blom, Organic Electrochemical Transistor for Biological Applications, Oral Presentation at the Workshop “Advanced Materials” 2018, European Union’s Horizon 2020 program, Duni, Bulgaria
3. **L. V. Lingstedt**, M. Ghittorelli, V. Mailänder, P. Gkoupidenis, P. W. M. Blom, Organic Electrochemical Transistor for Biological Applications, Oral Presentation at the Highlight Colloquium at the Max Planck Institute for Polymer Research 2018, Mainz, Germany
4. Attendance, Physics of Life, IFF Spring School 2018, Jülich, Germany
5. **L. V. Lingstedt**, P. Gkoupidenis, N. I. Crăciun, P. W. M. Blom, Secondary Doping of PEDOT:PSS-based Organic Electrochemical Transistors, Poster at the ECME Conference 2017, Dresden, Germany
6. **L. V. Lingstedt**, M. Ghittorelli, N. I. Crăciun, P. W. M. Blom, Improved stability of PEDOT:PSS-based electrochemical transistors, Poster at the International Winterschool on Bioelectronics 2016, Kirchberg, Austria.
7. **L. V. Lingstedt**, M. Ghittorelli, F. Torricelli, N. I. Crăciun, P. W. M. Blom, Electrical characterization of PEDOT:PSS-based electrochemical transistor, Poster at the F $\pi$ -12 Symposium 2015, Seattle, United States of America.